Intensity based Multispectral Terahertz Polarimetric Imaging Using Frequency-Selective Surfaces

by

Redwan AHMAD

MANUSCRIPT BASED THESIS PRESENTED TO ÉCOLE DE TECHNOLOGIE SUPÉRIEURE IN PARTIAL FULFILLMENT FOR THE DEGREE OF DOCTOR OF PHILOSOPHY
Ph.D.

MONTREAL, MAY 21 2026

ÉCOLE DE TECHNOLOGIE SUPÉRIEURE
UNIVERSITÉ DU QUÉBEC

BOARD OF EXAMINERS

THIS THESIS HAS BEEN EVALUATED

BY THE FOLLOWING BOARD OF EXAMINERS

Dr. François Blanchard, Thesis Supervisor
Department of Electrical Engineering, École de technologie supérieure

Dr. Martin Viens, President of the Board of Examiners
Department of Mechanical Engineering, École de technologie supérieure

Dr. Dominic Deslandes, Member of the jury
Department of Electrical Engineering, École de technologie supérieure

Dr. Martin Rochette, External Evaluator
Department of Electrical and Computer Engineering, McGill University

THIS THESIS WAS PRENSENTED AND DEFENDED

IN THE PRESENCE OF A BOARD OF EXAMINERS AND PUBLIC

APRIL 21 2026

AT ÉCOLE DE TECHNOLOGIE SUPÉRIEURE

ACKNOWLEDGEMENTS

The undertaking of this PhD has been a truly transformative experience, and it would not have been possible without the support, guidance, and encouragement of many remarkable individuals who accompanied me throughout this journey.

First and foremost, I would like to express my deepest gratitude to my PhD supervisor, Professor François Blanchard, for his outstanding mentorship, continuous guidance, and unwavering support throughout my doctoral studies. My words are not enough, thanks my supervisor for everything. His real-time feedback, patience, and insightful scientific discussions have been invaluable to my development as a researcher. I sincerely thank him for his trust, encouragement, and motivation over the years, as well as for instilling in me a strong sense of scientific rigor and independence that will continue to guide my future career.

I would also like to thank Professor Richard Al Hadi for his insightful discussions and valuable support related to CMOS detector characterization. I am grateful to the members of my thesis committee, Professor Martin Viens and Professor Dominic Deslandes from École de technologie supérieure, and Professor Martin Rochette from McGill University for the time and effort they devoted to evaluating my thesis and for their constructive feedback and thoughtful comments.

I would like to warmly acknowledge all my current and former colleagues at TeraÉTS for their continuous support and collegial environment, both inside and outside the laboratory. In particular, I would like to thank Dr. Xavier Ropagnol for his immense support throughout my PhD, including experimental setup development, careful manuscript reviews, stimulating technical discussions etc. I am grateful for his generosity with time and expertise, which significantly influenced my research and professional development. I am also grateful to Dr. Mariia Zhulbydina for her inspiration and support, as well as for her valuable assistance during different stages of my research. I would like to sincerely thank Dr. Joel Edouard Nkeck and Dr. Léo Guiramand for their valuable discussions throughout my PhD journey. My sincere thanks also go to Dr. Gervais, Rejeena, Gabriel, Deepak, Jonathan, Audrey, Salim, Leyla, Charles, Maxim and Xavier Pinheiro for their constructive discussions, encouragement, and

many memorable activities beyond the lab. Apart from TeraÉTS group members, I am especially thankful to Dr. Mathieu Gratuze for his support throughout my doctoral journey. I would also like to thank Normand and Mustapha for their valuable technical support and assistance with the fabrication of the frequency-selective surface chopper.

I would also like to acknowledge Dr. Ngoc-Trinh Duc and Dr. Chloé Bois from ICI Montréal for providing me with the opportunity to complete a four-month internship focused on printable electronics. This experience was both enriching and formative, broadening my technical perspective and strengthening the applied dimension of my PhD research.

Finally, I would like to express my deepest gratitude to my parents (Mr. Alauddin Ahmad and Mrs. Marjina Khatun), my wife (Mrs. Tanjia Sultana), my beloved daughter (Nusaybah Ahmad) and all family members for their unconditional love, patience, and unwavering support. They have been a constant source of strength, motivation, and inspiration throughout this journey. This achievement would not have been possible without their encouragement, sacrifices, and blessings.

I gratefully acknowledge the financial support provided by the Fonds de recherche du Québec – Nature et technologies (FRQNT), which funded three years of my doctoral studies.

Imagerie polarimétrique térahertz multispectrale basée sur l'intensité utilisant des surfaces sélectives en fréquence

Redwan AHMAD

RÉSUMÉ

Les technologies térahertz (THz) offrent des capacités uniques pour le contrôle non destructif, la caractérisation des matériaux et l'imagerie ; toutefois, leur adoption à grande échelle demeure limitée par la taille, le coût et la complexité des systèmes spectroscopiques et polarimétriques conventionnels. Cette thèse aborde ces défis en étudiant des surfaces sélectives en fréquence térahertz (FSS) reconfigurables et leur intégration dans des systèmes polarimétriques THz compacts basés sur la mesure d'intensité, avec un accent particulier sur des procédés de fabrication évolutifs et des architectures système pratiques.

À la suite d'une revue de littérature exhaustive couvrant les techniques de génération et de détection THz, les concepts de FSS reconfigurables, ainsi que la spectroscopie et l'imagerie polarimétriques THz, les contributions principales portent sur le développement de différentes techniques de reconfigurabilité appliquées à des FSS THz imprimées. Des réponses spectrales accordables sont démontrées à l'aide de structures inductives métalliques de type damier et de configurations de FSS basées sur des motifs de Moiré, où la reconfigurabilité est obtenue respectivement par translation latérale et par rotation relative de couches empilées. Ces approches permettent un accord spectral compact et mécaniquement simple, sans recours à des matériaux actifs ni à des schémas de polarisation complexes.

Les conceptions de FSS autoportantes sensibles à la polarisation sont ensuite étudiées pour permettre une modulation dépendante de la polarisation et sélective en fréquence dans le régime térahertz. Des géométries de FSS symétriques et asymétriques, fabriquées à l'aide de techniques de découpe laser, présentent des caractéristiques de transmission dépendantes de la polarisation distinctes, permettant leur utilisation comme polariseurs sélectifs en fréquence et comme filtres passe-bande accordables. À partir de ces composants, un système compact d'imagerie polarimétrique THz multispectrale, reposant exclusivement sur des mesures d'intensité, est développé à l'aide d'un détecteur à diode Schottky, et les résultats expérimentaux suivent étroitement les résultats de simulation attendus. En acquérant des images d'intensité pour plusieurs orientations de l'analyseur et à des fréquences discrètes, le système permet l'extraction directe de paramètres polarimétriques tels que les paramètres de Stokes (S0, S1, S2), ainsi que le degré et l'angle de polarisation linéaire, sans détection sensible à la phase ni recours à des lignes à retard mécaniques. Le système est validé par imagerie polarimétrique d'échantillons anisotropes, démontrant un contraste de polarisation élevé et une robustesse pratique.

Des études supplémentaires présentées dans les annexes étendent la portée de la thèse à un spectromètre polarimétrique térahertz compact basé sur la technologie CMOS, doté d'une sensibilité intrinsèque à la polarisation, ainsi qu'à une approche simplifiée basée sur un détecteur pyroélectrique pour la caractérisation des matériaux biréfringents. Collectivement,

ces travaux font progresser les technologies de surfaces sélectives en fréquence térahertz reconfigurables (FSS) et les systèmes polarimétriques compacts, contribuant au développement de plateformes de détection et d'imagerie térahertz évolutives, robustes et adaptées aux applications industrielles.

Mots-clés : imagerie polarimétrique térahertz, spectromètre multispectral compact, surfaces sélectives en fréquence sensibles à la polarisation (FSS), FSS reconfigurables, découpe laser, électronique imprimée.

Intensity based Multispectral Terahertz Polarimetric Imaging Using Frequency-Selective Surfaces

Redwan AHMAD

ABSTRACT

Terahertz (THz) technologies offer unique capabilities for non-destructive sensing, material characterization, and imaging; however, their widespread adoption remains limited by the size, cost, and complexity of conventional spectroscopic and polarimetric systems. This thesis addresses these challenges by investigating reconfigurable terahertz frequency-selective surfaces (FSSs) and their integration into compact, intensity-based THz polarimetric systems, with an emphasis on scalable fabrication and practical system architectures.

Following a comprehensive literature review covering THz generation and detection techniques, reconfigurable FSS concepts, and THz polarimetric spectroscopy and imaging, the core contributions focus on the development of distinct reconfigurable techniques on printed THz FSSs. Tunable spectral responses are demonstrated using inductive metallic checkerboard structures and Moiré-based FSS configurations, where reconfigurability is achieved through lateral translation and relative rotation of stacked layers, respectively. These approaches enable compact and mechanically simple spectral tuning without the need for active materials or complex biasing schemes.

Free standing polarization-sensitive FSS designs are subsequently investigated to enable frequency-selective polarization dependent modulation in the THz regime. Symmetric and asymmetric FSS geometries fabricated using laser-cutting techniques exhibit distinct polarization-dependent transmission characteristics, allowing their use as frequency-selective polarizers and tunable band pass filters. Building on these components, a compact multispectral THz polarimetric imaging system based solely on intensity measurements is developed using Schottky diode detector and experimental results closely followed the expected simulation results. By acquiring intensity images at multiple analyzer orientations and discrete frequencies, the system enables direct extraction of polarization metrics such as Stokes parameter (S_0, S_1, S_2), the degree and angle of linear polarization without phase-sensitive detection and mechanical delay stages. The system is validated through polarimetric imaging of anisotropic samples, demonstrating high polarization contrast and practical robustness.

Additional studies presented in the annexes extend the scope of the thesis to a compact CMOS-based THz polarimetric spectrometer with intrinsic polarization sensitivity, and a simplified pyroelectric-detector-based approach for birefringent material characterization. Collectively, this work advances reconfigurable THz FSS technologies and compact polarimetric systems, contributing toward scalable, robust, and industrially relevant THz sensing and imaging platforms.

Keywords: THz polarimetric imaging, compact multispectral spectrometer, polarization sensitive FSS, reconfigurable FSS, laser cutting, printable electronics

TABLE OF CONTENTS

LIST OF TABLES

LIST OF FIGURES

LIST OF ABBREVIATIONS AND ACRONYMS

AC	Amplitude contrast
AoLP	Angle of linear polarization
BEOL	Back-end-of-line
BPF	Band-pass filters
BS	Beam splitter
BW	Bandwidth
c-MCB	Capacitive MCB
CW	Continuous-wave
DoLP	Degree of linear polarization
EBL	Electron beam lithography
EO	Electro-optic
FDM	Fused Deposition Modeling
FDS	Frequency-domain spectroscopy
FDTD	Finite difference time domain
FEM	Finite-element method
FFT	Fast Fourier transform
FSP	Frequency-selective polarizer
FSS	Frequency-selective surfaces
FWHM	Full Width at Half Maximum
i-MCB	Inductive metallic checkerboard
MD	Modulation depth
MS	Metasurface

NIR	Near-infrared
NT	Normalized transmission
OAM	Orbital angular momentum
OAP	Off-axis parabolic
PCA	Photoconductive antenna
PE	Printable electronics
PET	Polyethylene terephthalate
PML	Perfectly matched layer
PS-FSS	Polarization-sensitive frequency-selective surfaces
QCL	Quantum cascade lasers
SD	Standard deviation
SLA	Stereolithography
SLM	Selective Laser Melting
SNR	Signal-to-noise ratio
SPP	Spiral phase plates
SRR	Split-ring resonator
SZP	Spiral zone plates
THz	Terahertz
THz-TDS	THz time-domain spectroscopy
TPS	THz polarimetric spectrometer
FTIR	Fourier-transform infrared
WGP	wire-grid polarizer

LIST OF SYMBOLS AND UNITS OF MEASUREMENT

$E(t)$	Electric field
f_{opt}	Operating frequency
f_{peak}	Peak center frequency
f_{0°	Operating frequency for 0˚ polarization
f_{90°	Operating frequency for 90˚ polarization
I_0	Intensity at 0˚ orientation of analyzer
I_{45}	Intensity at 45˚ orientation of analyzer
I_{90}	Intensity at 90˚ orientation of analyzer
I_{135}	Intensity at 135˚ orientation of analyzer
l	Topological charge
L_{slot}	Effective slot length
Q	Quality factor
T	Transmittance
T_{sample}	FFT amplitude of the analyzed sample
T_{ref}	FFT amplitude in the case of without sample
α_r	Relative polarization angle
μ_{noise}	Mean of the noise floor
σ_{noise}	Standard deviation of the noise floor
θ_s	Sample rotation angle
Δ_{AoLP}	Variation in angle of linear polarization
Δn	Birefringence
ΔT_{xy}	Variation in transmission
$\Delta\phi$	Phase retardation

INTRODUCTION

0.1 Background and motivation

Terahertz (THz) radiation, spanning frequencies from 0.1 to 10 THz, corresponding to wavelengths between 3 mm and 30 µm, occupies the spectral region between microwaves and infrared light (Chen et al., 2006; Ferguson et al., 2002; Ghann et al., 2017; Heidari, 2015). THz radiation has emerged as a key technology in applications including medical imaging, security systems, healthcare, pharmaceuticals, and communication (Jepsen et al., 2010). Among these, spectroscopic characterization of materials remains the most mature and widely established application of THz technology to date. In addition to its spectroscopic capabilities, this frequency range is particularly attractive for imaging applications due to its ability to penetrate many non-conductive materials, such as plastics, paper, textiles, and polymers, while remaining non-ionizing and safe for biological tissues (Nakanishi & Satozono, 2020; Wietzke et al., 2009). Beyond conventional amplitude-based imaging, these characteristics make THz radiation particularly well suited for polarimetric imaging (see Fig. 0.2). In this context, polarization acts as an additional measurement dimension, enabling polarization-dependent interactions that provide enhanced contrast associated with material anisotropy, birefringence, internal stress distribution, and structural orientation (Van Der Valk et al., 2005; Li et al., 2023).

THz time-domain spectroscopy (THz-TDS) evolved from the development of optically gated photoconductive switches introduced by Auston in the late 1970s and early 1980s (Auston,

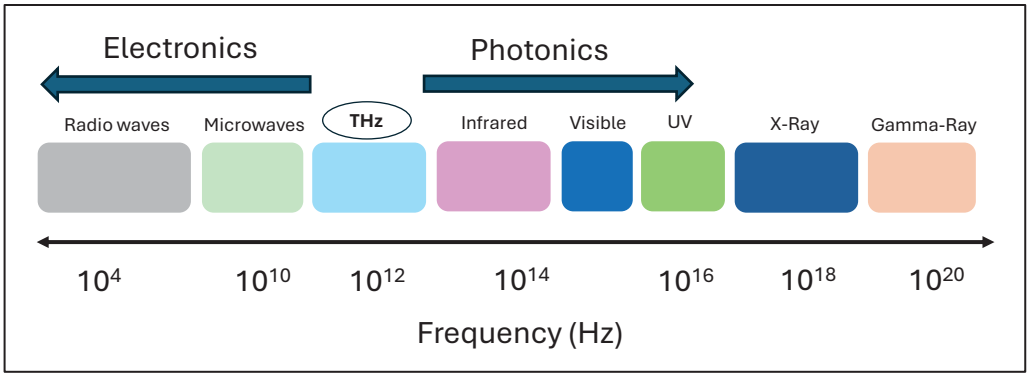

Figure 0.1 Spectral distribution of frequency in the electromagnetic spectrum

1975; Auston et al., 1983; Auston et al., 1984), enabling ultrafast generation and detection of electrical transients. By the early 1990s, these advances culminated in the development of THz-TDS, which enabled direct measurement of the electric field amplitude of THz pulses in the time domain (van Exter et al., 1989; Grischkowsky et al., 1990). The corresponding phase and broadband spectral information are subsequently obtained through Fourier transformation, allowing quantitative spectroscopic characterization of materials. This direct electric-field measurement fundamentally distinguishes THz-TDS from Fourier-transform infrared (FTIR) spectroscopy, which measures only intensity (Neu & Schmuttenmaer, 2018). In a typical THz-TDS configuration, an ultrafast optical pump pulse is used to generate the THz radiation, while a time-synchronized probe pulse samples the instantaneous THz electric field in a pump–probe scheme. A motorized mechanical delay line is employed to scan the relative arrival time between the THz and probe pulses, enabling reconstruction of the time-domain electric-field waveform. Two principal detection mechanisms are commonly employed in THz-TDS, namely electro-optic (EO) sampling and photoconductive antenna (PCA) detection (Warren et

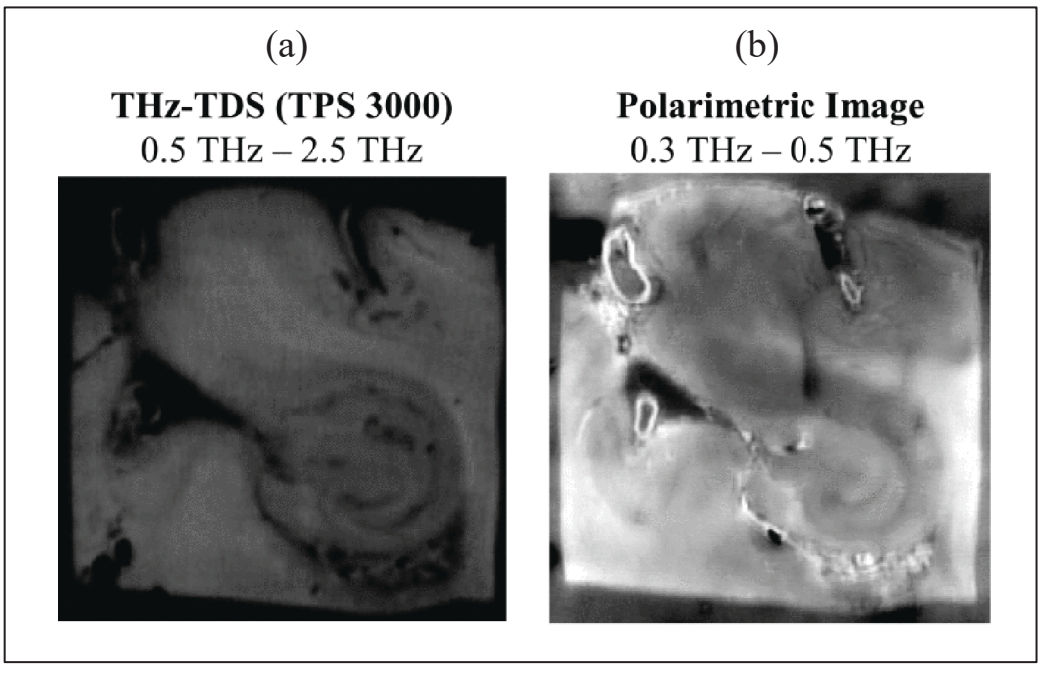

Figure 0.2 Representative images of a formalin-fixed, paraffin-embedded (FFPE) human hippocampal brain tissue sample obtained using (a) a commercial THz-TDS system and (b) a polarimetric imaging platform
Taken from (Srinivasan et al., 2017)

al., 1991; Jepsen et al., 2010; Wu et al., 2018). Although based on different physical principles, both techniques are inherently polarization sensitive. In their standard configurations, each method measures only a single projection of the THz electric field along a defined detection axis per scan (Xu et al., 2020).

These capabilities were later extended to polarization-resolved measurements, forming the foundation of early THz polarimetric spectroscopy and imaging approaches (Van Der Valk et al., 2005). However, the ultrabroadband nature of pulsed THz radiation, often spanning multiple octaves, complicates uniform polarization control across the entire spectrum. Conventional polarization optics exhibit strong frequency-dependent retardance and transmission, limiting broadband performance (Masson & Gallot, 2006; Takano et al., 2011). As a result, full polarization characterization, including Stokes or Mueller matrix reconstruction, typically requires multiple measurements, detector reconfiguration, or complex detection architectures. Furthermore, polarization measurements are highly sensitive to sample-induced depolarization, optical alignment, and environmental variations such as humidity and temperature, introducing uncertainty and imaging artifacts (Withayachumnankul et al., 2008; Watanabe, 2018; Harris et al., 2024). The dependence on mechanical delay stages and time-domain acquisition also prolongs measurement times, limiting real-time operation and reducing suitability for industrial or field applications (Molteni et al., 2023; Cherniak et al., 2023). In addition, phase-sensitive reconstruction and Mueller-matrix analysis impose substantial calibration and computational requirements, further constraining practical deployment (Neshat et al., 2012b; Xu et al., 2020; Chen & Pickwell-MacPherson, 2022; Huang et al., 2021b).

In contrast to time-domain approaches that rely on mechanical delay stages, continuous-wave (CW) frequency-domain spectroscopy (FDS) eliminates the need for temporal scanning (Kim et al., 2009; Rouvalis et al., 2010). However, CW polarimetric measurements introduce a different limitation: the requirement for sequential frequency sweeping. Since the THz frequency is tuned point-by-point, spectral acquisition can be time-consuming, particularly when high frequency resolution or broadband coverage is required. This inherently serial acquisition process restricts the suitability of CW systems for dynamic measurements or large-

area imaging applications. In addition, polarization analysis in CW systems required sequential projection of the THz field onto different polarization states using mechanically rotated wire-grid polarizers. Stokes parameter reconstruction therefore requires multiple measurements at each frequency point, further increasing acquisition time and system complexity (Martens et al., 2009). Each polarizer orientation demands independent calibration and precise alignment, making the measurement susceptible to mechanical inaccuracies and alignment drift. The extended acquisition duration also increases sensitivity to environmental perturbations, including vibration and thermal fluctuations, which can degrade measurement stability and overall reliability. Collectively, these requirements hinder the development of compact, fast, portable, and robust THz polarimetric imaging platforms capable of reliable operation outside controlled laboratory environments.

In the visible and near-infrared (VIS/NIR) range, compact polarimetric cameras commonly employ micro-polarizer arrays, where each super-pixel contains sub-pixels oriented at 0°, 45°, 90°, and 135° (Wolff & Andreou, 1995; Liu et al., 2025b). This enables simultaneous acquisition of polarization-resolved intensities and reconstruction of Stokes parameters (S_0, S_1, S_2), as well as derived quantities such as degree and angle of linear polarization. More generally, VIS/IR systems demonstrate that key polarization parameters can be retrieved using intensity-only measurements through spatial or spectral polarization modulation (Lapray et al., 2018; Raffoul et al., 2022). These systems achieve high-speed, robust, and compact imaging without relying on phase-resolved detection, however, their operation is primarily limited to surface or near-surface interactions due to strong scattering and absorption in many dielectric materials, restricting subsurface penetration and bulk material characterization (Applegate et al., 2020). These considerations motivate the exploration of alternative THz polarimetric imaging architectures that preserve polarization sensitivity while relying exclusively on intensity-based detection. In this context, frequency and polarization selective THz approaches offer a promising pathway toward compact, fast, and robust polarimetric imaging platforms. By directly sampling discrete THz frequency bands, such architectures eliminate mechanical delay scanning and significantly reduce system complexity. When combined with polarization sensitivity, they enable polarization-resolved measurements at selected frequencies using simple and compact detector technologies.

0.2 Problem statement and their potential solutions

THz frequency-selective surfaces (FSSs) play a crucial role in a wide range of applications, including spectral filtering, polarization control, sensing, and imaging systems (Ebrahimi et al., 2015). Achieving such functionalities relies on accurate patterning and fabrication of subwavelength resonant structures. The fabrication of THz FSSs has been demonstrated using a variety of techniques, including photolithography, printable electronics, laser-based microfabrication, and 3D printing (Sushko et al., 2017; Kashiwagi et al., 2016; Kubiczek et al., 2024; Wang et al., 2022). These fabrication approaches enable a wide range of FSS geometries and material platforms, facilitating precise control of resonance frequency, bandwidth, and polarization response. Beyond static implementations, reconfigurable THz FSSs have attracted significant attention as a means of achieving tunable spectral responses, enabled by approaches such as geometric modification, multilayer stacking, and external actuation mechanisms. Early studies primarily focused on altering the effective electromagnetic response of FSS structures using hybrid graphene-based designs, phase-change materials such as vanadium dioxide (VO_2), thermally tunable elements, and multilayer FSS architectures (Vegesna et al., 2014; Yan et al., 2016; Dong et al., 2018; Lv et al., 2022), enabling dynamic control of resonance frequency and transmission characteristics. While these strategies successfully demonstrate spectral reconfigurability, they often suffer from increased system complexity, higher fabrication cost, limited scalability, and the need for external stimuli such as electrical biasing, thermal control, or optical pumping. To overcome these limitations and to enable cost-effective and simplified reconfigurable THz filtering technologies, mechanical reconfigurability could be applied to printed THz FSSs emerges as a particularly promising alternative, offering robustness, simplicity, and compatibility with large-area fabrication.

An alternative route toward reconfigurability involves polarization-sensitive frequency-selective surfaces (PS-FSSs), where the spectral response is controlled by the polarization state of the incident wave. Several PS-FSS implementations have been reported, predominantly fabricated using photolithography-based techniques (Chen et al., 2013; Vegesna et al., 2014; Li et al., 2019). However, these approaches are frequently constrained by complex multilayer

designs or high-cost fabrication processes, limiting their practicality for scalable THz systems. In this context, rectangular-slot array FSSs are particularly attractive, as they can exhibit strong polarization-dependent transmission contrast when the incident polarization angle is varied with respect to the slot's long axis (Hong et al., 2013; Hong et al., 2017). **Despite this potential, a single-layer, free-standing frequency-selective polarizer exhibiting angular-dependent transmission behavior that follows Malus' law has not yet been reported in the literature, motivating further investigation in this direction.**

Furthermore, rotatable THz filter wheels represent an effective strategy for achieving tunability and reconfigurability in THz systems. A significant milestone in this area was the introduction of the first circular variable THz filter, reported by (Grossman, 2006), which demonstrated that spatially varying frequency-selective structures distributed along a rotating element can provide spectral selectivity through mechanical rotation (see Fig. 0.3(a)). Building on this concept, several compact, intensity-based THz spectrometers employing arrays of FSSs or metasurfaces mounted on rotating wheels have been reported (Carelli et al., 2012; Sebastian et al., 2026). These architectures, as shown in Fig. 0.3(b-c), offer a lightweight, low-cost, and mechanically robust alternative to conventional THz time-domain spectroscopy, by directly sampling discrete THz frequency bands in real time without relying on mechanical delay stages. A range of detectors, including bolometers and Schottky diode detectors, have been employed in filter-based THz spectrometers due to their compactness, robustness, and suitability for real-time operation (Carelli et al., 2012; Sebastian et al., 2026). Early metasurface-on-wheel spectrometers primarily relied on bolometric detection, which, although highly sensitive, suffers from slow response times that limit high-speed measurements (Carelli et al., 2012). Subsequent developments demonstrated multispectral THz spectrometers based on FSS wheels combined with Schottky diode detectors, enabling significantly faster acquisition speeds and real-time spectral readout (Sebastian et al., 2026). **However, these implementations were restricted to spectral intensity measurements and did not incorporate polarization sensitivity**. **The lack of polarization selectivity in existing filter-based THz spectrometers limits their applicability in polarimetric imaging and anisotropic material characterization, where polarization-dependent interactions carry**

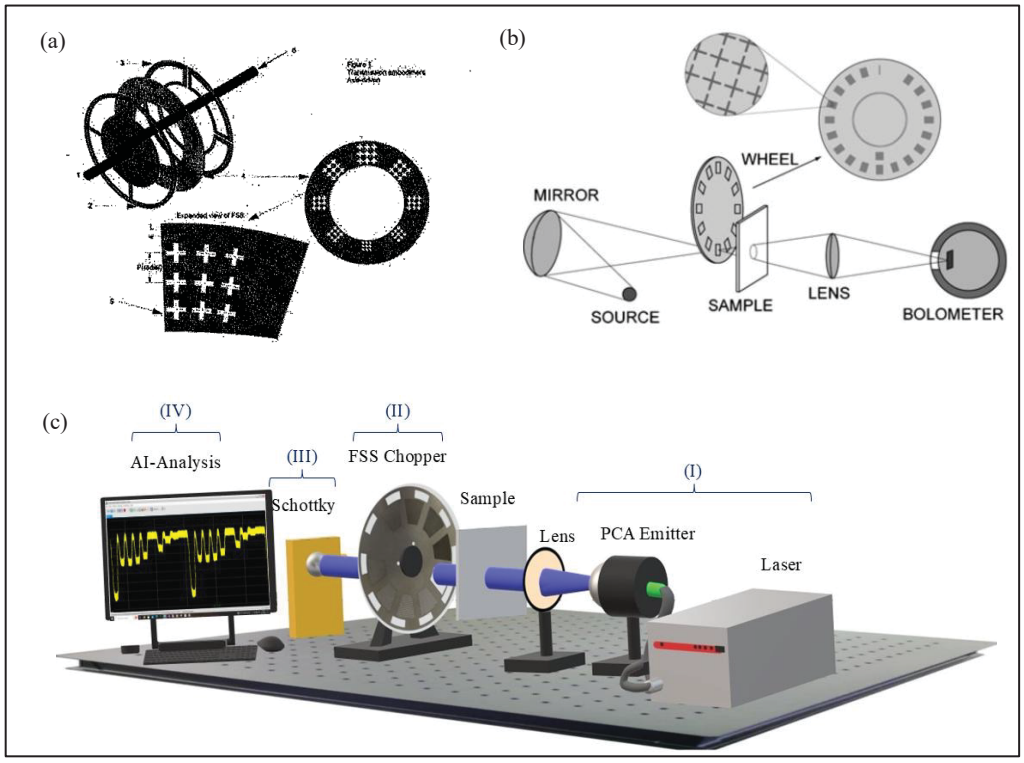

Figure 0.3 (a) Circular variable THz filter based on cross shape geometry Taken from (Grossman, 2006) (The image quality is limited due to the low resolution of the available online version)
(b) compact THz spectrometer based on bolometric detection Taken from (Carelli et al., 2012)
and (c) THz FSS based multi-spectral spectrometer using Schottky diode detector
Taken from (Sebastian et al., 2026)

essential information related to birefringence, structural orientation, and depolarization effects.

In analyzer-based THz polarimetric systems, polarization state projection is typically achieved using wire-grid polarizers placed along the THz beam path, either for sequential state selection or polarization modulation. Such implementations, including those reported by Gurjar *et al*. and Morris *et al*., rely on polarization optics positioned before detection to isolate specific field components. While effective, the use of multiple polarizing elements introduces additional alignment sensitivity (Gurjar et al., 2024b; Morris et al., 2012). A more compact strategy is to integrate polarization discrimination directly into the frequency-selective elements themselves.

Polarization-sensitive FSS can simultaneously function as band-pass filters and polarization analyzers, enabling polarization-resolved spectral measurements using a single rotating element. When PS-FSS architectures implemented on a rotatable wheel and combined with fast intensity-based detectors such as Schottky diode or CMOS detectors, provide a direct pathway toward real-time, multispectral THz polarimetric spectrometer and imaging. This concept forms the basis for compact, fast, and robust THz polarimetric imaging systems, addressing the limitations of existing THz-TDS-based polarimetric techniques and paving the way toward industrial deployment, as well as facilitating broader scientific applications in material characterization, anisotropy analysis, and polarization-sensitive spectroscopy.

0.3 Objectives of the research

Motivated by these considerations, the primary goal of this thesis is to develop compact, fast, and intensity-based multi-spectral THz polarimetric imaging platforms enabled by polarization-sensitive FSS. The specific research objectives are summarized as follows:

Objective 1: **To develop reconfigurable methods of THz FSS, enabling tunable spectral and polarization responses through geometrical design and mechanical reconfiguration.**

Objective 2: To design and fabricate free-standing, single-layer polarization-sensitive THz FSS using scalable and cost-effective fabrication techniques, with an emphasis on robustness, simplicity, and followed by well defined angular transmission.

Objective 3: To develop a compact multispectral THz polarimetric spectrometer and imaging system based on a polarization-sensitive FSS wheel architecture, enabling direct extraction of polarization metrics using intensity-only detection without phase-sensitive measurements.

0.4 Thesis structure

Following the introduction, the thesis is structured as follows. The following chapter provides a detailed review of relevant literature, introducing the theoretical background, prior developments, and methodological frameworks necessary for the subsequent chapters. Different types of THz generation and detection schemes are described. This chapter also

discusses prior work on THz reconfigurable FSS with different tunability and fabrication techniques. The literature review also discusses the challenges of conventional THz spectrometer and THz polarimetric imaging system. The following four chapters present reconfigurability techniques of THz FSS and compact THz polarimetric system to achieve the proposed research objectives, which resulted in the journal publications.

Chapter 2 is based on the published article (Ahmad et al., 2024) entitled "Reconfigurable screen-printed terahertz frequency selective surface based on metallic checkerboard pattern." In this chapter, a mechanically reconfigurable FSS is investigated through numerical simulations and experimental measurements. Two identical layers of inductive metallic checkerboard (i-MCB) FSS are employed, with reconfigurability achieved by laterally shifting one layer along the *x*- and *y*-axes while keeping the other fixed. The resulting variation in the spectral response is systematically analyzed. In addition, the polarization sensitivity of the i-MCB FSS configuration with a relatively shifted i-MCB is examined to assess its polarization-dependent transmission characteristics.

Chapter 3 is based on the published article (Ahmad et al., 2023) entitled "Reconfigurable terahertz Moiré frequency selective surface based on additive manufacturing technology." This chapter presents the design, fabrication, and characterization of a reconfigurable THz FSS based on a Moiré interference concept. Two identical FSS layers fabricated using additive manufacturing techniques are stacked and rotated relative to each other to achieve tunable spectral responses. The impact of relative rotational alignment on the transmission characteristics is studied through analytical modeling, numerical simulations, and experimental validation. The chapter demonstrates that Moiré-based reconfiguration provides an effective, mechanically simple approach to achieving tunable THz filtering responses while maintaining a compact, scalable fabrication strategy.

Chapter 4 is based on the published article (Ahmad et al., 2026) entitled "Polarization-sensitive terahertz frequency-selective surface based on a laser cutting technique". Whereas the preceding chapters focused on reconfigurability achieved with double-layer FSSs, this chapter presents the numerical and experimental investigation of free-standing single-layer polarization-sensitive FSS designs. The polarization-dependent transmission responses of both

FSS designs are systematically analyzed, demonstrating their suitability as polarization-dependent spectral modulators within specific THz frequency bands. By varying the incident polarization angle, the C-shaped FSS exhibits a tunable band-pass filtering response with well-defined spectral separation as the polarization state is rotated by 90°. In contrast, the rectangular-slot FSS operates as a frequency-selective polarizer, showing angular-dependent transmission that closely follows Malus' law. These results highlight the distinct polarization-modulation mechanisms enabled by symmetric and asymmetric FSS geometries, respectively, realized via a laser-cutting fabrication approach.

Chapter 5 is based on the submitted article entitled "Terahertz multi-spectral polarimetric imaging based on intensity measurement." This chapter presents the development and experimental demonstration of a THz polarimetric spectrometer and imaging system that relies exclusively on intensity-only measurements. The proposed approach employs polarization-sensitive FSS as both spectral filters and polarization analyzers, enabling compact and robust multi-spectral THz polarimetric imaging without phase-sensitive detection. By acquiring intensity images at distinct PS-FSS orientations, the system allows direct extraction and spatial mapping of polarization metrics, including the degree of linear polarization (DoLP) and angle of linear polarization (AoLP), at multiple discrete THz frequency bands and thereby measured frequency dependent birefringence through optimization algorithm. The capability of the proposed system is validated through polarimetric imaging of anisotropic samples, demonstrating high DoLP and AoLP contrast and highlighting the suitability of the approach for fast, practical, and industrially relevant THz polarimetric imaging applications.

Chapter 6 presents the conclusions and recommendations of this thesis. The main findings from each chapter are briefly summarized, highlighting the key contributions to THz FSS, reconfigurable filtering techniques, and multispectral polarimetric imaging and spectroscopy. The chapter also outlines potential directions for future research, including system optimization, advanced polarimetric architectures, and the translation of the proposed techniques toward practical industrial implementation as well as broader scientific applications in terahertz sensing and characterization.

In addition to the main chapters, this thesis includes three annexes that provide complementary investigations and extended experimental studies related to THz wave manipulation and polarization analysis. Annex I presents the design, fabrication, and experimental characterization of printed THz spiral zone plates for vortex beam generation, emphasizing low-cost and scalable printable electronics techniques for realizing phase-engineered THz diffractive optics. The feasibility of mass-producible THz phase-control components is demonstrated, with vortex beam generation experimentally validated using a THz microbolometric camera operating in both transmission and reflection configurations.

Annex II introduces a compact THz polarimetric spectrometer based on a CMOS detector with an integrated linearly polarized antenna, enabling intrinsic polarization-sensitive detection. In contrast to the Schottky-based polarimetric spectrometer discussed in the main body of the thesis (chapter 5), where the detector is polarization-insensitive and polarization-dependent spectral modulation is achieved using a PS-FSS wheel. This annex explores polarization analysis using a polarization-sensitive detector. The system operates at two discrete frequency bands and measures four linear polarization orientations. Simulation results are first examined and subsequently validated through experimental measurements, with the objective of evaluating the response of different PS-FSS analyzer orientations and highlighting the differences between polarization-sensitive and polarization-insensitive detection schemes.

Annex III investigates a simplified THz polarimetric measurement approach for the static characterization of birefringent samples, using a polarization-insensitive pyroelectric detector and a frequency selective polarizer. A broadband photoconductive antenna is employed as the THz source, while polarization information is obtained through external modulation by rotating the sample orientation. Although the inherently slow temporal response of the pyroelectric detector restricts dynamic measurements, this cost-effective and conceptually simple configuration provides a useful reference platform that complements the faster Schottky-based (Chapter 5) and CMOS-based polarimetric systems (Annex II) presented in this work.

CHAPTER 1

BACKGROUND AND LITERATURE REVIEW

1.1 Introduction

Over the past two decades, significant advances in ultrafast laser technology, nonlinear optics, and microfabrication have enabled robust and application-ready THz-TDS systems, along with a growing range of specialized THz sensing platforms. However, despite this progress, challenges remain in achieving compact, efficient, polarization-sensitive, and frequency-selective THz systems suitable for both laboratory and real-world environments. This chapter provides the foundational background necessary to contextualize the contributions of this thesis. It begins with an overview of THz generation mechanisms, including photoconductive and nonlinear optical approaches, followed by a detailed discussion of detection techniques, emphasizing coherent field-resolved methods such as photoconductive antennas and electro-optic sampling. The chapter then introduces THz time-domain spectroscopy as the primary framework for coherent THz measurement. Building on this foundation, FSS, metasurface-inspired architectures, and polarization-sensitive THz structures are reviewed, highlighting their role in tailoring amplitude, phase, and polarization responses. Reconfigurable and tunable THz FSS platforms are discussed in the context of emerging adaptive electromagnetic systems. Since fabrication plays a critical role in translating theoretical designs into practical devices, key microfabrication approaches including lithography, printable electronics, 3D printing, and laser-based techniques are subsequently summarized. The chapter further introduces compact THz spectrometers and polarization-resolved measurement systems, with particular attention to THz polarimetry and polarimetric imaging architectures. Existing PCA and electro-optic–based and alternative intensity-based approaches are reviewed, along with their advantages and limitations in scattering media and biomedical contexts. Finally, identifying current technological gaps and motivating the need for scalable, compact and fast multispectral polarimetric imaging platform. This literature review establishes the theoretical and technological framework upon which the research contributions of this thesis are developed.

1.2 THz generation

As discussed previously, THz radiation occupies the spectral region between microwaves and infrared radiation. Because of this intermediate position, THz emitters can be broadly classified into electronic and optical (photonic) approaches. Electronic sources, typically derived from microwave and radio-frequency technologies such as frequency multiplier chains, resonant tunneling diodes, and vacuum electronic devices, undergo substantial performance degradation at higher frequencies due to carrier transit-time effects, parasitic capacitance, and increasing conductive losses (Dhillon et al., 2017). Although electronic architectures have been extended into the THz regime, their output power and efficiency decrease significantly beyond several hundred gigahertz, making practical high-power operation above ~1 THz challenging (Mehdi et al., 2003; Ward et al., 2004). As a result, electronic solutions are most effective in the sub-THz to lower-THz range. In contrast, optical approaches can be broadly classified into three main categories: photoconductive antennas, photomixing techniques, and nonlinear optical generation (e.g., optical rectification and difference-frequency generation) (Warren et al., 1991; Jepsen et al., 2010; Wu et al., 2018; Kim et al., 2009). In this work, conducted within an ultrafast optical laboratory environment, we focus exclusively on optical THz generation methods. In particular, the generation techniques considered in this thesis include photoconductive antenna-based THz generation, optical rectification in nonlinear crystals, and continuous-wave photomixing.

1.2.1 Photoconductive broadband THz generation

The photoconductive antenna is the most widely used and extensively studied techniques for generating pulsed THz radiation. It consists of two metallic electrodes separated by a small gap fabricated on a semiconductor substrate exhibiting a short charge-carrier lifetime (Lepeshov et al., 2017; Burford et al., 2017) as illustrated in Fig. 1.1. When the photoconductive gap is illuminated by an ultrashort femtosecond laser pulse, photogenerated charge carriers are created within the semiconductor. Under an applied DC bias across the electrodes, these carriers are rapidly accelerated by the bias electric field, resulting in an ultrafast transient photocurrent $J(t)$. According to Maxwell's equations, the radiated electric

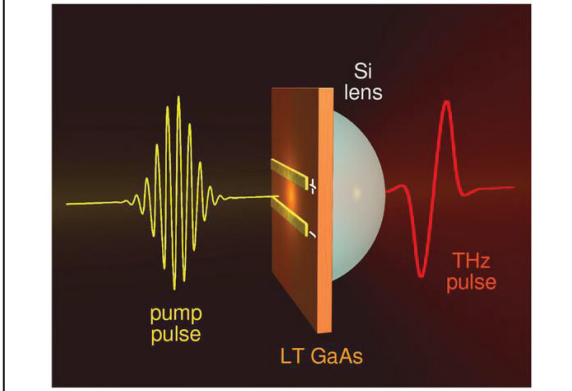

Figure 1.1 Illustration of a PCA employed for THz generation, where an ultrafast optical pulse excites charge carriers in a biased photoconductive gap, resulting in broadband THz emission
Taken from (Lepeshov et al., 2017)

field in the far field is proportional to the time derivative of the current density (Jepsen et al., 2010).

$$E_{THz}(t) \propto \frac{dJ(t)}{dt} \tag{1.1}$$

Thus, the rapid temporal variation of this photocurrent generates broadband THz radiation. The ultrafast rise and decay of $J(t)$ lead to a wide spectral bandwidth, and the emitted THz pulse is efficiently coupled to free space through the antenna structure.

The bandwidth and amplitude of the emitted THz pulse are primarily influenced by the antenna geometry particularly the electrode gap size and bias field distribution followed by the optical pulse duration, carrier mobility, and carrier lifetime (Liu et al., 2003). Typical PCA systems employ femtosecond lasers with pulse durations of 50–100 fs at wavelengths around near-IR, enabling THz bandwidths extending to several THz.

THz PCAs are most commonly realized using bulk gallium arsenide (GaAs) or indium gallium arsenide (InGaAs) substrates, owing to their fast carrier dynamics and compatibility with

ultrafast optical excitation (Salem et al., 2005; Winnerl et al., 2008; Moon et al., 2014; Tani et al., 1997; Warren et al., 1991; Takazato et al., 2007; Takazato et al., 2007b; Chimot et al., 2005; Suzuki et al., 2005; Wood et al., 2010). The choice of material is primarily dictated by the semiconductor bandgap energy relative to the optical pump wavelength. GaAs-based PCAs are optimized for excitation near 800 nm, making them well suited for Ti:Sapphire laser systems, whereas InGaAs-based devices are engineered for operation at 1.55 μm and are therefore compatible with fiber-laser platforms. In practice, GaAs remains a widely used material platform, particularly in the form of semi-insulating GaAs (SI-GaAs), valued for its high resistivity and low free-carrier absorption, and low-temperature-grown GaAs (LT-GaAs), which provides sub-picosecond carrier lifetimes suitable for ultrafast photoconductive THz generation and detection.

The THz emission in a PCA originates primarily from the ultrafast acceleration of photocarriers under an applied bias field, rather than from photon down-conversion processes. Consequently, the radiated THz energy is predominantly supplied by the external bias source, while the optical pulse mainly acts to generate photocarriers that enable the transient current. This mechanism allows comparatively high conversion efficiency when driven by oscillator lasers with modest pulse energies and peak intensities (e.g., ~80 MHz systems), which explains why PCAs are widely employed in oscillator-based THz platforms. Nevertheless, PCA performance is ultimately constrained by carrier screening, thermal accumulation at high repetition rates, bias-field saturation, and optical damage at elevated pump fluences.

1.2.2 Nonlinear generation of THz waves

In non-centrosymmetric crystals, a second-order nonlinear optical process known as optical rectification enables the generation of THz radiation. Commonly used nonlinear crystals for this purpose include zinc telluride (ZnTe), gallium phosphide (GaP), lithium niobate ($LiNbO_3$) etc. When an intense ultrashort optical pulse propagates through a second-order nonlinear medium, it induces a time-dependent nonlinear polarization that radiates broadband THz pulses via optical rectification (Tian et al., 2021; Wu et al., 2018), as schematically illustrated in Fig.1.2.

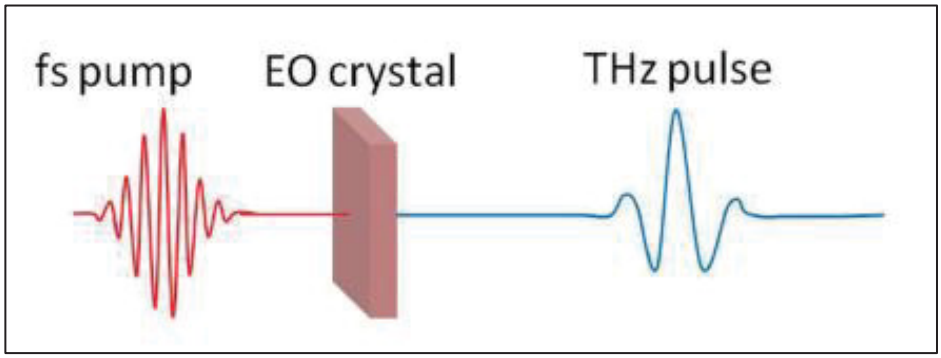

Figure 1.2 Graphical representation of nonlinear THz generation in an electro-optic (EO) crystal driven by ultrafast optical excitation
Taken from (Banerjee et al., 2021)

THz radiation in nonlinear crystals originates from second-order nonlinear optical interactions governed by the nonlinear polarization as follows (Boyd, 2008):

$$P^{(2)}(t) = \varepsilon_0 \chi^{(2)} E^2(t) \tag{1.2}$$

where ε_0 is the vacuum permittivity and $\chi^{(2)}$ is the second-order susceptibility tensor. This nonlinear polarization acts as a source term for new frequency components.

When two optical waves with angular frequencies ω_1 and ω_2 interact in such a medium, difference-frequency generation (DFG) occurs, producing radiation at

$$\omega_{DFG} = |\omega_1 - \omega_2| \tag{1.3}$$

The nonlinear polarization driving this process in the frequency domain can be written as

$$P^{(2)}(\omega_{DFG}) \propto \varepsilon_0 \chi^{(2)} E(\omega_1) E^*(\omega_2) \tag{1.4}$$

If the frequency separation between ω_1 and ω_2 lies in the THz range, coherent THz radiation is generated. In the case of femtosecond optical excitation, the pulse contains a continuum of spectral components. Mixing between nearby spectral components within the same pulse produces low-frequency components extending into the THz regime. This intrapulse difference-frequency mixing is commonly referred to as optical rectification (OR). In the time domain, the nonlinear polarization responsible for OR can be approximated as

$$P_{OR}(t) \propto \varepsilon_0 \chi^{(2)} \left| E_{opt}(t) \right|^2 \tag{1.5}$$

indicating that the generated THz field follows the temporal intensity envelope of the optical pulse. Because the emitted THz radiation originates from the rapidly varying nonlinear polarization, shorter excitation pulses yield broader THz spectra.

The temporal profile and bandwidth of the emitted THz pulse are primarily governed by the spectral bandwidth of the excitation pulse and by the phase-matching condition between the generated THz field and the optical pump pulse. Efficient THz generation via optical rectification requires velocity matching between the optical pump and the generated THz wave, as shown in Fig. 1.3. Specifically, the group velocity of the optical pump pulse must closely match the phase velocity of the THz wave, which implies that the THz refractive index n_{THz} should be close to the optical group index n_{g}. The condition becomes (Tóth et al., 2023)

$$v_{THz} = v_g^{pump} (\cos \gamma) \tag{1.6}$$

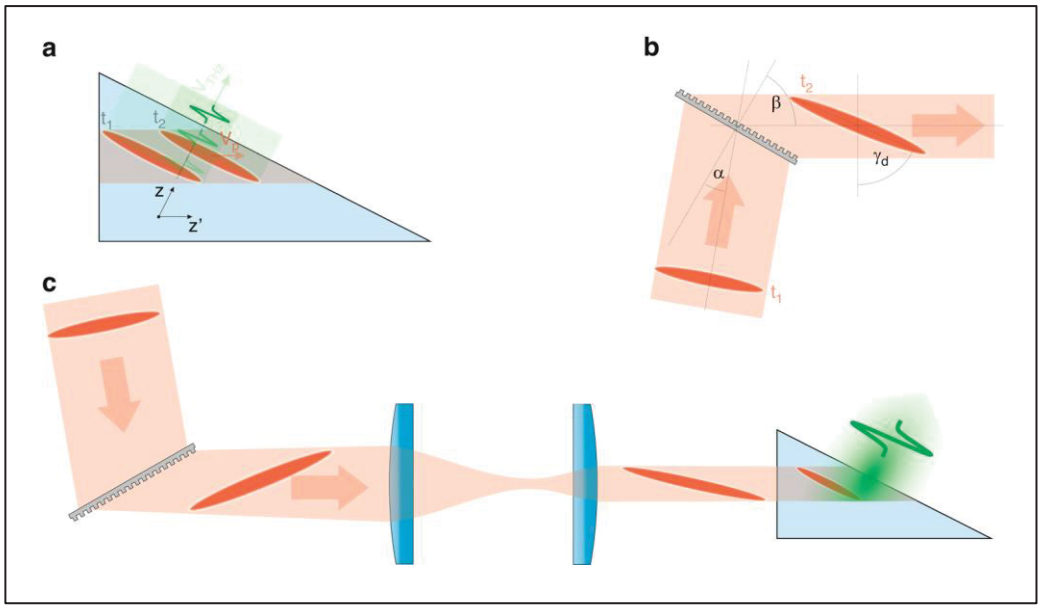

Figure 1.3 (a) Propagation of the tilted pump pulse front along z' and the generated THz radiation along *z*, with snapshots at t_1 and t_2. (b) Transmission grating–induced tilt of the initially normal pump pulse. (c) Schematic of the conventional tilted pulse-front pumping (TPFP) setup for THz generation Taken from (Tóth et al., 2023)

where v_{THz} is the THz phase velocity, v_g^{pump} is the optical pump group velocity, and γ is the pulse-front tilt angle between the pump pulse front and the THz propagation direction. Diffraction gratings and echelon-based schemes represent the most widely adopted techniques for generating pulse-front tilt.

In ZnTe, this condition is well satisfied for excitation wavelengths around 800 nm, enabling a simple collinear configuration and making ZnTe particularly well suited for use with Ti:sapphire laser systems. When a nonlinear crystal such as ZnTe (≈1 mm thickness) is excited by 100 fs laser pulses at a central wavelength of 800 nm, broadband THz transients with spectral content extending up to approximately 2.5 THz can be generated through optical rectification (Wu et al., 1996; Zhai et al., 2021). In addition to ZnTe, nonlinear crystals such as GaP, GaSe, and DAST also enable collinear phase-matching schemes for efficient THz generation (Vugmeyster et al., 2012; Schneider et al., 2006).

Lithium niobate (LN), by contrast, possesses a significantly larger second-order nonlinear coefficient, enabling higher potential optical-to-THz conversion efficiency. However, its optical group index (~2.2–2.3) differs substantially from its THz refractive index (~5.0–5.2), preventing collinear phase matching. To overcome this strong velocity mismatch, the tilted-pulse-front (TPF) technique is employed. By introducing angular dispersion to tilt the optical pulse front (~63°), the projected optical group velocity is matched to the THz phase velocity, enabling efficient non-collinear phase matching and enhanced conversion efficiency. Nevertheless, strong phonon-induced THz absorption in LN limits the usable spectral range, typically suppressing emission above approximately 4 THz (Blanchard et al., 2014; Guiramand et al., 2022; Hoffmann et al., 2007; Yeh et al., 2007; Carletti et al., 2023; Hirori et al., 2011; Hebling et al., 2002; Jang et al., 2020; Ma et al., 2022).

OR is widely used in THz-TDS because the nonlinear crystal is pumped within its transparency window, minimizing optical absorption and thermal effects, and enabling broadband THz generation for spectroscopic and imaging applications. The conversion efficiency scales with the square of the optical electric field, and thus with the square of the peak optical intensity, requiring high-intensity femtosecond pulses typically provided by amplified laser systems which can deliver μJ–mJ pulse energies.

1.2.3 Continuous wave THz generation

In contrast to pulsed THz sources, continuous-wave (CW) THz generation produces narrow-linewidth, frequency-stable radiation at a single frequency, while remaining widely tunable across the THz band. This makes CW systems particularly attractive for high-resolution spectroscopy, sensing, and communication applications. CW THz sources enable precise frequency tuning and long-term phase stability, making them well suited for measurements requiring narrow linewidths and absolute frequency control (Gu et al., 1999). Several approaches have been developed to generate CW THz radiation, including electronic frequency multiplication, quantum cascade lasers, and optical photomixing techniques. A widely used approach for generating CW THz radiation is photomixing, which relies on the optical beating of two continuous-wave laser sources with nearly identical optical wavelengths λ_1 and λ_2, whose frequency difference lies in the THz range. When these two optical fields are incident simultaneously on a biased semiconductor photomixer, their interference produces an intensity modulation at the optical beat frequency (Kim et al., 2009; Rouvalis et al., 2010; Kong et al., 2018). If the photoconductive material exhibits sufficiently fast carrier dynamics, characterized by short momentum relaxation and recombination times relative to the THz oscillation period, the generated photocurrent can follow the optical beat signal, resulting in an oscillating current at THz frequencies.

$$\nu_{THz} = c\left|\frac{1}{\lambda_1} - \frac{1}{\lambda_2}\right| \tag{1.7}$$

where c is the speed of light in vacuum. By precisely tuning the wavelength separation between the two lasers, the generated THz frequency can be continuously adjusted over a broad spectral range.

When the photomixer is integrated with a suitably designed antenna, such as a dipole, bow-tie, or logarithmic spiral antenna, the oscillating photocurrent is efficiently coupled into free space, resulting in the emission of CW THz radiation. In contrast to pulsed THz generation schemes, photomixing inherently produces a single-frequency (narrowband) THz output, with the spectral linewidth primarily determined by the coherence and frequency stability of the optical laser sources. In a typical CW THz spectroscopy system, the optical outputs of the same pair

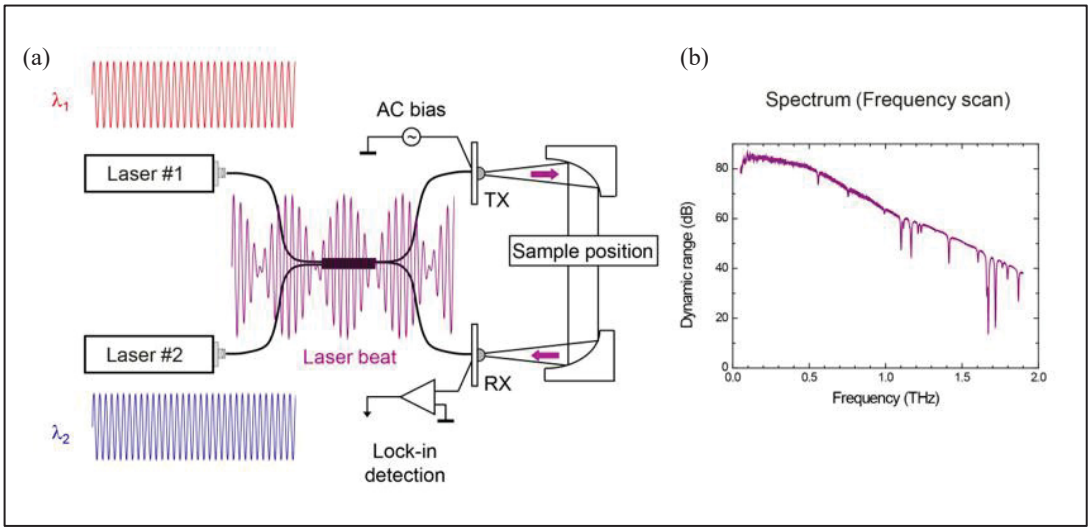

Figure 1.4 (a) Schematic of a CW THz spectroscopy system for THz generation and detection; and (b) measured spectrum obtained from a frequency scan
Taken from (TeraSense, 2018)

of single-frequency lasers are split and directed to both the transmitter and receiver photomixers, ensuring mutual coherence between THz generation and detection. This coherent configuration enables phase-sensitive detection of the THz field and is schematically illustrated in Fig. 1.4. By sweeping the frequency difference ν_{THz} between the two lasers, the system can perform frequency-domain THz spectroscopy over a wide bandwidth.

The bandwidth of a CW THz photomixing system is governed by factors similar to those in THz-TDS, including the frequency response of the photomixers, antenna characteristics, and optical alignment. However, a key advantage of CW THz spectroscopy is its exceptionally high frequency resolution, far surpassing that of conventional THz-TDS systems. This makes CW photomixing particularly attractive for applications requiring precise spectral discrimination, such as gas-phase spectroscopy, molecular rotational transitions, and high-Q resonant structures.

Despite these advantages, CW THz systems require highly stable and precisely controlled laser wavelengths, which increases system complexity and sensitivity to environmental perturbations. Although the absolute emitted THz power may be modest compared to pulsed systems, coherent CW photomixing platforms provide excellent dynamic range, narrow

linewidth, and wide tunability, enabling superior spectral resolution. These characteristics make CW THz spectroscopy a powerful and complementary technique to pulsed THz-TDS, particularly for high-resolution spectroscopic investigations.

1.3 THz detection

1.3.1 PCA based detection

THz detection systems employ a variety of technologies to capture and analyze THz radiation, each offering distinct operational principles, bandwidths, and levels of phase sensitivity. Among these, PCAs are the most widely used detectors in THz-TDS due to their broadband response and coherent detection capability. In particular, PCA detectors are most commonly employed in oscillator-based THz-TDS systems operating at high repetition rates (e.g., Ti:sapphire oscillators with nJ pulse energies). A typical photoconductive antenna consists of two closely spaced metallic electrodes fabricated on a semiconductor substrate, forming a photoconductive switch with a few-micron gap. In detection mode, unlike THz generation, the antenna is not externally biased. Instead, the incident THz electric field induces a transient voltage across the electrode gap, effectively acting as a time-varying bias field (Katzenellenbogen et al., 1991; Tani et al., 2002; Formanek et al., 2009; Kohlhaas et al., 2019). A schematic representation of this detection mechanism is provided in Fig. 1.5. When the photoconductive gap is illuminated by an ultrafast optical gating pulse, photocarriers are generated within the semiconductor, and the instantaneous THz-induced electric field accelerates these carriers, giving rise to a measurable photocurrent.

The transient photocurrent in a photoconductive antenna arises from the convolution of the incident THz electric field with the time-dependent photoconductivity induced by the ultrafast optical gate pulse,

$$J(\tau) \propto \int_{-\infty}^{\infty} E_{THz}(t) g(t-\tau) dt \tag{1.8}$$

Where τ is the relative delay between the THz and optical pulses and $g(t)$ describes the carrier response (Jepsen et al., 2010). In the limit of an ultrafast photoconductivity response, the

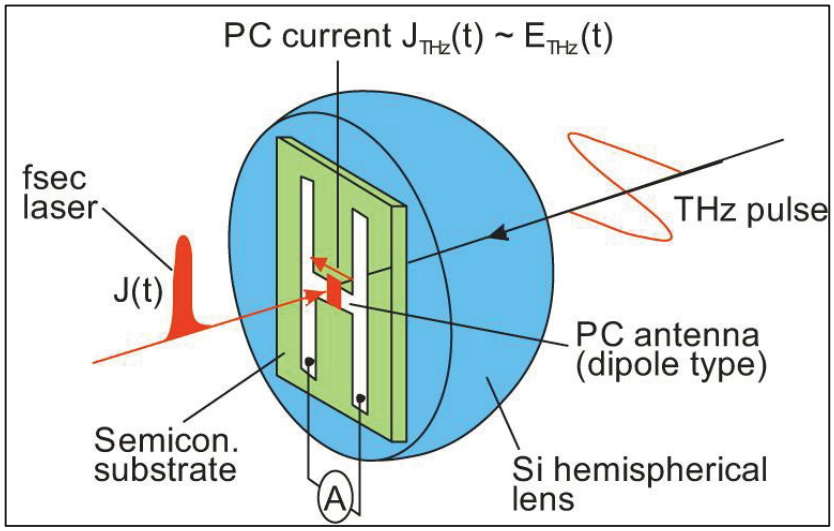

Figure 1.5 Schematic overview of the principle of PCA based THz detection
Taken from (Sizov et al., 2010)

detected current becomes directly proportional to the instantaneous THz electric field, enabling coherent, phase-resolved detection.

To improve the signal-to-noise ratio, the weak photocurrent induced by the THz field is typically converted into a measurable voltage using a low-noise transimpedance amplifier. The resulting amplified signal is directly proportional to the instantaneous THz electric field sampled at the moment of optical gating. In THz-TDS systems, both the THz emitter and the PCA detector are commonly driven by synchronized portions of the same femtosecond laser pulse train. This shared optical reference ensures precise timing synchronization between generation and detection, which is essential for coherent detection and accurate reconstruction of the THz waveform.

One of the most critical material parameters governing PCA detection performance is the carrier lifetime of the photoconductive substrate. In a PCA detector, the incident THz electric field induces a transient voltage across the electrode gap, but a measurable photocurrent is generated only when the optical gating pulse creates photocarriers. For efficient field-resolved detection, the photoconductivity must rise and decay on a timescale shorter than the oscillation period of the THz field. Therefore, a short carrier lifetime is essential to ensure that the induced

photocurrent remains directly proportional to the instantaneous THz electric field. Since the required temporal response becomes shorter for higher THz frequencies, achieving detection of higher-frequency components necessitates increasingly shorter carrier lifetimes (Jepsen et al., 2010; Neu & Schmuttenmaer, 2018).

Materials such as low-temperature-grown GaAs (LT-GaAs) are widely used because they provide sub-picosecond carrier lifetimes while maintaining sufficient carrier mobility for efficient photocurrent generation. Although the carrier mobility in LT-GaAs (typically a few hundred $cm^2/V \cdot s$) is significantly lower than in semi-insulating GaAs, the carrier lifetime remains the dominant factor for broadband PCA detection performance. In contrast, semi-insulating GaAs, despite its higher mobility, generally exhibits longer carrier lifetimes and is therefore less suitable for high-bandwidth PCA detection.

In both PCA emitters and detectors, a hemispherical silicon lens is commonly attached to the substrate on the THz side. This lens reduces total internal reflection at the semiconductor–air interface, narrows the THz emission and collection angle, decreases Fresnel losses, and significantly improves overall coupling efficiency and signal strength. While PCA-based detectors provide broadband, phase-sensitive THz detection and are particularly well suited to oscillator-based systems, their performance depends critically on ultrafast optical gating and precise optical alignment.

1.3.2 EO sampling

Another coherent detection technique is electro-optic (EO) sampling, which relies on the Pockels effect in a nonlinear crystal. In this process, the THz-induced birefringence in the nonlinear crystal leads to a change in the polarization of the optical probe, which can be measured using polarization optics and balanced photodetectors (Guiramand et al., 2022; Balos et al., 2023; Maeng et al., 2012; Banerjee et al., 2021). When a THz electric field propagates through an EO crystal, it induces a transient birefringence proportional to the instantaneous THz field strength. The induced change in refractive index can be expressed as (Beckh et al., 2021)

$$\Delta n(t) = \frac{1}{2} n^3 r_{eff} E_{THz}(t) \tag{1.9}$$

where n is the refractive index at the optical probe wavelength, r_{eff} is the effective electro-optic coefficient, and $E_{\text{THz}}(t)$ denotes the time-dependent THz electric field.

As a short optical probe pulse traverses the crystal of thickness L, the THz-induced birefringence results in a phase retardation (Blanchard et al., 2007; Beckh et al., 2021)

$$\Delta\phi(t) = \frac{2\pi}{\lambda} \Delta n(t) L = \frac{\pi n^3 r_{eff} L}{\lambda} E_{THz}(t) \tag{1.10}$$

This phase modulation is converted into an intensity variation using polarization optics and balanced photodetection. For small phase shifts, the detected signal is approximately proportional to the THz electric field.

By scanning the temporal delay between the THz pulse and the optical probe pulse, the full time-domain electric field $E_{\text{THz}}(t)$ can be reconstructed. Fourier transformation of the time-

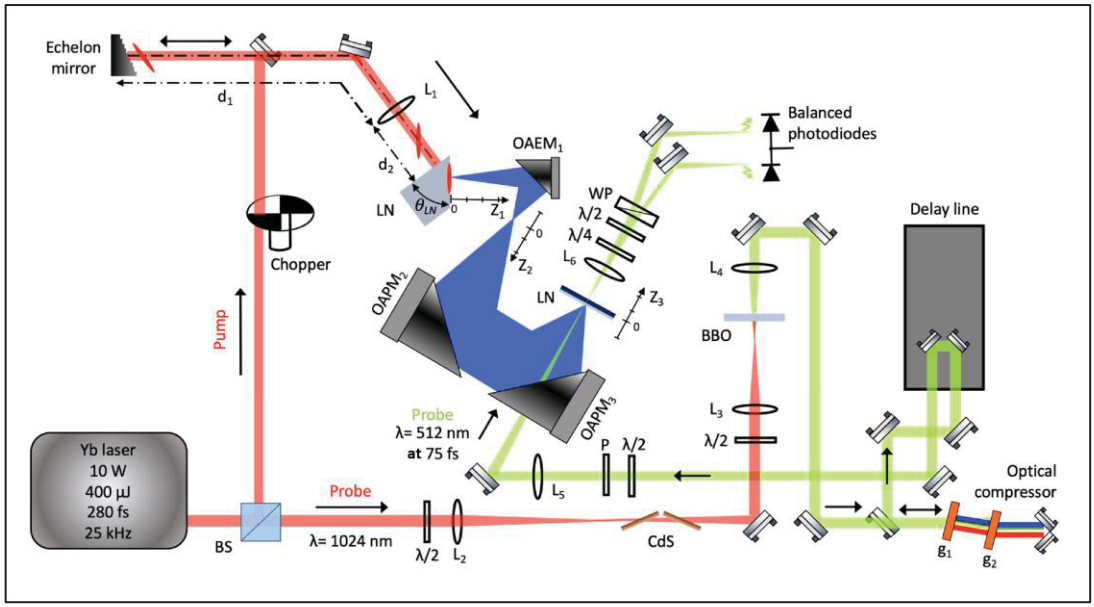

Figure 1.6 Schematic of the experimental configuration for THz pulse generation using $LiNbO_3$ (LN) and subsequent detection through EO sampling
Taken from (Guiramand et al., 2022)

domain waveform then yields the complex frequency-domain spectrum, enabling extraction of amplitude and phase information of the THz radiation.

Both photoconductive antennas and electro-optic sampling enable coherent detection, allowing simultaneous measurement of the amplitude and phase of broadband THz pulses. By scanning the relative time delay between the THz pulse and the optical probe, the temporal evolution of the THz electric field can be mapped with sub-picosecond resolution, as schematically illustrated in Fig. 1.6. The temporal resolution of EO sampling is fundamentally limited by the duration of the optical probe pulse, since the probe acts as a temporal gate for the THz field. To accurately resolve high-frequency THz components, the probe pulse duration should be significantly shorter than the oscillation period of the highest THz frequency of interest. In practice, probe pulses of approximately 50-100 fs are commonly recommended to achieve broadband detection extending to several THz. Fourier transformation of the time-domain signal provides access to the frequency-domain response, forming the basis of THz time-domain spectroscopy.

1.4 THz time domain spectroscopy

In the THz range, many materials exhibit unique spectral fingerprints that can be used for identification (Neu & Schmuttenmaer, 2018). A typical THz time-domain system consists of a femtosecond laser, an optical beam splitter, beam steering mirrors, delay stages, THz beam focusing, off-axis parabolic mirrors, and a THz emitter and detector, often based on photoconductive antennas or electro-optic sampling. A beam splitter (BS) divides the output of the femtosecond laser into two beams. One beam is used to generate the THz radiation, typically modulated at frequency *f*, while the other serves as a probe for detection. The probe beam passes through a mechanical delay line before interacting with the THz pulse at the detector, as illustrated in Fig. 1.7. The delay line is utilized to modify the arrival time of the probe pulse relative to the THz transient, thereby enabling time-resolved sampling of the THz electric field and reconstruction of the time-domain waveform.

Through this pump–probe detection scheme, the electric field of the THz pulse is directly measured in the time domain (van Exter et al., 1989; Grischkowsky et al., 1990). The spectral

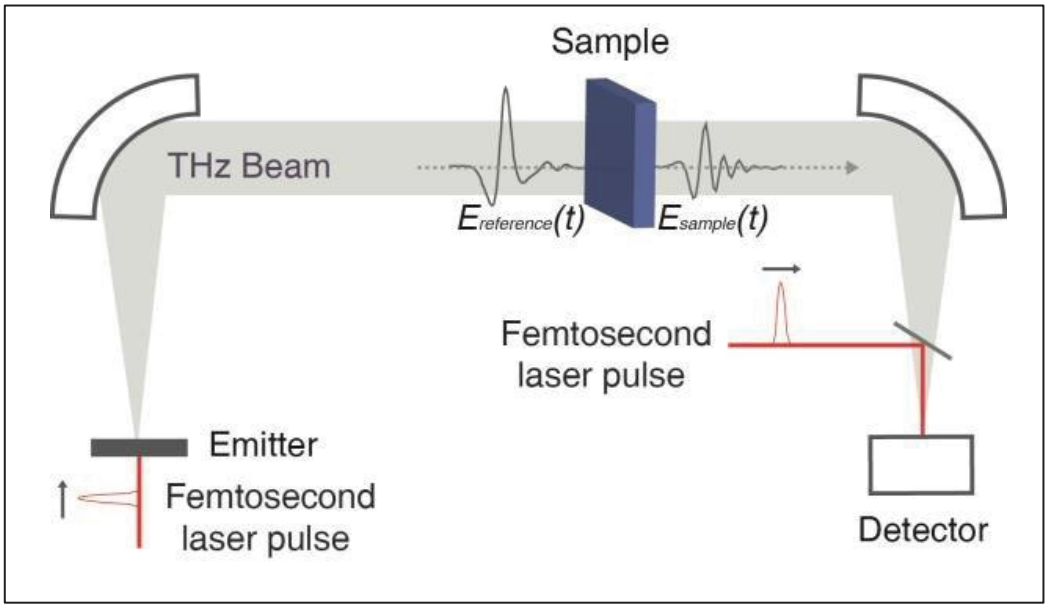

Figure 1.7 THz-TDS schematic using femtosecond laser pulses for coherent THz generation and detection
Taken from (Maeng et al., 2012)

information of the THz pulse is subsequently obtained by Fourier transformation of the measured transient electric field (Neu & Schmuttenmaer, 2018). Unlike traditional Fourier-transform spectroscopy, which detects only intensity, THz-TDS retrieves the full complex electric field. From the complex transmission function obtained by Fourier transforming both the reference and transmitted pulses, the complex refractive index and absorption coefficient of the material can be directly calculated without invoking Kramers–Kronig relations (Jackson, 1999). Consequently, THz-TDS enables simultaneous determination of the real and imaginary parts of the refractive index and allows contactless evaluation of the conductivity of metals, semiconductors, 2D materials, and superconductors.

1.5 THz Power Detectors

In contrast to coherent detection techniques, Schottky diode detectors, CMOS-based detectors, and pyroelectric detectors are generally employed for direct power (intensity) measurements and are particularly suitable for continuous-wave (CW) THz systems or frequency-domain spectroscopy (FDS) (Chernyadiev et al., 2024; Carelli et al., 2012; Sebastian et al., 2026).

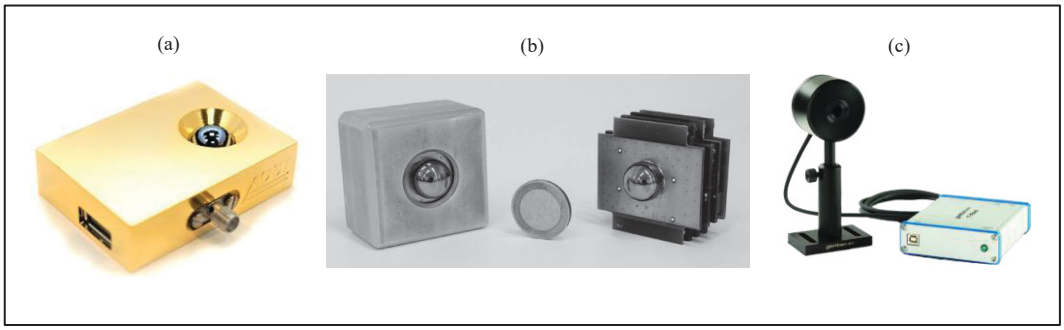

Figure 1.8 Schematic representations of (a) a Schottky diode detector
Taken from (ACST GmbH, n.d.)
(b) 1 k-pixel CMOS THz camera module for active THz imaging at room temperature
Taken from (Hadi et al., 2012)
and (c) TRAD system
Taken from (Gentec-EO., n.d.)

Unlike coherent detection approaches, intensity-based detectors do not require optical synchronization or mechanical delay stages, making them well suited for compact, robust, and field-deployable THz systems. The intensity-based detection approaches are particularly relevant to the metasurface- or FSS-enabled intensity-based polarimetric spectrometer and imaging architectures developed in later chapters and annexes of this thesis.

The incident THz power P_{THz} is related to the electric field amplitude through the time-averaged Poynting vector (Balani, 2005; Schlecht et al., 2019).

$$P_{THz} \propto \frac{|E_{THz}|^2}{2Z_0} \tag{1.11}$$

where Z_0 is the free-space impedance. The output signal of an intensity-based THz detector can generally be expressed as (Han et al., 2013).

$$V_{out} = R_v P_{THz} \tag{1.12}$$

where R_{v} denotes the voltage responsivity of the detector. This relationship indicates that the measured signal is proportional to the incident THz power rather than the instantaneous electric field amplitude.

Table 1.1. Performance comparison of Schottky, CMOS, and Pyroelectric THz detectors

Detector Type	Detection Mechanism	Typical NEP	Video BW	Response Time	Chopper needed
Schottky (slow / high sensitivity)	Nonlinear rectification in Schottky diode	~6–10 pW/√Hz	MHz range	~ns to tens of ns	Not required
Schottky (fast / high bandwidth)		~30–70 pW/√Hz	up to several GHz	~sub-ns to a few ns	Not required
CMOS THz detector	FET/CMOS rectification (plasmonic or antenna-coupled)	~20–60 pW/√Hz	kHz–MHz (architecture dependent)	~µs–ms	Often used for SNR
Pyroelectric detector	Thermal (pyroelectric effect)	~1–2 nW/√Hz ms-10 ms	Hz–kHz	~ms to tens of ms	Required

The temporal response of intensity-based THz detectors is characterized by a detector time constant τ, which determines the achievable video bandwidth. For a first-order detector response, the bandwidth can be approximated as

$$f_{BW} \approx \frac{1}{2\pi\tau} \tag{1.13}$$

Fast electronic detectors such as Schottky can therefore achieve video bandwidths of several gigahertz, enabling detection of rapidly modulated THz signals and compatibility with high-speed electronic acquisition systems. In contrast, the response time of pyroelectric detectors is governed by thermal processes and is significantly slower.

For these detectors, one of the most important performance metrics is the noise-equivalent power (NEP) [W/√Hz], which defines the minimum detectable THz power:

$$NEP = \frac{V_{noise}}{R_v} \tag{1.14}$$

where V_{noise} is the noise voltage spectral density (V/√Hz) and R_{v} is the voltage responsivity (V/W). A lower NEP indicates that the detector can detect weaker incident THz radiation. For example, Schottky diode detectors with moderate video bandwidth can exhibit NEP values as low as ~6 pW/√Hz, whereas ultra-fast Schottky detectors designed for several-GHz bandwidth typically show higher NEP values around ~38.8 pW/√Hz due to increased electronic noise (ACST GmbH, n.d.). In contrast, pyroelectric detectors generally exhibit significantly higher NEP values in the nW/√Hz range because their detection mechanism relies on slower thermal processes. A comparison among Schottky, CMOS, and pyroelectric THz detectors is summarized in Table 1.1. Overall, Schottky detectors provide an excellent balance of high sensitivity and fast electronic response, CMOS detectors enable compact and integrated THz sensing, while pyroelectric detectors offer broadband power detection but with slower thermal response and higher NEP.

1.5.1 Schottky diode detectors

Schottky diode detectors, based on metal–semiconductor junctions, provide high-speed operation at room temperature and are widely used for THz signal detection, mixing, and heterodyne reception when integrated into heterodyne receiver architectures (Yadav et al., 2023; Brinkmann et al., 2016; Sobornytskyy et al., 2013). Their fast response and compatibility with electronic readout circuits make them particularly attractive for applications in THz imaging, spectroscopy, and communication systems.

GaAs is a widely preferred material for THz Schottky diodes owing to its high electron mobility, sufficiently large bandgap that suppresses leakage current, and mature planar fabrication technology, enabling reduced RC time constants and low thermal noise (Laperashvili et al., 2010). Quasi-optical zero-bias InGaAs Schottky diode detectors integrated with planar log-spiral antennas, as illustrated in Fig. 1.9, have demonstrated ultra-wideband THz detection capability (Semenov et al., 2010). In such antenna-coupled configurations, the spiral antenna efficiently couples free-space THz radiation to the diode, enabling fast response

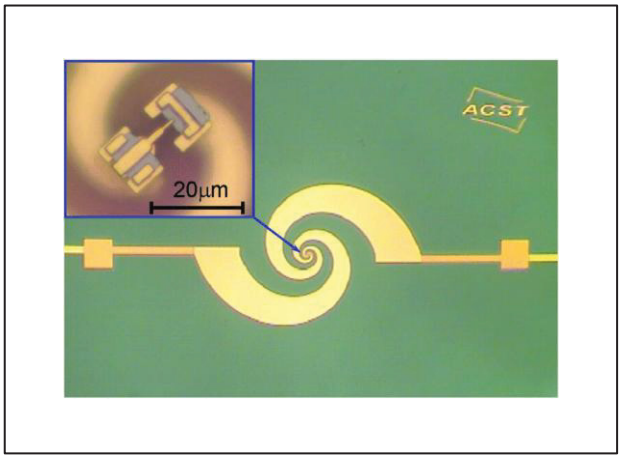

Figure 1.9 An ultrawideband detector is realized by integrating a log-spiral antenna with a zero-bias InGaAs Schottky diode
Taken from (Semenov et al., 2010)

and moderate sensitivity suitable for detecting short THz pulses as well as weak continuous-wave radiation. To date, several real-time THz imaging systems based on Schottky barrier diode detectors have been reported. For example, (Han et al., 2013b) demonstrated a broadband antenna-integrated 1×20 InGaAs Schottky barrier diode array detector, enabling a compact real-time THz line-scanning imaging system with a responsivity of approximately 98.5 V/W

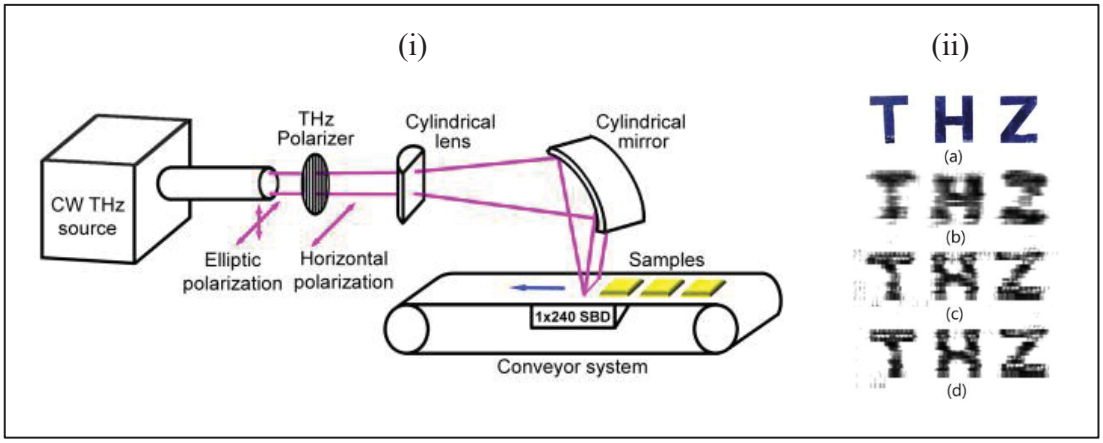

Figure 1.10 (i) THz line-scanning system with a gyrotron source, 1×240 SBD array detector, conveyor, wire-grid polarizer, HDPE cylindrical lens, and metal cylindrical mirror; (ii) Photograph of metal letters "THZ" and corresponding THz images (scan speed 25 cm/s, pixel size 0.5×0.5 mm²) for (b) unfocused/no polarizer, (c) focused/no polarizer, and (d) focused/with polarizer
Taken from (Han et al., 2014)

at 250 GHz and a noise-equivalent power (NEP) of ~106 pW/√Hz. Subsequently, (Han et al., 2014) reported a real-time continuous-wave THz line-scanning imaging system based on a 1×240 InGaAs Schottky barrier diode array detector operating at a single THz frequency, as depicted in Fig. 1.10.

1.5.2 CMOS based detectors

CMOS-based THz detectors utilize standard semiconductor fabrication technologies, enabling compact, low-cost, and highly integrated detector arrays suitable for scalable and portable THz imaging systems (Schuster et al., 2011; Hadi et al., 2019). Such integration allows the realization of large-format focal-plane arrays with on-chip readout circuitry, facilitating real-time THz imaging applications. Schuster et al. demonstrated broadband THz imaging using highly sensitive silicon CMOS detectors fabricated in a 130-nm CMOS technology. Their antenna-coupled nMOS detector achieved room-temperature operation with a responsivity above 5 kV/W and a reported NEP below 10 pW/√Hz around 300 GHz, highlighting the strong potential of CMOS technology for compact and low-cost THz imaging systems (Schuster et al., 2011). In the following, (Hadi et al., 2012) demonstrated a 1-k pixel THz camera implemented in 65-nm CMOS technology, consisting of a 32 × 32 array of antenna-coupled NMOS detectors, as illustrated in Fig. 1.11. The detectors operate through a distributed

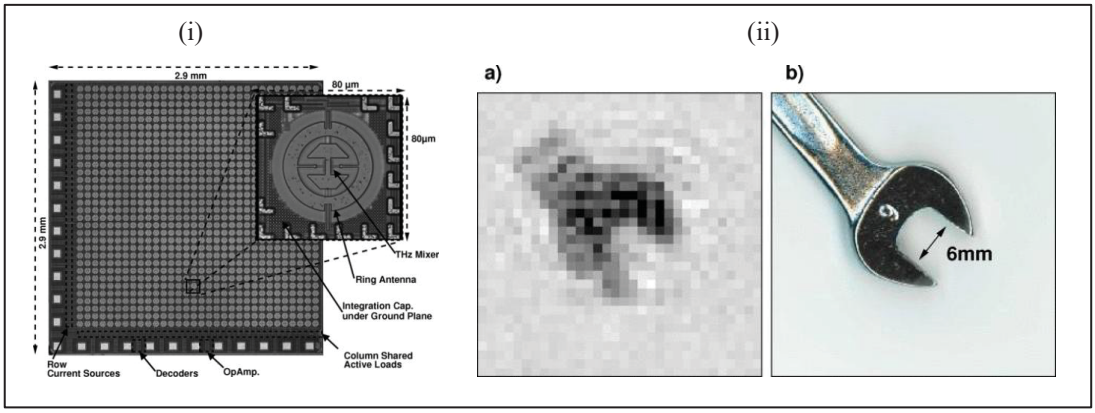

Figure 1.11 (i) Complete die micrograph of the 32×32 FPA chip (2.9 × 2.9 mm²) and topography of a single detector pixel (80 × 80 µm²). (ii) THz image of a 6 mm wrench extracted from a 25 fps video stream acquired at 650 GHz in transmission mode
Taken from (Hadi et al., 2012)

resistive self-mixing mechanism for direct THz detection. The fully integrated system enables room-temperature THz imaging at video rates up to 500 frames per second under continuous-wave illumination.

1.5.3 Pyroelectric detectors

Pyroelectric detectors operate based on temperature-induced changes in spontaneous polarization in pyroelectric materials, most commonly ferroelectric crystals or ceramics, and are widely used for broadband THz power measurements and thermal imaging. A representative example is the T-RAD radiometer, a USB-powered digital detector equipped with a 12-bit analog-to-digital converter and interfaced through a virtual COM port, as illustrated in Fig. 1.8(c).

Although pyroelectric detectors offer broadband spectral response and simple operation, they are thermal detectors that measure the time-averaged intensity or energy of incident THz radiation rather than the instantaneous electric field. Owing to their large thermal time constant and inherently slow response, they cannot provide temporal or phase-sensitive detection. Consequently, they are typically operated at low modulation frequencies (tens of hertz) using a mechanical chopper and lock-in detection (Müller et al., 2015). Pyroelectric detector arrays have also been employed for real-time THz imaging. For example, as illustrated in Fig. 1.12,

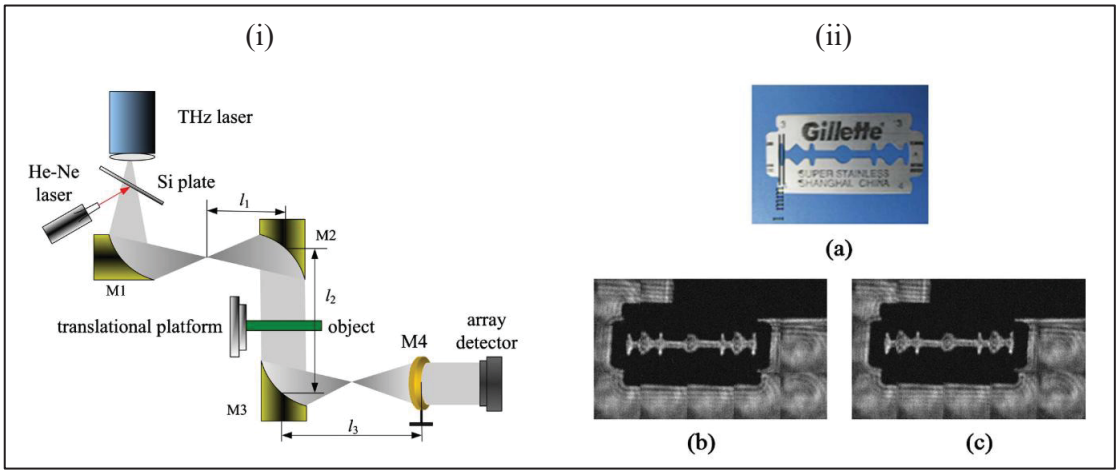

Figure 1.12 (i) Real-time THz scanning imaging using a pyroelectric array camera; (ii) THz scanning image of a razor blade
Taken from (Li et al., 2010)

(Li et al., 2010) demonstrated a THz scanning imaging system based on a 124 × 124 pyroelectric array camera and a 2.52 THz continuous-wave laser for large-area terahertz imaging. The system achieved a spatial resolution of approximately 0.4–0.6 mm using scanning and multi-frame averaging techniques.

1.5.4 THz camera

Recent advances in detector arrays have enabled the development of THz cameras capable of real-time imaging. Unlike single-pixel detectors that require raster scanning, THz cameras employ two-dimensional detector arrays, allowing direct acquisition of spatial information across the field of view. Depending on the detection mechanism, these cameras can be based on thermal detectors (e.g., microbolometers or pyroelectric arrays) or semiconductor-based detectors, enabling compact and room-temperature THz imaging systems.

Microbolometer THz cameras, such as those developed by the Institut National d'Optique (INO), operate as thermal power detectors and enable real-time THz imaging. For example, as shown in Fig. 1.13(i), the MICROXCAM-384i THz camera offers high sensitivity over a broad spectral range and provides 16-bit raw image data at up to 50 Hz through a Gigabit Ethernet (GigE) interface (Institut National d'Optique, n.d.). Sub-THz imaging cameras developed by

Figure 1.13 (i) MICROXCAM-384i-THz terahertz microbolometer camera;
Taken from (Institut National d'Optique, n.d.)
(ii) Tera-4096 sub-THz imaging camera
Taken from (TeraSense, n.d.)

TeraSense operate in the frequency range of approximately 0.05–0.7 THz and use semiconductor detector arrays based on plasmonic detection in a two-dimensional electron gas is demonstrated in Fig. 1.13(ii) (TeraSense, n.d.). These cameras provide room-temperature operation, responsivity up to about 50 kV/W, and a typical NEP around 1 nW/√Hz. The systems are available with different pixel-array sizes (e.g., 256, 1024, and 4096 pixels) and require an external THz source, enabling compact and relatively low-cost real-time sub-THz imaging for industrial inspection and security applications.

Although commercial THz cameras and several real-time THz imaging systems have been demonstrated, most existing approaches rely on intensity-only detection and do not provide polarization-resolved information. Consequently, multispectral THz polarimetric imaging, capable of simultaneously resolving spectral and polarization characteristics, remains largely unexplored in the literature.

1.6 Intensity based THz spectrometer

In industrial environments, there is a growing demand for compact THz spectrometers that offer fast, reliable, and cost-effective performance. Traditional THz time-domain spectroscopy systems often rely on bulky and complex delay stages to perform temporal scanning, which increases system size, cost, and limits scanning speed, factors that are impractical for high-throughput or in-line industrial applications. By contrast, compact THz spectrometers eliminate the need for mechanical delay lines, enabling real-time, robust spectral measurements (Carelli et al., 2012; Sebastian et al., 2026). A representative configuration is presented in Fig. 1.14. These systems can utilize intensity-based THz detectors such as Schottky diodes or CMOS THz detectors, which are well-suited for integration due to their small footprint, room-temperature operation, and compatibility with electronic readout circuits. As a result, compact THz spectrometers become ideal for deployment in industrial settings for material inspection, quality control, and non-destructive testing, where speed, reliability, and integration are critical.

Furthermore, machine learning techniques could be useful to classify materials or detect defects in real-time, making the system highly suitable for in-line quality control and

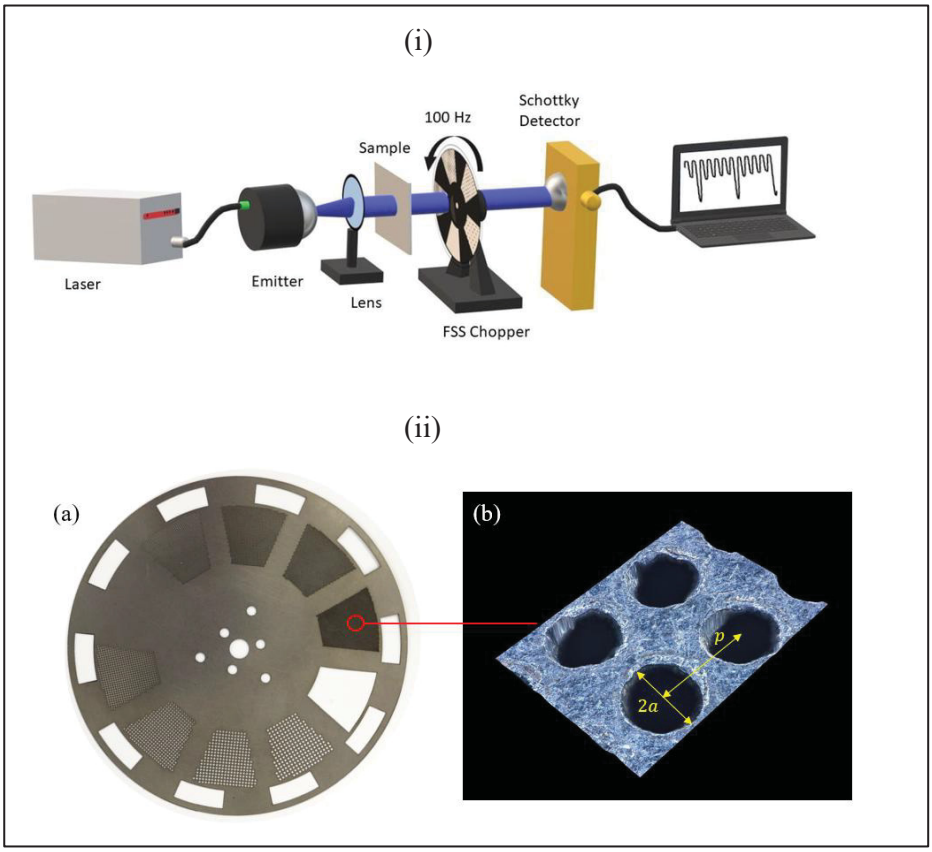

Figure 1.14 (i) Schematic illustration of an AI-driven compact THz multi-spectral spectrometer
Taken from (Sebastian et al., 2024)
(ii) (a) photograph of the fabricated chopper wheel and (b) the microscopic images of the holes
Taken from (Sebastian et al., 2026)

monitoring. Additionally, predictive models can estimate material properties such as thickness or composition directly from raw detector outputs. Altogether, AI transforms compact THz spectrometers into intelligent, autonomous tools capable of delivering rapid, reliable insights across a wide range of industrial sensing applications (Sebastian et al., 2026).

However, in compact THz spectrometer configurations reported to date, polarization information is not explicitly considered, and the detected signal is typically limited to total intensity measurements without polarization discrimination. Consequently, compact intensity-based THz polarimetric imaging systems have not yet been comprehensively reported. The absence of polarization-resolved capability restricts access to valuable material information

such as birefringence, anisotropy, and stress-induced optical effects, which are particularly important for advanced material characterization and industrial quality assessment.

1.7 THz polarimetry

THz polarimetric systems extend conventional THz spectroscopy by resolving not only the spectral amplitude but also the polarization state of the THz electric field, thereby enabling the investigation of material anisotropy, birefringence, dichroism, and polarization-dependent phase retardation. In general, THz polarimetry requires measurement of at least two orthogonal components of the THz electric field. When both amplitude and relative phase are accessed through coherent detection, polarization parameters such as the azimuth angle, ellipticity, and the complete Jones or Stokes vectors can be reconstructed. Time-domain implementations commonly rely on coherent detection techniques, such as EO sampling or photoconductive antennas, where polarization sensitivity is achieved through detector orientation, polarization modulation, or multi-contact receiver geometries.

The polarization state of electromagnetic radiation can be fully described by the four Stokes parameters S_0, S_1, S_2 and S_3. In the coherent field formulation, these parameters are expressed in terms of the complex orthogonal field components E_X and E_Y as:

$$S = \begin{pmatrix} S_0 \\ S_1 \\ S_2 \\ S_3 \end{pmatrix} = \begin{pmatrix} |E_X|^2 + |E_Y|^2 \\ |E_X|^2 - |E_Y|^2 \\ 2\,\mathrm{Re}(E_x E_y^*) \\ 2\,\mathrm{Im}(E_x E_y^*) \end{pmatrix} \tag{1.15}$$

Alternatively, in intensity-based polarimetric systems where only power measurements are available, the Stokes parameters can be obtained from projection measurements through different polarization analyzers as (Zhang et al., 2021; Wang et al., 2025):

$$S = \begin{pmatrix} S_0 \\ S_1 \\ S_2 \\ S_3 \end{pmatrix} = \begin{pmatrix} I_X + I_Y \\ I_X - I_Y \\ I_{45^\circ} - I_{135^\circ} \\ I_{LCP} - I_{RCP} \end{pmatrix} \tag{1.16}$$

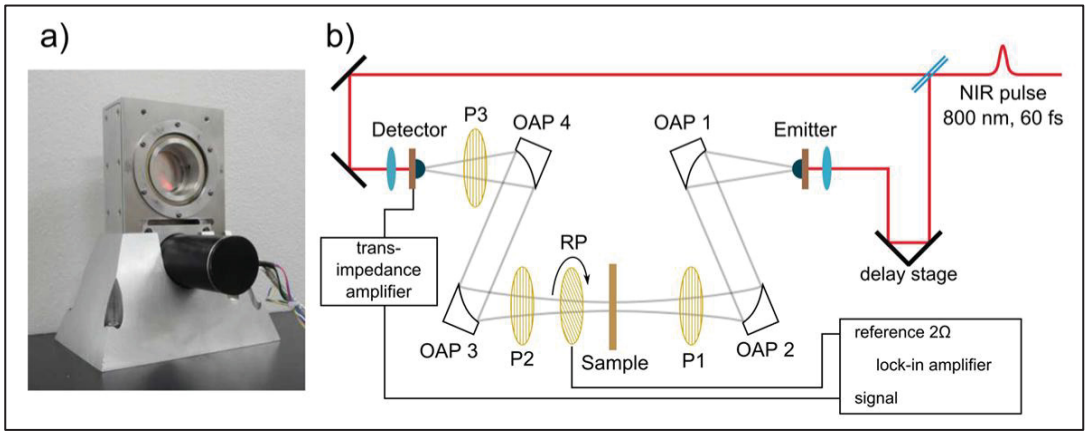

Figure 1.15 Rotating polarizer–based THz polarimetry: (a) rotator with QMC polarizer and (b) experimental layout illustrating polarization modulation and lock-in detection Taken from (Morris et al., 2012)

Here, I_X and I_Y denote the measured intensities corresponding to horizontal and vertical linear polarization components, respectively. I_{45° and I_{135° correspond to linear polarization states oriented at 45° and 135°, while I_{LCP} and I_{RCP} represent the intensities of left- and right-handed circular polarization components.

Over the past decade, various techniques have been developed to enable polarization-resolved THz measurements (Morris et al., 2012; Zhang et al., 2009; Xu et al., 2020). Morris *et al*. demonstrated a PCA-based THz time-domain polarimetry system in which both THz generation and detection are performed using femtosecond-laser-excited photoconductive antennas (Morris et al., 2012). The technique employs a fast-rotating wire-grid polarizer to modulate the THz polarization state, with lock-in detection used to extract the in-phase and quadrature components of the signal. A schematic of the experimental configuration is presented in Fig. 1.15. This enables direct retrieval of the two orthogonal electric-field components and precise determination of polarization rotation angle and ellipticity (~0.02°) over 0.1–2.5 THz, validated through birefringence measurements of sapphire. Subsequently, using EO sampling Zhang *et al*. demonstrated a polarization-sensitive THz-TDS method capable of measuring both orthogonal components of the THz electric field (Zhang et al., 2009). This approach enables discrimination between true absorption features and birefringence-induced polarization rotation, allowing accurate extraction of phase retardation

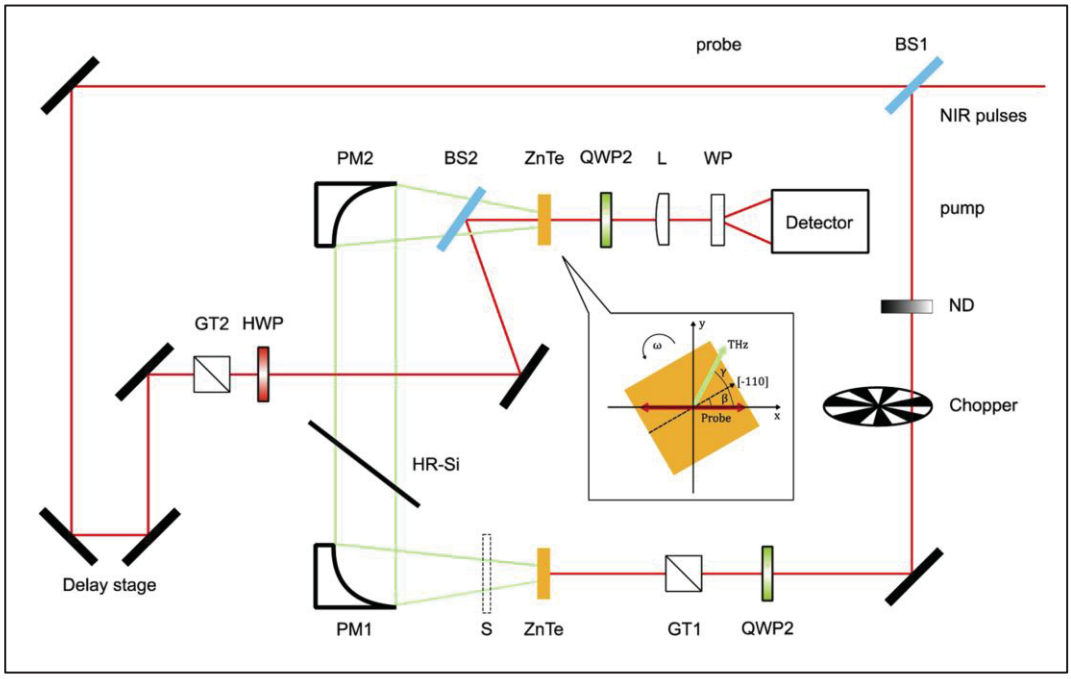

Figure 1.16 Schematic of the THz Time-Domain Polarimetry (THz-TDP) system based on EO sampling
Taken from (Xu et al., 2020)

and optical axis orientation in crystalline materials. Following (Xu et al., 2020) demonstrated a THz time-domain polarimetry (THz-TDP) system based on a rotating electro-optic sampling crystal, enabling reconstruction of the THz polarization state without external polarizers, as illustrated in Fig. 1.16. By extracting modulated signal components and applying Jones matrix calibration, the system achieves sub-degree angular precision and is validated through birefringence and ellipsometry measurements. While these coherent THz polarimetric approaches provide broadband and phase-resolved information, they inherently rely on time-domain sampling, requiring optical delay stages, probe-beam synchronization, and sequential acquisition of the THz waveform, which can limit portability and increase system complexity, alignment sensitivity, and measurement time.

1.8 THz polarimetric imaging

THz polarimetric imaging extends conventional THz imaging by exploiting the vector nature of the THz electric field, enabling spatially resolved characterization of polarization-dependent

interactions between THz radiation and matter. Unlike intensity-only imaging, which measures a single scalar quantity, polarimetric imaging captures changes in the polarization state of the THz wave, such as rotation, phase retardation, depolarization, and ellipticity that arise from material anisotropy, birefringence, structural orientation, surface roughness, and scattering. By acquiring polarization-resolved measurements at each image pixel and reconstructing the corresponding Jones, Stokes, or Mueller matrix parameters, THz polarimetric imaging provides additional contrast mechanisms that are otherwise inaccessible, particularly in weakly absorbing or highly scattering samples. These capabilities have proven valuable across a broad range of applications, including non-destructive evaluation, biomedical imaging, security screening, and material characterization, where polarization signatures can enhance sensitivity to microstructural features and subsurface heterogeneity. At the same time, the practical realization of THz polarimetric imaging requires careful consideration of measurement architectures, polarization encoding strategies, and calibration procedures, motivating the diverse range of techniques reviewed in the following subsections.

1.8.1 Electro-optic–based THz polarimetric imaging

Early THz polarimetric imaging systems were predominantly implemented using electro-optic time-domain detection, which enables direct access to the vector components of the THz electric field. A seminal contribution was reported by (Van Der Valk et al., 2005), demonstrated that measuring both transverse components of the THz field using a modified EO sampling scheme is essential for correctly interpreting THz images, as apparent attenuation may arise from polarization rotation rather than material absorption. Building on this concept, (Zhang et al., 2008) developed a systematic THz polarization imaging framework based on EO sampling with a ⟨110⟩-oriented ZnTe crystal, where orthogonal field components were obtained sequentially by rotating the detection crystal and analyzed using Jones-matrix formalism to reconstruct spatial maps of polarization rotation and phase retardation. Their results revealed that diffraction and scattering at sample edges induce strong polarization changes, providing contrast mechanisms not visible in conventional intensity images. However, this approach required raster scanning, sequential polarization acquisition, and mechanical rotation of optical components, leading to long imaging times and increased

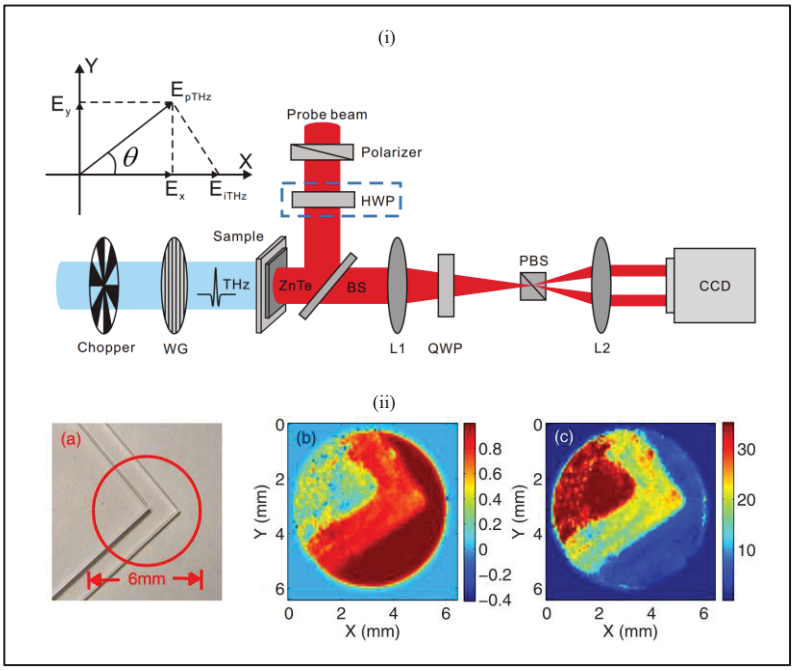

Figure 1.17 (i) Schematic of the THz detection system; (ii) (a) photograph of the sample; (b–c) polarization-resolved distributions of the energy ratio and polarization angle of the sample
Taken from (Wang et al., 2010)

sensitivity to alignment and calibration errors. To address these limitations, (Wang et al., 2010) introduced a balanced EO-detection scheme that enabled near-real-time THz polarimetric imaging by measuring orthogonal polarization components through probe-beam polarization control rather than crystal rotation, as schematically depicted in Fig. 1.17. While this significantly improved acquisition speed and angular precision, EO-based polarimetric imaging systems still inherently rely on time-domain waveform sampling, optical delay stages, and careful polarization calibration, which constrain throughput and system robustness.

1.8.2 THz polarimetric imaging in scattering media and biomedical applications

Subsequently, THz polarimetric imaging was extended to scattering, heterogeneous, and biological samples, where polarization contrast can reveal microstructural and anisotropic features that are otherwise obscured in amplitude-only images. Several studies demonstrated that polarization-resolved THz imaging can enhance contrast in biological tissues by exploiting differences in birefringence, fibrous alignment, and depolarization behavior. In particular, THz

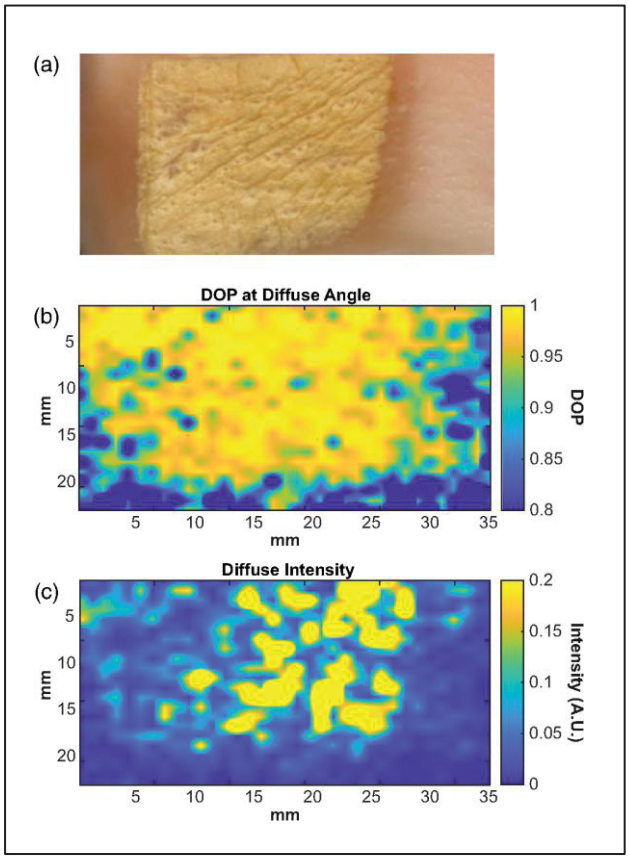

Figure 1.18 (a) Optical image of an ex vivo porcine skin burn sample; (b) degree-of-polarization (DoP) map and (c) diffuse-scattering intensity map measured at 0.6 THz using an oblique illumination geometry
Taken from (Heller et al., 2025)

polarimetric imaging has been applied to ex vivo breast tissue, showing improved discrimination between fibrous, fatty, and malignant regions through co- and cross-polarized imaging and Stokes-parameter analysis (Gurjar et al., 2024). Additional work demonstrates diffuse THz polarimetric imaging for sensing tissue microstructural changes through frequency-dependent intensity and polarization contrast as shown in Fig. 1.18, supported by Monte Carlo Mie-scattering modeling and experimental validation (Heller et al., 2025). Mueller-matrix-based THz imaging approaches further enabled quantitative extraction of birefringence and depolarization parameters, providing a more complete description of polarization changes induced by complex samples (Xu et al., 2024a). Reflection-mode THz

polarimetric imaging was also explored to accommodate opaque or thick samples, with spatially resolved Stokes-vector mapping demonstrating sensitivity to surface morphology and subsurface scattering (Xu et al., 2023; Xu et al., 2024b). Despite their enhanced contrast capabilities, these approaches generally require multiple polarization states per pixel, extensive averaging to suppress noise in scattering environments, and precise calibration to decouple sample-induced polarization effects from system artifacts, which limits imaging speed and scalability for large-area or real-time applications.

1.8.3 Compact and alternative THz polarimetric imaging architectures

More recent research has focused on reducing the complexity and measurement redundancy of THz polarimetric imaging systems through compact, single-pixel, and polarization-encoding

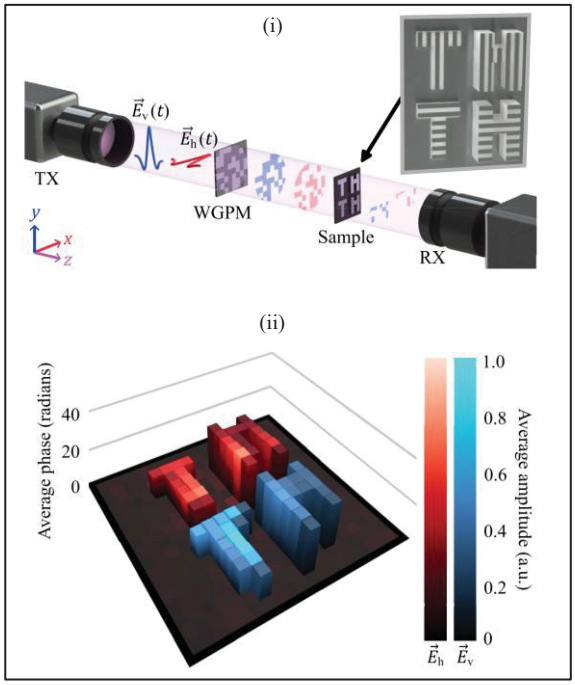

Figure 1.19 (i) Illustration of a single measurement in polarization-resolved THz single-pixel imaging (SPI) with pulsed THz detection; (ii) reconstructed polarization-resolved three-dimensional (3D) THz image obtained from the reconstructed THz electric-field amplitude
Taken from (Lowry et al., 2025)

architectures. Single-pixel THz polarimetric imaging techniques have been demonstrated, where polarization information is reconstructed from sequential measurements using a single detector combined with modulation or computational reconstruction as shown in Fig. 1.19, significantly reducing detector count but still requiring multiple measurements per image pixel (Lowry et al., 2025). In parallel, metasurface-assisted and polarization-selective structures have been introduced to encode polarization information directly into intensity contrast, enabling compact THz polarimetric imaging without conventional rotating polarizers or EO crystals (Baek et al., 2024). Recent two approaches further explored integrated and portable THz polarimetric imaging systems, emphasizing robustness, reduced alignment sensitivity, and compatibility with reflection-mode operation (Harris et al., 2024; Huang et al., 2021). While these approaches offer improved compactness and system simplicity, they often trade off measurement completeness, spectral bandwidth, and still require sequential measurements or calibration procedures to reconstruct full polarization information. Consequently, balancing polarization sensitivity, acquisition speed, and system complexity remains a central challenge in the development of practical THz polarimetric imaging systems.

1.9 Vortex beam generation

THz vortex beams are a class of structured electromagnetic waves characterized by a helical phase front of the form as

$$E(r,\phi,z) \propto e^{il\phi} \tag{1.17}$$

where l is the topological charge and ϕ denotes the azimuthal angle. Such beams carry orbital angular momentum (OAM), resulting in a phase singularity at the beam center and a corresponding null in intensity along the propagation axis. The ability to generate and control THz vortex beams has attracted increasing interest due to their potential applications in beam shaping, imaging, communications, and material characterization.

Several studies have demonstrated THz vortex beam generation using passive diffractive elements, particularly spiral phase plates (SPPs) and spiral zone plates (SZPs), which impose

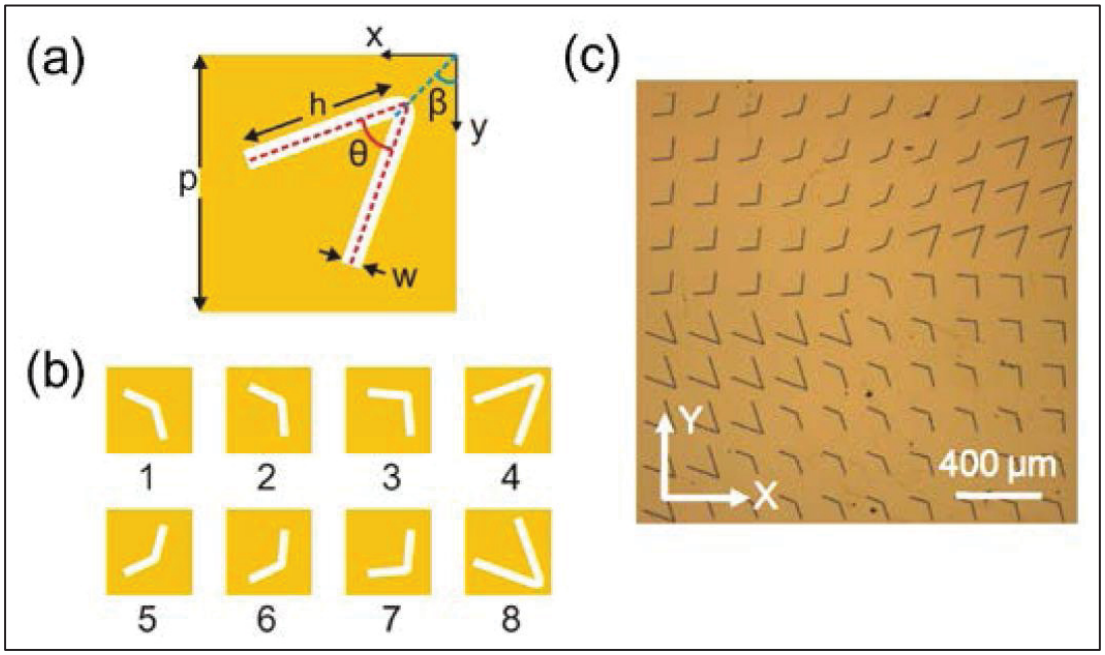

Figure 1.20 Complementary V-shaped antenna–based vortex phase plate: (a) phase-modulation unit cell, (b) antenna geometries providing discrete phase shifts from −3π/4 to π, and (c) photograph of the central region of the VPP for l=1
Taken from (He et al., 2013)

an azimuthally varying phase through controlled thickness or binary patterns (Miyamoto et al., 2016; Radivon et al., 2024; Ge et al., 2017; Paraipan et al., 2024). Polymer-based SPPs fabricated via stereolithography or molding exhibit stepped helical geometries optimized for specific THz frequencies and enable vortex beams with well-defined topological charges, verified through interferometric techniques (Liu et al., 2025; Pinnock et al., 2023). Broadband and high-power vortex generation has also been achieved using low-dispersion Tsurupica SPPs with azimuthal phase segmentation, making them suitable for monocycle THz vortex generation (Miyamoto et al., 2016). To address large-aperture requirements, femtosecond laser filament direct writing has been employed to fabricate centimeter-scale SZP on metal-coated substrates, enabling efficient vortex generation in diffraction-dominated THz systems (Zhang et al., 2020). More recently, advanced SZPs based on flexible and stretchable nanomaterial films, such as single-walled carbon nanotube layers, have been introduced to enable mechanically tunable vortex beam control through rotation, scaling, and radial deformation, extending the functionality of passive diffractive THz optics (Radivon et al., 2024). In parallel,

frequency-multiplexed vortex beam generation has been demonstrated using SPPs combined with metallic masks, allowing a single passive device to generate multiple vortex modes with different topological charges across a broadband THz spectrum (Tokizane et al., 2025).

An alternative compact approach relies on ultrathin metasurface-based vortex generators, where spatially varying phase is achieved using subwavelength resonant antenna geometries. Complementary V-shaped antenna metasurfaces have been designed to function as planar vortex phase plates, offering deeply subwavelength thickness while maintaining precise phase control. A representative configuration is presented in Fig. 1.20. The resulting THz vortex beams were characterized through holographic field reconstruction, allowing direct observation of phase singularities and propagation dynamics (He et al., 2013).

Beyond passive optical elements, active nonlinear optical schemes have been explored to generate THz vortex beams without structured diffractive components. In particular, soft-aperture difference-frequency generation in nonlinear crystals enables the direct generation of high-purity THz orbital angular momentum modes over a wide frequency range. This approach exploits spatial mode overlap and nonlinear wave mixing to suppress higher-order radial modes, yielding tunable and high-quality vortex beams without fabrication of phase-modulating structures (Miyamoto et al., 2019).

With the growing interest in compact and planar vortex beam generators, increasing attention is being directed toward scalable and cost-effective fabrication strategies. In this context, printable electronics, additive manufacturing, and laser-based microfabrication are emerging as promising platforms for realizing planar THz vortex generators. These approaches enable rapid prototyping, large-area fabrication, and compatibility with flexible or conformal substrates while maintaining sufficient structural resolution for phase and wavefront engineering. As research continues to move toward lightweight, integrable, and application-oriented THz systems, such fabrication routes offer attractive alternatives to conventional bulk optics and high-cost lithographic processes, particularly for metasurface- and diffractive-based vortex beam architectures.

1.10 THz frequency selective surfaces

Metamaterials offer powerful and flexible platforms to manipulate THz waves in ways that go far beyond the limitations of conventional optical components (Neu & Schmuttenmaer, 2018; Xiao et al., 2019). Metamaterials are artificially composite materials with properties derived from internal microstructure rather than the chemical composition of natural materials. Metamaterials can interact with THz waves in ways that conventional materials cannot since they can theoretically be designed to have certain material properties enabling high-extinction-ratio polarization control, frequency-selective filtering, perfect absorption, and compact wavefront engineering for THz spectroscopy and imaging systems (Landy et al., 2008). Besides, metasurface (MS), which is the two-dimensional (2D) version of the metamaterial, with a thickness smaller than the incident electromagnetic wavelength, allows the optical wavefront to be controlled over subwavelength thicknesses (Wu et al., 2020; Azad et al., 2016). Another variant is FSSs which are periodic structures that function primarily as spatial filters, selectively transmitting, reflecting, or absorbing specific frequencies based on resonance phenomena such as inductive and capacitive effects. Each unit element in an FSS is designed

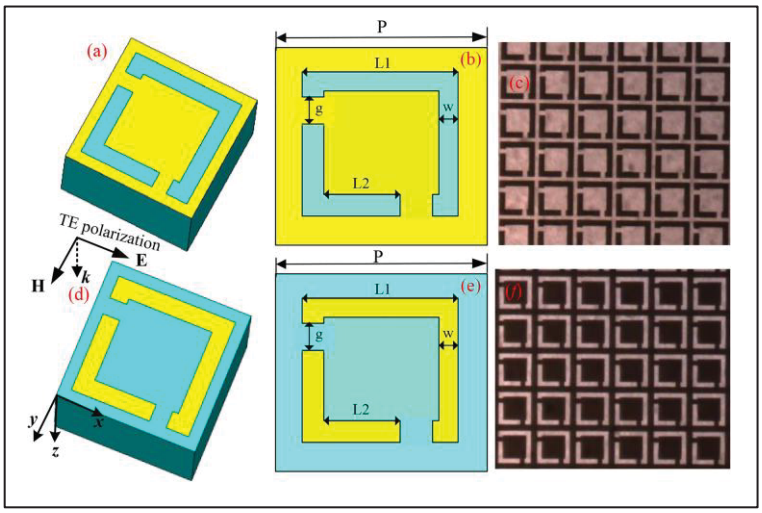

Figure 1.21 Schematic view of the unit cell of the frequency selective surfaces (a) filter and (d) complementary structure. Top-view geometries of the (b) filter and (e) complementary structure. Optical microscope images of the fabricated (c) filter and (f) complementary structure
Taken from (Sun et al., 2020)

to resonate at a particular frequency, and its shape, size, and arrangement determine the overall filtering response of the surface. The unit cells of traditional FSS are usually around half the operating wavelength, in contrast to metasurfaces, which are made up of sub-wavelength-scale components (Ebrahimi et al., 2015). A schematic representation of the FSS and its corresponding unit cell are illustrated in Fig. 1.21. Unlike metasurfaces, which manipulate phase and wavefronts at subwavelength scales, FSS primarily functions based on periodic resonant interactions, making them essential in frequency-dependent electromagnetic applications.

The frequency-selective response of a FSS originates from the excitation of induced surface currents J_s on periodically arranged metallic elements when illuminated by an incident electromagnetic wave. According to Maxwell's boundary conditions, the discontinuity of the tangential magnetic field across the metallic surface is directly related to the induced surface current density (Harrington, 2001; Selvanayagam & Eleftheriades, 2013),

$$\hat{n} \times (H_2 - H_1) = J_s \tag{1.18}$$

where $\hat{n}$ denotes the unit normal vector to the surface. These induced currents re-radiate electromagnetic fields, leading to constructive or destructive interference in the forward and backward directions, thereby producing frequency-dependent transmission and reflection characteristics.

The transmission and reflection responses of an FSS are commonly described using the complex transmission and reflection coefficients,

$$T(\omega) = \frac{E_t}{E_i} \tag{1.19}$$

$$R(\omega) = \frac{E_r}{E_i} \tag{1.20}$$

Where E_i, E_t, and E_r represent the incident, transmitted, and reflected electric field amplitudes, respectively.

Most FSS geometries exhibit resonant behavior that can be approximated using an equivalent lumped-element circuit model. In this representation, the metallic strips or conductive paths contribute an effective inductance L, while the gaps between adjacent elements introduce capacitance C. The fundamental resonance frequency is therefore given by

$$f_0 = \frac{1}{2\pi\sqrt{LC}} \tag{1.21}$$

This expression highlights that the resonant frequency is directly governed by the geometrical parameters of the unit cell. Increasing strip length typically increases the effective inductance, while reducing gap spacing increases capacitance; both effects lower the resonance frequency. Consequently, careful geometric design enables precise spectral tuning of the FSS response.

For a periodically arranged FSS, the unit-cell periodicity $p$must be chosen appropriately to avoid the excitation of higher-order diffraction modes (grating lobes). To ensure only the zeroth-order transmitted and reflected modes propagate, the periodicity must satisfy

$$p < \frac{\lambda}{n} \tag{1.22}$$

where λ is the free-space wavelength at the operating frequency and n is the refractive index of the surrounding medium. This condition suppresses unwanted diffraction orders and ensures stable angular and spectral performance.

FSS can be classified by two types as i) passive FSS and ii) active or reconfigurable FSS. Passive THz FSS consists of fixed metallic or dielectric unit elements that provide a predetermined filtering response based on their geometry, material properties, and periodicity. These structures are simple, stable, and widely used in applications where a static frequency response is sufficient. However, active THz FSS incorporates tunable elements such as graphene, VO_2, barium strontium titanate (BST) and others to dynamically adjust their frequency response (Vegesna et al., 2014; Yan et al, 2016; Lv et al., 2022). By applying an external stimulus, such as voltage, temperature, or optical excitation, active THz FSS can achieve reconfigurable filtering, and adaptive polarization control, making them highly

versatile for modern THz systems. While passive FSS is easier to fabricate and integrate, active FSS enables greater flexibility and functionality, making it a key enabler for the next generation of intelligent and adaptive THz technologies.

1.11 Reconfigurable THz FSS

(Yan et al., 2016) presents a novel design for THz modulators using hybrid graphene/FSS structures, demonstrating enhanced light–matter interaction, tunable modulation depth, reduced insertion loss, and improved operational speed. Key advantages include the ability to finely control modulation characteristics through geometric optimization and the use of patterned graphene to minimize active area and improve speed. However, challenges remain in the relatively high sheet conductivity of Chemical Vapor Deposition (CVD) graphene used, which restricts maximum transmission, and in the need for precise fabrication to optimize the device geometry. Also, thermally reconfigurable THz FSS has been presented in (Vegesna et al., 2014). This study demonstrates a reconfigurable THz FSS polarizer using Vanadium

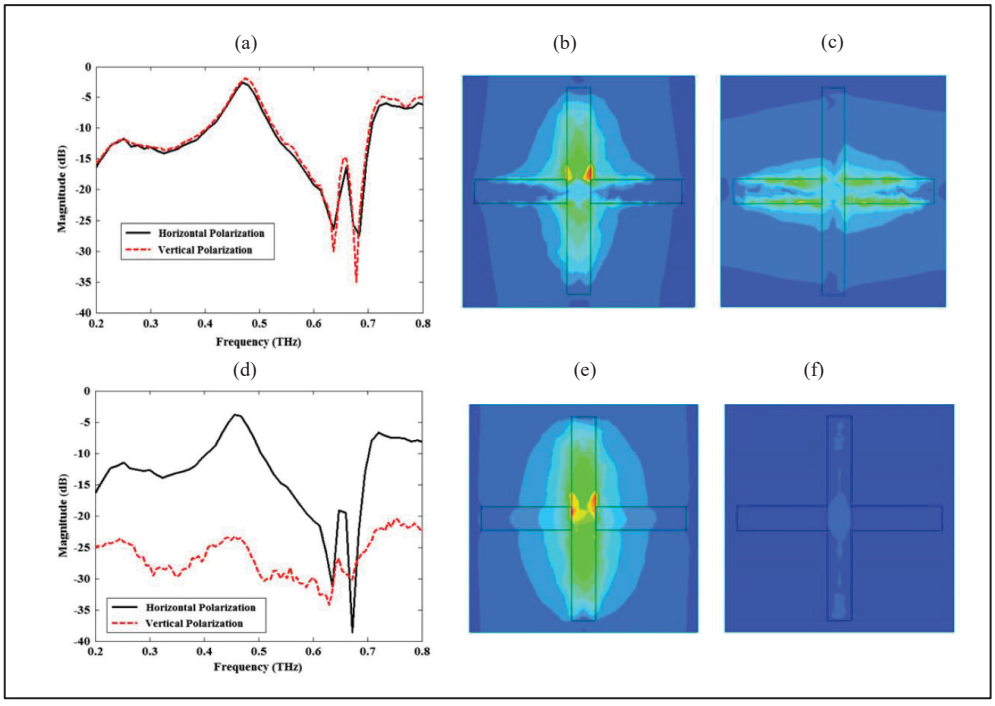

Figure 1.22 Measured frequency responses and electric-field magnitude distributions for horizontal and vertical polarizations at (a–c) room temperature (T = 28 °C) and (d–f) elevated temperature (T = 80 °C) Taken from (Vegesna et al., 2014)

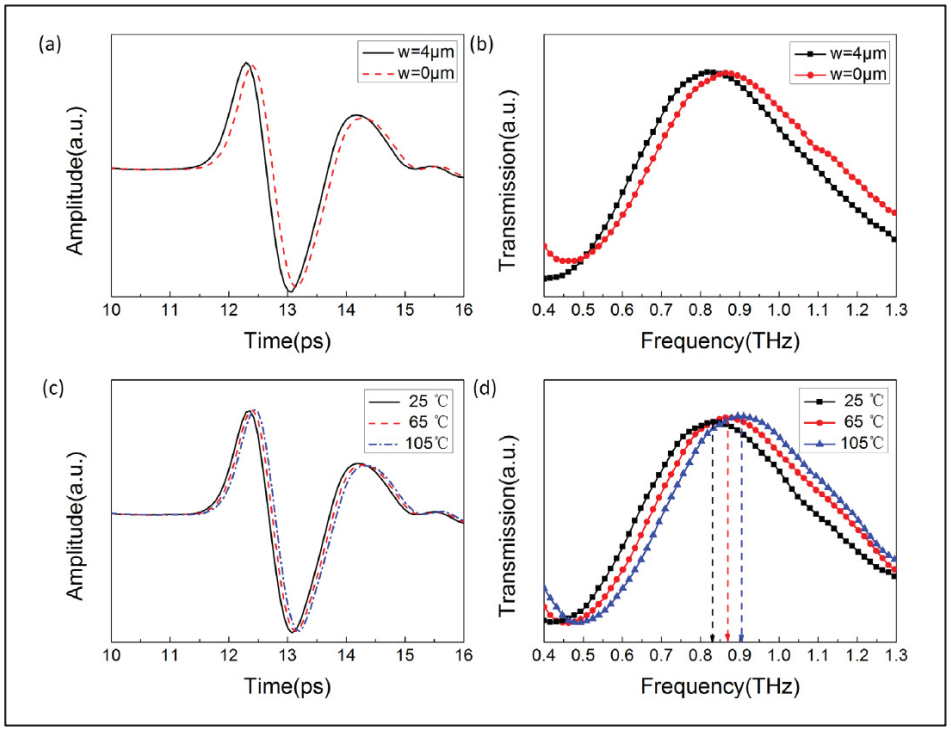

Figure 1.23 (a) Measured time-domain THz waveforms of the FSS with and without integrated electrical heating wires at room temperature; (b) corresponding frequency-domain responses; (c) Time-domain THz waveforms of the FSS recorded at various temperatures; and (d) corresponding frequency-domain spectra Taken from (Dong et al., 2018)

dioxide (VO_2), which enables dynamic switching between single- and dual-polarized transmission by leveraging its temperature-induced insulator-to-metal phase transition. The key advantages include achieving high extinction ratios (~25 dB) with a single FSS layer and tunable polarization states without the need for complex multi-layer assemblies (see Fig. 1.22). However, challenges remain in managing thermal control for reconfiguration and mitigating spurious resonances caused by fabrication variances in periodicity.

(Dong et al., 2018) presents a thermally tunable THz FSS using a BST thin film and embedded micro-scale electric heating wires. The key advantage is the precise, continuous tuning of the passband frequency (from 0.826 to 0.905 THz) by modulating the temperature-dependent permittivity of the BST, enabling integration with metamaterial-based THz, as depicted in Fig. 1.23. Following, (Lv et al., 2022) introduces a mechanically reconfigurable THz bandpass filter

based on a multilayer FSS structure. The key advantage of this design is its wide frequency tuning range (220–330 GHz) with high transmission efficiency (~80%) and low insertion loss (<1.3 dB), achieved without requiring complex biasing circuits. The reconfiguration is accomplished mechanically, by varying the air gap between FSS layers, which offers simplicity, polarization insensitivity, and stability under oblique incidence. However, challenges include the precision required in mechanical adjustment and alignment, as well as potential frequency drift at high incident angles due to aperture clipping and focal misalignment.

1.12 Polarization sensitive THz FSS

In polarization-sensitive FSS, the spectral response depends not only on frequency but also on the polarization state of the incident electromagnetic wave. When a linearly polarized THz plane wave impinges on an anisotropic unit cell, different surface current distributions are induced depending on the orientation of the electric field vector relative to the structural geometry (see Fig. 1.24).

For a normally incident plane wave with transverse electric field components E_x and E_y,

$$E_{inc} = \begin{pmatrix} E_x \\ E_y \end{pmatrix} \tag{1.23}$$

the transmitted field can be expressed in matrix form as

$$E_t = \begin{pmatrix} T_x(\omega) & 0 \\ 0 & T_y(\omega) \end{pmatrix} \begin{pmatrix} E_x \\ E_y \end{pmatrix} \tag{1.24}$$

where $T_x(\omega)$ and $T_y(\omega)$ represent the frequency-dependent transmission coefficients for x- and y-polarized components, respectively.

For an isotropic FSS,

$$T_x(\omega) = T_y(\omega) \tag{1.25}$$

indicating polarization-independent behavior. However, for anisotropic or polarization-sensitive FSS structures,

$$T_x(\omega) \neq T_y(\omega) \tag{1.26}$$

which establishes polarization selectivity. This inequality arises from the geometrical asymmetry of the unit cell, which produces different effective inductance–capacitance (LC) values along orthogonal directions. As a result, the resonance frequencies for the two polarizations differ:

$$f_{0x} = \frac{1}{2\pi\sqrt{L_x C_x}} \tag{1.27}$$

$$f_{0y} = \frac{1}{2\pi\sqrt{L_y C_y}} \tag{1.28}$$

This polarization-dependent resonance enables independent control of orthogonal electric field components, forming the basis for THz polarimetric filtering and angle-of-linear-polarization (AoLP) sensing.

By tailoring the orientation, aspect ratio, and symmetry of the apertures or resonant elements, these metastructures selectively enhance or suppress the transmission of specific linear polarization components while preserving the incident polarization state (Hong et al., 2013; Hong et al., 2017; Lee et al., 2006; Lee et al., 2017). The polarization selectivity arises from polarization-dependent surface current distributions and resonance excitation mechanisms, which lead to different effective inductive and capacitive responses for each polarization orientation. As a result, a single FSS layer can function as a frequency-selective polarizer, providing strong polarization contrast at targeted THz frequencies. Such polarization-sensitive FSS are particularly well suited for intensity-based THz polarimetric imaging, where polarization information is extracted from amplitude variations measured at different analyzer orientations, without requiring phase-sensitive detection or polarization transformation elements.

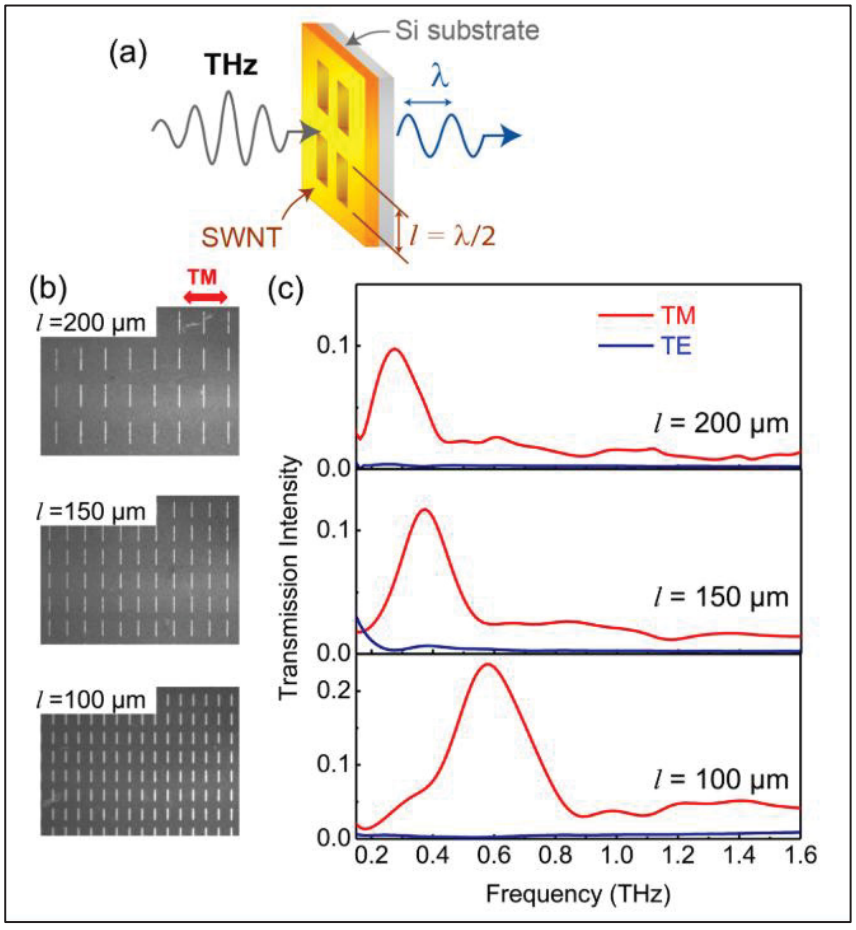

Figure 1.24 (a) Schematic diagram of the polarization-sensitive FSS structure; (b) fabricated FSS sample and (c) experimentally measured transmission characteristics for both orthogonal linear polarizations
Taken from (Hong et al., 2013)

1.13 Fabrication of THz devices

The development of fabrication techniques for THz devices has advanced significantly in recent years, driven by the demand for precise, scalable, and cost-effective manufacturing methods. To date, a variety of approaches have been employed to fabricate THz devices, including lithography-based processes, printable electronics, additive manufacturing (3D printing), and laser-based microfabrication techniques. A brief overview of these fabrication methods is presented below.

1.13.1 Lithography

Lithographic techniques remain indispensable for the high-precision fabrication of THz devices, providing the resolution and structural control required to engineer filters, polarizers, absorbers, and metasurfaces with tailored electromagnetic responses. Among these approaches, photolithography is the most widely adopted method, offering reliable, high-throughput processing for large-area THz components. The process typically involves ultraviolet (UV) exposure through a patterned mask to define features in a photoresist layer, followed by material deposition or etching, making it particularly suitable for planar THz filters and polarizers (Sushko et al., 2017; Ghavidel et al., 2021; Ferraro et al., 2017).

For instance, (Sushko et al., 2017) demonstrated the fabrication of two distinct FSS band-pass filters operating at 0.1 and 0.3 THz using standard photolithography, confirming its effectiveness for low-frequency THz structures. Building upon this, (Ghavidel et al., 2021) designed and fabricated single- and double-layer concentric split-ring resonator (SRR) structures with a center frequency of 250 GHz on RT5880 substrates, as shown in Fig. 1.25(a). The multilayer configuration exhibited increased bandwidth and improved angular stability compared to single-layer designs, highlighting the advantages of cascaded architectures for bandwidth control. Extending lithographic fabrication to flexible platforms, (Ferraro et al.,

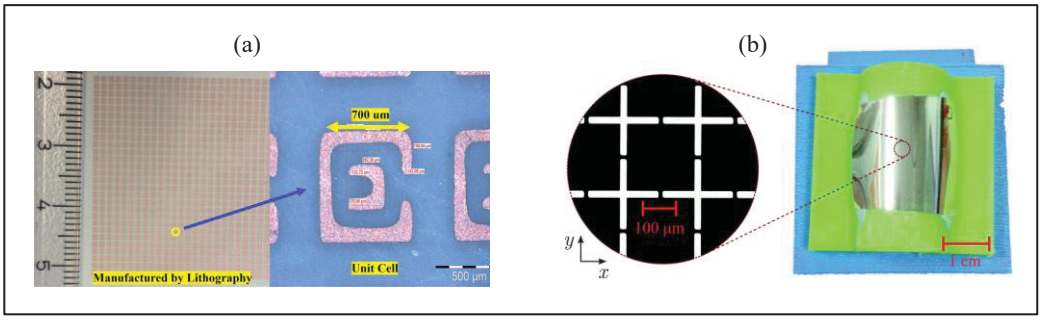

Figure 1.25 (a) Fabricated FSS band-pass filter consisting of 32 × 30 unit cells over an area of approximately 3 × 3 cm², produced via photolithography, along with a magnified view of a single unit cell
Taken from (Ghavidel et al., 2021)
and (b) Optical microscope image of the fabricated FSS filter alongside a photograph of the mechanically bent sample, demonstrating its structural integrity and flexibility
Taken from (A. Ferraro et al., 2017)

2017) patterned cross-aperture FSS arrays onto Zeonor polymer films, as dpecited in Fig. 1.25(b). A key feature of the proposed THz filters is their polarization-independent response, attributed to the square lattice configuration and the symmetry of the cross-shaped apertures. This polarization insensitivity was experimentally confirmed by rotating the fabricated samples within the *x*–*y* plane, i.e., perpendicular to the propagation direction of the *x*-polarized THz wave, while observing negligible variation in the transmission characteristics. In addition, (Ishak et al., 2022) employed electron-beam lithography followed by wet etching to realize an FSS resonating at 1.79 THz. The fabricated device demonstrated excellent agreement with simulations, high transmission efficiency (~0.94), and tight dimensional tolerances (±1.5 μm), underscoring the precision achievable with advanced lithographic techniques.

Overall, recent developments reaffirm lithography as a powerful and versatile platform for fabricating high-performance, scalable, and application-specific THz components, particularly where dimensional accuracy and spectral precision are critical.

1.13.2 Printable electronics

Printable electronics (PE) have emerged as a promising approach for fabricating THz devices due to their cost-effectiveness, scalability, and compatibility with flexible substrates. While certain PE fabrication processes can still rely on traditional rigid substrates such as silicon or glass, a major focus of printed electronics lies in the development of devices on flexible substrates. Unlike conventional microfabrication techniques that require high processing temperatures, PE technologies operate at relatively low temperatures. This compatibility enables the use of low-cost plastic films that are typically nonporous, mechanically compliant, and capable of withstanding both pre- and post-printing processes. Among flexible substrates, polyimide (PI), polyethylene terephthalate (PET), and polyethylene naphthalene (PEN) are the most widely used (Park et al., 2019). Although various conductive inks are commercially available, including copper, carbon, and graphene-based formulations, however silver (Ag) conductive inks remain the most widely adopted due to their superior electrical conductivity, chemical stability, and excellent printability, making them particularly suitable for high-performance printed electronic and THz devices. Several PE techniques have been employed for the fabrication of THz FSS, depending on the required feature resolution, conductivity,

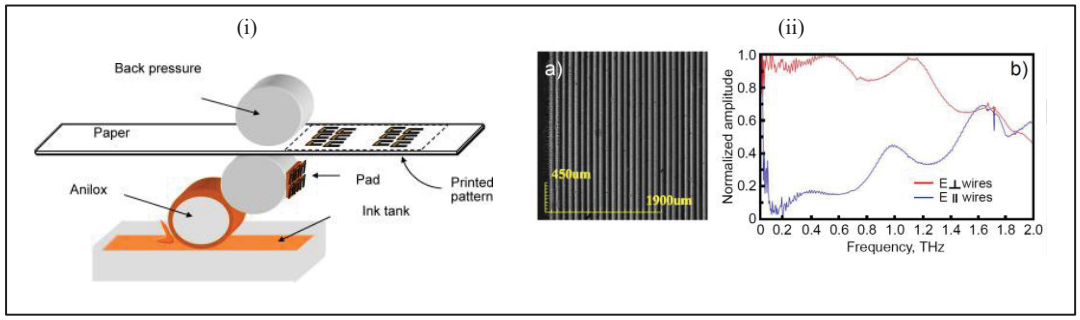

Figure 1.26 (i) Conceptual layout of the flexographic roll-to-roll printing system; (ii) (a)Fabricated wire-grid polarizer realized using a flexographic printing technique; (b) measured normalized transmission for electric-field polarizations parallel and perpendicular to the wire direction
Taken from (Mansourian et al., 2021)

scalability, and cost. Commonly used methods include flexography, screen-printing, inkjet printing etc.

1.13.2.1 Flexography

Flexography is a high-speed roll-to-roll (R2R) printing technique well suited for large-area manufacturing. The process generally consists of three main stages: (a) selection of ink and substrate, (b) pattern transfer during printing, and (c) post-printing sintering to achieve the desired electrical conductivity (Zhuldybina et al., 2021). This approach enables scalable fabrication of THz components, including band-pass filters and wire-grid polarizers, by depositing conductive inks onto flexible substrates (Zhuldybina et al., 2020; Mansourian et al., 2021; Zhuldybina et al., 2021). In reported implementations, THz devices were fabricated using an industrial R2R continuous press process in which silver nanoparticle (Ag) ink was printed onto a 125-µm-thick PET substrate. A representative sample is shown in Fig. 1.26(ii), including microscopic images of a flexography-printed wire-grid polarizer and its corresponding transmission response. Although the achievable lateral resolution is moderate (approximately 50–100 µm), it remains sufficient for many sub-THz applications, where feature sizes are comparatively large. With ongoing improvements in ink formulation, conductivity optimization, and multilayer registration accuracy, flexographic printing is

emerging as a promising platform for the cost-effective, high-volume production of flexible and conformal THz components for imaging, filtering, and beam-shaping systems.

1.13.2.2 Screen printing

Screen printing is a mature and cost-effective fabrication technique that has been increasingly adopted for THz device development due to its scalability, moderate resolution, and ability to deposit thick, highly conductive films. The process involves transferring functional inks or pastes through a patterned mesh screen onto a substrate, followed by thermal curing or sintering to achieve the desired electrical performance. A schematic representation of the fabrication procedure is shown in Fig. 1.27. Owing to its capability to deposit micrometer-thick metallic or resistive layers in a single step, screen printing enables strong electromagnetic interactions with THz waves, making it particularly suitable for absorbers, filters, and FSS (Youn et al., 2023). Although the achievable feature resolution typically lies in the range of 50–150 μm, with approximately 100 μm representing a reliable minimum feature size for THz FSS fabrication (Hyun et al., 2015; Ahmad et al., 2024), this resolution remains sufficient for structures operating in the sub-THz to low-THz regime, where feature dimensions are comparatively large and electrical conductivity is prioritized. The technique is also compatible with large-area substrates and roll-to-roll manufacturing platforms, supporting scalable and low-cost production of flexible and conformal THz components. With continued advances in

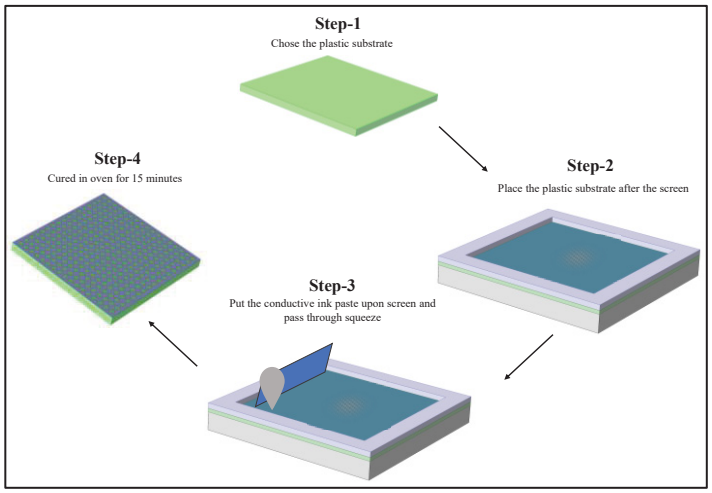

Figure 1.27 Schematic diagram of different steps of the screen-printing technique

ink rheology, mesh engineering, and substrate optimization, screen printing continues to evolve as a robust and industrially viable method for manufacturing reliable THz systems. Its balance of cost efficiency, material versatility, and process scalability makes it well suited for both rapid prototyping and commercial-scale THz applications.

1.13.2.3 Inkjet printing

Inkjet printing has emerged as a digitally controlled, maskless additive manufacturing technique that enables rapid, cost-effective, and flexible fabrication of THz components. With achievable feature resolutions down to approximately 20 μm, it is well suited for devices operating in the lower and intermediate THz frequency ranges, including FSSs, metamaterials, antennas, transmission lines, and polarizers. Its compatibility with both rigid and flexible substrates, combined with minimal material waste and on-demand prototyping capability, makes it a versatile platform for THz device research and development.

A representative application involves the inkjet printing of SRR arrays on paper using silver nanoparticle inks. These devices demonstrated polarization-sensitive resonances at 0.137 THz and 0.305 THz (Kashiwagi et al., 2016). Similarly, two distinct SRR structures fabricated on

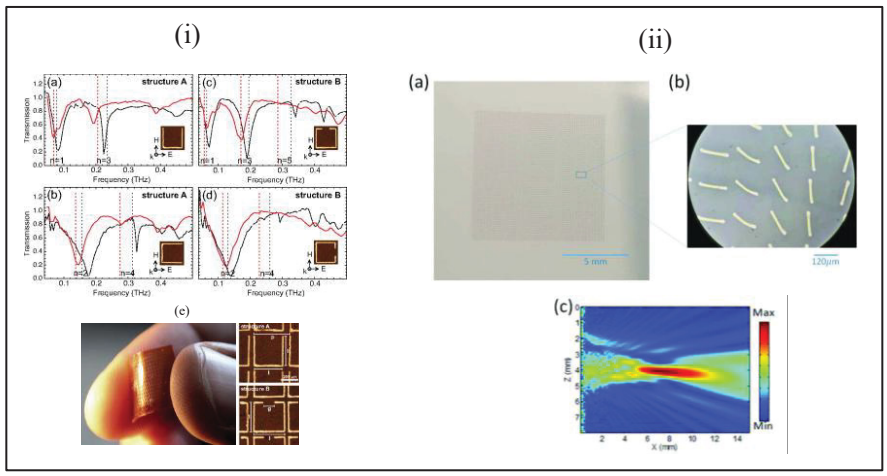

Figure 1.28 (i) Flexible metasurface and the transmission characteristics for different structures
Taken from (Walther et al., 2009)
(ii) Microscopic images and *xz* axis of beam profile of printed metasurface lens
Taken from (He et al., 2021)

polyimide substrates have been reported in (Walther et al., 2009) and the corresponding geometries and transmission characteristics are illustrated in Fig. 1.28(i). However, compared to photolithography-based counterparts, the printed structures exhibited broadened transmission minima and slight resonance shifts toward lower frequencies, primarily due to reduced conductivity and dimensional variations. In another study (Kashiwagi et al., 2018), two SRR arrays with different resonant frequencies were printed on separate paper sheets and subsequently stacked. In addition to the individual resonances of each array, a new resonance emerged as a result of interlayer electromagnetic coupling, demonstrating the feasibility of multilayer spectral engineering using inkjet printing.

For polarization control, inkjet-printed wire-grid polarizers on Kapton substrates achieved degrees of polarization exceeding 90% across the 0.3–1 THz range, with extinction ratios further improved through gap reduction and multilayer stacking (Farid et al., 2016). Similarly, one-dimensional and two-dimensional printed structures on photo paper exhibited efficient polarization performance between 0.1 and 0.4 THz, along with band-stop filtering behavior near 0.325 THz (Lee et al., 2010). Beyond spectral filtering and polarization control, inkjet printing has also been applied to advanced wavefront engineering. He *et al*. demonstrated a flexible cylindrical metasurface lens fabricated using inkjet-printed silver paste rods. By employing Pancharatnam–Berry phase modulation, the device achieved full 2π phase coverage and demonstrated clear THz beam focusing at 0.6 THz through holographic imaging (He et al., 2021).

Although challenges remain particularly in achieving high post-sintering conductivity, dimensional precision, and large-area uniformity, ongoing advances in ink formulation, substrate optimization, and multi-pass printing strategies continue to enhance device performance. Overall, inkjet printing represents a promising and scalable manufacturing platform for customizable and flexible THz photonic systems.

These printing techniques collectively enable the fabrication of lightweight, flexible, and large-area THz components, paving the way for next-generation applications in wearable electronics, conformal sensing, adaptive electromagnetic surfaces, and low-cost wireless communication systems. However, despite these advances, the integration of reconfigurable or actively tunable

functionalities within fully printed THz FSS architectures remains largely unexplored. In particular, the realization of mechanically reconfigurable active FSS structures fabricated entirely through printable platforms has not yet been comprehensively demonstrated.

1.13.3 3D printing

3D printing has emerged as a promising fabrication technique for THz devices, offering rapid prototyping, design flexibility, and cost-effective manufacturing. Figure 1.29 provides a graphical overview of representative 3D-printed THz components reported in the literature, including waveplates, GRIN lenses, zone plates, absorbers, band-pass filters, and metagrating lenses. These examples highlight the versatility of additive manufacturing techniques for realizing complex THz functional devices with tailored spectral, polarization, and wavefront

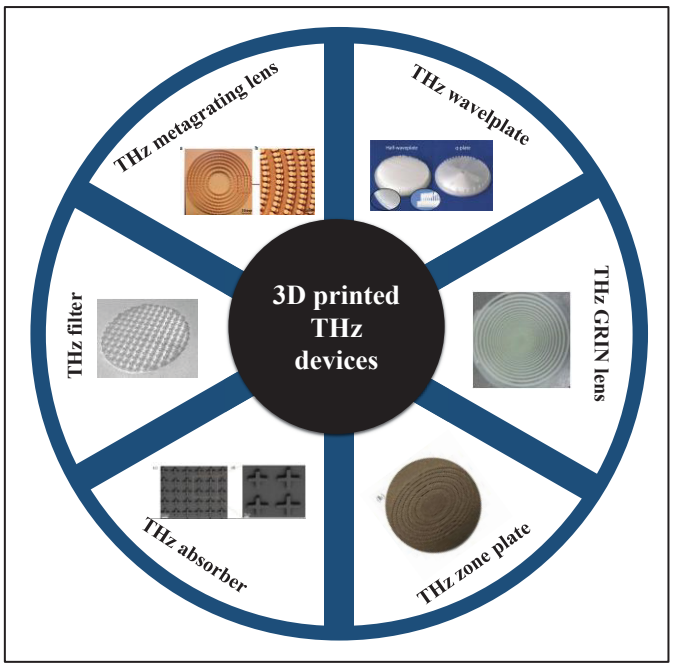

Figure 1.29 Graphical representation of different 3D printed THz devices such as waveplate (Taken from (Rohrbach et al., 2021)), GRIN lens (Taken from (Hernandez-Serrano et al., 2016)), zone plate (Taken from (Headland et al., 2016)), absorber (Taken from (Li et al., 2021)), band-pass filter (Taken from (Kubiczek et al., 2022)), and metagrating lens (Taken from (Zhang et al., 2023))

control properties. Several additive manufacturing methods, including Fused Deposition Modeling (FDM), Stereolithography (SLA), and Selective Laser Melting (SLM), have been explored for creating THz components such as waveguides, lenses, metamaterials, and polarizers. To begin with, FDM, one of the most accessible 3D printing techniques, involves extruding thermoplastic filaments layer by layer to build structures. Using this approach, a wide range of THz components have been demonstrated, including laterally periodic Fabry–Pérot resonator arrays forming frequency-selective quasi-surfaces, grating-based waveplates and phase plates, gradient-refractive-index lenses, and others (Kubiczek et al., 2024; Hernandez-Serrano et al., 2016; Rohrbach et al., 2021; Ortiz-Martinez et al., 2019; Missori et al., 2022). While FDM enables low-cost and rapid prototyping of THz devices, surface roughness, finite nozzle diameter, and printing tolerances can introduce scattering losses and disorder-induced spectral degradation at higher frequencies. Another popular 3D printing technique is SLA, which uses a laser or projected UV patterns to selectively cure a liquid resin, enabling the fabrication of high-resolution THz structures with smooth surfaces and feature

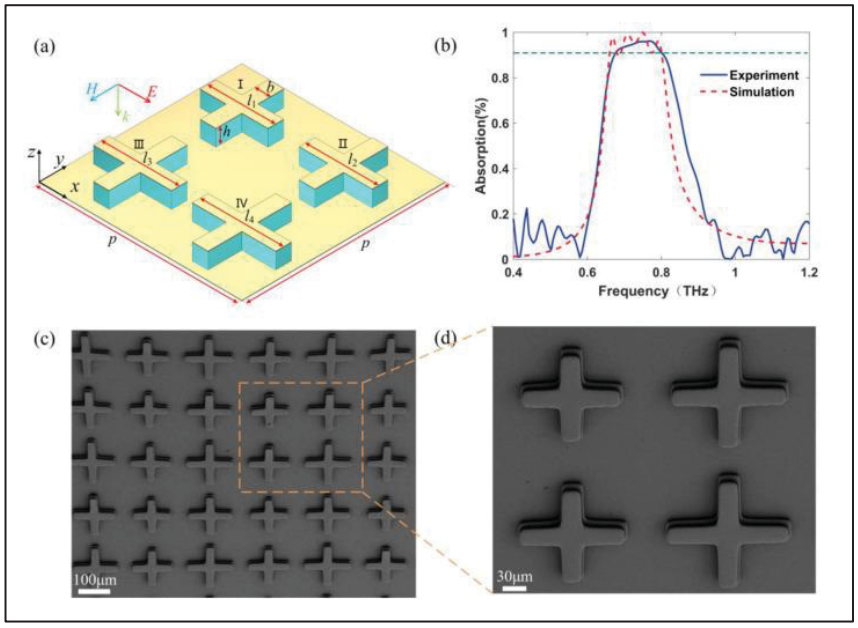

Figure 1.30 (a) Schematic of the broadband absorber composed of four cross-shaped resonators; (b) simulated and measured absorption spectra; (c) SEM image of a partial region of the 3D printed cross-shaped metamaterial absorber; and (d) SEM image of a single cross-shaped unit cell
Taken from (Li et al., 2021)

sizes down to tens of micrometers (depending on the printer and resin). Using SLA, a variety of THz devices have been demonstrated, including metal-coated 3D metamaterial resonators, grid type polarizers, and all-dielectric metasurface optics such as metalenses composed of square-pillar unit cells (Li et al., 2022; Li et al., 2021; Li et al., 2021b; Louisos et al., 2024; Jang et al., 2023). The reduced surface roughness and precise geometry offered by SLA minimize unwanted scattering, making it particularly suitable for THz optics and polarization-control components. In addition, SLM is a metal-based additive manufacturing technique that uses a high-power laser to fuse metallic powders, enabling the direct fabrication of highly conductive THz components such as periodic hole-array bandpass filters, reflective zone plates, waveguides, and metasurfaces. Typical geometries include sub-millimeter circular apertures or concentric ridge structures with millimeter-scale apertures, allowing robust realization of FSS and diffractive metallic metamaterials for THz beam shaping and filtering, primarily in the lower-THz regime (Ahmad et al., 2022; Headland et al., 2016).

1.13.4 Laser based microfabrication

Laser-based microfabrication techniques have become essential for fabricating high-precision THz devices, offering advantages such as high resolution, flexibility, and material versatility (Le et al., 2021; Lin et al., 2017; Thavamani et al., 2024; Fast et al., 2011; Chen et al., 2020; Zhou et al., 2023; Penchev et al., 2016; Lee et al., 2006; Ward et al., 2006; Ward et al., 2004). Figure 1.31 provides a graphical overview of laser-microfabricated THz devices, demonstrating how high-resolution laser patterning can realize compact elements for phase, polarization, and spectral control. Several laser-based processes, including Direct Laser Writing (DLW), Laser Cutting, Laser Ablation, and Laser Micromachining, are used to create intricate THz components like waveguides, metamaterials, and photonic structures.

1.13.4.1 Direct Laser Writing

Direct laser writing has emerged as a practical and versatile approach for fabricating THz components, enabling maskless, rapid, and scalable patterning across metallic films, polymers, and functional materials. Using this technique, a broad range of THz devices has been demonstrated, including multi-band FSS, broadband absorbers, Fresnel lenses, and spiral zone

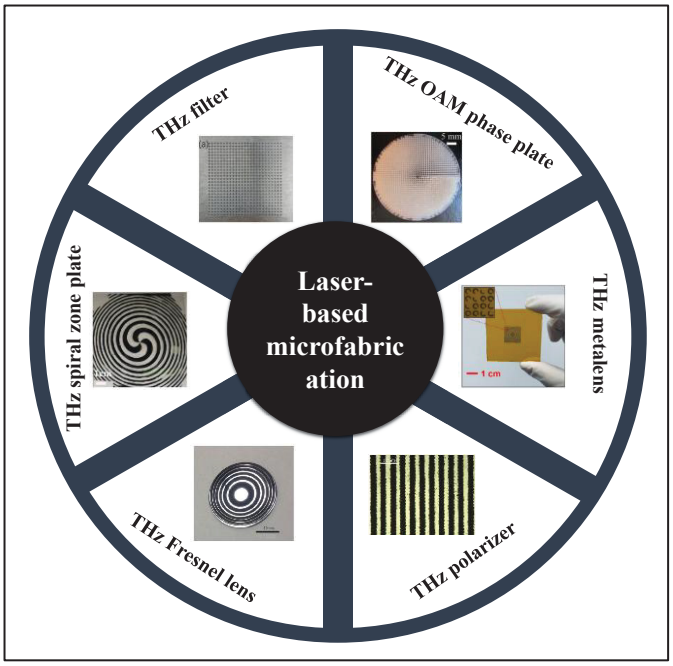

Figure 1.31 Graphical representation of THz devices based on laser based microfabrication such as OAM phase plate (Taken from (Guerboukha et al., 2019)), metalens (Taken from (Wang et al., 2022)), polarizer (Taken from (Fast et al., 2011)), Fresnel lens (Taken from (Komlenok et al., 2015)), spiral zone plate (Taken from (Zhang et al., 2020)), and filter (Taken from (Lin et al., 2017))

plates for vortex beam generation (Wang et al., 2022; Zhao et al., 2022b; Manikandan et al., 2018a; Minkevičius et al., 2017; Zhang et al., 2020; Cui et al., 2022; Nivas et al., 2025). DLW-fabricated structures typically exhibit unit-cell dimensions on the order of tens to hundreds of micrometers, which are well suited for many THz applications. For example, laser-induced graphene (LIG) metasurfaces have been produced over centimeter-scale areas with feature sizes in the tens-of-micrometers range (Wang et al., 2022). For large-aperture diffractive optics, filament-based femtosecond DLW enables high-throughput fabrication of 100 × 100 mm² spiral zone plates for vortex beam generation, achieving approximately 100 µm resolution with writing times on the order of minutes (Zhang et al., 2020) (see Fig. 1.32 (ii)). Despite its flexibility and maskless operation, DLW remains constrained by its serial writing nature, spot-

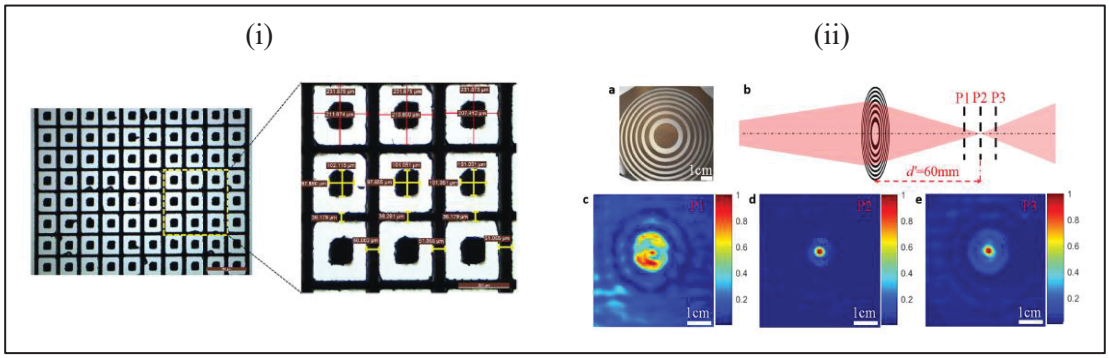

Figure 1.32 Fabricated THz devices using DLW (i) microscopic images of the fabricated square-ring FSS
Taken from (Zhao et al., 2022b)
and (ii) spiral zone plate with l=0 and the measured intensity distributions of the THz beam at three different positions (P1–P3)
Taken from (Zhang et al., 2020)

size-limited resolution, and potential thermal or edge imperfections introduced during processing. These factors can lead to dimensional deviations that shift or broaden THz resonances, particularly in fine-gap metasurface geometries where electromagnetic response is highly sensitive to fabrication tolerances.

1.13.4.2 Laser cutting

Another commonly used technique is laser cutting, which emerged as a versatile and scalable fabrication technique for THz components, enabling the realization of diffraction gratings, metasurfaces, porous lenses, and orbital angular momentum (OAM) phase plates (Ornik et al., 2019; Aqlan et al., 2021a; Taleb et al., 2020; Guerboukha et al., 2019; Sebastian et al., 2026; Aqlan et al., 2021b; Nakano et al., 2024; Huang et al., 2023). As depicted in Fig. 1.33(i), aluminum and polymer gratings fabricated via nanosecond laser machining exhibit diffraction responses in strong agreement with numerical simulations, validating dimensional accuracy at sub-millimeter scales (Ornik et al., 2019). Free-standing metasurfaces produced through laser beam machining eliminate substrate-induced losses and field confinement effects, significantly enhancing sensing performance (Taleb et al., 2020). Furthermore, laser-cut porous dielectric architectures allow effective refractive index engineering while reducing absorption losses, enabling planar low-loss THz beamforming components (Guerboukha et al., 2019).

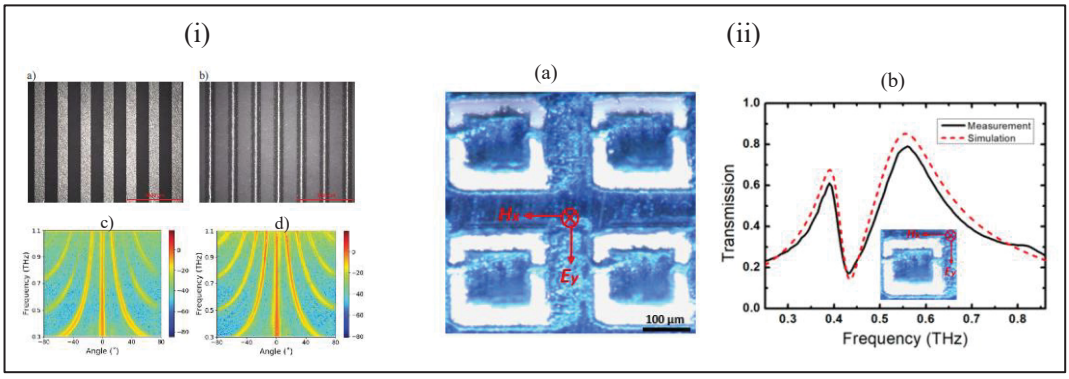

Figure 1.33 Fabricated devices using laser cutting: (i) Microscopic images of aluminum grating and PVC grating. Also, the diffracted intensity versus angle and frequency for aluminum and PVC grating
Taken from (Ornik et al., 2019)
and (ii) layout of the free-standing complementary asymmetric SRR structure. Measured and simulated transmission spectra of FCA-SRR with E-field orientation along the y-direction
Taken from (Taleb et al., 2020)

Collectively, these works demonstrate that laser cutting offers maskless, cost-effective, and mechanically robust fabrication for large-area THz optics and metamaterials.

1.13.4.3 Laser ablation

Laser ablation is a powerful maskless, subtractive microfabrication route for THz components, enabling rapid iteration of resonant surfaces and diffractive optics without cleanroom lithography (Hakamada et al., 2024; Komlenok et al., 2015; Voisiat et al., 2011; Manikandan et al., 2018b; Voisiat et al., 2017; Minkevičius et al., 2013; Esakkimuthu et al., 2019; Han et al., 2022). In one demonstration (Fig. 1.34(i)), (Hakamada et al., 2024) utilized ultraviolet femtosecond laser ablation to fabricate dense subwavelength hole arrays in a high-resistivity silicon membrane, thereby realizing a 0.8 THz metalens. The fabricated lens produced a focal spot of approximately 1 mm (FWHM) with a measured focusing efficiency of 67.8%. In another work, UV picosecond laser ablation was employed to fabricate cross-aperture metal-mesh band-pass filters in stainless-steel foil and molybdenum films supported on polyimide substrates, operating as resonant frequency-selective metal meshes with experimentally

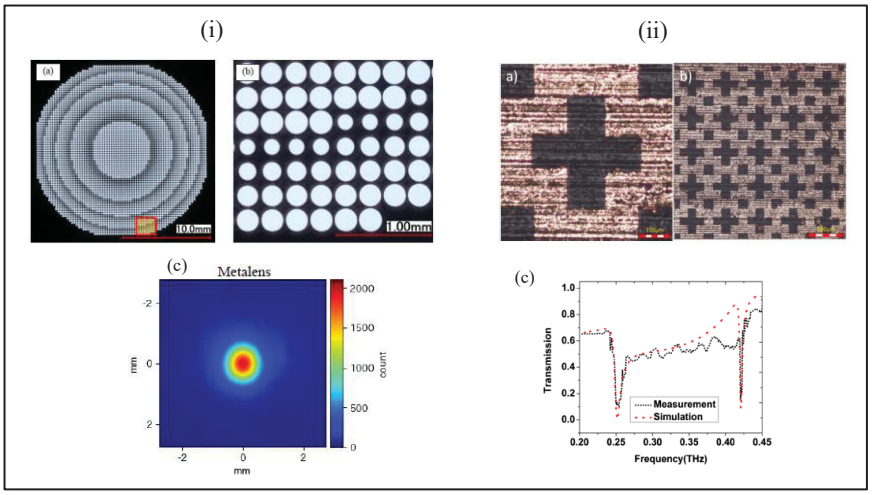

Figure 1.34 Fabricated devices based on laser ablation: (i) Microscopic images of the fabricated THz metalens and the profile at the focus
Taken from (Hakamada et al., 2024))
and (ii) optical microscopic images of the metamaterial and obtained THz transmission characteristics
Taken from (Manikandan et al., 2018b)

measured transmission spectra in close agreement with numerical simulations, while also revealing sensitivity of the passband characteristics to aperture edge rounding and fabrication-induced geometric deviations (Voisiat et al., 2011). Additionally, femtosecond laser ablation was used to pattern periodic copper metallic structures on a polyimide thin film, enabling a dual-band, polarization-insensitive metamaterial/FSS with resonances at 0.25 THz and 0.42 THz, exhibiting stable spectral responses under varying angles of incidence (Manikandan et al., 2018b). Collectively, these results demonstrate that carefully optimized laser ablation through control of pulse duration, fluence, and scan strategy can yield functional THz devices for filtering, focusing, and multi-band resonance engineering.

1.14 Summary and research gaps

The literature surveyed in this chapter highlights significant advancements in THz FSS, reconfigurable filtering strategies, fabrication approaches, and polarization-resolved THz measurement systems. Numerous passive THz FSS designs have been reported with well-defined spectral characteristics, and several reconfigurable concepts have demonstrated

dynamic tunability through electrical biasing, thermal control, or other external stimuli. While these approaches successfully enable resonance tuning and bandwidth control, they frequently depend on complex bias networks, temperature regulation systems, or multilayer integration. Such requirements increase fabrication complexity, reduce structural robustness, and limit scalability toward low-cost, large-area, and industrially viable implementations.

In addition, most reconfigurable THz FSS structures reported to date rely on microfabrication techniques such as photolithography, thin-film deposition, and cleanroom-based processing. Although these methods provide high resolution and repeatability, they are expensive and less compatible with large-area or flexible substrates. In contrast, printable-electronics-based THz FSS platforms remain largely unexplored for reconfigurable operation, despite their strong potential for scalable, low-temperature, and roll-to-roll-compatible fabrication. This reveals a clear gap in translating reconfigurable THz FSS concepts into cost-effective and manufacturable printed platforms.

Polarization-sensitive FSS designs have further expanded the functionality of THz structures by enabling polarization-selective transmission and anisotropic spectral responses. However, many reported implementations employ multilayer stacks, substrate-engineered architectures, or photolithography-based fabrication. While single-layer geometries such as rectangular-slot FSSs have been demonstrated, frequency-selective polarizers exhibiting well-defined Malus-law-type angular transmission behavior across distinct THz bands remain largely unreported. Consequently, the development of compact, single-layer, frequency-selective THz polarizers with predictable and quantitative angular responses represents an important unmet need.

Parallel progress has been achieved in THz polarimetric spectroscopy and imaging, predominantly through THz-TDS (PCA based and electro-optic sampling), and mechanically rotated polarization optics. These systems enable full electric-field reconstruction and comprehensive Stokes parameter extraction, but they inherently rely on coherent detection, optical delay stages, and sequential measurements. As a result, they are typically bulky, alignment-sensitive, and limited in acquisition speed, which constrains their translation to compact, real-time, and field-deployable platforms.

Overall, the existing body of work reveals a disconnect between advanced THz polarimetric capabilities and the practical requirements of scalable, robust, and intensity-based systems. In particular, intensity-only multispectral THz architectures capable of direct Stokes parameter retrieval without delay stages, coherent detection, or complex active tuning mechanisms remain largely absent in the literature. Addressing these gaps by integrating printable, potentially reconfigurable, and polarization-sensitive THz FSS platforms within compact intensity-based spectrometric and imaging systems forms the central motivation of this thesis.

CHAPTER 2

RECONFIGURABLE SCREEN-PRINTED TERAHERTZ FREQUENCY SELECTIVE SURFACE BASED ON METALLIC CHECKERBOARD PATTERN

Redwan Ahmad[1], Xavier Ropagnol[1,2], Ngoc Duc Trinh[3], Chloé Bois[3], François Blanchard[1]

[1]Département de génie électrique, École de technologie supérieure (ÉTS), Montréal QC H3C 1K3, Canada
[2]Institut national de la recherche scientifique, EMT research center, Varennes QC J3X 1P7, Canada
[3]Institut des communications graphiques et de l'imprimabilité, Montréal QC H2M 2E2, Canada

Paper published in *Flexible and Printed Electronics*, April 2024
available at https://doi.org/10.1088/2058-8585/ad3bca

2.1 Chapter overview

This chapter reports the development and experimental validation of a mechanically reconfigurable THz FSS realized using printable electronics. A screen-printed metallic checkerboard architecture is employed, in which mechanical lateral shifting of a stacked double-layer configuration enables tunable transmission behavior with a measured transmission contrast of up to 88%. In addition to amplitude modulation, polarization-sensitive behavior is investigated by independently shifting the FSS layers along the orthogonal *x*- and *y*-axes, resulting in distinct transmission responses for orthogonal linear polarization states. Numerical simulations and continuous-wave THz measurements confirm a high modulation depth and polarization-dependent amplitude contrast at the design frequencies, achieved without external electrical biasing or complex control mechanisms. These results establish printable, mechanically reconfigurable FSS as a robust and scalable platform for amplitude and polarization-selective control in THz systems, providing a foundation for the polarimetric imaging concepts developed in subsequent chapters of this thesis.

2.2 Abstract

We employed the screen-printing method to fabricate terahertz (THz) frequency selective surfaces (FSS) featuring an inductive metallic checkerboard (i-MCB) pattern based on

conductive silver ink onto a flexible polyethylene terephthalate (PET) substrate, chosen for its excellent THz transmission properties below 1 THz [Jin et al., 2006]. Analytical studies, along with simulations and experiments, were conducted to investigate the filtering characteristics of the printed FSSs, confirming their functionality as a band-pass filter. Subsequently, we demonstrated the reconfigurability of a two-layer system by vertically stacking two layers. This was achieved by systematically shifting the position of the second layer in the *x* or *y*-direction relative to the first layer. Experimental verification revealed a significant variation in normalized transmission, ranging from 94% to 6% at 0.15 THz for type-I:i-MCBs and 90% to 5% at 0.20 THz for type-II:i-MCBs, respectively. This study presents a simple scheme for a reconfigurable screen-printed i-MCB-FSS operating in the THz range. Consequently, our findings demonstrate that screen printing method can effectively be employed for the large-scale production of THz FSSs.

2.3 Introduction

To enhance the diversity of terahertz (THz) applications, there is a growing demand for the development and production of THz optics, encompassing polarizers (Ferraro et al., 2016), filters (Born et al., 2013), absorbers (Tao et al., 2008), phase shifters (Altmann at al., 2013), wave plates (Nouman et al., 2016), and more. In this context, frequency-selective surfaces (FSSs) play a crucial role. These thin, periodic structures, composed of both conductive and non-conductive materials and generally exhibiting features on the order of the wavelength size, are capable of transmitting or reflecting electromagnetic waves at specific frequencies (Anwar et al., 2018). Their versatility has led to extensive applications in manipulating THz waves, including polarization conversion (Li et al., 2019), transmission measurement in quasi-optical systems (Yang et al., 2020), remote sensing (Poojali et al., 2017), monochrometers (Grossman et al., 2006), and more. For more adaptive solutions, there has been as urge in demand for reconfigurable frequency-selective surfaces (RFSSs) in various applications, including frequency agility, beam steering, polarization control, and dynamic filtering (Pan et al., 2013; Vegesna et al., 2014; Zhai et al., 2018). In the microwave regions, distinct FSSs and RFSSs have long been demonstrated (Nauroze et al., 2019; Han et al., 2015; Li et al., 2018; Wu et al., 2019; Azemi et al., 2013). The reconfigurability of these devices generally involves a large

variety of tuning mechanisms, encompassing thermal tuning (Nauroze et al.,2019), rotational tuning (Han et al.,2015), electrical tuning (Li et al.,2018; Wu et al.,2019), mechanical tuning (Azemi et al., 2013), waterbased metamaterial absorbers (Wu et al., 2019b; Wen et al., 2022), and more. In the THz region, RFSSs have recently found applications using various tuning approaches, including a polarizer based on vanadium dioxide (Vegesna et al., 2014), a mechanically tunable filter using a polydimethylsiloxane substrate (Akter et al., 2019), modulators based on FSS-graphene stacked structures (Yan et al., 2016), a mechanically reconfigurable bandpass filter (Lv et al., 2022), electronically controlled flexible THz modulator (Wang et al., 2022), and thermally tunable FSS based on barium strontium titanate thin film and metamaterials (Dong et al., 2019). Numerous fabrication techniques, including photolithography (Vegesna et al., 2014; Yan et al., 2016), milling (Yang et al., 2020), and laser ablation (Esakkimuthu et al., 2019), have been employed for THz FSS fabrication, each chosen based on design requirements and materials. Despite their precision, these methods are time-consuming, expensive, and limited to small-scale production.

In the recent years, printable electronics pop up as an alternative solution for the fabrication of THz devices (Su et al.,2019; Ahmad et al., 2023; Zhuldybina et al., 2019; Zhuldybina et al., 2021). The advantages of PE include mass production capability with low cost per unit, good reproducibility, and more eco-friendly production (Bonnassieux et al., 2021). This process requires only three steps: selection of the right substrate and ink; printing the pattern upon the substrate; and sintering. Because of their high conductivity and low loss, conductive inks including copper, graphene, and others, are widely employed to transfer the pattern upon the flexible plastic substrate. The main PE-based fabrication technologies are flexography printing, hot stamping, screen-printing, and ink-jet printing (Zhuldybina et al., 2021b; Guerboukha et al., 2021). Despite the relatively low resolution of the printed pattern, which is in the order of a few tens of microns, printing THz devices with features on the order of the wavelength size remains adequate. Consequently, PE is highly suitable for the fabrication of THz FSS. Examples of printed THz devices include a band-pass filter (Ahmad et al., 2023), vortex phase plate (Zhuldybina et al., 2019), and polarizer (Zhuldybina et al., 2021). More recently, a printed reconfigurable flexible FSS has been demonstrated based on the Moiré interference technique (Ahmad et al., 2023). To date, printed THz devices have been created

exclusively through ink-jet printing, flexography, or hot stamping techniques. In contrast, the screen-printing method has been solely employed for the fabrication of devices within the microwave frequency range (Falade et al., 2018; Jilani et al., 2019; Badamchi et al., 2022).

In this work, we demonstrate the design, simulation, fabrication, and characterization of THz FSSs based on metallic checkerboard patterns (MCB) using screen printing as the fabrication technique. The analyzed FSS pattern is printed on a polyethylene terephthalate (PET) substrate with conductive silver (Ag) ink (CXT-0657). A polarization dependent reconfigurability is achieved by stacking two identical FSS layers and shifting the second layer relative to the position of the first layer. Notably, this reconfigurability is obtained without employing any external stimuli such as biasing voltage, temperature variation, or external continuous wave (CW) laser. Consistent with our simulations, experimental results reveal a maximum variation in transmission, ranging from 94% to 6% at a center frequency of 0.150 THz.

2.4 Methodology

2.4.1 Modelling and design of FSS

Being a complementary structure, MCB patterns have long been the subject of extensive studies in various fields of application (Compton et al., 1984; Takano et al., 2014; Nakata et al., 2019; Dawes et al., 1989; Higashira et al., 2017; Kondo et al., 2003; Nakata et al., 2013; Zhuldybina et al., 2020). According to Babinet's principle, the complementary structure of an obstacle (or object) presents complementary transmission spectra (Jackson, 1999). In the geometry of an ideal MCB, square metallic blocks are connected without any gap, as illustrated in Fig. 2.1(a), behaving as a half-beam splitter. When the square non-metallic block is reduced in size compared to its metallic counterpart, creating an asymmetric structure, we define a separation distance Δd relative to its physical dimensions (x, y, and Δz), as illustrated in Fig. 2.1(b). This specific case has been termed as inductive MCB (i-MCB) (Takano et al., 2014; Nakata et al., 2019). On the contrary, when the square metallic parts are smaller than their counterparts, we define it as capacitive MCB (c-MCB). The schematic of i-MCB and c-MCB pattern is represented in Fig. 2.1(c) and (d), respectively. The corresponding reactances (X_{in}

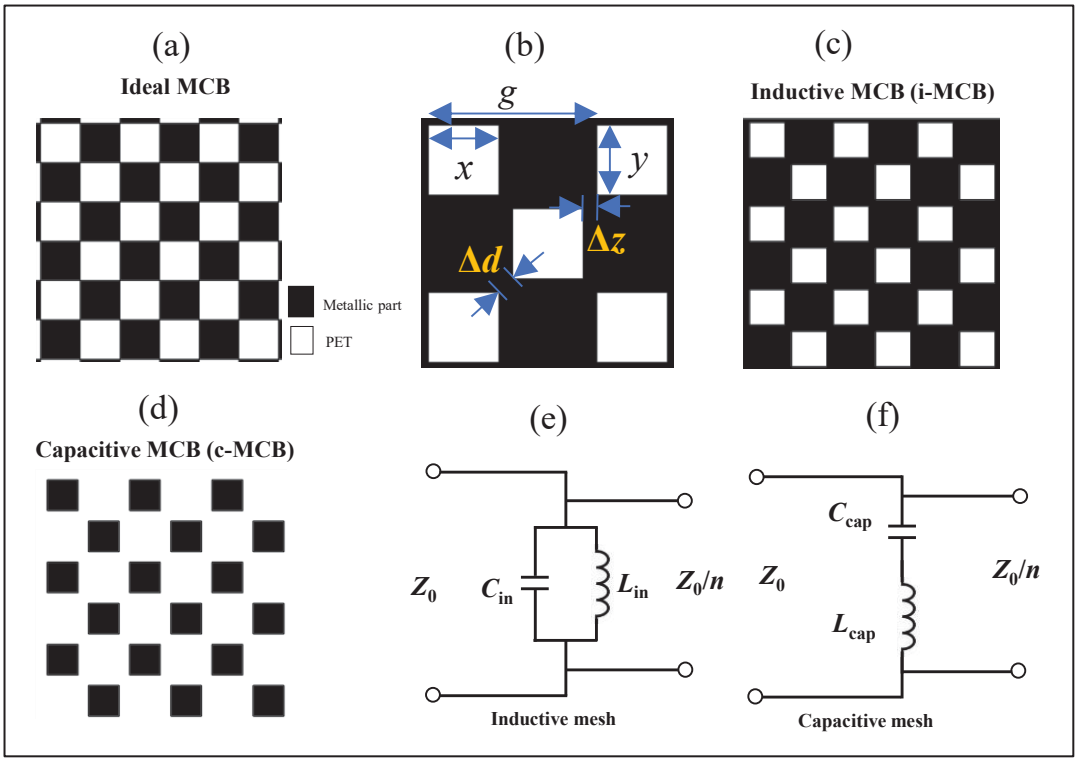

Figure 2.1 Schematic of metallic checkboard pattern (a) ideal MCB; (b) 2D view of i-MCB with geometrical notations; (c) inductive MCB (i-MCB); (d) capacitive MCB (c-MCB); (e)&(f) schematic diagram of equivalent circuit model of inductive and capacitive meshes upon substrate respectively

and X_{cap}) of the i-MCB and c-MCB are described by parallel and series combinations of inductances and capacitances (Dawes et al., 1989). See their electrical representations in Fig. 2.1(e) and (f), respectively. Here, Z_0 represents the impedance of free space, and n is the refractive index of the substrate. The resistivity (R) in the circuit models is neglected since the analysis assumes a low-loss conductor. The transmittance (T) could be calculated as follows (Dawes et al., 1989):

$$T_j = \frac{4nX_j^2}{1+(1+n)^2 X_j^2} \quad \text{where } j=in, cap \tag{2.1}$$

The reactance X_{in} of the parallel resonant circuit (L_{in}, C_{in}) and X_{cap} of the series resonant circuit (L_{cap}, C_{cap}) can be defined as (Dawes et al., 1989):

$$X_{in} = \frac{\omega L_{in}}{1-\omega^2 L_{in} C_{in}} \tag{2.2}$$

$$X_{cap} = \frac{\omega^2 L_{cap} C_{cap} - 1}{\omega C_{cap}} \tag{2.3}$$

For the limit $\omega \rightarrow 0$, X_{in} and X_{cap} become 0 and ∞. Based on their connection states among metal squares i.e., overlapped (i-MCB) or disconnected (c-MCB), the electromagnetic responses of the MCB FSS behave as band-pass and band-stop filter respectively. Furthermore, the peak transmission frequency (fpeak) of the inductive MCB (i-MCB) can be predicted using the following equation (Compton et al., 1984):

$$f_{peak} = \frac{c}{g} \tag{2.4}$$

where c is the speed of light and g is defined as $g = 2(x+\Delta z)$. Also, Δz is related as $\Delta z = \frac{\Delta d}{\sqrt{2}}$.

In the following analysis, we have carried out finite-difference time-domain (FDTD) simulations from Ansys Lumerical software to evaluate the transmission characteristics of inductive MCBs (i-MCBs) and capacitive MCBs (c-MCBs). Furthermore, the normalized transmission (NT) was calculated using Eq. (2.5):

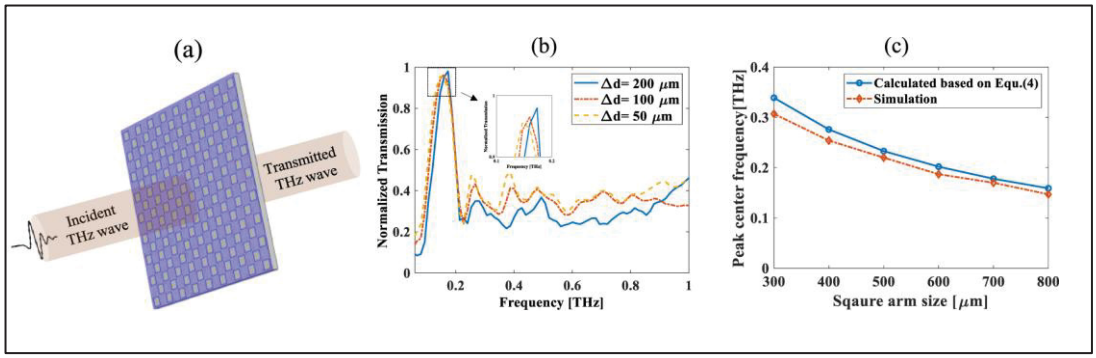

Figure 2.2 (a) Schematic of the analysed i-MCB (type-I) (b) the corresponding normalized transmission characteristics of i-MCB with different Δ*d* and inset figure depicts zoom view of peak normalized transmission; (c) peak center frequency as a function of the length of the square non-metallic block (*x*=*y*) in the case of i-MCB

$$NT(\omega) = \left| \frac{T_{sample}(\omega)}{T_{ref}(\omega)} \right| \tag{2.5}$$

where $T_{\text{Sample}}(\omega)$ and $T_{\text{Ref}}(\omega)$ are the transmission coefficient of the sample and reference (substrate), respectively (Ahmad et al., 2023).

Schematic of the i-MCB FSS with the operational principle is depicted in Fig. 2.2(a), where purple and gray colors denote the metallic and PET part, respectively. The simulated transmission characteristics of i-MCB for different Δd are presented in Fig. 2.2(b) and confirmed that the i-MCB behaves as expected, acting like a band-pass filter (Takano et al., 2014). The center frequency increases as the non-conductive zone shrinks, from 0.150 THz to 0.173 THz. Only a slight difference is noticed in the transmission characteristics when Δd is increased, which is explained by the smaller total open aperture of the filter. Conversely, although not shown here, c-MCB behaves like a band-stop filter (Takano et al., 2014). As depicted in Fig. 2.2(c), it is evident that increasing the length of the square hole (x) while maintaining a fixed gap Δd of 200 μm gradually reduces the corresponding peak center frequency. Essentially, the peak center frequency of the i-MCB can be shifted to the higher or lower portion of the THz region by decreasing or increasing the lattice of the square pattern of MCB, respectively.

For all subsequent transmission analyses of the i-MCB structure using our simulation tool or experimentally, we maintained a constant Δd of 200 μm. We investigated two i-MCB structures with different lattice sizes: type-I with square block dimensions of 700×700 μm² and type-II with square block dimensions of 500×500 μm².

2.4.2 Fabrication of THz FSS and experimental setup

FSS's pattern was printed upon a plastic substrate using silver ink utilizing a screen-printing technology (EKRA X1-SL Semi-Automatic Screen Printer) (Badamchi et al., 2022). Though we have used a flat-bed screen printing system as a fabrication tool, both flexible and rigid substrates could be employed to print upon it. However, in this work as a substrate, widely used low-cost PET has been chosen due to having excellent terahertz transmission properties as well as mechanical properties, including strength, flexibility, etc. Correspondingly, the

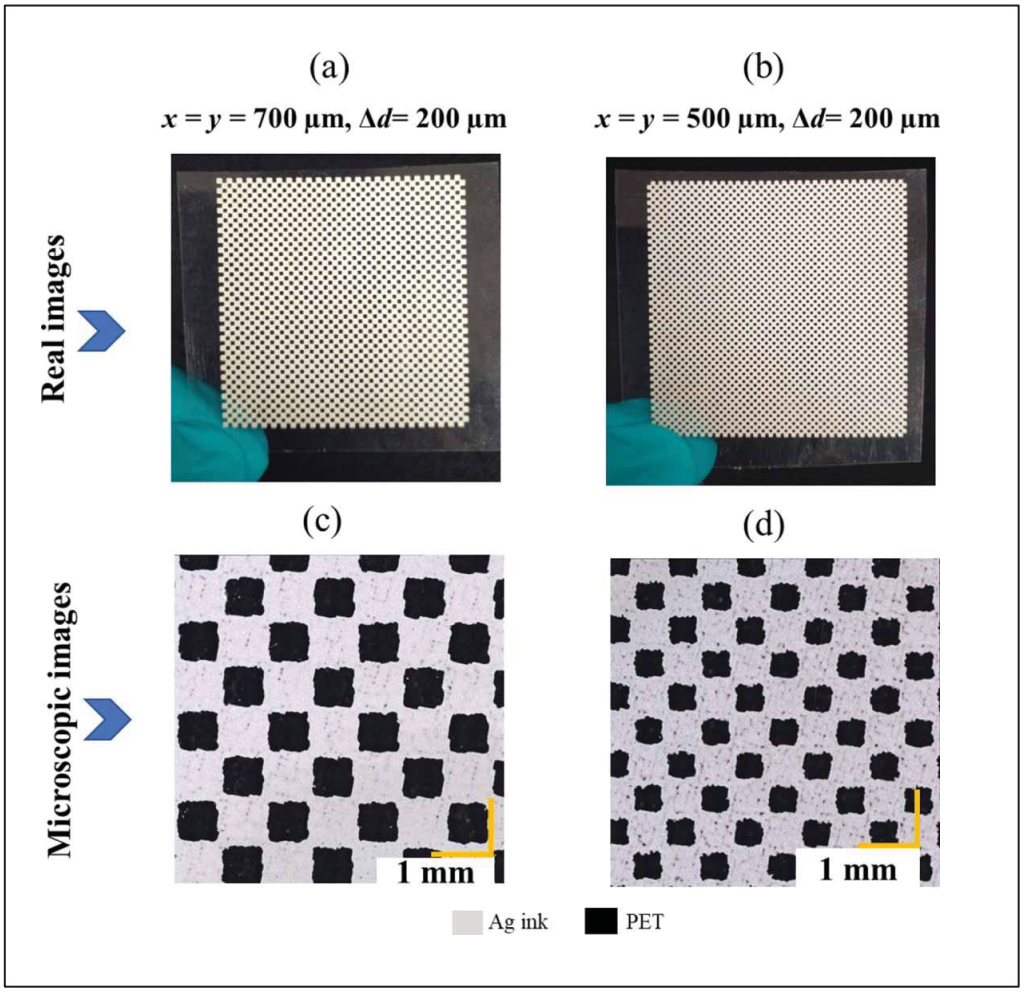

Figure 2.3 (a) & (b) Real images of type-I:i-MCB and type-II:i-MCB respectively, (c) & (d) microscopic images of type-I:i-MCB and type-II:i-MCB respectively

thickness of the PET substrate is 125 µm and the properties of the used substrate can be found in (Multi-Plastics, n.d.). Consequently, analyzed MCBs were printed and cured in the oven with hot air at a temperature of 90°C. The resulting sample had a thickness of ~2 µm and conductivity measured as 5.0×10^6 S/m using the 4-point probe method. The fabricated sample of type-I&II: i-MCB has the following dimensions: square non-metallic part was ~700×700 μm^2 and ~500×500 μm^2 respectively and in both cases the distance between diagonally cornered two square blocks, Δd as ~200 µm. The sample was 40 mm in length by 40 mm in width as dimension. The microscopic images of the fabricated MCBs are shown in Fig. 2.3. Microscopic images were taken on a digital microscope (Model: Keyence VHX-7000). From

microscopic images, it is evident that some irregularities on edges are noticeable in the square non-metallic block shapes due to ink spreading, which is typical for the screen-printing method (Zhuldybina et al., 2021b).

To validate the simulation results and experimentally examine the transmission features of the fabricated frequency selective surfaces, we utilized a commercial continuous wave (CW) THz spectroscopy system (TOPTICA photonics' TERASCAN 1550). The experimental setup is illustrated in Fig. 2.4(a). The THz emitter and receiver are based on the InGaAs photodiode and InGaAs photomixer respectively. The THz waves were collimated and refocused onto the detector using a pair of off-axis parabolic (OAP) mirrors, with a 2-inch grid polarizer ensured linear polarization of the incident THz wave. Additionally, an iris was employed just before the sample holder to control the beam size, making it compatible with the sample dimensions. It is important to note that, in our experiment, we utilized a resolution of 50 MHz to discern the characteristics of our band-pass filters.

2.5 Results and discussion

2.5.1 Single layer of FSS

The center frequencies were calculated by equation (2.4) for the two i-MCB structures, i.e. type-I and type-II, which are 0.178 THz and 0.233 THz respectively. Following this prediction, the normalized transmission of the two samples was evaluated by simulation and experimentally. Figure 2.4(b) and (c) show the results of the simulation and experimental analysis of our two sample types. A simulated transmission peak (f_{peak}) at 0.173 THz and 0.226 THz is obtained, whereas the experimental transmission peaks are 0.180 THz and 0.243 THz for type-I and II samples, respectively, in perfect agreement with the previous calculation. It is noticeable that, as the size of the square non-metallic block (x) is reduced from 700 µm to 500 µm, the corresponding peak transmission frequency is shifted towards higher frequency with a very small transmission reduction from 98% to 96%. Both types of i-MCB behave as band-pass filters, exhibiting simulated bandwidths of 100 GHz and 110 GHz, and experimental bandwidths of 125 GHz and 120 GHz for types I and II, respectively. These results show good agreement between the simulated and experimental data. Experimentally obtained normalized

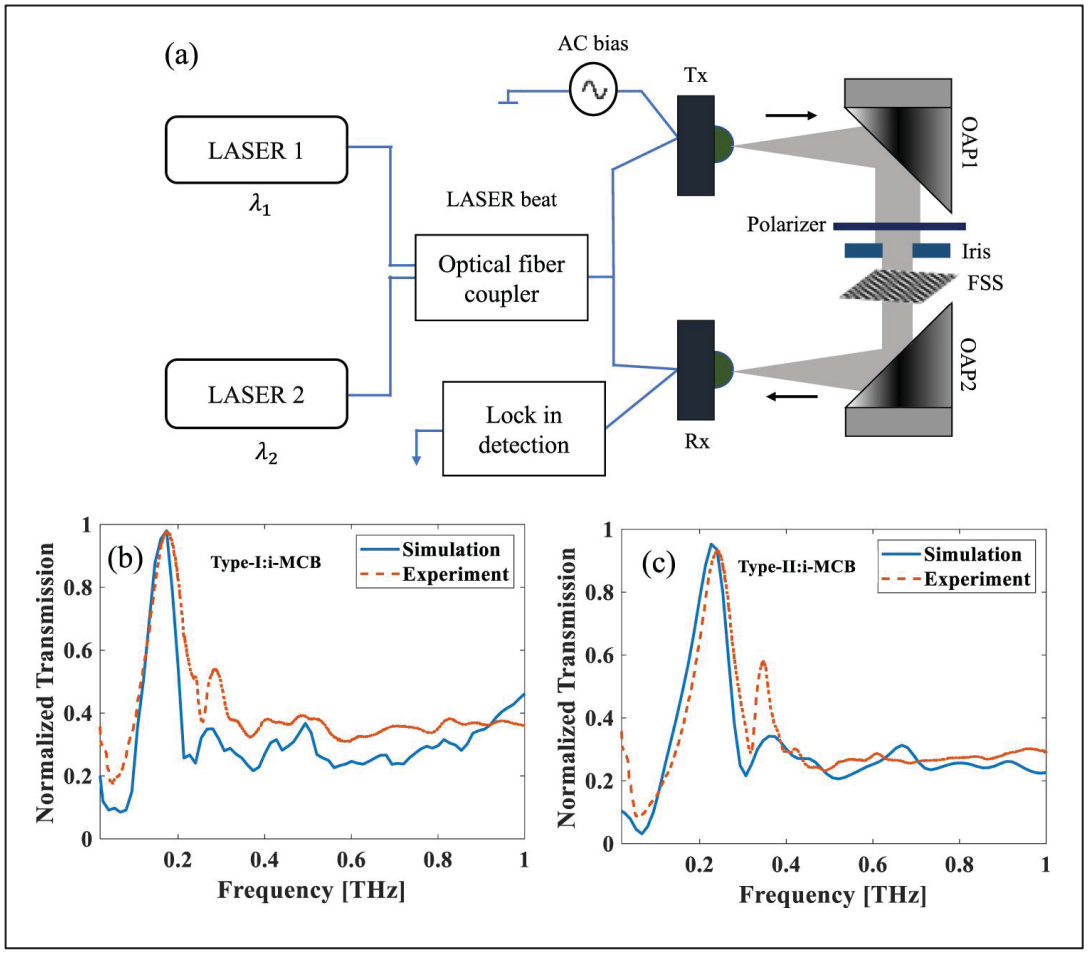

Figure 2.4 (a) Schematic view of the experimental setup; (b) simulated and experimentally characterized normalized transmission as a function of frequency for type-I: i-MCB; and (c) simulation and experimental characterization of normalized transmission in the case of type-II: i-MCB

transmission in both types of i-MCB are also consistent with the simulation results with insignificant variances.

2.5.2 Reconfigurability of FSS

2.5.2.1 Simulation analysis

To achieve reconfigurability, we used two identical MCB layers, one of which is movable relative to the second. The aim of this reconfigurability is to maximize transmission variation without affecting filter frequency or spectral width. For this purpose, two identical layers of i-

MCB (front and back layer) have been superimposed (Fig. 2.5(a)), and shifting was done on the back layer along the *x* or *y*-axis to obtain the reconfigurability. Shifting was performed along the *x*-axis from 0 µm to 700 µm in the case of type-I i-MCBs, as illustrated in Fig. 2.5(c-g). Similarly, in the case of type-II i-MCBs, shifting was done from 0 to 500 µm (figures not shown here). Observing Fig. 2.5(c-g), it is evident that shifting the back layer increases the conductive area as well as the distance between the corner edges of two non-metallic blocks of the stacked layers ($\Delta d_{\text{stacked}}$). With a shift of 700 µm, a fully conductive pattern is formed, capable of blocking or reflecting incoming THz waves.

FDTD simulations were conducted to characterize the reconfigurable i-MCB FSS. In Fig. 2.5(h), it is observed that for the case of type-I i-MCB, shifting along the *x*-axis from 0 µm to 700 µm produces a normalized transmission change from 95% to almost 0% at the peak frequency of 0.146 THz. Note that the polarization direction of the incoming THz beam is set linearly in the *x*-direction. It is noteworthy that both the non-shifted pattern and the pattern

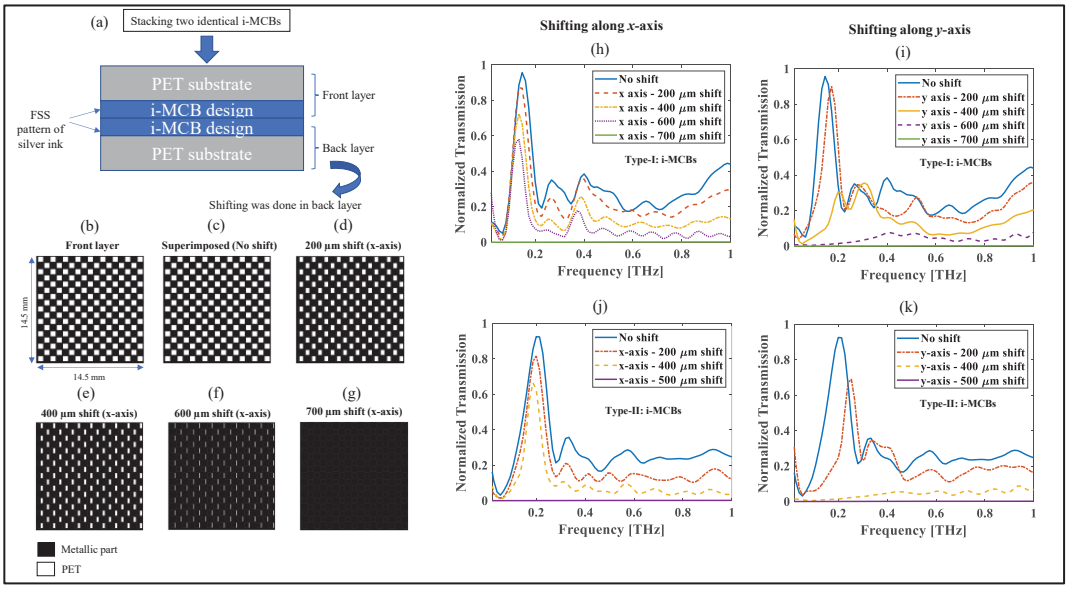

Figure 2.5 Schematic view of (a) stacked layers of i-MCBs; (b) front layer of i-MCB; (c-g) graphical representation of stacked layers for different shifting as 0 µm, 200 µm, 400 µm, 600 µm and 700 µm along the *x*-axis in the case of type-I: i-MCBs; simulated normalized transmission as a function of frequency for different shifting of the back layer along (h) *x*-axis in the case of type-I: i-MCBs, (i) *y*-axis in the case of type-I: i-MCBs, (j) *x*-axis in the case of type-II: i-MCBs, and (k) *y*-axis in the case of type-II: i-MCBs

shifted by 700 µm exhibit polarization insensitivity due to their symmetrical shapes. Conversely, the patterns shifted by 200 µm, 400 µm, and 600 µm are polarization-sensitive, given their rectangular configurations. To assess the impact of polarization, we analyzed the corresponding normalized transmission for shifting along the *y*-axis at 0 µm, 200 µm, 400 µm, 600 µm, and 700 µm.

In Figure 2.5(i), the transmission at the peak frequency of 0.146 THz shows a distinct difference for changes along the *y* direction compared to changes along the *x* direction. While the transmission tends to remain stable, it suddenly attenuates, indicating a lack of precise control of the peak transmission when shifting in the opposite direction to the THz wave polarization. More specifically, a noticeable difference emerges along the *x* and *y* axis, particularly for type-II: i-MCBs, shifts along the x-axis (0 µm, 200 µm, 400 µm, and 500 µm) produce normalized transmissions of 92%, 80%, 65%, and 0%, respectively at 0.195 THz (Fig. 2.5(j)). By contrast, shifting along the *y*-axis cannot be evaluated, as the peak shifts slightly to a higher frequency and suddenly disappears at an offset of 400 µm (Fig. 2.5(k)).

To evaluate the performances of the proposed THz reconfigurable FSS, the variation in normalized transmission needed to be calculated for various shifting along the *x* or *y*-axis at the operating frequency. The operating frequency (f_{opt}) is calculated as the peak center frequency when the back layer of two i-MCBs is not shifted i.e., 0 µm shift along the *x* or *y*-axis. The variation in normalized transmission is defined as follows:

$$Variation(\%) = \left| T_{0\,\mu m(f_{opt})} - T_{x\,\mu m(f_{opt})} \right| \times 100\% \tag{2.6}$$

Where $T_{0\ \mu m}$ and $T_{x\ \mu m}$ are the normalized transmission of the 0 µm and *x* µm shift along the *x* or *y*-axis, respectively, at the operating frequency (f_{opt}). The variation in normalized transmission has been calculated based on the simulation results for both types of i-MCBs. It is noticeable that type- I: i-MCBs exhibit maximum variation in normalized transmission as of ~95% at 0.146 THz for 700 µm shifting irrespective of the *x* or *y*-axis with reference to no shifted pattern whereas type-II: i-MCBs exhibit maximum variation in normalized transmission as of ~92% at 0.195 THz for 500 µm shifting.

Next, we explored the effects of superimposing two layers of type-I: c-MCB. Shifting was applied along both the *x* and *y*-axis at a fixed distance. The resulting simulated images, illustrating the movement along the *x*-axis, are presented in Fig. 2.6(a-e). The metallic component progressively grows as the shift occurs along the *x*-axis. Notably, achieving a complete metallic coverage, as observed in the case of i-MCB, is unattainable with the c-MCB, see Fig. 2.6(a) to (e). Consequently, this scenario results in a square lattice FSS when the back layer of c-MCBs is shifted along the *x* or *y*-axis by approximately 840 µm.

The simulation analysis considered various shifts along the *y*-axis, including 0 µm, 200 µm, 400 µm, 600 µm, and 840 µm, as depicted in Fig. 2.6(f). In Fig. 2.6(f), it is observed that the notch frequency of the corresponding band-stop filter progressively shifts to higher frequencies as the *y*-axis undergoes a gradual shift from 0 µm to 840 µm. The resulting notch frequencies are 0.146 THz, 0.174 THz, 0.186 THz, 0.213 THz, and 0.280 THz for shifts of 0 µm, 200 µm, 400 µm, 600 µm, and 840 µm, respectively. Additionally, under no-shift conditions, the

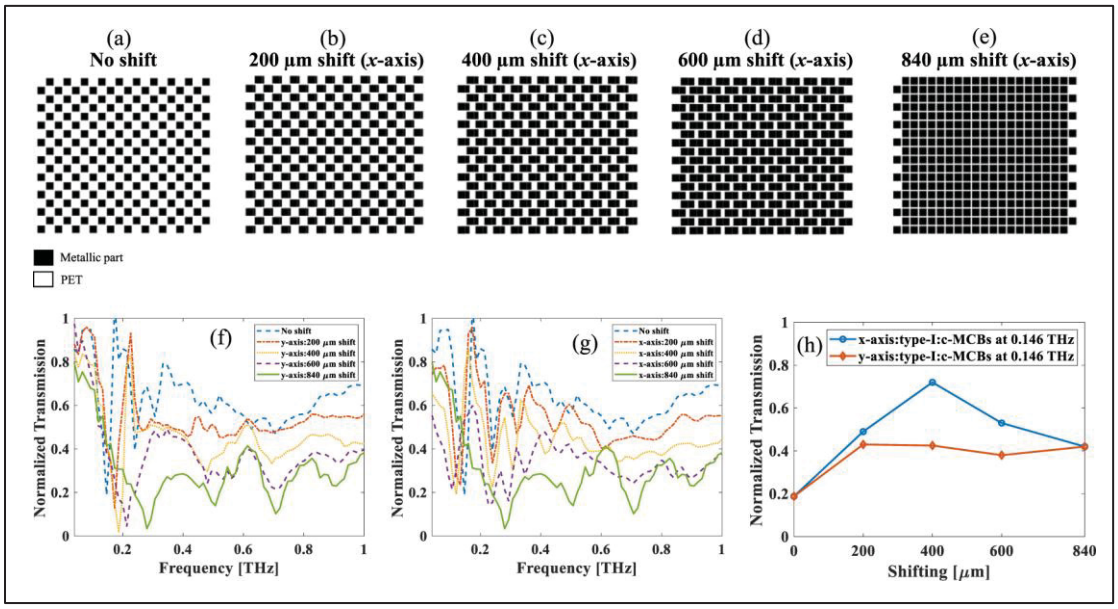

Figure 2.6 In the context of type-I: c-MCBs, simulated graphical representation of stacked layers for different shifting as (a) 0 µm, (b) 200 µm, (c) 400 µm, (d) 600 µm, and (e) 840 µm along the *x*-axis; simulated normalized transmission as a function of frequency for different shifting of back layer along the (f) *y*-axis and (g) *x*-axis in the case of type-I: c-MCBs; (h) normalized transmission as a function of shifting along the *x* and *y*-axis for type-I: c-MCBs

corresponding normalized transmission is 18.8%, while for an 840 µm shift, it decreases to 3.34%. Similarly, as the shift occurred toward the *x*-axis, the notch frequency gradually shifted towards the lower frequency range (see Fig. 2.6(g)). The associated notch frequencies are 0.133 THz, 0.120 THz, and 0.106 THz for shifts of 200 µm, 400 µm, and 600 µm, respectively. Notably, the notch frequency for both no shift and an 840 µm shift towards the *x*-axis remains unchanged compared to the *y*-axis shift, owing to the polarization-insensitive symmetrical structure. However, for both cases of *x* and *y* shift, this reduction in transmission comes with the trade-off of significant broadband attenuation, meaning that there is nearly no transmission of the THz beam through the filter when the two layers completely overlap. Also, from Fig. 2.6(h) it is evident that, the spectral responses of the stacked layers of c-MCBs were not fulfilling the aims of this proposed method to be performed as a reconfigurable FSS. Correspondingly it is seen that, the variation in NT at 0.146 THz is not noteworthy as compared to i-MCBs. Due to this, the c-MCB was deemed less appealing as a reconfigurable FSS in terms of variation in normalized transmission at f_{opt} and only i-MCBs were explored experimentally.

2.5.2.2 Experimental analysis

To corroborate the simulation findings, an experimental analysis was conducted utilizing the continuous-wave THz frequency domain spectroscopy system, as illustrated in Fig. 2.4(a), with a specific focus on two identical layers of i-MCB. In line with the simulation data, two identical type-I pattern i-MCB were superimposed. The back layer was systematically shifted along the *x* and *y*-axis at intervals of 0 µm, 200 µm, 400 µm, 600 µm, and 700 µm, and their corresponding microscopic images are depicted in Fig. 2.7(a) to (i), respectively. The layers were aligned such that the printed pattern, created using conductive ink, touched each other, with PET substrates positioned on the outer side of each layer. Also, the corresponding accuracy of the shifting and $\Delta d_{stacked}$ of the stacked layers is validated through the microscopic images. These superimposed frequency-selective surfaces were then placed between two off-axis parabolic mirrors in the collimated THz beam path. Based on the experimental analysis, it is noted that for type-I i-MCBs, the normalized transmission at 0 µm and 700 µm shifting is 94% and 6%, respectively, at 0.150 THz (refer to Fig. 2.7(j)). Additionally, the normalized

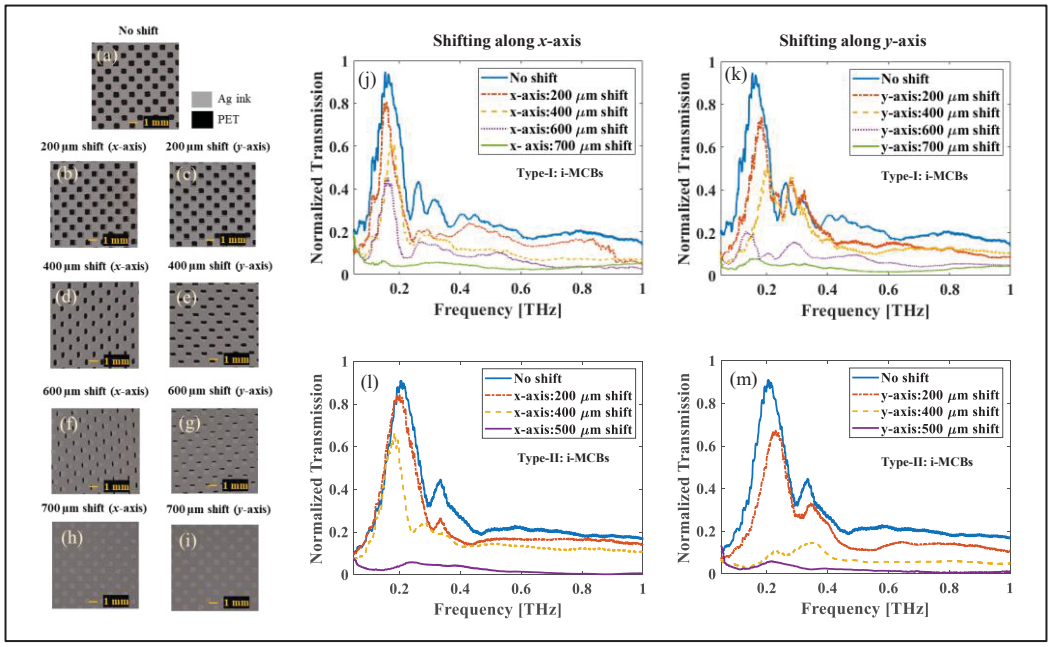

Figure 2.7 Microscopic images of superimposed type-I: i-MCBs (a) no shift; (b-c) 200 µm shifting; (d-e) 400 µm shifting; (f-g) 600 µm shifting; (h-i) 700 µm shifting along the *x* and *y* axis; Experimentally obtained normalized transmission as a function of frequency for different shifting of the back layer along the (j) *x*-axis in type-I: i-MCBs, (k) *y*-axis in type-I: i-MCBs, (l) *x*-axis in type-II: i-MCBs, and (m) *y*-axis in type-II: i-MCBs

transmission is 80%, 45%, and 38% at 0.150 THz for shifts of 200 µm, 400 µm, and 600 µm along the x-axis, respectively. Furthermore, when the back layer was shifted towards the *y*-axis, the normalized transmission values were observed to be 48%, 22%, 17%, and 7% at 0.150 THz for shifting of 200 µm, 400 µm, 600 µm, and 700 µm, respectively (see Fig. 2.7(k)). Similarly, employing two identical type-II i-MCB and shifting along both the *x* and *y*-axis (refer to Fig. 2.7(l-m)), the maximum variation in normalized transmission for *x*-direction shifting was recorded from 90% to 5% at 0.20 THz for a 500 µm shift, as illustrated in Fig. 2.7(l). Conversely, for y-direction moving, the normalized transmission was recorded as 58% and 8% for 200 µm and 400 µm shifting.

In the following, normalized transmission as a function of shifting along the *x* and *y*-axis in the case of type-I & II-i-MCBs are plotted in Fig. 2.8(a-b). The experimental analysis indicates significant variations in normalized transmission at the peak center frequency for type-I and

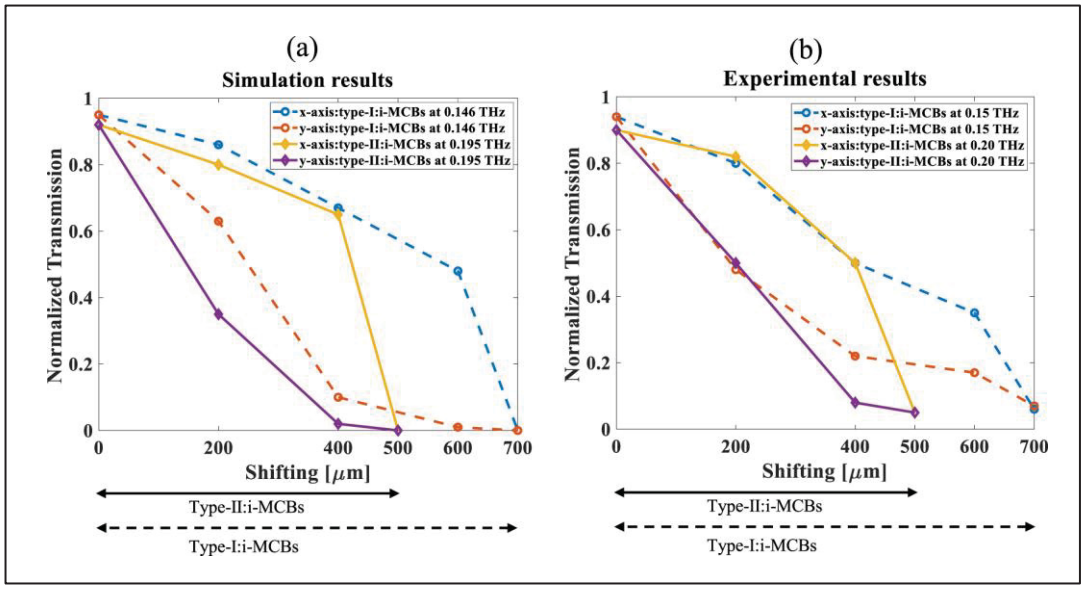

Figure 2.8 Normalized transmission as a variation of shifting of the back layer along the *x* and *y*-axis in the case of type-I:i-MCBs (no shift, 200 µm, 400 µm, 600 µm, and 700 µm) and type-II:i-MCBs (no shift, 200 µm, 400 µm, and 500 µm) (a) simulation results, and (b) experimental results

type-II i-MCBs, particularly with 700 µm and 500 µm shifting, reaching 88% and 85%, respectively, compared to the no-shift condition. Although overall consistent with simulation results, a minor discrepancy is noted, especially for the 700 µm shift in type-I i-MCBs and the 500 µm shift in type-II i-MCBs. Possible contributing factors include fabrication defects during screen printing, ink spreading, non-uniform block production, varying distances between samples during superimposition, and alignment errors. Mitigating these issues, such as limiting ink spreading and ensuring close alignment between identical samples, could enhance the variation in normalized transmission at the operating frequency.

Finally, in Tab. 2.1, we have compared our proposed work in terms of several design and output parameters with the relevant published works on printed FSS based on flexible substrate. As seen from Tab. 2.1, our proposed reconfigurable method exhibits larger variation in transmission at f_{opt} as compared to others printed THz FSS. Besides, proposed printed reconfigurable THz i-MCB-FSSs offer a notable advantage: achieving reconfigurability without the need for external stimuli like biasing voltage or photoexcitation. Mechanical

Table 2.1. Comparison with other relevant published works

Ref.	Fabrication method	Substrate	Reconfigurability	Modulation depth / variation	Operating frequency
(Ahmad et al., 2023)	Flexography	PET	Yes	41%	0.220 THz
(Wang et al., 2022)	Standard lithography, magnetron sputtering metal deposition	Polyimide - STO	Yes	40.1%	1.08 THz
				44.7%	1.16 THz
(Falade et al., 2018)	Screen-printing	Kapton, PET	No	No	29 GHz
					60 GHz
(Jilani et al., 2019)	Screen-printing	Kapton, PET	No	No	60 GHz
(Badamchi et al., 2022)	Screen-printing	PET	No	No	2.4 GHz.
This work	Screen-printing	PET	Yes	Type-I: 94% to 6%	0.15 THz
				Type-II: 90% to 5%	0.20 THz

shifting, remotely controlled by a motorized translation stage can activate or reconfigure the THz FSS simply as well as accurately. As shown in Fig. 2.2(c), reducing the size of the square non-metallic block shifts the peak center frequency towards higher frequencies, allowing for maximum variation in normalized transmission on the higher frequency range of THz. This flexibility in block size selection offers adaptability to specific operating frequency requirements and fabrication capabilities. The peak center frequency could potentially be adjacent to 0.3 THz with an i-MCB block size of 300 μm and Δd in accordance with the conventional screen printing meshes with a printing resolution in the range of ~100-200 μm. Subsequently, fine-scale silicon stencils with high printing resolution (<50 μm) (Hyun et al., 2015) could be used for fabricating i-MCB with a peak center frequency of more than 0.3 THz by reducing the block size as well as the gap Δd.

2.6 Conclusion

In summary, our study involved the analysis and fabrication of THz band-pass filters utilizing screen printing technology for efficient manipulation of THz waves. The reconfigurability aspect was achieved by superposing two i-MCB-patterned THz band-pass filters, requiring the simple shift of one layer along the x or y-axis relative to the other. This implementation resulted in significant experimental variations in normalized transmission, ranging from 94% to 6% at 0.15 THz and 90% to 5% at 0.20 THz for proposed type-I&II: i-MCBs, respectively. The demonstrated reconfigurable i-MCB printed FSSs hold promise for cost-effective development, opening up avenues for diverse applications such as THz amplitude modulation, spectroscopy, sensing, and imaging.

CHAPTER 3

RECONFIGURABLE TERAHERTZ MOIRÉ FREQUENCY SELECTIVE SURFACE BASED ON ADDITIVE MANUFACTURING TECHNOLOGY

Redwan Ahmad[1], Mariia Zhuldybina[1,2] Xavier Ropagnol[1,3], Ngoc Duc Trinh[2], Chloé Bois[2], Juan Schneider[4] and François Blanchard[1]

[1]Département de Génie Électrique, École de Technologie Supérieure (ÉTS), Montréal, QC H3C 1K3, Canada
[2]Institute des Communications Graphiques et de L'imprimabilité, Montréal, QC H2M 2E2, Canada
[3]Institut National de la Recherche Scientifique, EMT Research Center, Varennes, QC J3X 1P7, Canada
[4]Nanogrande Technologies, Montréal, QC H2N 1A4, Canada

Paper published in *Applied Sciences*, March 2023
available at https://doi.org/10.3390/app13053302

3.1 Chapter overview

This chapter presents an investigation of mechanically reconfigurable THz frequency-selective surfaces using a rotational Moiré-based reconfiguration strategy. In contrast to the lateral displacement approach presented in the previous chapter, reconfigurability is achieved here by rotationally stacking two identical FSS layers, enabling continuous and passive tuning of the transmission amplitude through Moiré interference effects. The chapter presents the design, fabrication, and characterization of Moiré-based THz FSS implemented using additive manufacturing techniques, including printable electronics and three-dimensional printing. Numerical simulations and continuous-wave THz measurements demonstrate tunable amplitude modulation at sub-THz frequencies without external biasing or active control. This work highlights rotational Moiré reconfiguration as a simple, scalable, and mechanically robust approach for amplitude modulation, providing a complementary pathway to the mechanically shifted FSS architectures explored earlier in this thesis.

3.2 Abstract

We designed and fabricated a terahertz (THz) frequency selective surface (FSS) based on two dis-tinct additive manufacturing technologies, namely, printable electronics (PE) and three-

dimensional (3D) printing. Silver nanoparticle ink was printed on a polyethylene terephthalate (PET) substrate utilizing a large-scale roll-to-roll industrial PE technique with a flexographic printed unit, while the 3D-printed THz FSS was fabricated based on a powder bed fusion-selective laser melting system. The filtering characteristics of both types of FSS were verified through calculation, simulation, and experiments. Furthermore, the rotational tuning approach was applied to two identical FSSs to form reconfigurable FSSs which could be defined as Moiré FSSs. Based on the numerical results obtained, our proposed technique which used a PE-based Moiré FSS achieves a 58% modulation depth at 0.25 THz, while experimental verification found a modulation depth of 41% at 0.22 THz, confirming that its adoption is simple and cost-effective. To the best of our knowledge, this is the first demonstration of a Moiré reconfigurable printed FSS operating in the THz region.

3.3 Introduction

Terahertz (THz) waves, with frequencies ranging from 0.1 to 10 THz and wavelengths from 0.03 to 3 mm, have potential applications in various domains, including communications, spectroscopy, imaging, security, and medical diagnostics (Tonouchi, 2007; Wu, et al., 2020; Zhao et al., 2022). For each of these applications, it is critical to control the wavefront, and this can be done through generation and detection processes, or by inserting a filter, modulator, an absorber, etc., inside the THz path (Luo et al., 2014; Siday et al., 2019). The frequency selective surface (FSS) is a two-dimensional frequency filter with transmission and reflection characteristics that can be designed to have high-pass, low-pass, band-pass, or band-stop characteristics (Anwar et al., 2018). Compared to metasurfaces (MS), which have sub-wavelength structures, one of the characteristics of standard FSS structures is that their unit cell size is about half that of the operational wavelength (Ebrahimi et al., 2015). In addition to filtering properties, THz FSSs also have been reported as polarization converters (Euler et al., 2010) and absorbers (Cheng et al., 2014), among other applications (Xia et al., 2013; Zhuldybina et al., 2020; Silalahi et al., 2021). Notwithstanding this great variety of the features characterizing them, the parameters of these FSSs remain passive, and can consequently only be used for specific intended applications. A tunability technique may also be used to control the peak transmission amplitude of an FSS, resulting in the formation of a reconfigurable

amplitude modulator at a certain frequency. The key materials that have been identified as potential candidates for developing THz reconfigurable modulators include semiconductors (Chen et al., 2006; Jia et al., 2022), liquid crystal (Isić et al., 2015; Liu et al., 2022), graphene (Yatooshi et al., 2015), vanadium dioxide films (Zhang et al., 2014), etc. To date, multiple tunability approaches, such as photoinduced (Zhang et al., 2014), mechanical (Pryce et al., 2011), electrical (Yang et al., 2021), electronical (Wang et al., 2022), and rotational (Han et al., 2015) methods, have been used to produce modulators with active control. Impressively, over the last ten years, the performance of the THz modulator has improved dramatically, with modulation speeds increasing from the kilohertz (kHz) to the gigahertz (GHz) (Zhang et al., 2015) and modulation depths have been recorded at up to 80% (Zhang et al., 2014), 90% (Isic et al., 2019), and 93% (Isić et al., 2015).

So far, the vast majority of reconfigurable THz modulators have required costly facilities such as clean rooms and multiple production steps, making them ill-suited for large-scale production. Moreover, the size of the unit cell of the FSS with an operating frequency in the lower part of the THz region (sub-millimeter/millimeter wavelength) is a few hundreds of microns, and the fact is that it is usually not necessary to use such a costly fabrication technique with sub-µm resolution for prototyping THz FSSs (Zhuldybina et al., 2020). As an alternative, a new manufacturing method has emerged, named additive manufacturing, which can be used to fabricate different THz FSS structures with unit cell sizes measuring a few hundreds of microns. This technique is a low-cost and high-speed process and al-lows printing on a very large scale. It is also environmentally beneficial as it produces less raw material waste than conventional methods (Castro-Camus et al., 2020; Irimia-Vladu et al., 2017). It is striking that the high precision of additive manufacturing technique, i.e., printable electronics even allows their own non-contact inline inspection by printing THz FSS (Zhuldybina et al., 2019; Zhuldybina et al., 2021b). There have already been a few reports on THz devices made via additive manufacturing, including vortex phase plates (Zhuldybina et al., 2019), diffractive THz lenses (Furlan et al., 2016), gradient-refractive-index lenses (Hernandez-Serrano et al., 2016), band-pass filters (Ahmad et al., 2022; Sushko et al., 2017), etc. Additionally, 3D printing has been used to create a holographic metasurface antenna that operates in the GHz range (Yurduseven et al., 2019). Furthermore, printed flexible THz metamaterials and

metasurfaces have been reported over the past few years. For instance, a THz metamaterial based on electrohydrodynamic jet printing (Yudistira et al., 2013) and a printed metallic checkerboard based on flexographic printing (Zhuldybina et al., 2020) have been reported. However, in these demonstrations, it should be noted that none of these devices are reconfigurable or tunable. To do so, mechanically tunable terahertz metamaterials based on a flexible PDMS substrate have been demonstrated by J. Li *et al*. (Li et al., 2013), but require a standard photolithography fabrication method. To the best of our knowledge, no reports on the demonstration of a reconfigurable printed THz FSS exist in the literature to date. To achieve this, the Moiré pattern interference scheme represents an interesting and simple way to realize tunability from printed structures. Recent examples of Moiré interference have been used for electromagnetic re-configuration at the atomic scale (He et al., 2021b), in a tunable metasurface lens (Iwami et al., 2020), on a hyperbolic Moiré metasurface (Liu et al., 2022), and to control the transmission amplitude of electromagnetic waves in the GHz frequency range (Han et al., 2015).

In the present work, we demonstrate the design, fabrication, and analysis of the filtering properties of THz FSSs produced by two different additive manufacturing approaches, i.e., printable electronics (PE) and 3D printing. The PE-based FSS was made from a silver nanoparticle ink and printed on a PET substrate, while the 3D-printed FSS was fabricated using aluminum foil. In the next step, FSSs are used to develop a reconfigurable THz FSS. To that end, the Moiré FSS was implemented using two identical FSSs based on a triangular air hole array. The proposed THz Moiré-printed FSS can be con-trolled by simply adjusting the rotation angle between two identical structures. In agreement with our simulations, the experimental results show a decrease in transmission from 90% to 53% at a center frequency of 0.22 THz in the case of the PE-based Moiré FSS, covering a spectral width of ~250 GHz at full width at half maximum (FWHM).

3.4 Modeling, fabrication, and experimental characterization of THz FSSs

The FSS pattern designed in this work is similar to that reported recently in the GHz frequency range (Kim et al., 2017), but with dimensions of the air hole diameter and the distance be-tween two holes much smaller to be suitable for THz applications. Real and microscopic

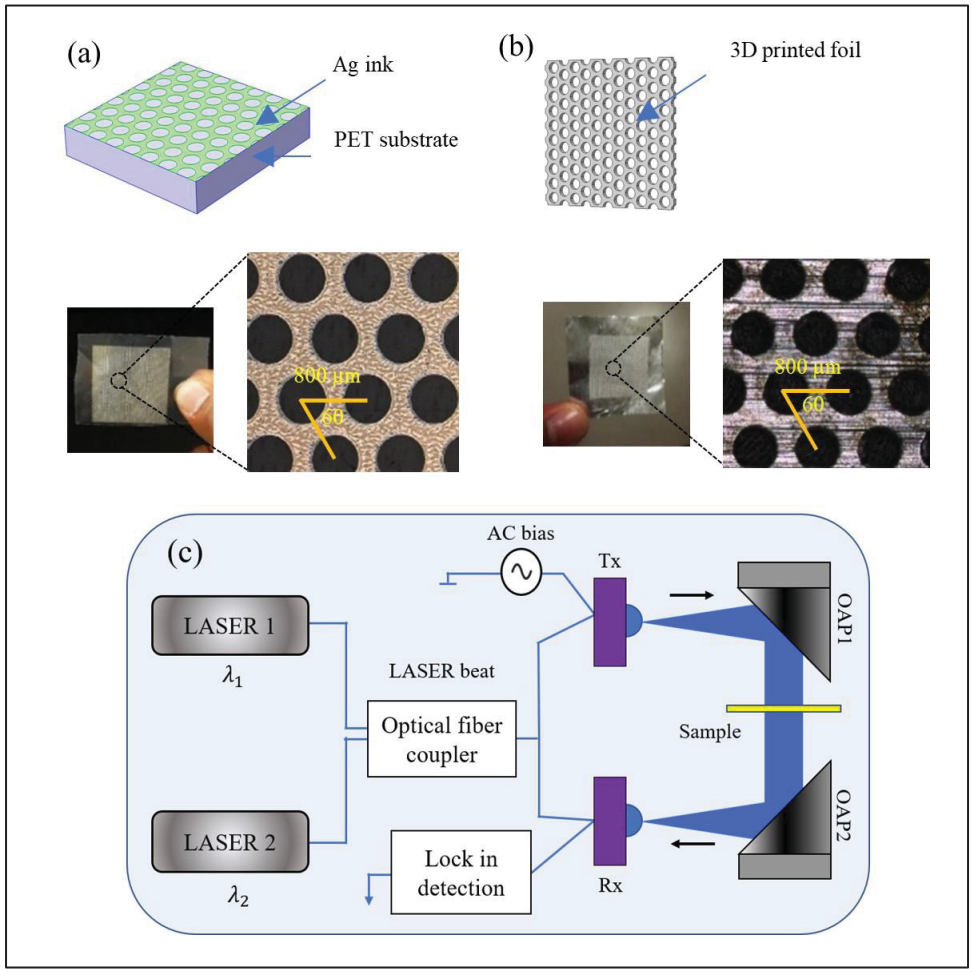

Figure 3.1 THz FSS (a) based on printable electronics using silver (Ag) ink and PET as a substrate; (b) based on 3D printing made from aluminum foil. (c) Experimental setup of CW THz spectroscopy. Here Tx, Rx, and OAP stand for transmitter, receiver, and off-axis parabolic mirror, respectively

images of the FSS based on PE and 3D printing are shown in Figure 3.1(a,b) respectively. For the PE sample, they were printed on a flexible substrate using silver (Ag) nanoparticle ink (PFI-600, NovaCentrix, Austin, TX, USA) using an industrial roll-to-roll (R2R) continuous press with flexography printing units (OMET Varyflex, Lecco, Italy). With the R2R printer, a variety of plastic substrates are available, including polyethylene terephthalate (PET), polyethylene naphthalate (PEN), and polyimide (PI). The processing temperatures for PET, PEN, and PI are 150°C (heat stabilized), 200°C, and 360–400°C, respectively (Park et al., 2019). PEN and PI can be more expensive when compared to the PET substrate. Since the

printed FSSs were dried inline with hot air at a maximum temperature of 100°C, this allows us to choose PET as the printing substrate, which is the cheapest available and most widely used substrate. The thicknesses of the FSS pattern and PET substrate were 352 nm and 125 µm respectively, while the conductivity of the printed sample was 4.40×10^6 S/m. The diameter of the sample's air hole was ~600 µm with a distance between the centers of the two air holes (the pitch) of ~800 µm, all covering an area of 40×40 mm^2. A second FSS structure with the same air hole diameter and pitch size was fabricated using the 3D printing technique (printer model: MPL-1 from Nanogrande company). The main difference between the two types of fabrication is the presence of the PET substrate in the PE method while the 3D printing sample has no substrate. This one has simply a thickness of 100 µm obtained by the selective fusion by laser on metal powder bed obtaining a conductivity of approximately 2.50×10^7 S/m.

To investigate the features of the fabricated FSSs, we employed a commercial continuous wave (CW) THz spectroscopy system (TERASCAN 1550 from TOPTICA photonics). The experimental setup is illustrated in Figure 3.1c. The terahertz emitter and receiver are based on an InGaAs photodiode and InGaAs photomixer, respectively. The radiated THz waves were collimated and refocused onto the detector by a pair of 2-inch diameter and 3-inch focal length off-axis parabolic mirrors. Note that in our experiment, we used a resolution of 50 MHz to resolve the characteristics of our analyzed BPF. To extract the normalized transmission characteristics of the PE-based and 3D-printed THz BPF, the following equation was applied:

$$NT(\omega) = \left| \frac{T_{sample}(\omega)}{T_{ref}(\omega)} \right| \tag{3.1}$$

where $T_{\text{sample}}(\omega)$ and $T_{\text{ref}}(\omega)$ are the transmission of the sample and reference, respectively. The experimental results of PE-based and 3D-printed FSS, accordingly, are shown with a solid blue line in Figure 3.2(a,b). It was observed from experimental measurements that PE-based filters offered a larger bandwidth covering from 130 to 380 GHz, as compared to the 3D-printed filter, which came in at 250 to 430 GHz (i.e., at FWHM).

To confirm our experimental observation, we performed finite difference time domain (FDTD) simulations on both FSSs using Ansys Lumerical software to characterize the properties of the

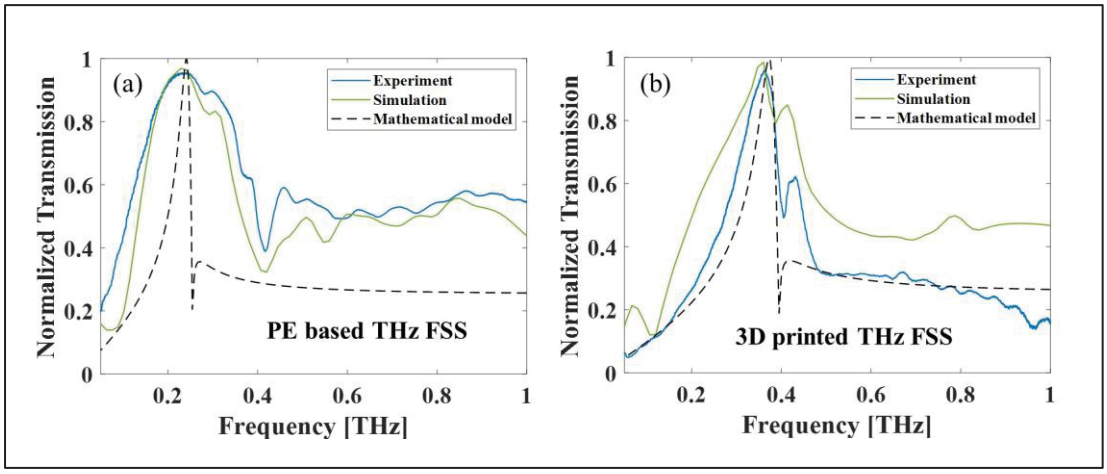

Figure 3.2 Normalized transmission as a function of frequency in the case of a single layer of THz FSS, (a) printable electronics-based; (b) 3D printed

investigated FSSs. During the simulations, we designed and analyzed a 6 mm length by 6 mm width sample, which was positioned between the THz source and the detector section. Figure 3.2(a,b) illustrates the transmission characteristics obtained with the simulation (green line). To validate our simulation and experimental results and evaluate the filter response of both types of THz FSSs, we used the well-known numerical modeling reported by (Chen et al., 1973). It was demonstrated that the model can accurately predict the transmission characteristics of FSS, consisting of circular apertures with triangular lattices. The transmission coefficients T can be obtained as (Chen, 1973):

$$T = \frac{1}{1 - j\left[A + B\tanh\left(\beta l\right)\right]} - \frac{1}{1 - j\left[A + B\coth\left(\beta l\right)\right]} \tag{3.2}$$

where β is the phase constant and l is thickness of the sample. To calculate the parameters A and B as functions of hole spacing and hole size, respectively, the following Equations (3.3) and (3.4) can be applied (Kim et al., 2017; Chen, 1973):

$$A = 12\left(\frac{4}{3}\left(\frac{\lambda}{d}\right)^2 - 1\right)^{\frac{1}{2}}\left[\frac{J_1'\left(\frac{4\pi a}{\sqrt{3}d}\right)}{1 - \left(\frac{4\pi a}{1.841\sqrt{3}d}\right)^2}\right]^2 - \frac{12}{\left(\frac{4}{3}\left(\frac{\lambda}{d}\right)^2 - 1\right)^{\frac{1}{2}}}\left[\frac{J_1\left(\frac{4\pi a}{\sqrt{3}d}\right)}{\frac{4\pi a}{\sqrt{3}d}}\right]^2 \tag{3.3}$$

$$B = 0.33\left(\frac{d}{a}\right)^2\left(\left(\frac{0.293\lambda}{a}\right)^2 - 1\right)^{\frac{1}{2}} \tag{3.4}$$

The circular holes' centers are separated by a distance of *d*, the radius of the circular hole is denoted by *a,* and λ stands for the wavelength. J_1 and J_1' are the first kind of Bessel function and the derivative, respectively. The phase constant can be obtained as follows:

$$\beta = \frac{2\pi}{\lambda}\left(\left(\frac{0.293\lambda}{a}\right)^2 - 1\right)^{\frac{1}{2}} \tag{3.5}$$

The above mathematical model is useful to accurately anticipate the transmission characteristics of a THz FSS without substrate, which is the case of the THz FSS made using 3D printing. On the other hand, for an effective prediction of the PE-based THz FSS's transmission characteristics, we ought to take into consideration the effect of the PET substrate. To this end, we replaced the λ with λ_2 in Equations (3.3) and (3.5) and defined as $\lambda_2 = \lambda \times (n/n_2)$, where n and n_2 are the refractive indices of air (1.00) and PET (1.74 at 0.5 THz) (Jin et al., 2006), respectively. As such, the calculated transmission characteristics for the two types of FSSs were evaluated using Equation (3.2). Figure 3.2(a,b) illustrates the transmission characteristics obtained with the mathematical model (black dotted line) and shows the calculated peak transmission frequencies for the PE and 3D-printed FSSs at 247 and 370 GHz,

Table 3.1. Comparison between PE-based and 3D-printed THz FSS

Parameters	**PE-Based THz FSS**	**3D-Printed THz FSS**
Lattice type	Triangular	Triangular
Fabrication method	R2R flexography	Powder bed fusion-selective laser melting system
Material	Ink: Ag Substrate: PET	Aluminum foil
Thickness	Ink: 352 nm Substrate: 125 μm	100 μm
Conductivity	4.40×10^6 S/m	2.50×10^7 S/m
Peak resonance frequency (experimental)	0.235 THz	0.365 THz
Bandwidth (experimental)	250 GHz	180 GHz

respectively. From the calculation, it is clear that both FSSs behave like band-pass filters (BPF). The experimental measurements and simulation results demonstrated that the peak transmission frequency of the PE-based THz BPF is at a lower frequency region as compared to the 3D-printed THz BPF due to the PET substrate. The peak transmission frequency for a single PE-based THz filter was determined to be 228, 247, and 235 GHz from simulation, calculation, and measurement, respectively. Similarly, the peak transmission frequency of a single 3D-printed THz filter obtained by simulation, calculation, and measurement are 360, 370, and 365 GHz, respectively. In Figure 3.2, we can see from experiments that the 3D-printed THz BPF provides a sharper transmission with a higher quality factor than the PE-based THz BPF. In addition, the stopband is exactly the same as the calculated value and more pronounced than that obtained with the PE filter. This difference in stopband performance can be explained by the larger amount of conductive material in the case of the 3D-printed sample as compared to the PE sample. In terms of peak frequency transmission, predicted filter responses for both types of filters were fairly comparable to those obtained from simulations and experiments. However, there are some apparent differences among simulated, calculated, and measured results in terms of bandwidth (BW). Particularly in the case of PE-based THz filters, a significant difference in BW was found. One reason for this discrepancy could be related to the absorption characteristics of THz waves in the PET substrate, which were not taken into account in the numerical modeling. The comparison between the PE-based and 3D-printed THz FSS in terms of several design and output parameters is presented in Table 3.1.

3.5 Analysis of Moiré THz printed FSS

To study the Moiré interference effect, the simulation was performed while stacking two identical BPFs made from printed FSSs, with the orientation of the second one being changed relative to the first, with a rotation angle ranging from 0° to 90°, with a 10° step. It can clearly be seen that as the superposition angle increases, the number of smaller groups with new periodic patterns also increases because of the geometric design of the hexagonal air-hole array. Thus, two identical THz FSS are being used to form reconfigurable THz FSS. From Figure 3.3, it is obvious that the patterns for the 40°, 50°, and 60° rotations look like those for the 20°, 10°, and 0° rotations, respectively. Similarly, the Moiré patterns for the 70°, 80°, and

90° rotations are symmetrical with the 10°, 20°, and 30° rotations, respectively. Clearly, beyond the 30° rotation angle, the Moiré patterns repeat symmetrically, which is why we evaluated the azimuthal response of the THz transmission from a 0° to a 30° rotation angle, with a 10° step. PET was taken into consideration as a substrate of the analyzed FSS.

Figure 3.4(a–d) shows the corresponding electric field distribution in the near-field for different rotation angles. The 2D simulated electric field distribution was obtained by placing the frequency domain field and power monitor in the near-field for different rotation angles. It is noteworthy that as the rotation angle was changed from 0° to 30°, unique Moiré patterns were observed with distinct field distributions, i.e., the spatiotemporal electromagnetic responses. Additionally, to evaluate the performances of the proposed THz amplitude modulator, the modulation depth needed to be calculated for various rotation angles at one fixed frequency, which was determined as the operating frequency where the maximum transmissions occur when the two samples are rotated with a 0° angle. The modulation depth (*MD*) is defined as follows:

$$MD(\%) = \frac{T_0(\omega) - T_x(\omega)}{T_0(\omega)} \times 100\% \tag{3.6}$$

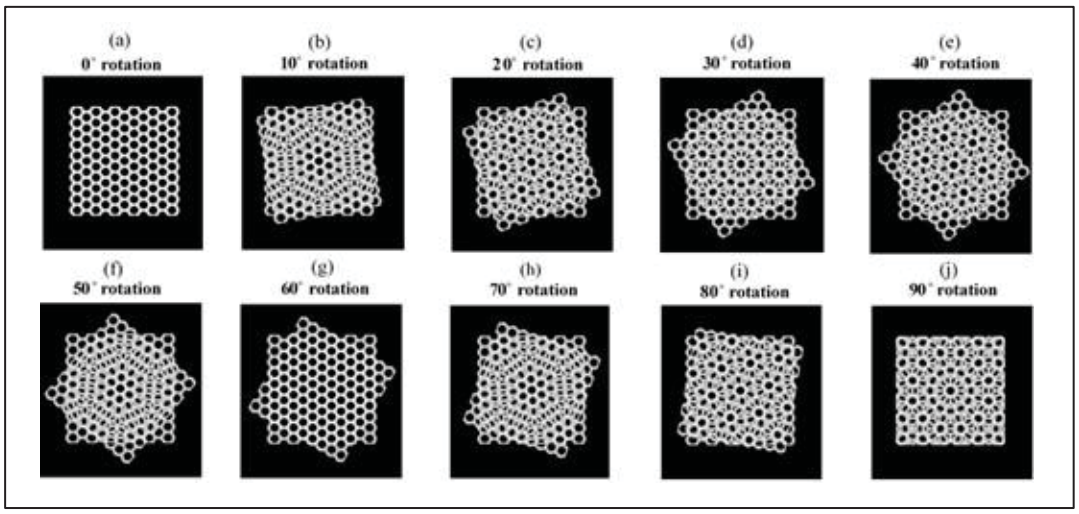

Figure 3.3 Simulated Moiré pattern images for the rotation angle of (a) 0°; (b) 10°; (c) 20°; (d) 30°; (e) 40°; (f) 50°; (g) 60°; (h) 70°; (i) 80°; (j) 90°

where $T_0(\omega)$ and $T_x(\omega)$ are the normalized transmission of the 0° and x° rotation, respectively, at the operating frequency (ω). Figure 3.5(a) shows the simulated normalized transmission at various rotation angles. As can be seen in the figure, the peak normalized transmission gradually decreases when the second sample is rotated from 0° to 20°, and for a 30° rotation angle, the normalized transmission is again increased with respect to the 20° rotation. It is also worth noting that the maximum expected transmission peak for the 0°, 10°, 20°, and 30° rotation angles are 97%, 70%, 48%, and 58%, respectively. The maximum transmission peak was obtained for a 0° rotation at 0.25 THz, which is hereafter called the operating frequency to calculate the modulation depth for different rotation angles. Accordingly, the normalized transmission decreased from 93% to 39% at 0.25 THz when the rotation angle was adjusted from 0° to 20°, resulting in a modulation depth of 58% (see Figure 3.5(b-left axis)). Likewise,

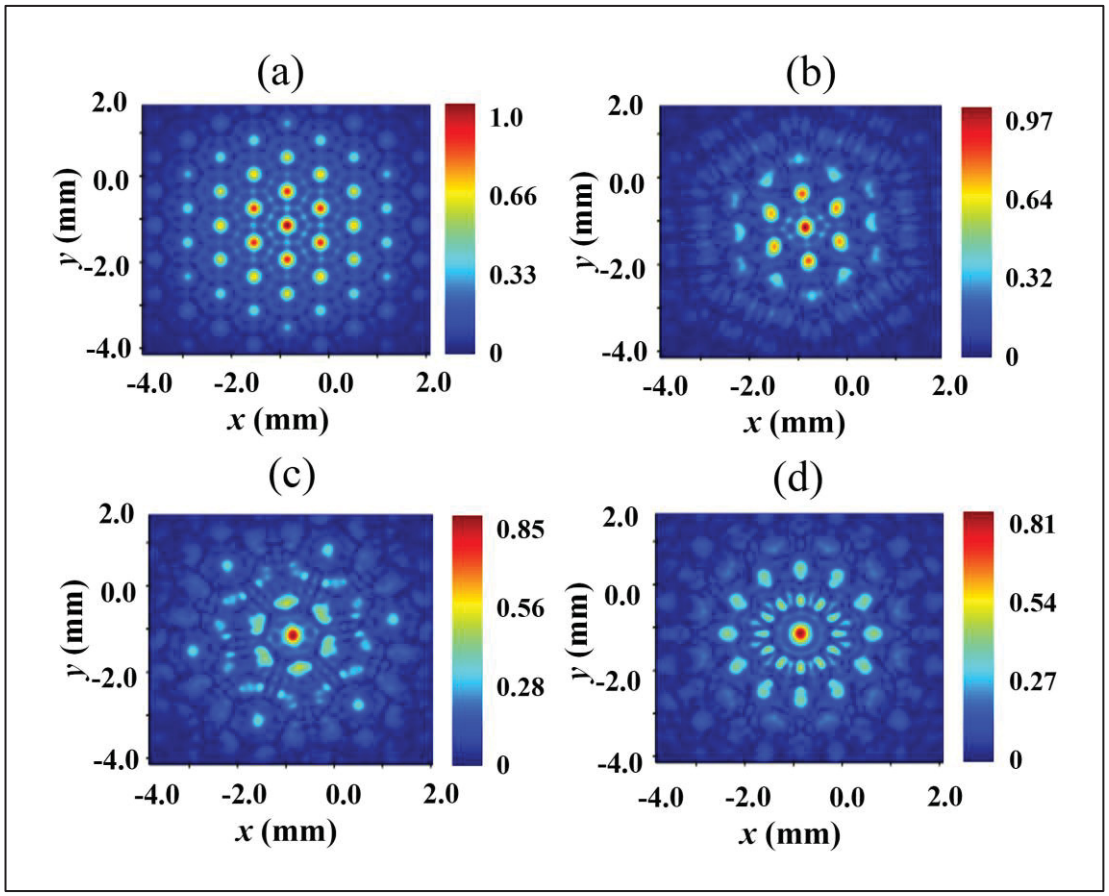

Figure 3.4 Numerically obtained electric field distribution in near-field in the case of: (a) 0° rotation; (b) 10° rotation; (c) 20° rotation; (d) 30° rotation

the modulation depth was calculated as 28% and 46% for the 10° and 30° rotation angles, respectively (see Figure 3.5(b-right axis)). Changes in bandpass filtering bandwidth could also be seen when the second sample was rotated from 0° to 30°. At FWHM, the filtering bandwidth became 238, 175, 230, and 160 GHz for 0°, 10°, 20°, and 30° rotation angles, respectively. It can also be seen that the peak resonance frequency is also shifted towards the higher frequency range due to the geometry of the Moiré pattern for different rotation angles. The corresponding peak resonance frequency becomes 0.241, 0.254, 0.275, and 0.280 THz for the 0°, 10°, 20°, and 30° rotation angles, respectively. From both the FWHM bandwidth and peak resonance frequency for different rotation angles, it is evident that the rotation angle of 30° exhibits the highest Q factor among all the rotation angles, with the FWHM bandwidth dropping to its lowest value (160 GHz). As mentioned earlier, the Moiré patterns repeat symmetrically after a 30° rotation. To validate this, we studied the modulation depths over an azimuthal range up to 120°, as shown in Figure 3.5(c). From this figure, it can easily be estimated that a total of five "zero" modulation depths with 60° intervals will be obtained for a full 360° rotation, in agreement with the hexagonal array of the designed filters. Finally, the simulation clearly showed that the transmission of the incident THz wave could thus be controlled at the operating frequency by employing only the rotational tuning approach.

In order to validate our simulation results, we studied the visual effect of Moiré interference patterns using a 633 nm diode mounted on a 2*f* imaging system and coupled to a CMOS camera (model: DCC3260M). To form a Moiré FSS, we employed two identical PE-based FSSs positioned as close as possible to each other. It should be recalled that two PE-based samples were arranged such that the conductive ink parts touched one another, and on the two exterior surfaces are PET substrates. The alignment of the two printed samples was also performed using a 2*f* imaging system, with one held fixed in one sample holder and the other with a rotatable mount to rotate at some fixed angles. The respective Moiré patterns obtained for 10°, 20°, and 30° angle rotations with the printed samples are shown in Figure 3.6(a–c), respectively. It can be seen that the simulated and experimental images are consistent and quite similar (e.g., see between Figure 3.4(a–d) and 3.6(a–c)).

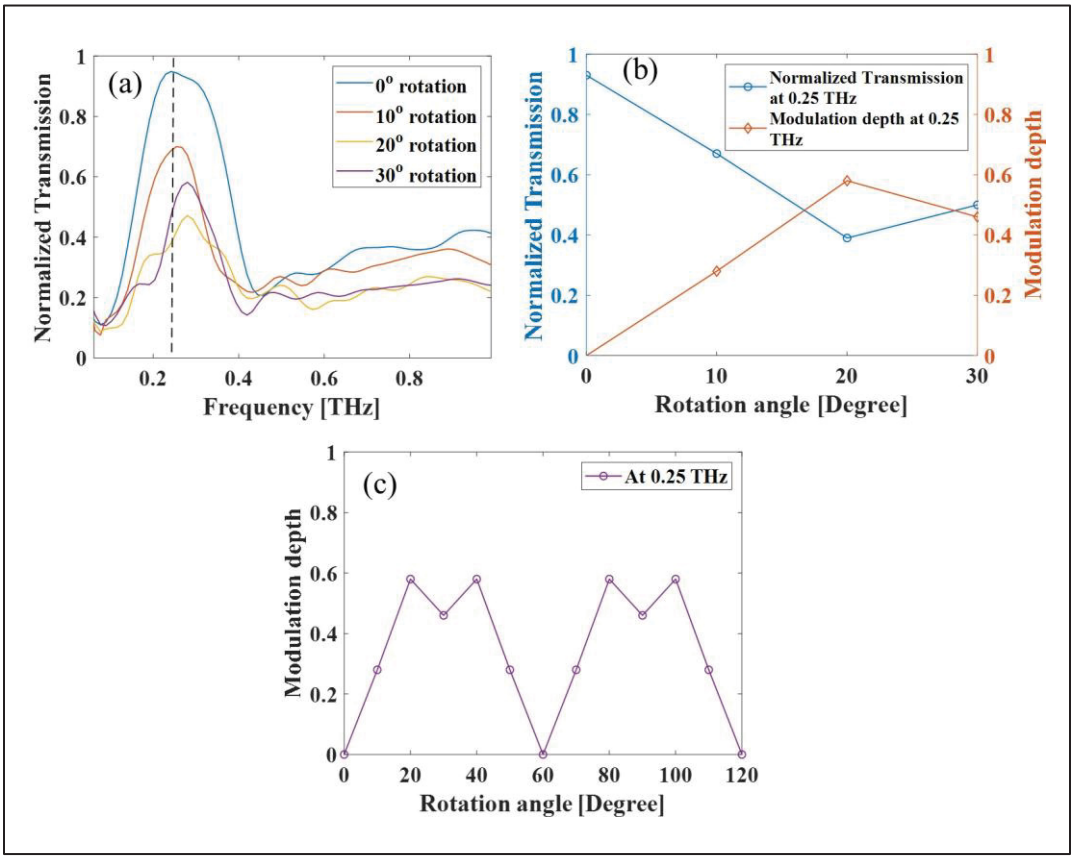

Figure 3.5 (a) Simulated normalized transmission for different rotation angles as 0°, 10°, 20°, and 30°; (b) normalized transmission (blue line) and modulation depth (orange line) as a function of rotation angles at operating frequency of 0.25 THz; (c) simulated modulation depth as a function of rotation angles from 0° to 120° at 0.25 THz

In the following step, the normalized transmissions for various rotation angles were measured by using two PE-based THz FSSs (shown in Figure 3.6(d)). At 0.22 THz, we extracted the normalized transmission for 0°, 10°, 20°, and 30° rotation angle and obtained 90%, 66%, 53%, and 58%, respectively. Their respective modulation depths were calculated using Equation (3.6). Furthermore, from Figure 3.6(d), it can be seen that as the rotation angle changed from 0° up to 30°, significant variations in the transmission and modulation depths were observed. The lowest transmission of an incident THz wave obtained at 0.22 THz for the 20° rotation angle was 53%, corresponding to a maximum modulation depth of 41%. Additionally, for the 10° and 30° rotation angles the modulation depth was calculated as 26% and 35%, respectively. It can be seen that our experimental results show some deviations from the simulation results.

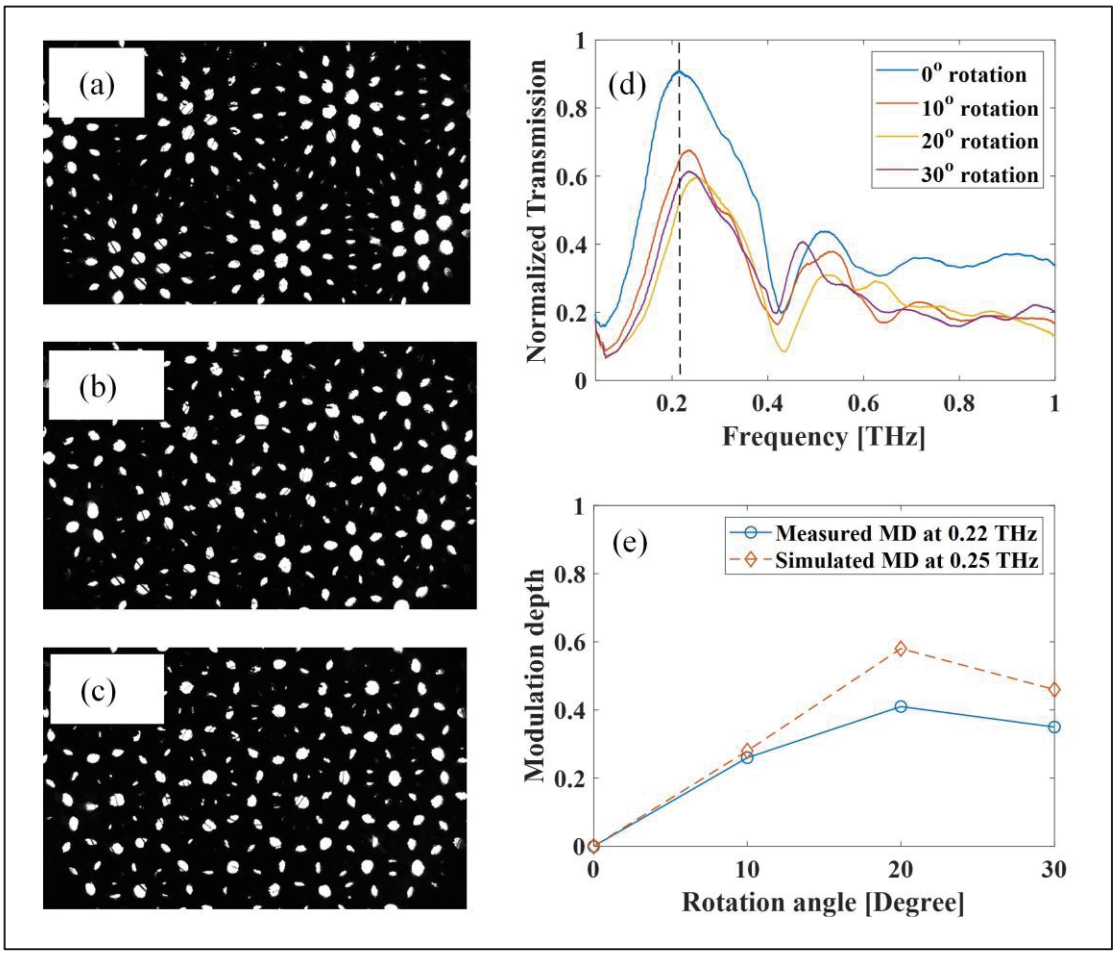

Figure 3.6 Moiré pattern image taken using 2f imaging system for (a) 10° rotation; (b) 20° rotation; (c) 30° rotation. (d) Experimental normalized transmission as a function of frequency for different rotation angles. (e) Obtained modulation depth in the case of simulation and measured findings as a function of rotation angles

From our observations, three factors are critical in this experiment based on PE-based samples: (1) a presence of air gap spacing be-tween the two samples, (2) a hole-to-hole misalignment during the superposition of the two samples, and (3) a reproducibility error of the identical fabricated samples (although in the case of printable electronics-based samples, this error is insignificant). These three factors could explain the difference between the experimental results and a perfect situation (simulation). Despite the differences in values between the simulated and the experimental transmission and modulation depths, the general behavior was the same in both cases, and we obtained a maximum modulation depth for the 20° rotation (as

shown in Figure 3.6(e)), in agreement with the simulation. One of the major advantages of our analyzed printed Moiré reconfigurable THz FSS is that no external stimulus, such as a bias voltage or photoexcitation, needs to be applied in order to achieve the tunability of the transmitted wave. To achieve reconfigurability, two samples could simply be superposed over one another, with only one layer needing to be rotated relative to the other. Furthermore, this rotation can be done and controlled remotely with a motorized translation stage to make THz FSS become active.

Additionally, we used two FSSs which were 3D printed, as shown in Figure 3.1(b), to characterize the Moiré interference effect by varying the rotation angle between the samples, just as we did with samples made of PE. However, the high malleability and non-flat surface of the 3D-printed samples made it difficult to superimpose them on each other, and this surface variation resulted in a significant misalignment error, i.e., the holes did not form the desired interference patterns. Because of their non-flat surface, the analyzed 3D printed Moiré FSS was not performed effectively in terms of modulation depth (figure not shown here) when compared to PE-based Moiré FSS. Moreover, the aforementioned problems could be minimized by increasing the printing layers to make it a flat surface in the case of 3D-printed FSSs in order to achieve the desired modulation depth.

3.6 Conclusion

In conclusion, we analyzed THz band-pass filters fabricated based on two different additive manufacturing technologies. It can be noted that both technologies allow the efficient manipulation of THz waves, i.e., band-pass filtering through the printing of FSSs. It can be seen that 3D-printed THz BPF offers a narrow pass-band i.e., a higher quality factor as compared to the PE-based analyzed THz BPF. Additionally, the implementation of the Moiré interference technique based on the printed FSSs can potentially open up new possibilities for the mass production of reconfigurable THz FSS at lower cost. Remarkably, the maximum modulation depth obtained experimentally at 0.22 THz is 41% for a 20° rotation, which is relatively adjacent to the expected value obtained by simulation, which was 58% at 0.25 THz in the case of PE-based Moiré FSS. By improving the alignment and limiting the air gap between the two samples, the discrepancy between the simulation and the experimental results

could be minimized and the modulation depth could be improved. This validates the usefulness of the proposed printing technology and of the Moiré THz reconfigurable FSS.

CHAPTER 4

POLARIZATION-SENSITIVE TERAHERTZ FREQUENCY-SELECTIVE SURFACE BASED ON A LASER CUTTING TECHNIQUE

Redwan Ahmad[1], Xavier Ropagnol[1,2], and François Blanchard[1]

[1]Département de Génie Électrique, École de Technologie Supérieure (ÉTS), Montréal, Quebec H3C 1K3, Canada

[2]Institut National de la Recherche Scientifique, EMT Research Center, Varennes, Quebec J3X 1P7, Canada

Paper published in *Journal of the Optical Society of America B*, January 2026
available at https://doi.org/10.1364/JOSAB.578338

4.1 Chapter overview

This chapter presents the design, numerical analysis, fabrication, and experimental characterization of free-standing polarization-sensitive THz FSS based on rectangular and C shape slot. Unlike the amplitude-only reconfigurable FSS architectures discussed in previous chapters, the structures investigated here exhibit strong polarization-dependent transmission responses arising from geometrical anisotropy and asymmetric current distributions. The demonstrated polarization-selective amplitude contrast establishes the rectangular slot FSS (R-FSS) designs as effective frequency-selective polarizers, forming a key enabling component for the intensity-based terahertz polarimetric imaging systems developed in subsequent chapters of this thesis. In R-FSS, the transmitted amplitude follows Malus' law with polarization rotation, whereas the peak center frequency remains invariant. While C-shaped slot FSS supports polarization-dependent single, distinct resonances with high modulation depth and well-defined spectral separation, suitable candidates for polarization dependent tunable band-pass filter.

4.2 Abstract

In this study, we experimentally and simulatively investigated the characteristics of two distinct frequency-selective surfaces (FSS) sensitive to terahertz (THz) wave polarization.

These structures were fabricated using a laser-cutting technique on stainless steel. The unit cells of the two studied FSS are rectangular-slot and C-slot respectively. Analysis of the azimuthal dependence from 0° to 90° of the C-slot array FSS confirms the shift of the peak center frequency of the normalized transmission towards a higher value, and with an intermediate condition between its two modes of operation for the median values, enabling dual-frequency operation with high polarization selectivity. In contrast, for the rectangular-slot array FSS, no frequency shift was observed as a function of rotation angle, only an attenuation of transmission at peak center frequency, similar to the response of a frequency-selective polarizer. This study identifies potential candidates for polarization-dependent detection applications, such as THz multi-spectral polarimetry and THz polarimetric imaging.

4.3 Introduction

In recent years, a wide range of terahertz (THz) applications have emerged, leveraging polarization properties for a variety of purposes, including medical imaging and diagnostics, non-destructive testing, the study of birefringent properties of materials, and the dynamic measurement of refractive index variations (Yang et al., 2024; Zhang et al., 2010; Nakagawa et al., 2022; Van Der Valk et al., 2005; George et al., 2012; Blanchard et al., 2014b). To access information on the polarization state of a THz wave, several approaches are possible, but most commonly through the coherent detection of the electric field using time-domain methods for spectroscopy (Neu & Schmuttenmaer, 2018) and imaging purposes (Blanchard et al., 2013). Alternatively, a simple method consists of using polarization-dependent filters (Li et al., 2017) in between the emitter and receiver. For example, frequency-selective surfaces (FSS) may have a design featuring polarization-sensitive response (Chen et al., 2015), offering excellent control over electromagnetic wave propagation to extract the specific polarimetric response at a given frequency. At THz frequencies, a polarization-sensitive FSS (PS-FSS) consists of a two-dimensional (2D) structure whose geometric size of its unit cell is comparable to the operating wavelength (Ebrahimi et al., 2015) and is usually asymmetrical or oriented in a particular way, favoring one polarization over another to ensure optimum polarization sensitivity.

Over the past several decades, quasi-optical filters based on periodic metallic structures have been extensively developed in the microwave and mm-wave ranges for spectral shaping,

dichroic separation and multi-band operation (Beruete et al., 2004; Aznabet et al., 2008; Zhang et al., 1991; Kim et al., 2017). These concepts have been adapted to the THz domain, using split-ring resonators (SRR) (Debus & Bolivar, 2007), graphene-based active layers (Zhu et al., 2014; Ma et al., 2021), and cross-shaped structures (Yan et al., 2016; Voisiat et al., 2011; Ferraro et al., 2017b). Despite these advances, achieving precise and robust polarization control within specific THz bands remains a notable challenge. This limitation becomes particularly critical in applications requiring multi-spectral or frequency-resolved polarization measurements under broadband THz illumination, where existing structures often lack sufficient polarization contrast and tunability. To develop polarization-sensitive THz-FSS, various strategies such as single-band to dual-band resonances (Lin et al., 2019; Xu et al., 2021), polarization-dependent tunable triple-band absorber (Zhan & Fan, 2023), narrow-band polarization modulators (Chen et al., 2013), dual-band polarization converters (Li et al., 2019), and single- to dual-band polarizer (Vegesna et al., 2014), have been explored. However, existing approaches are often hindered by their reliance on either complex multi-layer structural designs, or the use of high-cost fabrication methods like photolithography (Chen et al., 2013; Li et al., 2019; Vegesna et al., 2014). For instance, FSS with polarization selection and dual-band polarization conversion characteristics has been reported by (Li et al., 2019). The top and bottom metallic periodic arrays in this FSS give band-pass and band-stop properties for TE and TM polarized incidences, respectively as well with some conditions followed by this analyzed FSS could be used as dual-band linear-to-circular polarization conversion. Additionally, by integrating metallic resonators with vanadium dioxide (VO_2) patches, Subash et al. proposed a design technique to build a reconfigurable THz FSS polarizer with an extinction ratio of ~25 dB as the temperature is varied from 28° C to 80° C (Vegesna et al., 2014). However, such reconfigurability usually requires multi-layer structures and external stimuli, adding to the complexity of the system.

A potential solution lies in the use of single-layer anisotropic FSS geometries, such as rectangular and C-shaped designs, which could improve polarization sensitivity and modulation depth without complicated manufacturing procedures. To date, several studies have been reported using C-shaped (Lee et al., 2006; Sahu & Chaudhuri, 2024; Zhang et al., 2013) and rectangular shape structures (Hong et al., 2017; Lee et al., 2017; Hong et al., 2013)

in THz region. However, the polarization-dependent multiple-resonance behavior of C-shaped structures can be disadvantageous for applications that require a single, well-defined spectral response for each polarization state, such as reconfigurable or tunable band-pass filters, single-frequency modulators, and systems relying on well-isolated polarization channels where precise spectral selectivity and uniformity are essential. In contrast, the rectangular shape FSS structures reported in (Hong et al., 2017; Lee et al., 2017; Hong et al., 2013) demonstrated relatively low transmission contrast (ΔT_{xy}), with maximum values of approximately 55%, 30%, and 41% as of reported in (Hong et al., 2017), (Lee et al., 2017), and (Hong et al., 2013), respectively. However, for frequency-selective polarizer applications, a high contrast in transmission between horizontally and vertically polarized THz waves is beneficial to ensure robust polarization selectivity and improved functional performance. Importantly, fabrication of such components commonly involves expensive photolithography, predominantly requiring dielectric substrates (Chen et al., 2013; Vegesna et al., 2014; Zhang et al., 2013; Hong et al., 2017; Lee et al., 2017; Hong et al., 2013). As a result, dielectric losses and time-domain echoes are introduced, impairing overall system performance. A promising solution is to use free-standing polarization-sensitive FSSs and can be efficiently fabricated by laser cutting technique. Laser cutting offers several advantages compared with other fabrication techniques such as photolithography, inkjet printing, or screen printing. It is a mask-free, rapid-prototyping process that allows precise patterning of metallic or dielectric films without requiring cleanroom facilities. Importantly, laser cutting enables the fabrication of free-standing, substrate-free FSS structures, which is particularly attractive for THz-TDS measurements because it minimizes unwanted echoes and reflections that normally arise from dielectric substrates. To date, laser-cutting technology has been widely employed to efficiently fabricate free-standing THz components, including wire-grid polarizers (Born et al., 2015), Fabry–Perot cavity antennas (Aqlan et al., 2021a), bandpass filters (Born et al., 2015; Sebastian et al., 2024), asymmetric SRR (Taleb et al., 2020), periodic array of circular apertures (Cao & Nahata, 2004) and extraordinary-transmission arrays (Camacho et al., 2020). To the best of our knowledge: (1) no free-standing THz frequency-selective polarizer with high transmission contrast has been reported; and (2) no substrate-free polarization sensitive C-shaped FSS has

been shown to produce a single, distinct resonance in the specific THz bands for each polarization state with high modulation depth.

In this work, we present the design, simulation, fabrication, and characterization of polarization-sensitive THz FSSs based on rectangular slot FSS with non-uniform spacing between two consecutive slots along *x* and *y* axes and C-slot FSS with extended gaps. The analyzed FSS models are realized by creating an array of slots from two distinct structures on stainless steel. Variations in rotation and geometric shape are evaluated. Since the manufacturing process is based on laser cutting, the FSS is realized as a complementary structure, in which each unit cell consists of air apertures in a metallic sheet. According to experimental results, modulation depths of around 97% are achieved at operating frequencies of 0.415 THz and 0.310 THz for rectangular-slot FSS and C-slot FSS, respectively. It is also evident that there is good agreement between the simulated results and the measured data. This analysis also discusses the reconfigurable approach of these two proposed FSSs for a future THz polarimetric measurement prototype.

4.3.1 Contribution

Key contributions of this work to the development of THz polarization-sensitive FSSs include:

- By utilizing symmetric and asymmetric unit cell configurations, illustrate two distinct mechanisms for achieving polarization selectivity: amplitude contrast (R-FSS) and spectral shift (C-FSS).
- The C-slot FSS is optimized in gap spacing to yield a single, distinct resonance for each vertical and horizontal polarization, providing a substantial frequency separation between the two states.
- A generalized design model for the C-slot FSS is demonstrated, enabling the estimation of design parameters that yield a resonance frequency doubling when the electric field orientation shifts from perpendicular to parallel with respect to the long axis of C structures.
- The optimization of the rectangular-slot FSS structure is directed toward the development of a free-standing frequency selective polarizer with enhanced variation in transmission (ΔT_{xy}) by tuning the periodicity along the *x*- and *y*-axes of the array.

• The free-standing nature of both FSS structures avoids losses typically introduced by dielectric substrates. To do so, laser cutting technique was employed for fabrication.

4.4 Design methodology and simulation results

4.4.1 Rectangular-slot FSS (R-FSS)

The schematic of the proposed R-FSS with design parameters is shown in Fig. 4.1(a). The length and width of each rectangular slot are designated by the letters *l* and *w*, respectively. In addition, the parameters *x* and *y* indicate the separation between two successive slots in horizontal and vertical orientation respectively. The thickness of the R-FSS was chosen as 125 μm, according to the available rigid stainless-steel sheets compatible with the laser-cutting process. The slot width (*w*) is set equal to the slot spacing (*x*) along the *x*-axis to maintain a balanced metal–aperture ratio. Depending on the orientation of the rectangular slot, the R-FSS may exhibit polarization-sensitive behavior at a certain peak center frequency. This inherent polarization selection enables the structure to function as a frequency-selective polarizer (FSP). The anisotropic geometry of proposed FSP allows to selectively transmit THz waves whose electric field is perpendicular to the long axis of the slots, while suppressing components parallel to it.

The resonance response of the rectangular-slot FSS can be interpreted using a simplified LC framework, which offers clear physical insight into the roles played by the slot dimensions. The slot length primarily determines the effective inductive path associated with the circulating surface currents, whereas the slot width governs the effective capacitance through the electric-field coupling across the aperture. Accordingly, the resonance frequency of the rectangular slot can be approximated using the following relation:

$$f_{res} = \frac{1}{2\pi\sqrt{LC}} \tag{4.1}$$

In a thin metal sheet containing rectangular apertures, the circulating surface currents flow predominantly along the long edges of each slot, making the effective inductance *L* strongly dependent on the slot length (*l*). Increasing *l* extends the current path and increases the stored magnetic energy, whereas the slot width *w* mainly influences the effective capacitance C

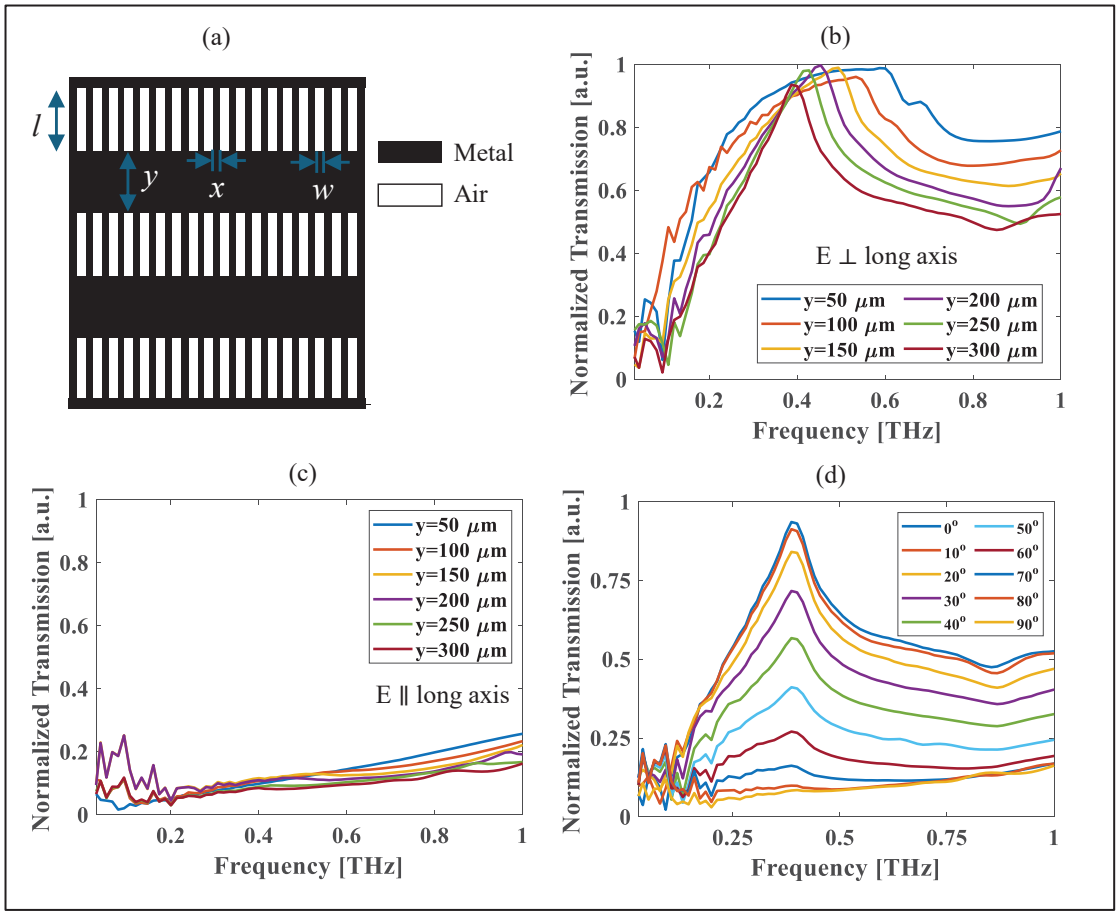

Figure 4.1 (a) Schematic of the proposed R-FSS; simulated normalized transmission spectrum for (b) $\alpha_r = 0^\circ$ and (c) $\alpha_r = 90^\circ$ (l=400 μm, w=50 μm, x=50 μm, and y is varied); (d) normalized transmission as a function of relative polarization angle (l=400 μm, w=50 μm, x=50 μm, and y=300 μm)

through the electric-field coupling across the aperture. Consequently, the resonance frequency is governed primarily by the slot length and can be approximated as:

$$f_{res} \propto \frac{1}{l} \tag{4.2}$$

To predict the behavior of the analyzed R-FSS, we used the Lumerical FDTD (Finite-Difference Time-Domain) simulation software. Perfectly matched layer (PML) boundaries were applied along all three axes to suppress unwanted reflections. In the mesh settings of FDTD simulation, an auto non-uniform mesh was used to balance accuracy and computational efficiency. To further enhance accuracy around the subwavelength apertures, a mesh-override

region was applied over the sample area, enforcing finer spatial resolution along all three axes. Simulations were performed using a Gaussian broadband THz source as the emitter and a time-domain monitor as the detector, with the free-standing FSS positioned between them. The metallic component of the FSS was modeled as stainless steel with its corresponding material properties. Time-domain data were recorded using a time monitor that captured 4096 uniformly spaced temporal snapshots. Following this, a fast Fourier transform (FFT) was applied to the time-domain data to obtain the corresponding spectral amplitude. Normalized transmission (NT) is calculated as follows (Ahmad et al., 2024):

$$NT = \frac{T_{sample}}{T_{ref}} \tag{4.3}$$

where T_{sample} and T_{ref} are the FFT amplitude of the analyzed sample and without sample as reference respectively.

In addition, the variation of transmission (ΔT_{xy}) and modulation depth (MD) could be calculated using the following equation:

$$\Delta T_{xy} = T_{0^\circ} - T_{90^\circ} \tag{4.4}$$

$$MD = \frac{T_{0^\circ} - T_{90^\circ}}{T_{0^\circ}} \tag{4.5}$$

where T_{0° and T_{90° are the normalized transmission at 0˚ and 90˚ relative polarization angle (α_{r}) respectively.

Figure 4.1(b) shows the normalized transmission response as a function of distance between two rectangular slots along the *y* axis. In this figure, the design parameter *l* is fixed as 400 µm, while *w* and *x* are fixed at 50 µm, and the corresponding polarization of the incident wave is horizontal (α_{r}=0˚), i.e., perpendicular to the long axis of the aperture. As the spacing *y* between the two slits increases, a resonance peak appears, exhibiting a response characteristic of a bandpass filter. It is also noticeable that as the *y* parameter is increased, the corresponding peak center frequency is shifted to a lower frequency. At *y*=300 µm, the normalized transmission coefficient reaches 0.92 at the maximum center frequency of 0.4 THz. At this spacing, the slot

length (l) is 400 µm, which explains the maximum transmission observed at a frequency corresponding to approximately $\lambda/2$, i.e., 0.4 THz, which also aligns with the approximate aperture-resonance condition (García-Vidal et al., 2005):

$$f_{res} \approx \frac{c_0}{2l} \tag{4.6}$$

where l and c_0 are the effective length of the long axis and the speed of light respectively.

Figure 4.1(c) illustrates the case of an incident THz wave with vertical polarization (α_r=90˚). With this orientation, the electric field is parallel to the long axis of the aperture, the signal is strongly attenuated for all values of y, as expected for a wire grid polarizer (Mansourian et al., 2021). There is a slight variation in the normalized transmission coefficient at peak frequency as y increases. For y=300 µm, the normalized transmission coefficient at 0.4 THz is 0.08. For case-1, we obtain the optimized parameters as, l=400 µm, w=50 µm, x=50 µm, and y=300 µm. Thus, the final dimensions were obtained through a brief manual iterative refinement to achieve the targeted polarization-dependent transmission. According to the simulation results, the modulation depth and variation in NT in this configuration is 91.3% and 0.84 at 0.4 THz respectively. Subsequently, the relative polarization angle was varied from 0° to 90° with 10° steps, a gradual decrease in transmission is observed while the peak center frequency is almost constant as shown in Fig. 4.1(d). This behavior is in agreement with Malus' law by satisfying the following equation (Lee et al., 2017):

$$T(\alpha_r) = T_0 \cos^2(\alpha_r) \tag{4.7}$$

Where, T_0 is the maximum transmission obtained at α_r=0°. Following to investigate the impact of structural scaling on resonance behavior, we systematically varied the optimized geometric parameters while maintaining a constant filling factor. Specifically, the design parameters of case-1 were increased by 10%, 25%, and 75% to form case-2, case-3, and case-4, respectively. This adjustment extended the slot length (l) to 440 µm, 500 µm, and 700 µm. As a result, a progressive downward shift in the resonance frequency was observed, with peak center frequencies shifting to 0.360 THz, 0.320 THz, and 0.226 THz, respectively. This frequency shift is primarily attributed to the increase in the structure's effective inductance (L), which

depends strongly on the slot dimensions. In the R-FSS, increasing the slot length extends the current path around the aperture, leading to a higher inductive loading and a corresponding downward shift in the resonance frequency, consistent with the LC-resonance behavior of rectangular-slot FSS structures. Although changes in slot geometry also influence the effective capacitance (*C*), the dominant contribution to the resonance shift in this case arises from the inductive term.

4.4.2 C-slot FSS (C-FSS)

The C-shape resonator is well known and is often referred to as the split-ring resonator (Hao et al., 2024). It is a unit cell used in many types of metasurfaces or metamaterials (Lee et al., 2006; Sahu & Chaudhuri, 2024; Zhang et al., 2013; Shiri et al., 2023; Zhao et al., 2017; Blanchard et al., 2012; Papari et al., 2023). C-shaped structures support two resonant modes for horizontally polarized excitation, whereas vertical polarization typically yields a single predominant peak (Lee et al., 2006). Given the limited resolution of our laser-cutting system, we consider our C-shape resonator to be a frequency-selective surface rather than a metasurface. It's important to note that these anisotropic resonances are sensitive to the polarization of the input THz wave as well as the periodicity, length, width, and gap of the C-shape FSS.

Following that, the C-FSS was simulated using the finite-element method (FEM). The C-shaped FSS contains a curved air aperture into the metal, along with narrow slot regions and polarization-dependent LC-type current paths along the slot edges, all of which are more accurately resolved with FEM-based modeling (Ansys HFSS). The slitless circular shape (d=0 μm) mainly exhibits a single resonance at both polarization angles. This behaves like a bandpass filter with a peak center frequency of 0.275 THz, see Fig. 4.2(a). In Figs. 4.2(b-f), the addition of a gap (d) is studied numerically for polarization transition from perpendicular to the parallel orientation relative to the gap. Extending the gap (d) i.e. increasing the metal transition and setting the α_r=0˚ leads to the appearance of two strong resonances. When the element spacing is increased from 50 μm to 306 μm, the center frequency of the filtered response shifts to a higher frequency. This is explained by the reduced distance traveled by the electric field through the semicircular slot. Point to be noted in the case of d=306 μm, two

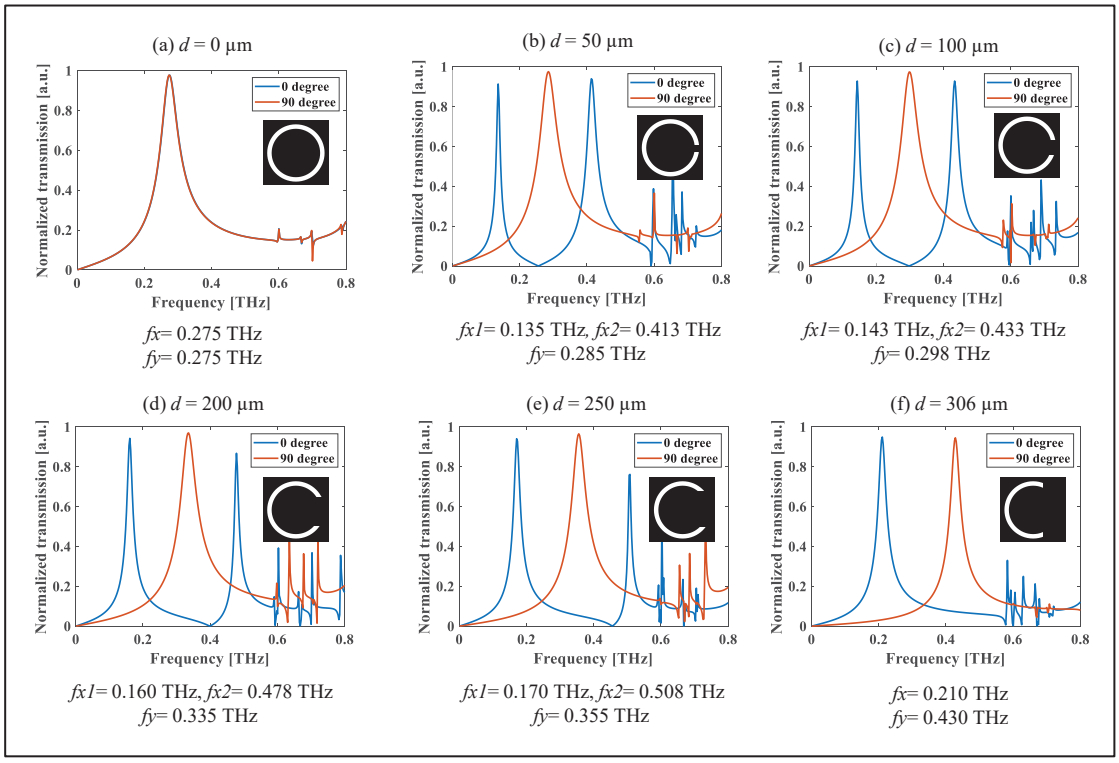

Figure 4.2 Simulation results of NT as a variation of gap (d) of C-FSS for both α_r = 0˚ and 90˚ with design parameters as a=400 µm and b=33.33 µm: (a) 0 µm; (b) 50 µm; (c) 100 µm; (d) 200 µm; (e) 250 µm and (f) 306 µm

edges are flattened as shown in inset of Fig. 4.2(f). It can also be seen that, in the case of a small gap, i.e. 50 µm, two dominant resonances are observed and as the gap increases, the second resonance progressively attenuates, resulting in a single dominant resonance peak. As the gap becomes larger, the weakened capacitive coupling suppresses the higher-order resonance, while the fundamental low-frequency mode governed by the longest current path under $\alpha_r = 0°$ excitation remains.

In contrast, for $\alpha_r = 90°$, the structure exhibits a single resonance at a frequency higher than the modified fundamental mode observed for $\alpha_r = 0°$. This produces the observed ordering, where $f_{90°}$ is higher than the surviving $f_{0°}$ resonance when the gap spacing in C-shaped aperture becomes wider. In Figs. 4.2(b-f), we also noticed the same behavior with a single resonance, whatever the gap size, from 50 µm to 306 µm. Additionally, as the gap (d) increases, the central

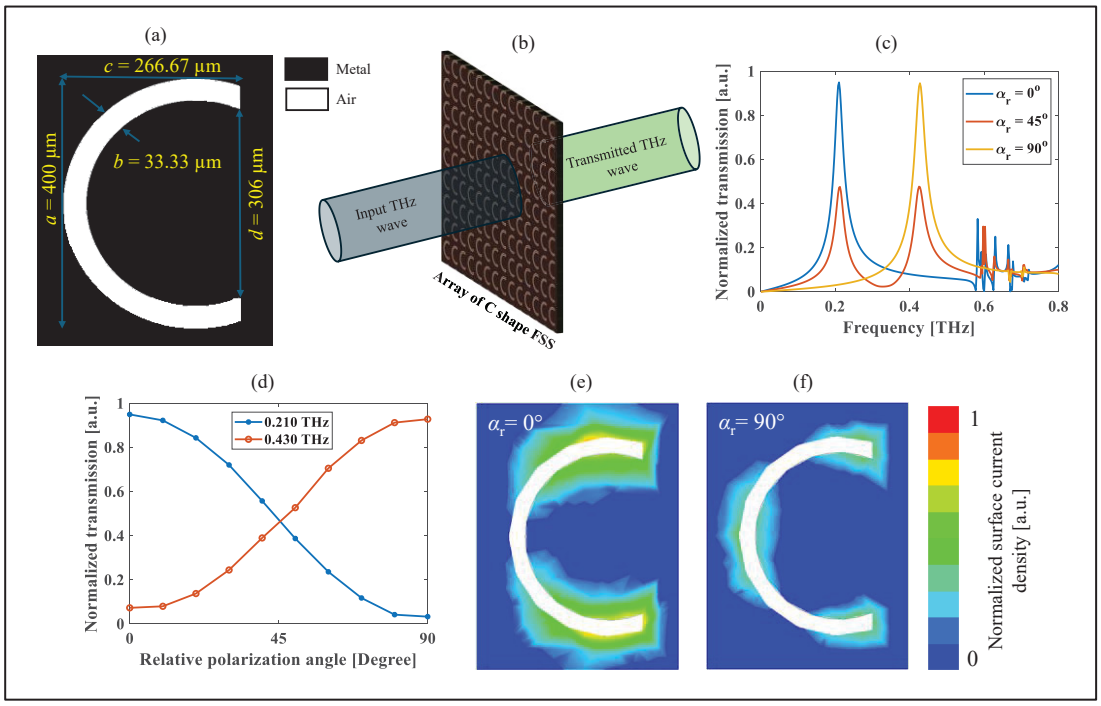

Figure 4.3 Schematic of (a) unit cell and (b) array of C-FSS; (c) simulation results of normalized transmission as a function of frequency for three different relative polarization angle such as 0˚, 45˚ and 90˚ (a=400 µm, b=33.33 µm, c=266.67 µm and d=306 µm); (d) simulation results of normalized transmission as function of polarization angle (from α_r=0° to 90° with 10° steps) at two different operating frequency of 0.210 THz and 0.430 THz; (e) simulated surface-current distribution for the C-slot FSS at a relative polarization angle of 0°; (f) corresponding surface-current distribution for a relative polarization angle of 90°

frequency of the corresponding peak shifts to a higher frequency, from 0.285 THz to 0.430 THz.

Based on these observations, we considered an optimum gap (d) size of 306 µm for further analysis. Next, the effect of slot width (b) on the transmission characteristics is investigated and illustrated in Fig. S4.1 (see supplementary information-section 1). For α_r=0°, an increase in slot width leads to a noticeable rise in residual transmission at higher frequencies. By balancing the trade-off between maximizing peak transmission and minimizing residual transmission, optimal design parameters were selected. Indeed, the optimized gap width (d) and slot width (b) allow the appearance of only two distinct frequencies depending on the

polarization of the incident THz wave. This case is simpler to study than a transmission with three interrelated frequency components, and could therefore be used as a tunable, polarization-sensitive bandpass filter.

A schematic example diagram of the simulated C-FSS is presented in Figs. 4.3(a,b). In the following step, we have analyzed the dependence relative to the polarization of the incident THz wave. At $\alpha_r = 0^\circ$, the resonance is 0.210 THz with NT= 95 %, whereas it is 7% at 0.430 THz. On the other hand, at $\alpha_r = 90^\circ$, the resonance was noticed at 0.430 THz with NT= 94 % whereas at 0.210 THz the transmission is about 3%. At $\alpha_r = 45^\circ$ almost 50% of peak transmittance is noticed at both resonances, see Figs. 4.3(c,d). The corresponding MD at f_{0° and f_{90° are 0.968 and 0.92, respectively. Here f_{0° and f_{90° represent the peak center frequency for 0˚ and 90˚ polarization angle, respectively.

From simulation analysis, it is evident that the peak center frequency for $\alpha_r = 90°$ is almost doubled compared to $\alpha_r = 0°$. To validate this statement, we also carried out a simulation analysis, by decreasing (case-1) and increasing (cases-3 and 4) the design parameters (a, b, c, d) while maintaining the same fill factor. Finally, based on the simulation analysis, we defined optimized parameters for four different cases and summarized them in table 4.1.

Table 4.1. Optimized parameters of C-FSS

Type	***a* (µm)**	***b* (µm)**	***c* (µm)**	***d* (µm)**	f_{0° **(THz)**	f_{90° **(THz)**
Case-1	300	25	200	229.5	0.281	0.575
Case-2	400	33.33	266.67	306	0.210	0.430
Case-3	500	41.66	333.33	382.5	0.168	0.348
Case-4	600	50	400	459	0.141	0.29

In all cases, we noticed that the behavior of $f_{90^\circ} \approx 2f_{0^\circ}$ was still valid. What's more, when we increase the dimensions of the design parameters, we notice that the central frequency of the peak is shifted to a lower frequency, as expected. It is also noteworthy that by selecting parameters as $c = \frac{2a}{3}$ and $b = \frac{a}{12}$, a single-peak resonance can be achieved. In addition to the four primary cases discussed, further numerical investigations were conducted by varying

design parameters to develop the generalized model, as presented in the supplementary information-section 2. For all configurations, the ratio $\frac{\lambda_{0^\circ}}{d}$ remains close to 4.6, whereas $\frac{\lambda_{90^\circ}}{d}$ is approximately 2.25 (see Table S4.1: supplementary information). Where λ_{0° and λ_{90° represent the peak resonance wavelength for $\alpha_r = 0^\circ$ and 90° respectively. This relationship can be used to determine the appropriate design parameters for achieving a specific peak resonance frequency.

Subsequently, the normalized surface-current distributions at the respective resonance frequencies for $\alpha_r = 0°$ and 90° are presented in Figs. 4.3(e–f). For $\alpha_r = 0°$, the incident electric field is directed across the opening of the C-shaped slot, strongly exciting the two vertical arms of the structure. This drives charge buildup and intense surface currents concentrated at the inner corners of the slot, giving rise to two dominant current-density hotspots. In contrast, for $\alpha_r = 90°$, the electric field couples primarily along the curved segment of the C-slot. These distinct current patterns highlight how the asymmetric geometry of the C-slot supports different polarization-dependent resonant pathways for the two excitation states.

4.5 Fabrication and experimental setup

In our work, both the C-FSS and R-FSS structures were fabricated using an LPKF ProtoLaser U3 system. Stainless steel was selected as the metal sheet for laser cutting because it strongly absorbs laser radiation, enabling efficient and precise machining with relatively low laser power. Electromagnetically, stainless steel behaves as a near-perfect reflector in the THz regime, making it well suited for realizing free-standing metallic FSS structures. The laser used for cutting is based on a diode-pumped YAG with a wavelength and focal beam diameter of 355 nm and 15 μm respectively. The minimum achievable cutting width is ~18 μm, which is sufficient to accurately realize subwavelength slot features in the lower THz band. In addition, the scan-to-scan positional precision of the laser machining system is approximately ±2 μm, ensuring excellent dimensional repeatability across the patterned area.

Experimental characterization of the fabricated FSS was carried out using a commercial THz time-domain spectrometer (THz-TDS), the Toptica TeraFlash pro system, and the experimental schematic and photograph are shown in Fig. 4.4(a,b) respectively. The THz

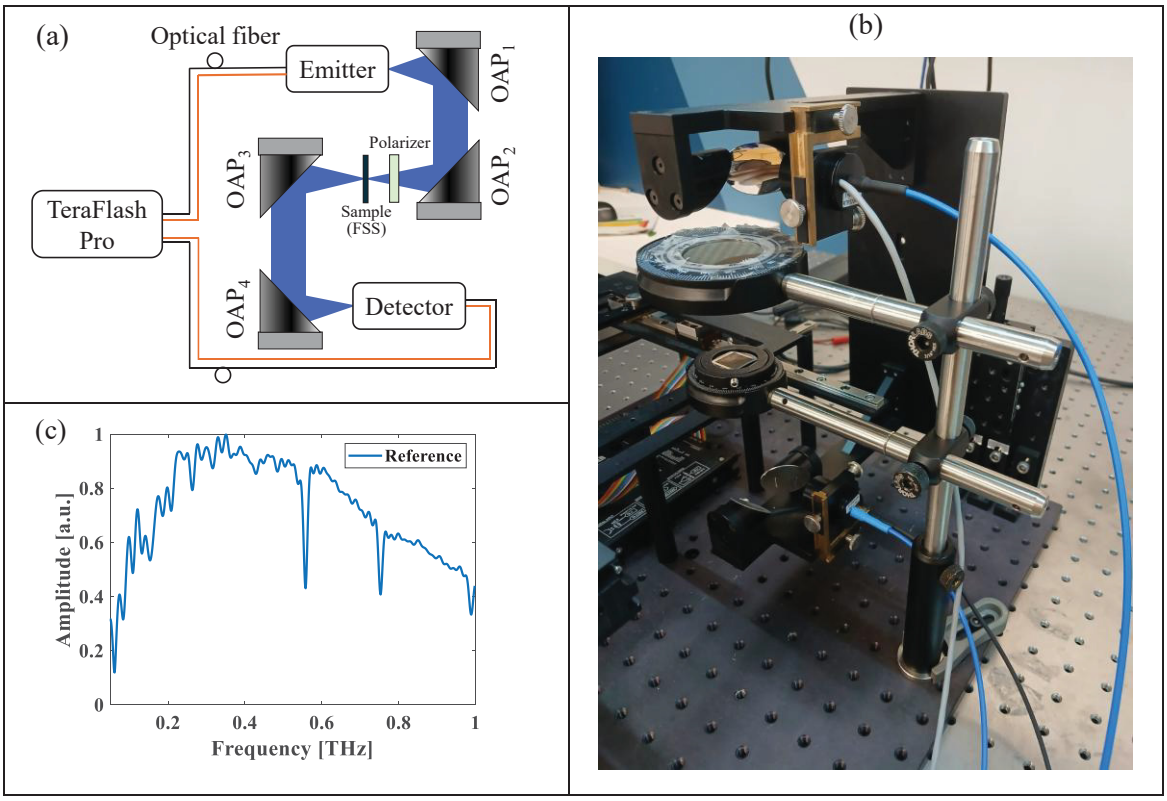

Figure 4.4 (a) Schematic layout of the experimental setup; (b) photograph of the THz-TDS system used for characterization; and (c) reference transmission spectra measured without any sample inserted

signal is emitted and detected by photoconductive antennas (PCAs), each coupled to a 1560 nm fiber and equipped with a rear-mounted integrated silicon lens. The system provides broadband spectral coverage from 0.1 to 6 THz and achieves a dynamic range of ~100 dB. The emitted THz beam has a diameter of roughly 1 mm at 1 THz, and as the beam waist scales inversely with frequency ($w \propto 1/f$), the spot size increases at lower THz frequencies. To ensure that multiple FSS unit cells are uniformly illuminated, the sample was positioned near the focal plane where the beam is most tightly confined. THz waves are guided by 4 off-axis parabolic mirrors (OAP) and a focusing position is defined between OAP2 and OAP3 where we placed the sample (FSS). Also, a wire-grid polarizer was placed before the sample to ensure that only a single linear-polarization component illuminates the structure, enabling polarization-resolved measurements. Each recorded time-domain waveform spans 50 ps and the corresponding reference spectrum, obtained without placing any sample at the focal position,

is shown in Fig. 4.4(c). This spectrum represents the system's intrinsic response and is used to normalize the sample's transmission.

4.6 Experimental results of the R-FSS

The microscopic image of the fabricated rectangular slot FSS (case-1) is depicted in Fig. 4.5(a). The thickness of the fabricated R-FSS is 125 µm. In our experimental analysis for ease, we choose to rotate the sample instead of changing the polarization angle of the emitter as done in the simulation analysis. Fig. 4.5(b) shows the transmission characteristics of the fabricated R-FSS (case-1) as a function of relative polarization. It is seen that for α_r=0˚, the transmission characteristics behave as a band-pass filter with a peak center frequency at 0.415 THz and the operating full width at half maximum (FWHM) bandwidth of 250 GHz. The peak transmission

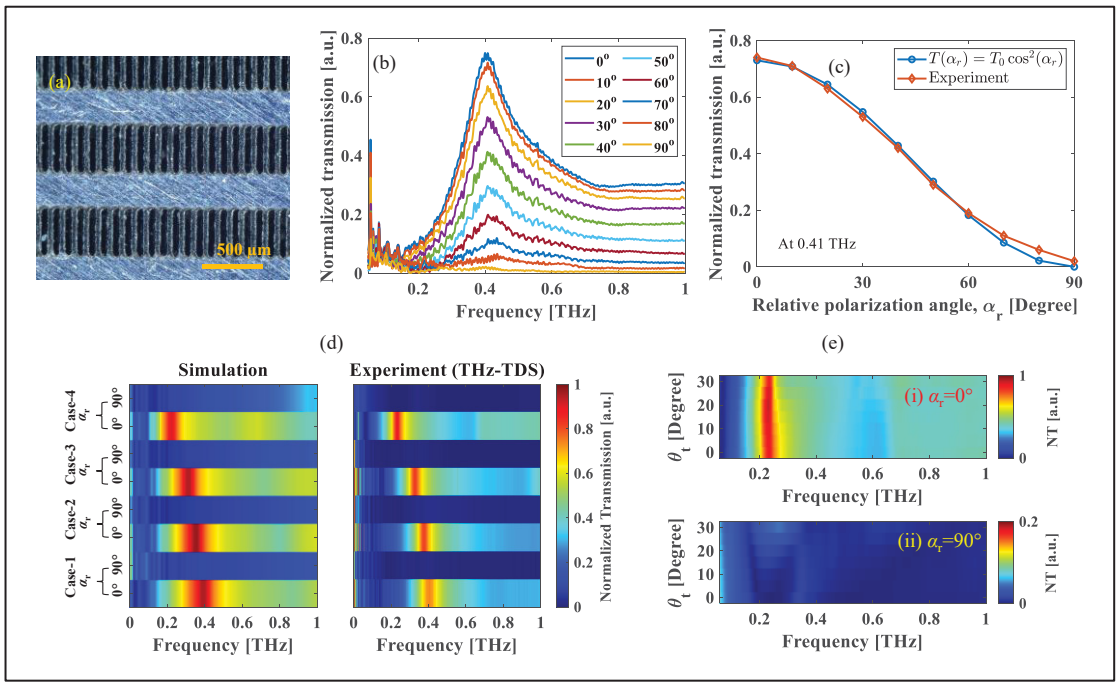

Figure 4.5 (a) Microscopic images of R-FSS (case-1); (b) normalized transmission for different rotation angles from 0˚ to 90˚ (R-FSS dimensions: *l*=400 µm, *w*=50 µm, *x*=50 µm, *y*=300 µm); (c) the analysis between theoretical and experimentally obtained azimuthal angle dependent transmission characteristics for case-1 at 0.41 THz; (d) side-by-side comparison of the simulated and experimentally obtained normalized transmission spectra for the R-FSS, evaluated across the four fabrication cases (case-1 to case-4); (e) angular-tilt dependence of the on-axis normalized transmission for the R-FSS (case-4): (i) α_r=0° and (ii) α_r=90°

coefficient becomes 0.75 for 0˚ relative polarization angle. By rotating the FSS, the polarization of the incident wave becomes gradually parallel to the *y* direction and then the transmission is gradually attenuated. At 45˚ the transmission becomes almost half compared to 0˚ rotation. And finally, with 90˚ rotation the transmission coefficient becomes 0.02 at operating frequency 0.415 THz, blocking the incident THz wave. Which in turn exhibits a modulation depth of 97.3%. This characteristic illustrates that the analyzed R-FSS behaves as a frequency-selective polarizer or polarization dependent THz band-pass filter and could be useful for frequency-selective THz polarimetric systems. Furthermore, the azimuthal angle-dependent transmission characteristics at the peak center frequency are compared with the theoretical prediction from equation (4.7). The corresponding graphical analysis is illustrated in Fig. 4.5(c).

By modifying the design parameters (*l*, *w*, *x*, *y*), we can adjust the operating frequency of the proposed R-FSS. To validate this concept, we also manufactured three other R-FSS as defined in table 4.2 for cases 2, 3, and 4. The transmission characteristics measured at α_r=0° and 90° are presented in Fig. 4.5(d), together with the corresponding simulation results. A strong correlation is observed between the experimental data and the simulated responses, confirming the accuracy of the model. In summary, the center frequencies of cases-1, 2, 3, and 4 are 0.415 THz, 0.370 THz, 0.331 THz, and 0.230 THz, respectively. Also, for 0˚ azimuthal angle, the corresponding FWHM bandwidth of the band-pass filter becomes 250 GHz, 200 GHz, 180 GHz, and 150 GHz for cases-1, 2, 3, and 4, respectively. It is interesting to note that as the operating peak center frequency moved to a lower frequency, the corresponding FWHM bandwidth decreased, which in turn increased the quality factor (*Q*). Moreover, when there is

Table 4.2. Modulation depth of different cases of R-FSS

Type	f_{peak} **(THz)**	***MD***	***Variation in NT at f_{peak} (0˚ to 90˚)***
Case-1	0.415	0.973	0.73
Case-2	0.370	0.975	0.80
Case-3	0.331	0.988	0.83
Case-4	0.230	0.989	0.87

no rotation (0˚), the transmission coefficient at the peak center frequency gradually increases as the design parameters (l, w, x, y) are increased while maintaining the same filling factor. This shift is accompanied by a gradual transition toward lower frequencies, with the corresponding normalized transmission coefficients reaching approximately 0.82, 0.84, and 0.88 for cases-2, 3, and 4, respectively (at α_r=0°). Notably, in all cases, a 90˚ rotation completely blocks the THz signal, functioning as a wire grid polarizer in a cross-orientation relative to the emitter. Experimentally, the measured modulation depth (MD) for cases 2, 3, and 4 is 0.975, 0.988, and 0.989, respectively. In summary, table 4.2 presents the experimentally obtained peak center frequencies, variations in normalized transmission, and modulation depths for different R-FSS configurations.

Following, to assess the angular robustness of the structure, the R-FSS (case-4) was subsequently tilted up to θ_t = 30° with 5° steps in the x–z plane for both polarization configurations (α_r = 0° and 90°). As shown in Figs. 4.5(e(i-ii)), the normalized transmission exhibits minimal variation across the entire tilt range, demonstrating that the FSS maintains a highly stable on-axis response for moderate angular perturbations.

4.7 Experimental results of the C-FSS

The microscopic image of the fabricated extended gap C- FSS is depicted in Fig. 4.6(a). The C-FSSs were fabricated on a 75-μm stainless-steel sheet to accommodate its more delicate, narrowly spaced slot geometry. For case-1, at α_r=0° i.e., E field is perpendicular to the long axis of the C structure, the resonance frequency is observed at 0.31 THz (see Fig. 4.6(b)). In contrast, when the structure is rotated by 90° i.e., E field is parallel to the long axis of the C structure. This alignment shifts the resonance at higher frequency and for case-1, it increases to 0.64 THz. Following, we have characterized the C-FSS (case-1) experimentally with different relative polarization angles from 0˚ to 90˚ with 10˚ steps. As the rotation angle increases, a trade-off between the two operating frequencies becomes evident. At α_r = 45°, nearly identical transmission levels are observed at the two peak center frequencies. The comparison between the simulated and measured responses for different relative angles is presented in Fig. 4.6(c). Despite this good agreement in the expected physical behavior, a minor discrepancy is observed between simulation and experiment in terms of operating

Table 4.3. Modulation depth of 4 different configurations of C-FSS

Type	$f_{exp\text{-}0deg}$ (THz)	$f_{exp\text{-}90deg}$ (THz)	*MD* ($f_{0°}$)	*MD* ($f_{90°}$)
Case-1	0.31	0.64	0.966	0.848
Case-2	0.22	0.46	0.945	0.852
Case-3	0.17	0.35	0.921	0.876
Case-4	0.15	0.29	0.906	0.846

frequency and normalized transmission. This deviation can be attributed primarily to two factors. First, fabrication tolerances associated with the laser-cutting process, such as small dimensional deviations or edge roughness can shift the resonance frequency. Second, variations in beam alignment and sample placement during THz-TDS measurements can

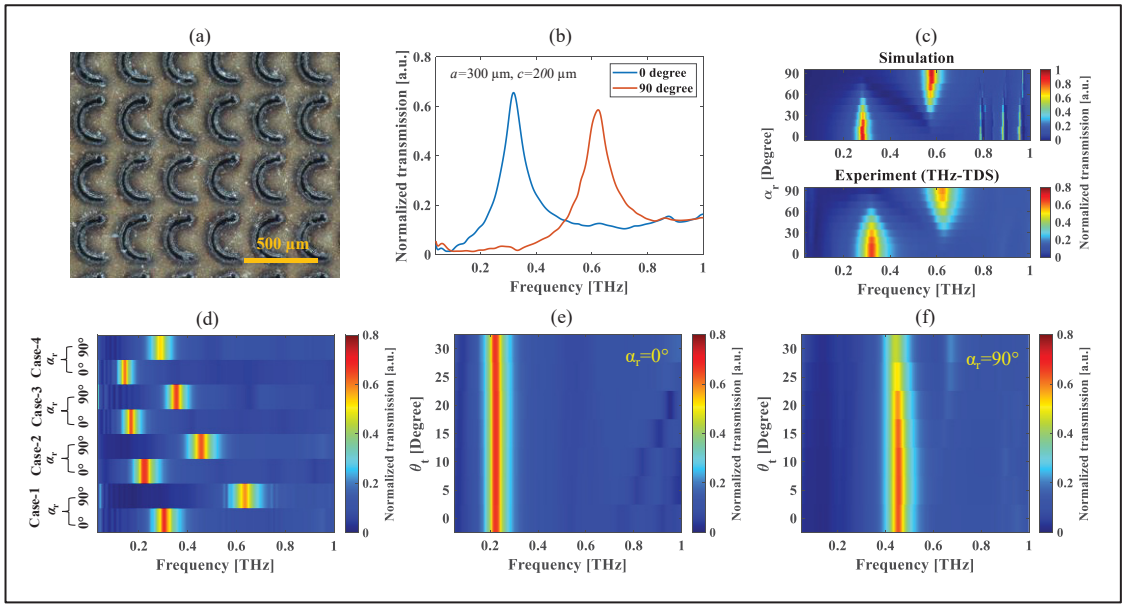

Figure 4.6 (a) Microscopic image of the fabricated C-FSS corresponding to case-1; (b) Measured normalized transmission spectra for two orthogonal polarization states (0° and 90°) demonstrating polarization-dependent resonance behavior; (c) comparative illustration of simulated and experimental responses for varying polarization angles from 0° to 90°, confirming the angular sensitivity of the C-FSS (case-1); (d) transmission characteristics for all four fabricated cases, highlighting performance differences under 0° and 90° excitations; effect of angular tilt on the on-axis normalized transmission of the C-FSS (case-2) for (e) α_r=0° and (f) α_r=90°

slightly modify the effective illumination conditions, thereby influencing the amplitude and resonance position. More importantly, in the simulations of C-FSS, a plane-wave excitation was employed, while the THz-TDS measurements use a Gaussian beam with a finite spatial profile. This difference in illumination leads to a slight residual transmission at higher frequencies in the simulated spectra, which is absent in the experimental results. Subsequently, by modifying the design parameters, we fabricated three additional C-FSS structures, with their parameters summarized in table 4.3.

The corresponding transmission characteristics for α_r=0˚ and 90˚ for cases 1 to 4 are shown in Fig. 4.6(d). At α_r=0˚, the peak center frequencies for cases 1, 2, 3, and 4 are 0.31 THz, 0.22 THz, 0.17 THz, and 0.15 THz, respectively. Under 90˚ rotation, these frequencies shift to 0.64 THz, 0.46 THz, 0.35 THz, and 0.29 THz, respectively. Also, based on the experimentally obtained and simulation results we developed a generalized model to predict resonance frequency at both orthogonal polarizations. The resonance frequency for α_r=0° and 90° is governed by following equations:

$$f_{0^\circ} \approx \frac{c_0}{2L_{slot}} \tag{4.8}$$

$$f_{90^\circ} \approx \frac{c_0}{L_{slot}} \tag{4.9}$$

Where L_{slot} demonstrates effective slot length and is quantified as $L_{slot} = a + c$. As the orientation shifts from 0˚ to 90˚, the peak transmission coefficient undergoes a distinct flip between f_{0° and f_{90°, with the peak center frequency nearly doubling in all cases. Subsequently, we calculated the modulation depth for each case using the equation (4.5) and the corresponding values are summarized in Tab. 4.3. From this analysis it is seen that, modulation depths at f_{0° is consistently higher than at f_{90°, a similar behavior also observed in simulations. This behavior can be attributed to the band-pass filtering characteristics, as observed in Fig. 4.6(b). The filtering response lacks a sharp roll-off; instead, a small residual transmission persists beyond the cut-off frequency into higher frequencies.

Following, an angular-stability analysis was carried out by tilting the sample in the *x–z* plane up to $\theta_t = 30°$ in increments of 5°. For $\alpha_r = 0°$, the incident electric field strongly drives the circulating current path along the C-shaped slot, allowing the resonator to remain efficiently excited even under moderate tilt (see Fig. 4.6(e)). As a result, the normalized transmission shows minimal variation across the full angular range, indicating robust on-axis angular stability. In contrast, for $\alpha_r = 90°$, significant reduction in normalized transmission observed at $\theta_t > 20°$ due to the reduction in the effective electric-field component interacting with the structure and becomes more sensitive to angular tilt, as observed experimentally and depicted in Fig. 4.6(f).

4.8 Comparison with prior work

The comparison of proposed designs with prior published work in terms of several output parameters is demonstrated in table 4.4. By optimizing the asymmetric array spacing along the *x* and *y* axes, our proposed R-FSS achieves maximum transmission variation of 87% for case-4 as the relative polarization angle changed from 0° to 90°, which is greater than the reported polarization-sensitive FSS (Hong et al., 2017; Lee et al., 2017; Hong et al., 2013), also employed inexpensive and simple fabrication procedure as compared to (Chen et al., 2013; Li et al., 2019; Vegesna et al., 2014; Hong et al., 2017; Lee et al., 2017; Hong et al., 2013). More importantly, no requirement of external stimuli as used in (Vegesna et al., 2014). Another important parameter for FSS modulator is the single frequency resonance. In (Chen et al., 2013), authors reported single reflection resonance peak at 45° and 135° polarization angle with a certain gap in operating frequency. However, in that work modulation depth was not considered during investigation and suffers from complex design and expensive fabrication tools. By considering four parameters such as having a single transmission resonance peak at vertical or horizontal polarization independently, inexpensive fabrication tool, free-standing structure, and enhanced modulation depth, the proposed optimized C-FSSs perform well as compared to (Chen et al., 2013; Lee et al., 2006; Sahu & Chaudhuri, 2024; Zhang et al., 2013). The proposed free-standing C-FSS exhibits polarization dependent resonance with $f_{0°} = 0.31$ THz and $f_{90°}=0.64$ THz for case-1. Notably, the corresponding modulation depths reach 96.6% at $\alpha_r=0°$ and 84.8% at $\alpha_r=90°$, demonstrating strong polarization selectivity.

Table 4.4. Comparison of proposed polarization sensitive FSS with others' work

Ref.	**Design shape**	**Fabrication technique**	**Material**	**Substrate**	**Operating frequency**		**Single f_{peak} in each polarization**	**MD / variation in transmission (ΔT_{xy})**
(Chen et al., 2013)	Electric LC	Semiconductor processing technology	Copper	Polyimide	45°: 0.94 THz	135°: 0.57 THz	Yes	----
(Lee et al., 2006)	C-shape	Femtosecond laser machining	Aluminium foil (17 μm)	-----	Horizontal: 0.28 THz & 0.70 THz	Vertical: 0.62 THz	No	-----
(Sahu & Chaudhuri, 2024)		-----	Copper	-----	TM: 3.7 THz and 11.2 THz	-----	No	-----
(Zhang et al., 2013)		Photolithography	Aluminium	Si	+45°: 0.77 THz	-45°: 0.35 THz and 1.03 THz	No	-----
(Hong et al., 2017)	Rectangular shape		AgNW films	Quartz	0.63 THz		N/A	ΔT_{xy} =~55%
(Lee et al., 2017)			Thin gold film (150 nm)	Si	0.92 THz			ΔT_{xy} =~30%

Table 4.4. Comparison of proposed polarization sensitive FSS with others' work (continued)

Ref.	Design shape	Fabrication technique	Material	Substrate	Operating frequency	Single f_{peak} in each polarization	MD / variation in transmission (ΔT_{xy})
(Hong et al., 2013)			SWNT films	Si	0.28 THz, 0.38 THz, and 0.57 THz		ΔT_{xy} =~10%, 12%, and 24%
				PDMS	0.4 THz		ΔT_{xy} =~41%
(Li et al., 2019)	Parallel and series LC resonators (Total layer=6)		Aluminum	BCB polymer as spacer	0.62 THz		----
(Vegesna et al., 2014)	Cross shape		Gold and VO_2	Sapphire	0.47 THz		----
This work	Rectangular slot	Laser cutting	Stainless steel	No substrate (free-standing)	Case-1 0.415 THz Case-2 0.370 THz Case-3 0.331 THz Case-4 0.230 THz		ΔT_{xy}= 73% ΔT_{xy} = 80% ΔT_{xy} = 83% ΔT_{xy} = 87%
	C-slot				f_{0° / f_{90° Case-1 0.31 THz / 0.64 THz Case-2 0.22 THz / 0.46 THz Case-3 0.17 THz / 0.35 THz Case-4 0.15 THz / 0.29 THz	Yes	*MD* 96.6% and 84.8% 94.5% and 85.2% 92.1% and 87.6% 90.6% and 84.6%

TM= Transverse magnetic, AgNW = silver nanowire, SWNT= Single-walled carbon nanotubes , As_2Se_3= Arsenic triselenide, BCB= Benzocyclobutene, PDMS= Polydimethylsiloxane, ---- = not reported

4.9 Discussion and conclusion

The two FSS geometries were deliberately chosen to examine how structural symmetry governs polarization-dependent behavior in the THz regime. R-FSS is a geometrically symmetric design in which anisotropy originates mainly from the elongated aperture, producing polarization-dependent amplitude variations at an essentially fixed resonance frequency. In contrast, C-FSS with extended gap possesses inherent structural asymmetry, resulting in markedly stronger anisotropy and enabling polarization-induced shifts in the resonance frequency.

In the case of the rectangular slot FSS with sufficient vertical separation ($y>x$) between the rectangular unit cells, a maximum transmission contrast (ΔT_{xy}) of 87% observed as the sample's rotation angle or the source's polarization angle shifts from 0˚ to 90˚. Similar to recent work on chopper-based multispectral frequency filtering (Sebastian et al., 2024), our proposed R-FSS offers a promising solution for realizing polarization-sensitive frequency-selective surfaces capable of extracting polarization-dependent spectral information by employing multiple units oriented at 0°, 45°, 90°, and 135° to obtain full Stokes parameter reconstruction. Moreover, the cost-effective fabrication of the proposed devices enables multi-spectral THz polarimetry and THz polarization imaging using a simple broadband source and intensity sensor.

In contrast, the C-FSS exhibits a single resonance peak in both vertical or horizontal polarization independently, functioning as a reconfigurable and polarization-sensitive bandpass filter. Notably, while the C-FSS has a lower transmission coefficient compared to the R-FSS, however it demonstrates a higher Q-factor, making it more frequency-selective. This makes it highly suitable for polarization-resolved THz spectroscopy, birefringence sensing, and tunable filtering applications. Importantly, both FSS structures are free-standing and fabricated using a straightforward commercial laser-cutting process on stainless steel, eliminating the need for substrates, lithography steps, or cleanroom infrastructure.

4.10 Supplemental document

4.10.1 By varying slot width in the C-shape frequency selective surface (FSS)

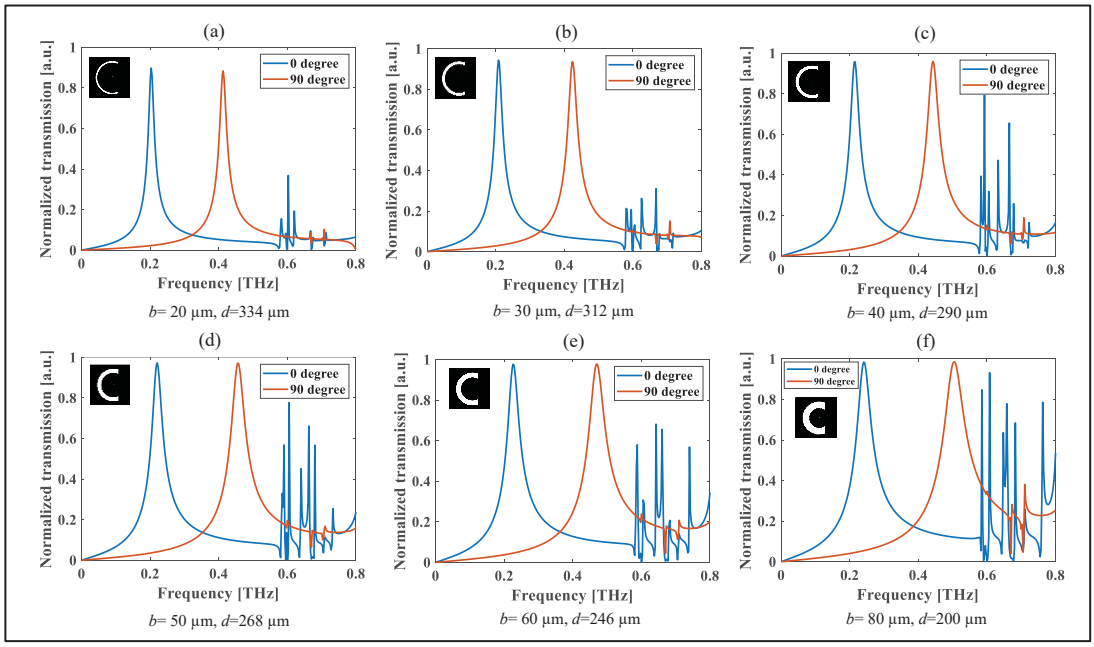

Figure S4.1 Simulation results of transmission characteristics as a variation of slot width (b) and gap (d) of C-FSS for both α = 0˚ and 90˚ with design parameters as *a*=400 µm and *c*=266.67 µm: (a) *b*= 20 µm , *d*=334 µm; (b) *b*= 30 µm , *d*=312 µm; (c) *b*= 40 µm , *d*=290 µm; (d) *b*= 50 µm , *d*=268 µm; (e) *b*= 60 µm , *d*=246 µm and (f) *b*= 80 µm , *d*=200 µm

The influence of slot width (*b*) and gap (*d*) in case-2: C-shape FSS (C-FSS) on transmission characteristics and peak center frequencies is illustrated in Fig. S4.1. The analysis indicates that increasing the slot width (*b*) results increase of residual transmission at higher frequencies for the 0° orientation. Additionally, a reduced slot width i.e. 20 µm leads to a noticeable drop in transmission at the peak center frequency.

4.10.2 Proportional variation of design parameters in the C-FSS

Subsequently, we performed a parametric simulation analysis by varying all design parameters of C-FSS proportionally. The corresponding results are summarized in table S4.1. From this investigation, several noteworthy conclusions can be drawn. For instance, when the design

parameters are set to $c = \frac{2a}{3}$ and $b = \frac{a}{12}$, the ratio of the resonance wavelength at 0° and 90° polarization to the gap *d*, denoted as $\frac{\lambda_{0^0}}{d}$ and $\frac{\lambda_{90^0}}{d}$ respectively remain constant in all cases. So, for this particular configuration, relationship can be written as, $\lambda_{0°} = \sim 4.6d$ and $\lambda_{90°} = \sim 2.25d$.

Table S4.1. Modulation depth of 4 different configurations of C-FSS

a **(µm)**	***b*** **(µm)**	***c*** **(µm)**	***d*** **(µm)**	$f_{0°}$ **(THz)**	$f_{90°}$ **(THz)**	$\lambda_{0°}$ **(µm)**	$\lambda_{90°}$ **(µm)**	$\lambda_{0°} / \lambda_{90°}$	$\lambda_{0°} / d$	$\lambda_{90°} / d$
200	16.66	133.33	153	0.420	0.832	714	360	1.98	4.66	2.35
300	25	200	229.5	0.281	0.575	1066	521	2.04	4.64	2.27
400	33.33	266.67	306	0.210	0.430	1427	697	2.04	4.66	2.27
500	41.66	333.33	382.5	0.168	0.348	1784	861	2.07	4.66	2.25
600	50	400	459	0.141	0.29	2126	1033	2.05	4.63	2.25
700	58.33	466.67	535.5	0.121	0.248	2477	1208	2.05	4.62	2.25
800	66.67	533.33	612	0.106	0.220	2828	1362	2.07	4.62	2.225

CHAPTER 5

TERAHERTZ MULTISPECTRAL POLARIMETRIC IMAGING BASED ON INTENSITY MEASUREMENT

Redwan Ahmad[1], Charles Simard[1], Rejeena R Sebastian[1], Jonathan Lafreniere-Greig[1], Xavier Ropagnol[1,2], and François Blanchard[1]

[1]Département de Génie Électrique, École de Technologie Supérieure (ÉTS), Montréal, Quebec H3C 1K3, Canada
[2]Institut National de la Recherche Scientifique, EMT Research Center, Varennes, Quebec J3X 1P7, Canada

Paper accepted in *Photonics Research*, April 2026
available at https://doi.org/10.1364/PRJ.589189

5.1 Chapter overview

This chapter addresses the limitations of conventional THz polarimetric systems that rely on phase-sensitive detection and complex optical architectures by presenting an alternative intensity-based framework for multispectral polarimetric imaging. It introduces a compact THz polarimetric spectrometer and imaging system that operates exclusively on intensity measurements, eliminating the need for coherent detection, mechanical delay stages, or phase retrieval. By integrating PS-FSSs as combined spectral filtering and polarization analysis elements, the proposed approach enables robust, multispectral polarimetric imaging within a simplified and scalable system architecture. The chapter demonstrates how intensity images acquired at discrete PS-FSS orientations can be used to directly extract and spatially map key polarization parameters, such as DoLP and AoLP across multiple THz frequency bands, enabling frequency-dependent birefringence characterization. The capability of the proposed system is experimentally validated using a quartz crystal sample, whose well-defined anisotropy provides a reliable benchmark for polarimetric imaging. The results highlight strong DoLP and AoLP contrast and underscore the suitability of the approach for fast, practical, and industrially relevant THz sensing and imaging applications.

5.2 Abstract

A compact terahertz (THz) polarimetric spectrometer and imaging system is demonstrated using polarization-sensitive frequency-selective surfaces (PS-FSS) and rapid, intensity-based detection. Real-time Stokes parameter extraction enables angle-of-linear-polarization (AoLP) measurements and quantitative retrieval of the birefringence of a 1-mm-thick *x*-cut quartz crystal, used here as a benchmark anisotropic sample. The extracted birefringence is in good agreement with THz time domain spectroscopy-based measurements, validating the accuracy of the proposed THz polarimetric approach. Signal-to-noise ratios (SNR) up to 87 dB across 0.23–0.41 THz ensure reliable discrimination of the measured spectral components above the noise floor. Extending this approach to raster-scanned THz imaging using distinct PS-FSS orientations (0°, 45°, 90°, and 135°) enables simultaneous mapping of frequency-dependent Stokes parameters. The resulting degree of linear polarization (DoLP) and AoLP maps exhibit well-resolved polarimetric contrast, consistent with numerical simulations and independent visible polarimetric measurements. Operating entirely without field-resolved detection or mechanical delay stages, the system provides a robust and compact platform for THz polarimetric spectroscopy and imaging of anisotropic materials.

5.3 Introduction

Polarimetric imaging has emerged as a powerful tool for material characterization, enabling the detection of anisotropy, stress-induced birefringence, and molecular orientation through polarization-resolved measurements (Baek et al., 2022). In the visible and near-infrared (NIR) spectrum, compact polarimetric cameras are widely available, typically employing micro-polarizer arrays in which each super-pixel consists of four sub-pixels oriented at 0°, 45°, 90°, and 135° (Liu et al., 2025b). This configuration enables the simultaneous acquisition of polarization-resolved intensities, as shown in Fig. 5.1(a), allowing reconstruction of the Stokes parameters (S_0, S_1, S_2) and derived quantities such as the degree of linear polarization (DoLP) and angle of linear polarization (AoLP) (Lapray et al., 2018; Raffoul et al., 2022). Such systems have found extensive applications in biomedical imaging, surface inspection, and industrial quality control by revealing microstructural variations and surface textures that are not accessible with conventional intensity-only imaging (Zuo et al., 2023; Zhang et al., 2024; He et al., 2021c). Recent advances in visible- and infrared-wavelength polarimetric cameras,

including metasurface-based Stokes imaging polarimeters, further highlight the progressive development of polarization-resolved imaging technologies, supported by earlier developments and subsequent extensions of metasurface concepts into the mid-infrared (Li et al., 2025; Tan et al., 2024; Zhao et al., 2018). Despite their versatility, visible and infrared polarimetric systems are fundamentally limited by shallow penetration depths in dielectric and scattering materials. In contrast, terahertz (THz) radiation offers enhanced penetration into non-metallic materials such as plastics, wood, ceramics, and paper (Nakanishi & Satozono, 2020; Wietzke et al., 2009), positioning THz polarization-resolved characterization and imaging as a promising complementary modality for mapping polarization-dependent contrast in a wide range of industrial and scientific samples (Xu et al., 2020; Morris et al., 2012; Chai et al., 2020; Huang et al., 2021; Harris et al., 2024; Xu et al., 2023; Gurjar et al., 2024).

A wide range of THz polarimetric imaging techniques, predominantly based on THz time-domain spectroscopy (THz-TDS), have been developed to probe material anisotropy and enhance imaging contrast (Van Der Valk et al., 2005; Zhang et al., 2008; Wang et al., 2010; Lowry et al., 2025; Xu et al., 2024a; Xu et al., 2024b; Heller et al., 2025; Baek et al., 2024). Early demonstrations employed ZnTe-based electro-optic polarization imaging to achieve full electric-field reconstruction and birefringence mapping (Van Der Valk et al., 2005), later extended through Jones-matrix analysis and balanced electro-optic detection to improve sensitivity and spatial resolution (Zhang et al., 2008; Wang et al., 2010). While these coherent THz-TDS approaches provide effective polarization retrieval, they inherently rely on mechanical delay lines, resulting in bulky and complex systems that are poorly suited for compact or real-time operation. To reduce system complexity, alternative strategies have been explored, including polarization-resolved single-pixel THz-TDS employing Hadamard coding (Lowry et al., 2025), portable reflection-based scanners measuring orthogonal polarization states (Xu et al., 2024b), and Monte Carlo-based approaches developed for biomedical applications (Xu et al., 2024a; Heller et al., 2025). However, these approaches typically require computationally intensive reconstruction, which limits real-time performance. Polarization-sensitive metasurface absorbers that encode THz polarization states into infrared thermal images have also been demonstrated (Baek et al., 2024), although this method is inherently limited by indirect readout mechanisms and slow response times. Collectively, these studies

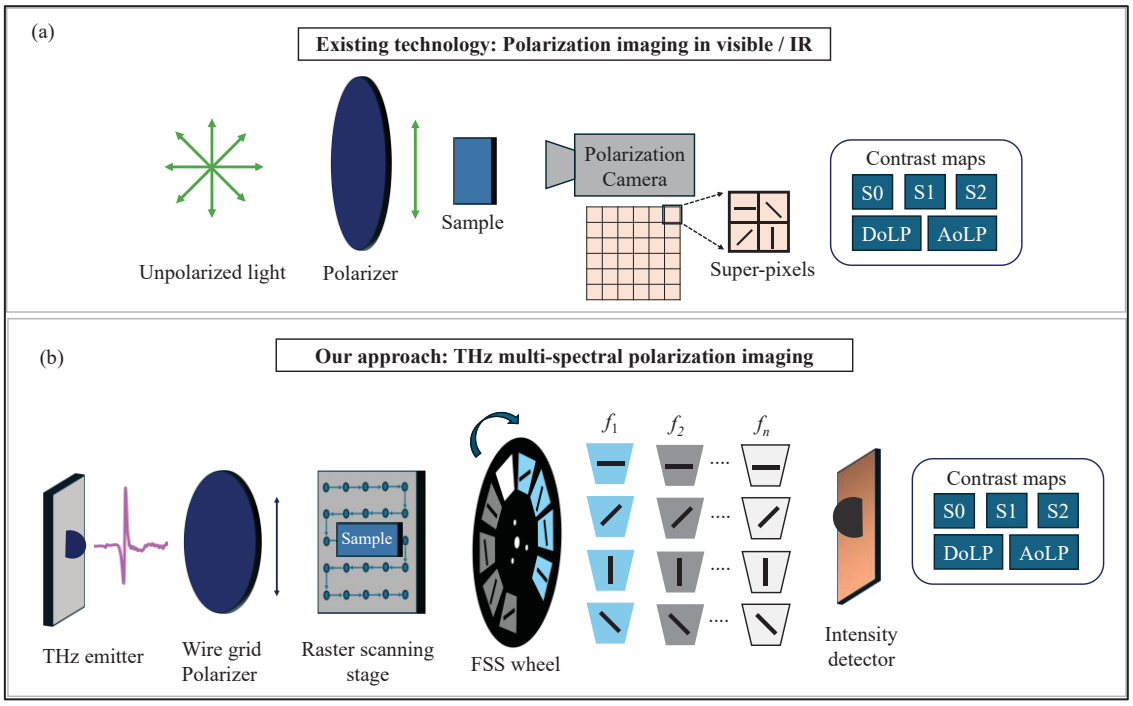

Figure 5.1 Comparison of operating principles between (a) conventional polarimetric imaging at visible and near-infrared wavelengths, and (b) the proposed intensity-based multispectral THz polarimetric imaging approach

demonstrate the feasibility of THz polarimetric imaging for revealing polarization-dependent material contrast and anisotropy beyond conventional amplitude-based THz imaging (Li et al., 2023), yet remain largely dependent on coherent detection or indirect reconstruction. More recently, intensity-based THz systems employing frequency-selective surfaces (FSS) have enabled real-time multispectral measurements without mechanical delay lines (Carelli et al., 2012; Sebastian et al., 2026); however, these implementations are limited to spectral intensity detection and lack polarization sensitivity. The integration of polarization-sensitive frequency-selective surfaces (PS-FSS) offers a promising route toward simultaneous frequency- and polarization-selective THz detection in the intensity domain (Ahmad et al., 2025). In our previous work, we demonstrated a proof-of-concept single-frequency (0.41 THz) intensity-based polarimetric system (Ahmad et al., 2025), though with limited SNR. However, multispectral polarimetric imaging, as well as quantitative DoLP/AoLP reconstruction and birefringence retrieval using intensity-only detection, have not yet been realized.

In this work, we present a compact, intensity-only THz polarimetric spectrometer (TPS) that enables multispectral extraction of the Stokes parameters without coherent detection or mechanical delay stages. As illustrated in Fig. 5.1(b), the system integrates a set of frequency-selective polarizers into a metallic chopper wheel comprising sixteen sectors corresponding to four frequency bands and four analyzer orientations (0°, 45°, 90°, and 135°), allowing intensity-based retrieval of S_0, S_1, and S_2. The performance of the TPS is validated through polarization-resolved measurements of a 1 mm thick stacked quartz crystal, from which frequency-dependent Stokes parameters, DoLP, AoLP, and birefringence are quantitatively retrieved. We further demonstrate the extension of this approach to raster-scanned THz polarimetric imaging using double-layer stacked quartz crystals arranged in co-axial and cross-axial configurations, where reconstructed Stokes maps, DoLP, and AoLP images reveal distinct polarization contrasts associated with parallel and orthogonal optical-axis alignments. To provide independent validation, visible-wavelength Stokes imaging is performed on the same samples using a polarization camera, and the agreement between the visible and THz results confirms the robustness of the proposed intensity-based multispectral polarimetric framework and illustrates the continuity of polarization-dependent material contrast from the visible to the THz regime. All experimental results are further supported by numerical simulations, showing consistent agreement with the measured polarization response across the investigated frequency range.

5.4 Polarization-sensitive FSS chopper wheel

To develop a multispectral polarimetric spectrometer, we integrate polarization discrimination and frequency selectivity within a single device. This is achieved using polarization-sensitive frequency-selective surface geometries, enabling selective transmission as a function of both polarization state and operating frequency. This behavior contrasts with that of conventional broadband polarizers and has been previously demonstrated in our earlier work (Ahmad et al., 2026).

Building on this established design, we implement PS-FSSs based on rectangular slot arrays, integrated into a rotating chopper wheel. A photograph of the fabricated device is shown in Fig. 5.2(a). The chopper wheel comprises sixteen PS-FSS sectors, formed by combining four

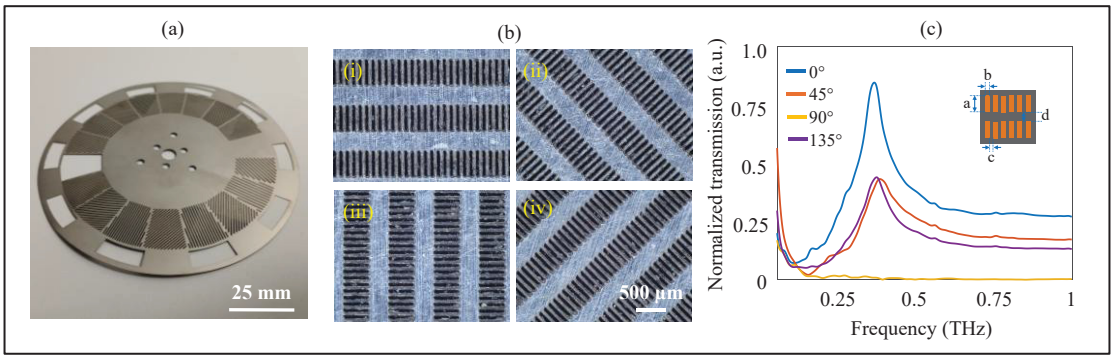

Figure. 5.2 (a) Photograph of fabricated PS-FSS chopper wheel; (b) microscopic images of PS-FSS of 0°, 45°, 90° and 135° orientation respectively; and (c) normalized transmission of PS-FSS (a=440 µm, b=c=55 µm, and d= 330 µm) for horizontal (0°), 45°, vertical (90°) and 135° polarization. Inset figure demonstrates the schematic of PS-FSS with representation of design parameters (a, b, c, and d)

distinct peak center frequencies with four polarization orientations (0°, 45°, 90°, and 135°). These orientations enable intensity-based retrieval of the Stokes parameters (S_0, S_1, and S_2) at each operating frequency. In addition, two sectors are reserved as open and blocked apertures to measure reference and noise signals, respectively. The PS-FSS chopper wheel was fabricated from 125 µm-thick stainless steel using laser micromachining (LPKF ProtoLaser U3). Microscopic images of the PS-FSS unit cells at polarization orientations of 0°, 45°, 90°, and 135° are shown in Fig. 5.2(b)(i–iv). The geometrical parameters of the rectangular slot array include the slot length a, slot width b, and the periodic spacings c and d along the horizontal and vertical directions, respectively.

We used TOPTICA TeraFlash Pro, a commercially available THz-TDS system, to experimentally characterize the PS-FSS in terms of peak center frequency and normalized transmission. Normalized transmission (NT) could be calculated as follows (Ahmad et al., 2024):

$$NT = \frac{T_{sample}}{T_{ref}} \tag{5.1}$$

where T_{sample} and T_{ref} are the spectral amplitudes of the analyzed sample and without the sample (air) as a reference, respectively.

Figure 5.2(c) shows the normalized transmission, referenced to air, for polarization angles of 0°, 45°, 90°, and 135° for a representative PS-FSS with slot length a = 440 μm, slot width b = 55 μm, horizontal gap c = 55 μm, and vertical gap d = 330 μm. For 0° polarization, where the incident electric field is perpendicular to the long axis of the rectangular slots, the structure exhibits a band-pass response with a peak transmission at a center frequency f_c=0.37 THz. In addition to the dominant passband, a weak residual transmission is observed at higher frequencies. For vertical polarization (90°), the PS-FSS suppresses transmission to approximately 1% across a broad spectral range, demonstrating strong polarization discrimination. At intermediate polarization angles (45° and 135°), the transmission spectra are nearly identical, with peak transmission reduced to approximately 50% of that observed at 0°.

Notably, while the transmitted amplitude at the center frequency varies with polarization angle according to Malus' law, the peak center frequency remains invariant with respect to rotation. This behavior indicates that polarization rotation modulates the transmission amplitude without altering the resonant response of the PS-FSS, confirming its operation as a frequency-selective polarizer with high polarization selectivity. To enable multispectral operation, three additional PS-FSS designs were implemented by varying the slot length (700 μm, 500 μm, and 400 μm) and proportionally scaling the slot width and periodic gaps, yielding center frequencies of 0.23 THz, 0.33 THz, and 0.41 THz, respectively. Each PS-FSS was integrated into the rotatable chopper wheel at four polarization orientations (0°, 45°, 90°, and 135°).

5.5 Frequency-selective THz polarimetric system

Figure 5.3 provides an overview of the experimental setup, signal-processing workflow, and measurement configurations of the proposed frequency-selective THz polarimetric system. As shown in Fig. 5.3(a), THz radiation is generated using a photoconductive antenna (PCA) (THz-P-Tx: RTP220468B, TOPTICA Photonics) driven by a femtosecond fiber laser operating at 1560 nm wavelength, with an 80 fs pulse duration, 80 MHz repetition rate, and 30 mW average optical power. The emitted THz beam is collected and focused onto the sample using two off-axis parabolic mirrors (M1 and M2). The incident polarization is fixed to horizontal and purified using a wire-grid polarizer placed immediately before the sample. The transmitted

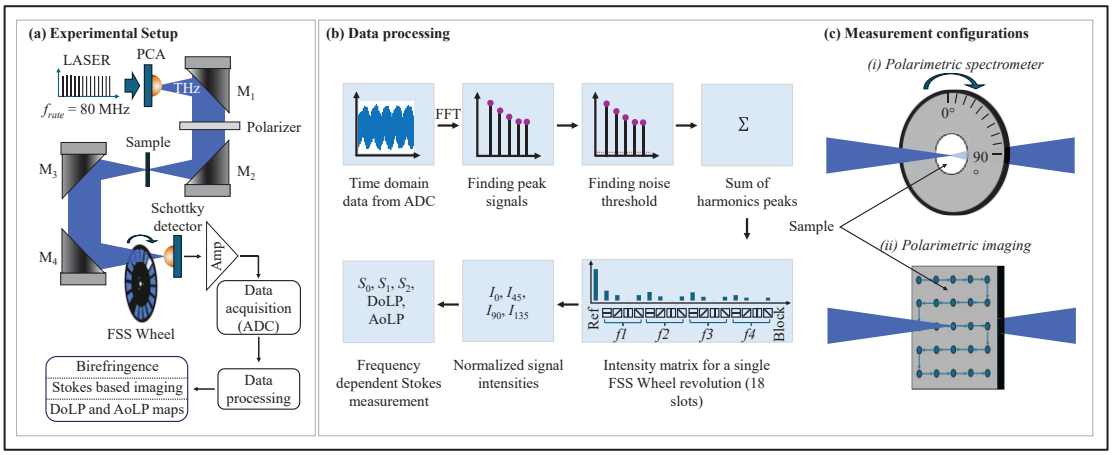

Figure 5.3 (a) Schematic of the experimental setup; (b) data acquisition and processing module, illustrating real-time FFT analysis used to extract polarization-dependent spectral amplitudes; (c) system configurations: (i) polarimetric spectrometer and (ii) polarimetric imaging system, showing raster-scanning implementation for spatially resolved Stokes parameter retrieval and the corresponding degree and angle of linear polarization (DoLP and AoLP) mapping

signal is detected using a Schottky diode detector (3DL 12C LS2500 A2 from ACST), with a spherical silicon lens used to improve coupling efficiency. The combined PCA emission spectrum and detector responsivity fully cover the four operating frequency bands of the PS-FSSs (Appendix A, Fig. A5.1). The detected THz signal is amplified using a Mini-Circuits ZFL-2000GH+ broadband amplifier and digitized with a 14-bit Acqiris SA240P high-speed acquisition card operating at 4 GS/s. This high sampling rate enables the extraction of the periodic response at the 80 MHz modulation frequency and its harmonics well above the low-frequency noise floor.

The acquisition cycle is set by the chopper rotation period (10 ms). Each cycle generates approximately 500 MB of data, which are processed into 18 slot-resolved values, reducing the dataset to only a few kilobytes. In practice, system-level overheads such as data transfer and processing result in an acquisition time of ~0.5 s, with an additional ~0.3 s required for fast Fourier transform (FFT)-based analysis, yielding a total latency of ~0.8 s. Further reductions could be achieved through continuous acquisition and batch processing implemented directly on the FPGA of the ADC card. Despite longer acquisition and processing times, the

measurement itself is completed within 10 ms, preserving real-time capability for spectroscopic applications.

As illustrated in Fig. 5.3(b), time-domain voltage traces are transformed into the frequency domain using a fast Fourier transform (FFT), yielding a comb of spectral peaks at the repetition frequency and its harmonics. Harmonic amplitudes exceeding a predefined noise threshold are retained and summed to enhance the signal-to-noise ratio (SNR), producing normalized intensity values for each PS-FSS slot and analyzer orientation. These intensity channels (I_0, I_{45}, I_{90}, and I_{135}) are used to compute frequency-dependent Stokes parameters (S_0, S_1, and S_2) and derived polarization metrics, including the degree and angle of linear polarization (DoLP and AoLP).

As shown in Fig. 5.3(c), the system operates in two measurement configurations. In the polarimetric spectrometer mode, the sample is mounted on a rotation stage at the focal plane to measure polarization-resolved transmission as a function of orientation. In the polarimetric imaging mode, the sample is raster-scanned using a motorized XY translation stage (Zaber X-MCB2), enabling spatially resolved acquisition of the Stokes parameters and corresponding DoLP and AoLP maps. In both configurations, a rotating PS-FSS chopper wheel positioned directly in front of the detector provides simultaneous multispectral and polarization-resolved modulation. The 4-inch diameter wheel, driven by a Thorlabs MC2000B controller, provides four analyzer orientations (0°, 45°, 90°, and 135°) at each frequency band, enabling real-time polarimetric readout within a single wheel rotation.

5.5.1 Spectral extraction and SNR analysis

Figure 5.4 illustrates the signal-processing performance and noise characteristics of the detection scheme. Figure 5.4(a) shows a representative time-domain voltage trace acquired over a single PS-FSS slot, along with a zoomed-in view highlighting the periodic modulation. The corresponding FFT magnitude spectrum (Fig. 5.4(b)) exhibits discrete harmonic peaks at integer multiples of the 80 MHz repetition frequency, extending up to 2 GHz. Noise performance was evaluated by varying the number of averaged acquisitions. As shown in Fig. 5.4(c), the mean noise level remains approximately constant at ~24 counts, while the standard

deviation decreases from ~10 counts at N=2 to ~6 counts at N=10, indicating a stable baseline and consistent performance of the Schottky–amplifier–ADC detection chain. The resulting noise floor for ten averages is shown in Fig. 5.4(d).

To quantify signal visibility above the noise floor, the amplitude contrast (AC) is defined as

$$AC = 20\log_{10}\frac{\sum_{i=1}^{M}(A_i - \mu_{noise_i})}{\sigma_{noise}} \tag{5.2}$$

Where A_i denotes the amplitude of the i-th harmonic component, M is the number of harmonics considered, and μ_{noise} and σ_{noise} represent the mean and standard deviation (SD) of the noise floor, respectively.

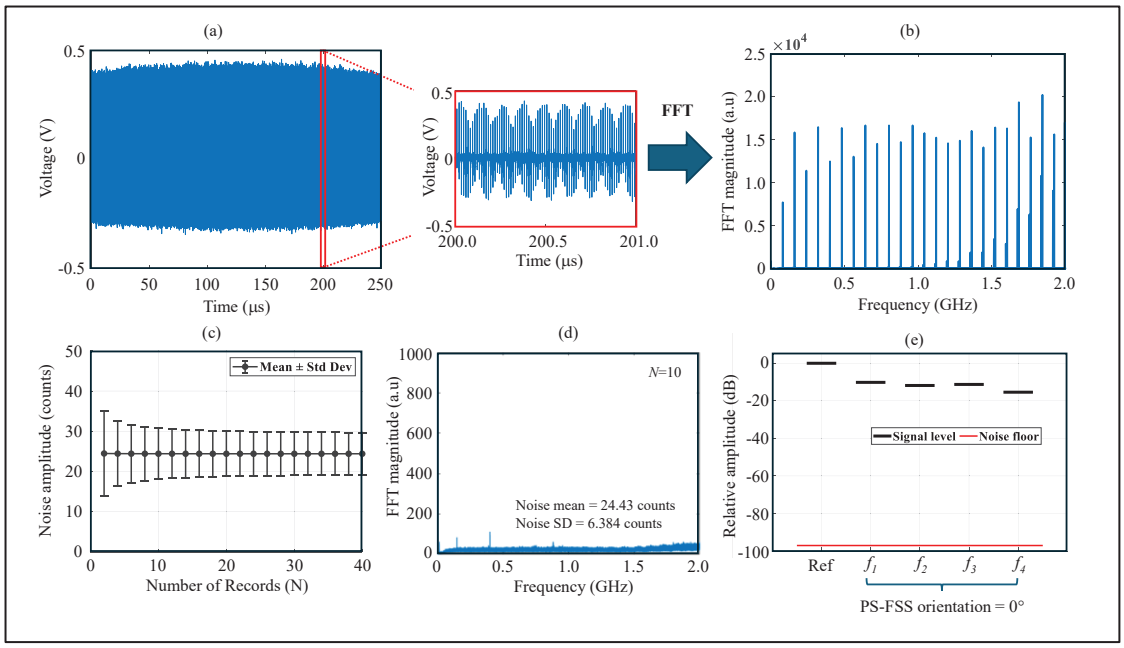

Figure 5.4 (a) Representative time-domain voltage waveform and (b) corresponding FFT magnitude spectrum of the reference slot; (c) mean value and standard deviation of the noise level as a function of the number of averaged records, demonstrating the stability of the acquisition system; (d) FFT magnitude noise floor measured in the absence of a THz signal; (e) amplitude contrast for the reference slot and for the four operating center frequencies (f_1=0.23 THz, f_2=0.33 THz, f_3=0.37 THz, and f_4=0.41 THz)

Figure 5.4(e) shows the amplitude contrast for the reference slot and the four PS-FSS frequency bands. The reference slot exhibits a maximum contrast of 97 dB, while PS-FSS slots at 0° orientation yield contrast values between 81 dB and 87 dB across the 0.23–0.41 THz range, demonstrating high sensitivity and excellent measurement repeatability.

Although the system does not directly measure the temporal electric-field waveform, the intensity-modulated response provided by the PS-FSS wheel enables robust reconstruction of polarization-dependent transmission as a function of frequency and orientation. This approach enables real-time multispectral THz polarimetric spectroscopy and imaging without the complexity of coherent THz time-domain systems.

5.6 Polarimetric spectrometer

To evaluate the functionality of the proposed polarimetric spectrometer, an *x*-cut quartz crystal was investigated through both simulation and experiment. Although the system employs a single fixed input polarization state, polarization analysis is achieved using four discrete analyzer orientations (0°, 45°, 90°, and 135°), while the detector records intensity only. Under these conditions, the Jones-matrix formalism provides a physically rigorous description of the phase retardation between the ordinary and extraordinary axes of the birefringent medium, governing the evolution of AoLP as the sample is rotated. This framework is therefore well-suited for predicting polarization-dependent observables from intensity-only, multispectral measurements obtained using the rotating PS-FSS wheel and Schottky diode detector. Details of the simulation model are provided in appendix B.

5.6.1 Stokes parameter reconstruction

The polarization state of the transmitted THz wave is described using the Stokes formalism. The Stokes parameters S_0, S_1, and S_2 were computed from the measured intensities at the four analyzer orientations according to standard definitions (Raffoul et al., 2022):

$$S_0 = I_0 + I_{90} \tag{5.3}$$

$$S_1 = I_0 - I_{90} \tag{5.4}$$

$$S_2 = I_{45} - I_{135} \tag{5.5}$$

where I_0, I_{45}, I_{90} and I_{135} denote the measured intensities at analyzer angles of 0°, 45°, 90°, and 135°, respectively. Since the system is sensitive only to linear polarization, the circular polarization component S_3 cannot be retrieved. From the Stokes parameters, the degree and angle of linear polarization are defined as (Raffoul et al., 2022):

$$DoLP = \frac{\sqrt{S_1^2 + S_2^2}}{S_0} \tag{5.6}$$

$$AoLP = \frac{1}{2}\tan^{-1}\left(\frac{S_2}{S_1}\right) \tag{5.7}$$

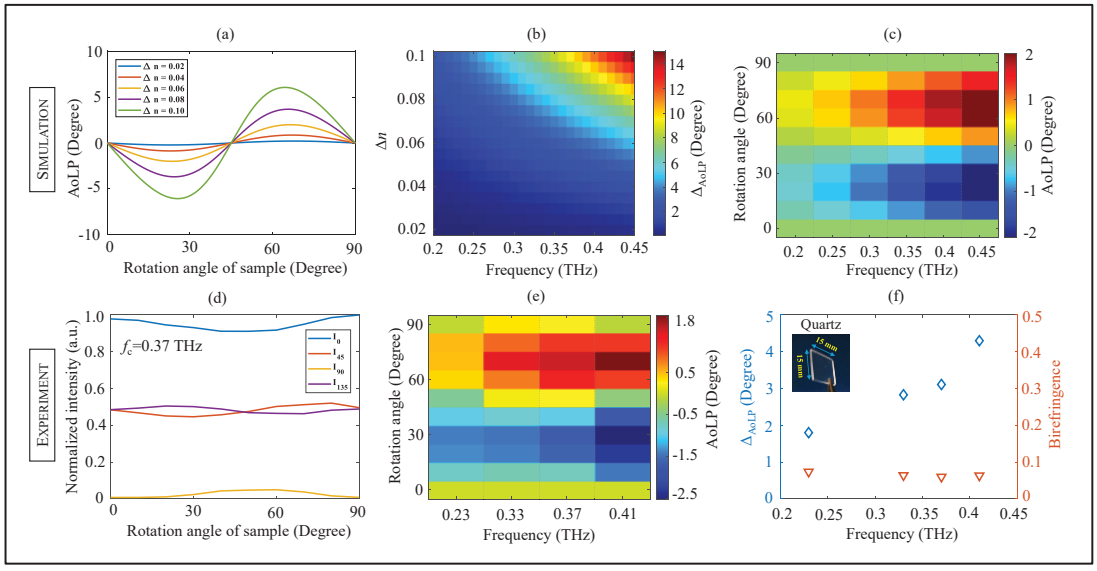

Figure 5.5 Simulation results: (a) AoLP as a function of sample rotation angle for a 1-mm-thick sample with varying birefringence at 0.41 THz; (b) simulated AoLP variation as a function of frequency and birefringence for a 1-mm-thick sample; (c) simulated AoLP map as a function of operating frequency and sample rotation angle. Experimental results: (d) normalized intensities measured at analyzer orientations of 0°, 45°, 90°, and 135° at f_c=0.37 THz for 1-mm-thick stacked quartz sample; (e) measured AoLP at four center frequencies (0.23, 0.33, 0.37, and 0.41 THz) as a function of quartz rotation angle from 0° to 90°; (f) peak-to-peak AoLP variation at the four center frequencies (left axis) and the corresponding frequency-dependent birefringence of a 1-mm-thick stacked quartz sample (right axis)

5.6.2 Simulation results

In the simulations, the sample rotation angle θ_s was varied from 0° to 90°, while the birefringence Δn was swept from 0.02 to 0.1 for a 1-mm-thick sample at a center frequency of 0.41 THz. As shown in Fig. 5.5(a), increasing birefringence leads to a systematic increase in the peak-to-peak AoLP variation (Δ_{AoLP}), with two extrema appearing near 22.5° and 67.5°. The corresponding frequency-dependent behavior of Δ_{AoLP} over the 0.2–0.45 THz range is shown in Fig. 5.5(b), confirming that AoLP evolves jointly with frequency and birefringence due to frequency-dependent phase retardation. The combined dependence of AoLP on operating frequency and sample rotation angle for a 1-mm-thick quartz sample is summarized in Fig. 5.5(c), where higher frequencies yield stronger AoLP modulation.

To further assess thickness effects, a comprehensive Jones-matrix simulation was performed for a fixed birefringence of Δn=0.05, while sweeping the sample rotation angle (0–90°), thickness (0.1–4 mm), and frequency (0.10–0.40 THz). The results (Fig. A5.2(i–iv)) show that increasing thickness produces proportionally larger phase retardation and stronger AoLP modulation, while higher frequencies shift the AoLP response smoothly across the full angular range. These trends highlight the coupled influence of thickness and frequency on THz birefringence measurements.

5.6.3 Experimental validation

Experimentally, a 1-mm-thick stacked quartz sample (15 mm × 15 mm) was mounted on a precision rotation stage and measured in 10° increments (Fig. 5.3(c)(i)). For each orientation, intensity measurements were recorded at four center frequencies (0.23, 0.33, 0.37, and 0.41 THz) and four analyzer orientations. Representative normalized intensity traces I_0, I_{45}, I_{90}, and I_{135} at f_c=0.37 THz are shown in Fig. 5.5(d). Each channel exhibits the expected modulation arising from the evolving projection of the rotated polarization state onto the analyzer axes. In particular, the I_{45} and I_{135} traces intersect near 50% normalized intensity at approximately 45° intervals, consistent with the symmetry of ±45° analyzer projections.

Notably, the Schottky detector incorporates a broadband log-spiral antenna that is intrinsically sensitive to both orthogonal linear polarization components. This dual-polarization sensitivity

results in a measurable modulation of the I_{90} channel as the quartz plate is rotated, reflecting the combined influence of the evolving polarization state and detector response.

Using the measured intensity values, the Stokes parameters were calculated using Eqs. (5.3)–(5.5), normalized by S_0, and the AoLP was subsequently extracted using Eq. (5.7). As shown in Fig. 5.5(e), rotation of the sample produces a periodic AoLP modulation with two extrema of opposite sign over a 90° rotation period. The peak-to-peak AoLP variation increases monotonically with frequency (Fig. 5.5(f), left axis), in agreement with the simulation results.

5.6.4 Birefringence retrieval

To quantitatively extract the birefringence of the quartz sample, an optimization-based fitting procedure was implemented using the measured Δ_{AoLP} values at the four operating frequencies and the known sample thickness. A Jones-matrix forward model was used to simulate the AoLP response as a function of rotation angle, and a direct-search algorithm minimized the discrepancy between simulated and experimental Δ_{AoLP}. The retrieved frequency-dependent birefringence values are shown in Fig. 5.5(f) (right axis), yielding an average birefringence of approximately $\Delta n \approx 0.06$ over the 0.23–0.41 THz range. These values are consistent with independent THz-TDS measurements and reported literature values (Castro-Camus et al., 2006). A small residual discrepancy on the order of $\sim 5\times10^{-3}$ is attributed to alignment tolerances, finite polarization purity, and interface-induced depolarization effects.

Potential strategies to minimize or compensate for these offsets, including improved alignment procedures, the use of narrow band-pass filters, and depolarization correction, are briefly discussed in section 5.8 (Future Perspectives).

5.7 Polarimetric imaging

Subsequently, we performed a comparative investigation of Stokes-based imaging in both visible and THz ranges using intensity-only detection. In both cases, stacked quartz samples consisting of two 0.5 mm-thick plates were investigated. Two sample configurations were investigated based on the relative orientation of the birefringent crystal fast axes with respect to their slow axes: a co-axial configuration with aligned fast axes and a cross-axial

configuration with orthogonal fast-axis orientations. Sample rotation was used to probe the resulting polarization-dependent behavior in both the visible and terahertz spectral domains.

5.7.1 Visible polarimetric camera

The experimental configuration of the visible polarimetric imaging system is shown in Fig. 5.6(a). A commercially available polarization camera (Alkeria CELERA P series) was used to acquire Stokes-resolved images of the stacked quartz samples. Each super-pixel consists of four sub-pixels with integrated linear polarizers oriented at 0°, 45°, 90°, and 135°, enabling simultaneous acquisition of polarization-resolved intensities and reconstruction of the Stokes parameters, as well as derived quantities such as DoLP and AoLP (Guiramand et al., 2024). The effective output resolution after super-pixel processing is 1232 × 1028 pixels.

The samples were illuminated using a continuous-wave 516 nm laser. A spatial filter was placed at the Fourier plane of the beam to ensure a uniform illumination profile, and a linear polarizer was positioned before the sample to define the incident polarization state. The sample was mounted on a rotation stage, allowing measurements at different azimuthal orientations θ_s to evaluate the angular dependence of the Stokes parameters. Due to the sample dimensions exceeding the active sensor area, the recorded images correspond to a portion of the sample.

Figure 5.6(b) presents the measured DoLP maps for co-axial and cross-axial stacking configurations at sample orientations of $\theta_s = 0°$ and 45°. For the co-axial configuration, high DoLP values approaching unity are observed at $\theta_s = 0°$, while a pronounced reduction in DoLP occurs at $\theta_s = 45°$, consistent with polarization transformation induced by accumulated birefringent phase retardation (Fig. 5.6(b)(i–ii)). In contrast, the cross-axial configuration exhibits consistently high DoLP across both orientations, reflecting partial cancellation of the birefringent phase retardation and confirming theoretical expectations (Fig. 5.6(b)(iii–iv)). These results demonstrate the sensitivity of Stokes-based imaging to the relative orientation of anisotropic layers.

The corresponding AoLP maps at 516 nm for the co-axial configuration at $\theta_s = 0°$ and 45° are shown in Fig. A5.3(a)(i–ii), while those for the cross-axial configuration are presented in Fig. A5.3(a)(iii–iv). The largest AoLP variations are observed for $\theta_s = 45°$, indicating enhanced

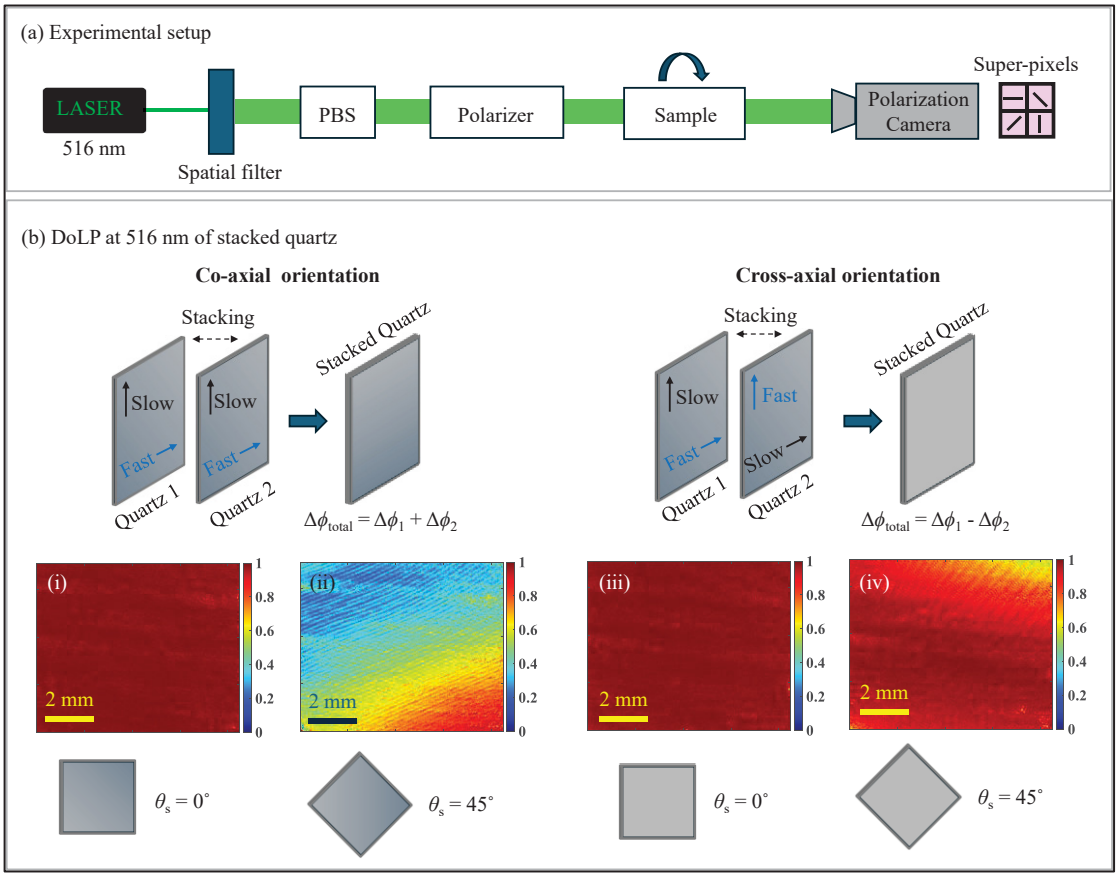

Figure 5.6 (a) Experimental setup for visible-wavelength Stokes polarimetric imaging at 516 nm using a polarization camera. PBS denotes a polarizing beam splitter. (b) Measured DoLP maps of stacked quartz for co-axial fast-axis orientation at analyzer angles of (i) 0° and (ii) 45°, and for cross-axial fast-axis orientation at (iii) 0° and (iv) 45°

interaction between the incident polarization and the birefringent axes of the stacked quartz. These experimental observations are further corroborated by numerical simulations shown in Fig. A5.3(b).

5.7.2 Multispectral polarimetric THz imaging

THz polarization-resolved imaging was subsequently performed at the selected center frequencies using the PS-FSS analyzer. The same stacked quartz sample was investigated, and raster scanning was carried out with a step size of 1 mm. For raster scanning, the quartz samples were placed on a holder incorporating a thin, THz-transparent plastic membrane with

negligible impact on transmission. Measurements were conducted for both co-axial and cross-axial stacking configurations. Representative Stokes S_0 maps acquired at 0.23 THz for sample orientations of $\theta_s = 0°$ and 45° under co-axial alignment are shown in Fig. 5.7(a)(i–ii), with the corresponding DoLP distributions presented in Fig. 5.7(a)(iv–v). The S0 images primarily reflect the sample geometry and orientation, while the DoLP maps reveal pronounced polarization-dependent contrast. In particular, a reduction in DoLP at $\theta_s = 45°$ is observed for the co-axial configuration, consistent with birefringent phase retardation and in good agreement with numerical simulations (Fig. A5.4(a–b)).

A direct comparison between co-axial and cross-axial configurations, shown in Fig. 5.7(a)(ii–iii), further highlights this distinction. While the corresponding S0 images appear similar, their DoLP maps (Fig. 5.7(a)(v–vi)) exhibit clear differences, demonstrating the ability of the proposed system to discriminate optical-axis alignment through polarization-sensitive contrast. The extracted AoLP maps for three representative cases, namely co-axial stacking at θs = 0° and 45°, and cross-axial stacking at $\theta_s = 45°$, are shown in Fig. 5.7(a)(vii–ix). Across the interior of the quartz crystal, the AoLP remains close to 0°, consistent with theoretical expectations and simulations (Fig. A5.4(c–d)), while localized deviations are observed near the sample edges due to depolarization and finite spatial resolution.

Figure 5.7(b) presents corresponding polarization-resolved images acquired at 0.33 THz. Similar trends are observed at this frequency, with S_0 maps remaining largely invariant across configurations, while DoLP and AoLP maps continue to exhibit polarization-dependent contrast associated with birefringence and sample orientation. Comparable Stokes, DoLP, and AoLP images were also obtained at center frequencies of 0.37 THz and 0.41 THz (not shown), demonstrating the multispectral capability of the proposed THz polarimetric imaging system.

To quantitatively assess the polarimetric performance, line profiles were extracted from the raster-scanned DoLP and AoLP maps at 0.23 THz, as shown in Fig. 12 (Appendix F). For the stacked quartz samples, the DoLP in the cross-orientation configuration is theoretically expected to be unity. Experimentally, the deviation (Δ) in the quartz region remains within $\Delta \approx 1\times10\text{-}3$ (see Fig. 12(ii)), indicating near-ideal polarization behavior within the measurement uncertainty. Slightly larger deviations (up to $\Delta \approx 2\times10\text{-}2$) are observed at the quartz–plastic

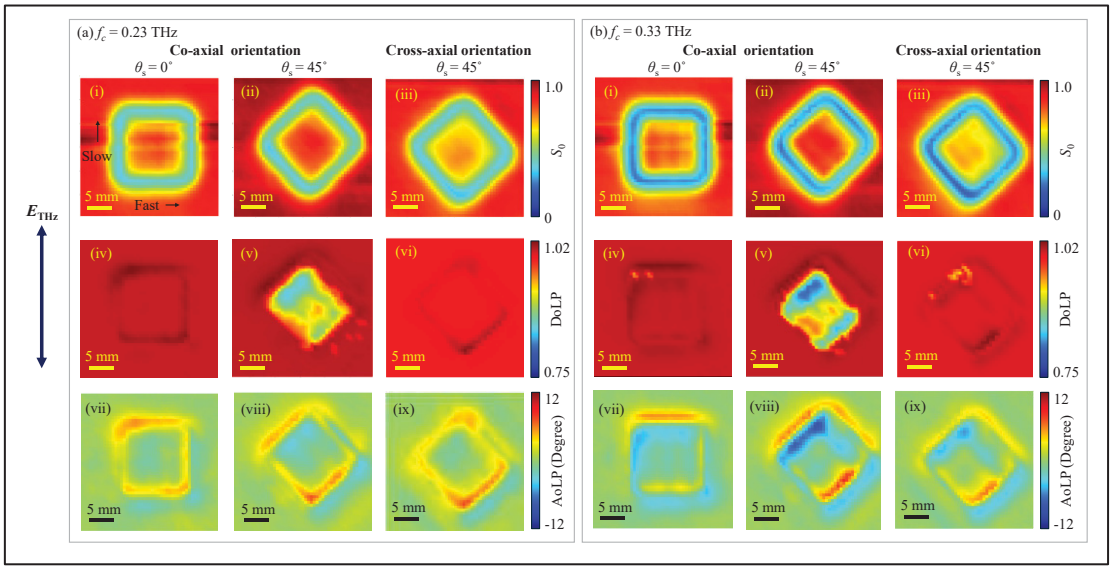

Figure 5.7 Polarization-resolved THz images of the stacked quartz sample at (a) 0.23 THz and (b) 0.33 THz. Panels (i–iii) show the reconstructed Stokes S₀ for (i) 0° co-axial, (ii) 45° co-axial, and (iii) 45° cross-axial sample orientations. Panels (iv–vi) present the corresponding DoLP maps, while panels (vii–ix) display the extracted AoLP maps. The images reveal distinct polarization-dependent contrast between co-axial and cross-axial configurations, with localized variations in DoLP observed near the sample edges

interface, where the combined influence of scattering effects and spatial averaging within the measurement spot becomes more pronounced. These effects are present in both orientation configurations but are more evident near material boundaries due to the transition between adjacent regions. In the co-orientation configuration, a strong contrast is expected, and an experimental contrast of approximately 0.15 is observed in the quartz region, as illustrated in Fig. 12(iv).

For both co- and cross-orientation configurations of the stacked quartz samples at $\theta_s = 45°$, the AoLP is expected to be 0°, as shown in Appendix E (Fig. 11). The measured AoLP variation remains within ±1° in the quartz region (see Fig. 12(vi, viii)), confirming low background polarization noise and good angular stability. Minor variations within the quartz region can also be attributed to slight thickness non-uniformity of the samples. More pronounced variations are observed at the quartz–plastic interface, primarily due to boundary effects, where

localized polarization distortion occurs. Overall, these results demonstrate that the proposed system achieves strong polarimetric contrast while maintaining good quantitative accuracy.

Although stacked quartz is employed here as a representative birefringent sample for proof-of-concept validation, the demonstrated methodology is broadly applicable to polarization-resolved THz imaging of anisotropic materials. By eliminating the need for coherent detection and mechanical delay stages, the proposed compact, intensity-based framework provides a practical route toward multispectral THz polarimetric imaging for material characterization and nondestructive inspection.

5.8 Future perspectives

Due to the wideband nature of the band-pass filters employed in the present system, the extracted birefringence represents a weighted average over the filter bandwidth rather than a strictly monochromatic value at the center frequency. Future implementations could improve frequency specificity by employing narrower band-pass filters with sharper spectral roll-off and by increasing the number of operating frequency channels, thereby reducing dispersion-induced averaging effects and enhancing measurement accuracy.

In intensity-based, frequency-selective THz systems using band-pass filters, Fabry–Pérot reflections are inherently suppressed for thin samples such as the 0.5–1 mm quartz crystals investigated here, owing to the weak amplitude of internal echoes. For thicker samples, however, multiple reflections may introduce measurable distortions. Incorporating Fabry–Pérot effects into the numerical modeling and signal processing framework represents a promising route to compensate for such artifacts and improve quantitative accuracy in future studies.

While the current system operates up to 0.41 THz, further optimization of the polarization-sensitive frequency-selective surface (PS-FSS) design could extend the accessible frequency range. The Schottky detector employed in this work remains operational up to approximately 1.0 THz, supporting the feasibility of broader spectral coverage. In addition, emerging CMOS-based THz receiver technologies offer a promising alternative for broadband applications

(Ahmad et al., 2025b), particularly where large-area integration and system scalability are desired.

Finally, extending the simulation framework to explicitly account for depolarization effects arising from complex field interactions, particularly at lower frequencies, could further improve birefringence estimation accuracy and interpretation of polarization-resolved THz images.

5.9 Conclusion

We have developed a compact, multispectral THz polarimetric spectrometer and imaging system based on frequency-selective polarizers integrated into a rotating chopper wheel, enabling fast, intensity-only polarization detection without coherent probe beams or mechanical delay lines. The proposed system enables retrieval of the birefringence of quartz in agreement with established literature values and demonstrates raster-scanned THz polarimetric imaging with distinct DoLP and AoLP contrast for co-axial and cross-axial crystal orientations. By reconstructing Stokes parameters directly from intensity measurements, this approach avoids phase-resolved detection while improving system compactness, robustness, and experimental simplicity. Overall, the demonstrated platform provides a promising pathway toward practical intensity-based THz polarimetric spectroscopy and imaging for material characterization and non-destructive evaluation.

5.10 Appendix-A: THz emitter characterization and reference birefringence measurement

The THz emitter based on a PCA was characterized using a commercial THz-TDS system (TOPTICA TeraFlash Pro), with both emission and detection performed using PCA modules. As shown in Fig. A5.1(a) (left axis), the emitter exhibits a broadband spectral response with a peak centered near 0.35 THz. The normalized responsivity of the Schottky diode detector, shown on the right axis of Fig. A5.1(a), reaches its maximum around 0.1 THz and gradually decreases toward higher frequencies.

In addition, the birefringence of the stacked quartz sample (total thickness of 1 mm) was independently determined using the same THz-TDS system as a reference measurement. From

the time-domain data, the refractive index n and birefringence Δn were extracted according to Eqs. (8) and (9) (Jepsen, 2019):

$$n(f) = 1 + \frac{c\Delta\phi}{2\pi fd} \tag{5.8}$$

$$\Delta n = n_e - n_o \tag{5.9}$$

where c is the speed of light, f is the frequency, and d denotes the thickness of the birefringent sample. The terms n_e and n_o correspond to the extraordinary and ordinary refractive indices, respectively, and $\Delta\phi$ represents the phase retardation between orthogonal polarization components, defined as $\Delta\phi = \phi_x - \phi_y$.

Figure A5.1(b) shows the frequency-dependent birefringence of the x-cut stacked quartz crystal over the 0.1–1 THz range. The inset of Fig. A5.1(b) displays the corresponding phase retardation as a function of frequency for the same sample.

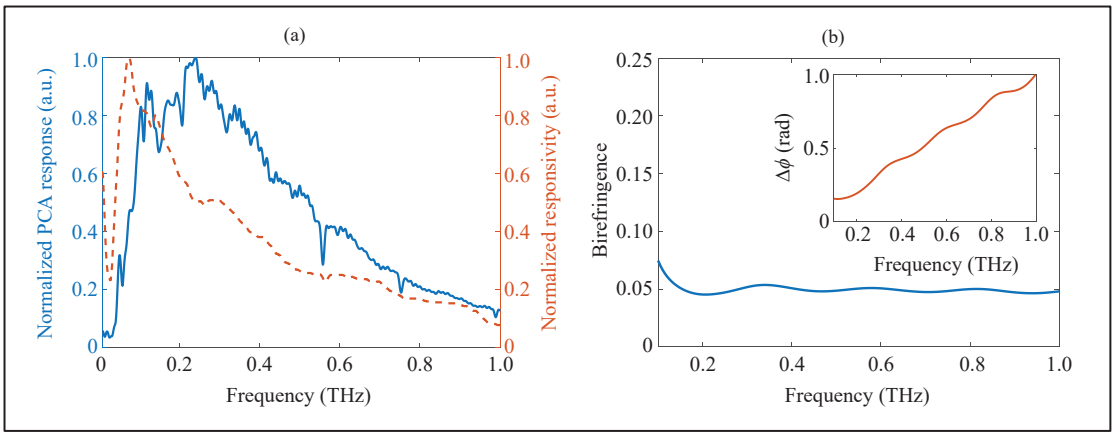

Figure A5.1 (a) Normalized emission spectrum of the THz photoconductive antenna (left axis) and normalized responsivity of the Schottky diode detector (right axis), showing the broadband spectral overlap between the emitter output and detector sensitivity. (b) frequency-dependent birefringence of a 1 mm thick stacked quartz crystal obtained from THz-TDS. The inset shows the corresponding phase retardation as a function of frequency for the same sample

5.11 Appendix-B: Jones-matrix model for polarization evolution in a birefringent sample

The polarization evolution of a linearly polarized THz wave propagating through a birefringent material can be described using the Jones-matrix formalism. When the birefringent sample is rotated by an angle θ with respect to the laboratory reference frame, the effective Jones matrix of the system is given by (Barakat, 1998; Menzel et al., 2015):

$$J_{rotated}(\theta) = R(\theta)\, J_{sample}\, R(-\theta) \tag{5.10}$$

where $R(\theta)$ and $R(-\theta)$ are the rotation and inverse rotation matrices, respectively. These matrices are expressed as

$$R(\theta) = \begin{bmatrix} \cos\theta & -\sin\theta \\ \sin\theta & \cos\theta \end{bmatrix} \tag{5.11}$$

$$R(-\theta) = \begin{bmatrix} \cos\theta & \sin\theta \\ -\sin\theta & \cos\theta \end{bmatrix} \tag{5.12}$$

The Jones matrix of the birefringent sample itself is written as.

$$J_{Sample} = \begin{bmatrix} e^{i\frac{\Delta\phi}{2}} & 0 \\ 0 & e^{-i\frac{\Delta\phi}{2}} \end{bmatrix} \tag{5.13}$$

where $\Delta\phi$ is the birefringence-induced phase retardation between the ordinary and extraordinary polarization components. This phase retardation is given by:

$$\Delta\phi = \frac{2\pi f d \Delta n}{c} \tag{5.14}$$

where f represents the frequency, d is the sample thickness, Δn denotes the birefringence, and c corresponds to the speed of light.

The transmitted electric field after propagation through the rotated birefringent sample is obtained as (Neshat & Armitage, 2012; Singh et al., 2025):

$$E_{out} = J_{rotated} E_{in} \tag{5.15}$$

where E_{in} represents the incident electric field vector.

Polarization analysis is performed using a linear analyzer oriented at an angle α. The corresponding Jones matrix is given by:

$$J_{analyzer}(\alpha) = \begin{bmatrix} \cos^2(\alpha) & \cos(\alpha)\sin(\alpha) \\ \cos(\alpha)\sin(\alpha) & \sin^2(\alpha) \end{bmatrix} \tag{5.16}$$

The electric field transmitted through the analyzer is therefore

$$E(\alpha) = J_{analyzer}(\alpha) E_{out} \tag{5.17}$$

and the detected intensity is calculated as

$$I(\alpha) = \left| E(\alpha) \right|^2 \tag{5.18}$$

5.12 Appendix-C: Simulated AoLP response as a function of thickness and frequency

To gain further insight into the evolution of birefringence-induced phase retardation, numerical simulations were performed to evaluate the AoLP response of a birefringent sample with a fixed birefringence of Δn = 0.05 over a broad range of sample thicknesses and operating frequencies. The resulting AoLP distributions, shown in Fig. A5.2(i–iv), illustrate how the AoLP depends on the accumulated phase difference between the ordinary and extraordinary field components. As both frequency and thickness increase, the phase retardation becomes more pronounced, leading to stronger AoLP variations as a function of sample rotation angle. These simulations demonstrate that even modest changes in birefringence or propagation length can produce measurable AoLP variations, highlighting the sensitivity of AoLP-based

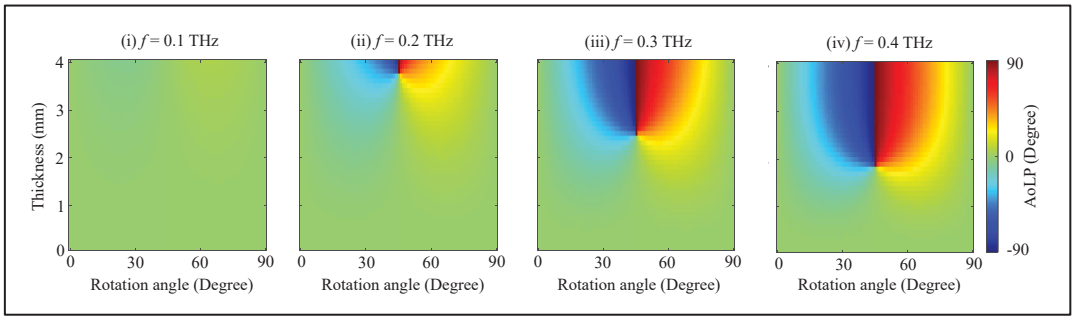

Figure A5.2 Simulated AoLP as a function of sample thickness and rotation angle for distinct operating frequencies: (i) 0.1 THz, (ii) 0.2 THz, (iii) 0.3 THz, and (iv) 0.4 THz, illustrating the evolution of birefringence-induced phase retardation with both thickness and frequency

measurements to birefringent phase accumulation and supporting its use for qualitative assessment of polarization effects in anisotropic materials.

5.13 Appendix-D: Visible-wavelength AoLP imaging and simulation comparison

AoLP images of a 1 mm thick stacked quartz sample were acquired at 516 nm using a polarimetric CCD camera, as shown in Fig. A5.3(a). As a reference, an initial AoLP image was recorded without the sample, yielding an AoLP value close to 0°. Measurements were then performed for both co-axial and cross-axial stacking configurations, with the sample oriented at $\theta_s = 0°$ and 45°.

For the co-axial configuration, a clear angular dependence of the AoLP is observed. At $\theta_s = 0°$, the measured AoLP remains close to 0°, whereas at $\theta_s = 45°$, the AoLP shifts toward higher values approaching 90°, reflecting the accumulation of birefringence-induced phase retardation in the aligned quartz plates. This behavior is characteristic of anisotropic birefringent media and indicates a strong polarization-modulating response.

In contrast, for the cross-axial configuration, the AoLP remains approximately constant across both rotation angles, indicating substantial suppression of the net birefringent effect due to the orthogonal alignment of the optical axes. This response is consistent with the expected cancellation of phase retardation in the cross-oriented stacking geometry.

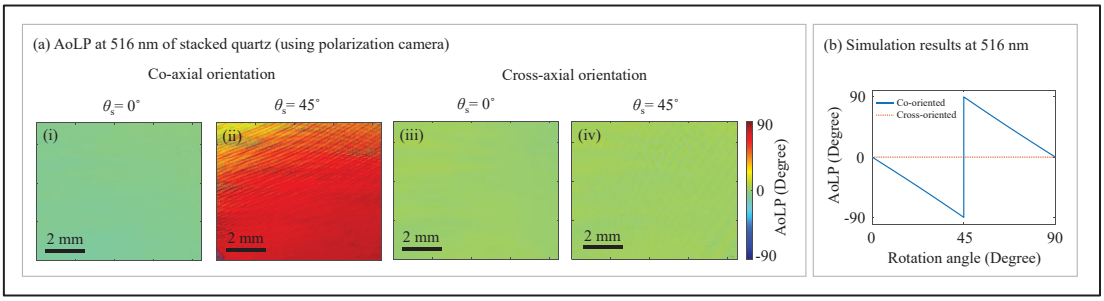

Figure A5.3 (a) Experimentally obtained AoLP maps at 516 nm for the stacked quartz sample: (i–ii) co-axial orientation at 0°, and 45°, and (iii–iv) cross-axial orientation at 0°, and 45°. (b) Corresponding simulation results showing AoLP as a function of rotation angle for a 1 mm stacked quartz sample at 516 nm for both co-axial and cross-axial orientation

Numerical simulations performed using a birefringence value of Δn = 0.009 (Ghosh, 1999) reproduce the main trends observed experimentally. The corresponding simulated AoLP response at 516 nm is shown in Fig. A5.3(b), demonstrating qualitative agreement with the experimental measurements and supporting the interpretation of the visible wavelength polarimetric results.

5.14 Appendix-E: Simulated DoLP and AoLP dependence on birefringence and sample rotation

Numerical simulations were performed to investigate the dependence of the DoLP and the AoLP on the sample rotation angle and birefringence at a center frequency of 0.41 THz. The simulations considered two stacked birefringent plates, each with a thickness of 0.5 mm, arranged in both co-axial and cross-axial configurations. The birefringence Δn was varied from 0.02 to 0.1.

Figure A5.4(a) shows the simulated DoLP response for the co-axial configuration. A pronounced modulation of DoLP is observed as a function of rotation angle, with a minimum occurring near 45°. The depth of this modulation increases with increasing birefringence, indicating enhanced polarization sensitivity for stronger birefringent contrast. In contrast, for the cross-axial configuration shown in Fig. A5.4(b), the DoLP remains close to unity across

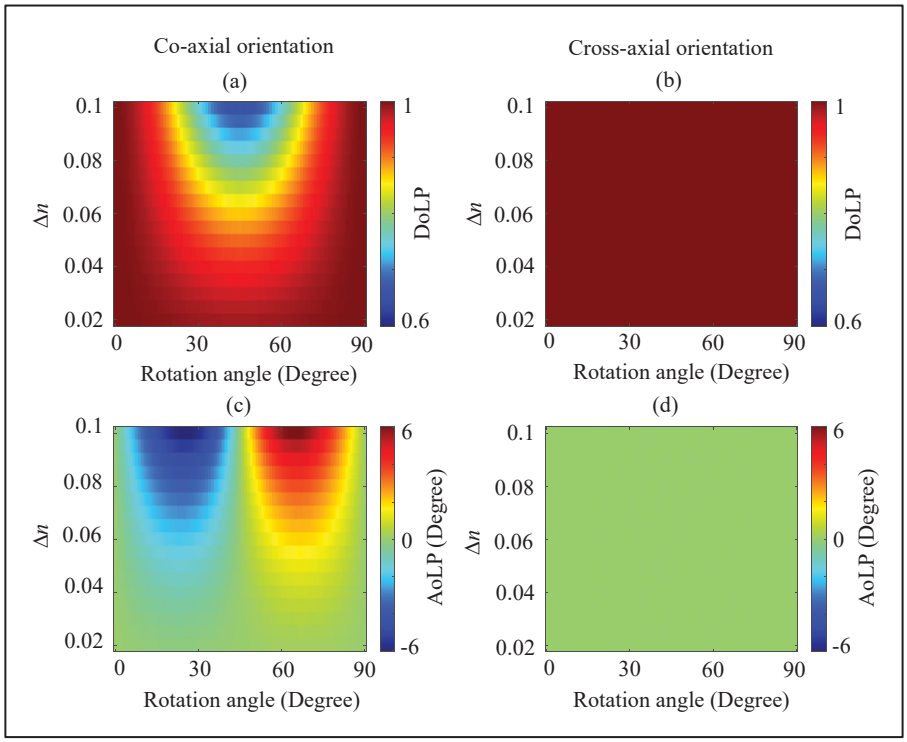

Figure A5.4 Simulated DoLP as a function of sample rotation angle by varying birefringence in (a) co-axial and (b) cross-axial configurations of two 0.5-mm-thick birefringent sample. The corresponding AoLP responses as a function of rotation angle for different birefringence values are shown in (c) co-axial and (d) cross-axial configurations

the full range of rotation angles, reflecting effective compensation of birefringent phase retardation due to the orthogonal alignment of the optical axes.

The corresponding AoLP simulations are presented in Fig. A5.4(c–d). For the co-axial configuration (Fig. A5.4(c)), the AoLP exhibits a characteristic angular dependence, remaining close to 0° at rotation angles of 0°, 45°, and 90°, while showing pronounced extrema near 22.5° and 67.5°. The magnitude of these AoLP variations increases as the birefringence increases, consistent with stronger phase retardation. In contrast, for the cross-axial configuration (Fig. A5.4(d)), the AoLP remains approximately constant at 0° over all rotation angles and birefringence values, indicating suppression of net polarization rotation.

These simulations further support the interpretation of the experimental THz polarimetric imaging results by illustrating the distinct DoLP and AoLP signatures associated with co-axial and cross-axial birefringent stacking geometries.

5.15 Appendix-F: Line profile analysis of experimental polarimetric maps

To further illustrate the agreement between experimental and expected polarimetric responses, representative line profiles extracted from the raster-scanned maps are presented in Fig. A5.5. The profiles are taken along the indicated dashed line and capture the spatial variation across the structured region. A consistent correspondence in the overall trend, characteristic features, and relative contrast is observed, confirming that the reconstructed polarimetric quantities follow the expected behavior.

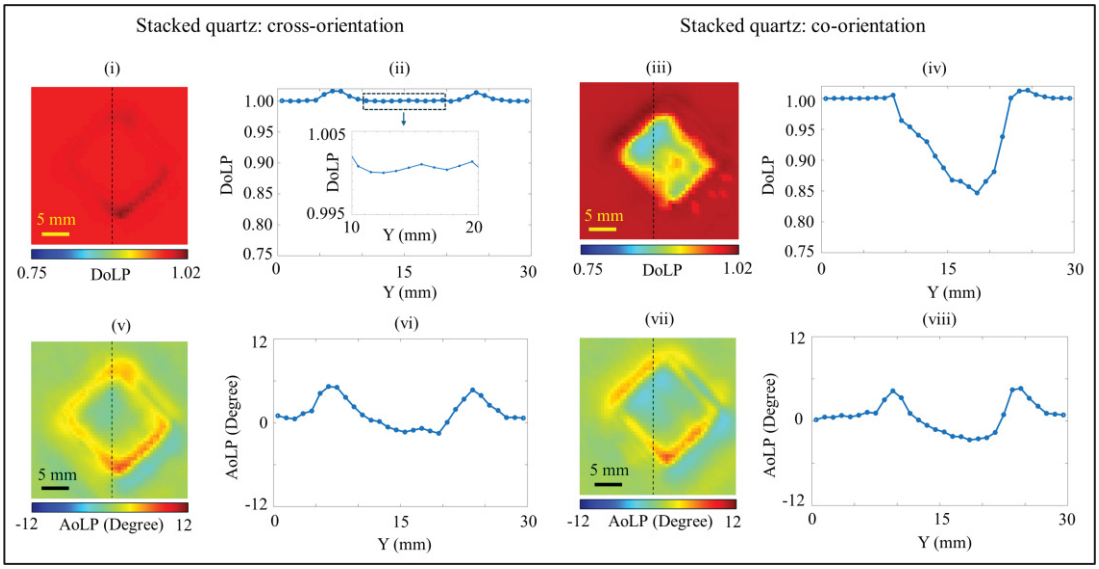

Figure A5.5 DoLP and AoLP imaging of stacked quartz at 0.23 THz. (i, iii) DoLP maps and (ii, iv) corresponding line profiles extracted along the y-axis for cross- and co-orientation, respectively, inset of (ii) presents a zoomed-in view of the DoLP line profile along the y-axis; (v, vii) AoLP maps and (vi, viii) corresponding line profiles for the same configurations

CONCLUSION

This thesis has systematically investigated the design, fabrication, and application of FSS for THz spectral and polarimetric control, with a particular emphasis on planar, reconfigurable, and scalable architectures compatible with practical deployment. Across four interconnected projects, the work demonstrates how engineered FSS geometries can enable tunable spectral filtering, polarization modulation, and multi-spectral polarimetric imaging using compact and intensity-based detection schemes.

As a first contribution, this thesis introduces and experimentally validates a mechanically reconfigurable inductive metallic checkerboard FSS. By laterally shifting two identical checkerboard layers, controllable tuning of the transmission spectrum was achieved without altering the unit-cell geometry or introducing active components. The investigation further revealed polarization-dependent effects arising from relative displacement, highlighting the sensitivity of checkerboard-based FSS responses to geometric symmetry and alignment. This work establishes a simple and robust method for achieving tunable THz filtering through mechanical reconfiguration.

The second contribution introduces a Moiré-based reconfiguration technique applied to an additively manufactured FSS to achieve mechanically reconfigurable spectral control. Through controlled relative rotation of two identical FSS layers, the system exhibited tunable spectral responses governed by Moiré interference. Analytical modeling, numerical simulations, and experimental measurements collectively demonstrated that Moiré-based reconfiguration provides a powerful and scalable approach for achieving spectral tunability while preserving fabrication simplicity. This chapter further underscores the feasibility of printable and additively manufactured FSS technologies for mass-producible THz devices.

As a third contribution, the focus shifts to polarization-sensitive FSS designs for reconfigurability, where two distinct geometries a rectangular-slot FSS and an asymmetric C-shaped FSS are fabricated using laser-cutting techniques and systematically characterized. The results revealed fundamentally different polarization dependent reconfigurability mechanisms associated with symmetric and asymmetric unit-cell designs. While the rectangular-slot FSS

operated effectively as a frequency-selective polarizer, the C-shaped FSS enabled polarization-dependent tunable band-pass behavior. This chapter demonstrates how geometric anisotropy can be exploited to tailor polarization responses within specific THz frequency bands.

As a final contribution, this thesis concludes by integrating polarization-sensitive FSSs into a compact, multispectral THz polarimetric imaging system based solely on intensity measurements. By employing PS-FSS elements as combined spectral filters and polarization analyzers, the proposed system enables fast and precise extraction of polarization metrics such as the degree and angle of linear polarization without phase-resolved detection. Experimental imaging of anisotropic samples confirmed strong polarization contrast across multiple discrete frequencies, demonstrating the practicality of the approach for fast, robust, and industrially relevant THz polarimetric imaging.

Collectively, the results presented in this thesis establish FSSs as versatile and powerful building blocks for THz spectral and polarimetric systems. The demonstrated approaches emphasize simplicity, mechanical reconfigurability, and fabrication scalability, offering clear pathways toward low-cost, high-throughput, and application-driven THz devices. This work contributes to advancing practical THz technologies by bridging fundamental electromagnetic design with manufacturable solutions suitable for real-world deployment.

RECOMMENDATIONS

The results presented in this thesis demonstrate the feasibility of compact, frequency-selective, and polarimetric THz systems, as well as simplified detection architectures. Building on this foundation, several research directions can be pursued to further enhance system performance, scalability, and applicability across both industrial and scientific domains.

First, future work could explore the development of advanced anisotropic FSSs, particularly C-shaped and rectangular-shaped unit-cell geometries. These asymmetric designs offer enhanced polarization sensitivity, tunable resonance behavior, and stronger field confinement. By exploiting geometric asymmetry and orientation-dependent resonances, such FSS structures could enable improved transmission contrast, and tailored spectral responses.

Second, while this thesis primarily investigates a Schottky-based polarimetric spectrometer, future systems could incorporate CMOS-based detectors with polarization-insensitive architectures. When combined with polarization-selective FSS elements, CMOS detectors could offer a low-cost, scalable alternative while maintaining polarimetric capability through external modulation. Such an approach would leverage the advantages of CMOS technology including integration, speed, and manufacturability without requiring polarization sensitivity at the detector level.

Third, the use of narrowband frequency-selective polarizers represents an important opportunity for improving measurement accuracy. Narrower spectral bandwidths would reduce frequency averaging effects inherent in broadband detection, thereby enabling more precise birefringence and anisotropy measurements. This would be particularly beneficial for materials with strongly frequency-dependent polarization responses.

Fourth, although the proposed system demonstrates operation across up to four discrete frequency bands, future implementations could significantly increase the number of accessible frequencies. Advances in fabrication precision, optimized material selection, and improved optical design such as enhanced beam collimation and spectral isolation could enable densely

packed multi-band FSS architectures, facilitating richer multispectral polarimetric analysis within a single compact platform.

Fifth, a potential extension of the proposed multispectral polarimetric THz system is the adoption of single-pixel imaging techniques to eliminate raster scanning while maintaining system simplicity. By combining structured illumination or coded frequency-selective masks with intensity-based detection, spatial, spectral, and polarization information could be computationally reconstructed using inverse modeling or compressed sensing approaches. Such an implementation would enable compact, cost-effective polarimetric imaging without the need for detector arrays, and could significantly improve acquisition speed for industrial inspection applications.

Finally, while a high-speed data acquisition card was employed in this work to ensure precise and reliable signal capture, future cost-optimized systems could replace this component with audio-grade sound cards or other low-cost acquisition solutions. Such alternatives would further reduce system cost and complexity, making the technology more accessible for educational, industrial, and field-deployable applications, particularly where ultra-high acquisition rates are not required.

Overall, these possible directions highlight the strong potential for continued development of compact, low-cost, and scalable THz polarimetric systems, reinforcing the broader objective of transitioning THz technologies from laboratory-based instruments toward practical, mass-producible platforms.

ANNEX I

FABRICATION AND CHARACTERIZATION OF PRINTED TERAHERTZ SPIRAL ZONE PLATES

This annex is based on an extended version of the following published conference paper by providing a more comprehensive theoretical description, additional numerical simulations, and expanded experimental characterization: Redwan Ahmad, Léo Guiramand, Mariia Zhuldybina, Xavier Ropagnol, Ngoc Duc Trinh, Chloé Bois, and François Blanchard "Printed Terahertz Spiral Zone Plate for Vortex Beam Generation," 2023 48th International Conference on Infrared, Millimeter, and Terahertz Waves (IRMMW-THz), Montreal, QC, Canada, 2023, pp. 1-2.

Overview

This annex presents the design, fabrication, and characterization of printed THz spiral zone plates (SZPs) for vortex beam generation. The work emphasizes the use of low-cost, scalable printable electronics techniques to realize phase-engineered THz diffractive optics, demonstrating the feasibility of mass-producible THz phase-control components. Vortex beam generation is experimentally validated using a THz microbolometric camera operating in both transmission and reflection modes, confirming effective wavefront manipulation through printed metastructures.

I.1 Introduction

Optical and THz vortex beams carrying orbital angular momentum (OAM) exhibit a helical phase structure that enables advanced wavefront control beyond conventional amplitude and polarization modulation (Imai et al., 2014; Erhard et al., 2017). Such beams have attracted growing interest for applications in imaging, beam shaping, and information encoding. In the THz regime, however, the generation and characterization of vortex beams remain challenging due to bulky optical components and limited fabrication options.

Among the various vortex-generating techniques, spiral zone plates offer a compact and efficient solution by simultaneously enabling focusing and azimuthal phase modulation (Zhang

et al., 2020; Gao et al., 2011). Their planar geometry makes them particularly attractive for THz systems. Recent progress in printable electronics has further enabled the realization of low-cost, large-area THz diffractive and phase-engineered structures using additive fabrication techniques.

In this annex, printed THz spiral zone plates fabricated using scalable printable electronics processes are investigated as a supplementary study on THz phase engineering. The SZPs are experimentally characterized using THz imaging, including validation of vortex beam generation in both transmission and reflection configurations with a THz microbolometric camera. This annex supports the overall thesis objective by demonstrating the feasibility of using printable electronics to realize planar THz devices for wavefront manipulation, further highlighting the potential of scalable and low-cost fabrication techniques for mass-producible THz functional components.

I.2 Simulation results

To investigate phase manipulation and vortex beam generation in the THz regime, a set of spiral zone plates with different topological charges was designed. The structures were engineered to operate at a target frequency of 0.36 THz and to produce a focused vortex beam at a focal distance of 2.0 cm. By varying the topological charge, the influence of orbital angular momentum order on the resulting vortex beam characteristics could be systematically examined. The corresponding design schematics have been depicted in Fig. A I-1(a-c).

Each spiral zone plate was implemented within a square aperture of 3×3 cm^2 and realized on a flexible polyethylene terephthalate substrate, selected for its mechanical robustness, low cost, and compatibility with printable electronics fabrication processes. The planar and flexible nature of the substrate enables scalable manufacturing and facilitates integration into compact THz optical systems.

The phase profile of a spiral zone plate combines a focusing term with an azimuthal phase modulation and can be expressed in polar coordinates (r,φ) as

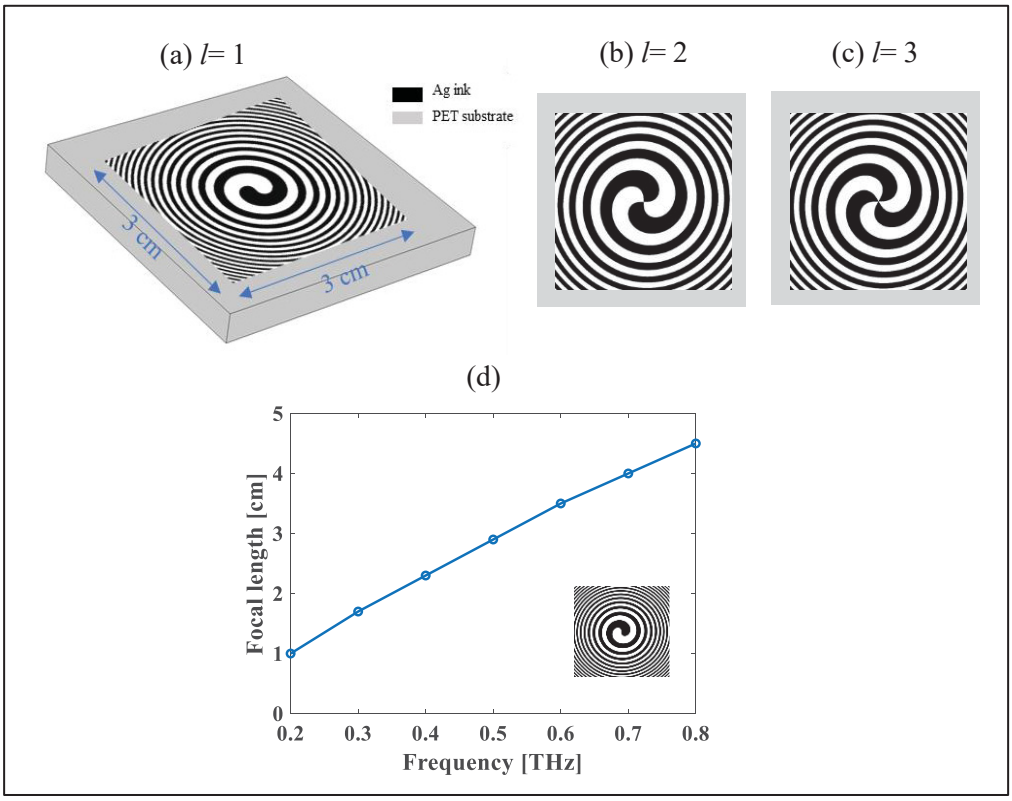

Figure-A I-1 (a) Graphical representation of the spiral zone plate designed for topological charge l=1; (b–c) graphical representations of the spiral zone plate corresponding to topological charges l=2 and 3, respectively; and (d) focal length as a function of the operating frequency

$$SZP(r,\varphi) = \exp\left(il\varphi - \frac{i\pi r^2}{\lambda f}\right) \tag{A-I-1}$$

where l denotes the topological charge associated with the orbital angular momentum state, λ is the incident THz wavelength, and f is the designed focal length of the spiral zone plate. The quadratic radial phase term produces focusing behavior analogous to a Fresnel zone plate, while the azimuthal term introduces a phase singularity that gives rise to a vortex beam with a characteristic on-axis intensity null.

This combined phase functionality allows spiral zone plates to simultaneously control the spatial phase and angular momentum of THz waves using a single planar diffractive element,

making them particularly attractive for compact and fabrication-tolerant phase-engineering applications.

Numerical simulations were performed using the finite-difference time-domain (FDTD) method implemented in Lumerical software to analyze the intensity and propagation characteristics of the vortex beams generated by the spiral zone plates over a frequency range from 0.2 to 0.8 THz. The simulations reveal a clear frequency-dependent focusing behavior, whereby the focal length increases monotonically with increasing operating frequency (see Fig. A I-1(d)). This trend is observed consistently for all analyzed topological charges, indicating that the dispersive focusing behavior is an inherent property of the spiral zone plate design rather than a function of the vortex order.

Following simulations were performed to investigate the amplitude and phase distributions generated by the printed spiral zone plates at their designed focal plane for different topological charges. For the case of l=1, the simulated amplitude distribution at the focal plane exhibits a pronounced intensity null at the beam center, which is a characteristic signature of an optical vortex carrying orbital angular momentum. Correspondingly, the phase distribution reveals a single helical phase singularity, indicating a 2π phase winding around the beam axis, as shown in Fig. A I-2(a,d). This confirms that the printed SZP successfully imparts the intended spiral phase profile to the incident THz wave.

Similar simulations were carried out for higher-order topological charges. For l=2, the phase distribution displays two intertwined spiral phase arms, corresponding to a 4π phase accumulation, while the associated amplitude distribution maintains a central intensity minimum, as depicted in Fig. A I-2(b,e). In the case of l=3, three distinct spiral phase arms are observed in the phase map, corresponding to a total azimuthal phase accumulation of 6π, with the amplitude distribution again exhibiting a central null, as shown in Fig. A I-2(c,f). These results demonstrate that the SZP design enables controlled generation of higher-order vortex beams with increasing topological charge.

To further examine the focusing behavior of the SZP-generated vortex beams, the electric-field amplitude distribution was analyzed along the propagation (z) direction over a range from 15

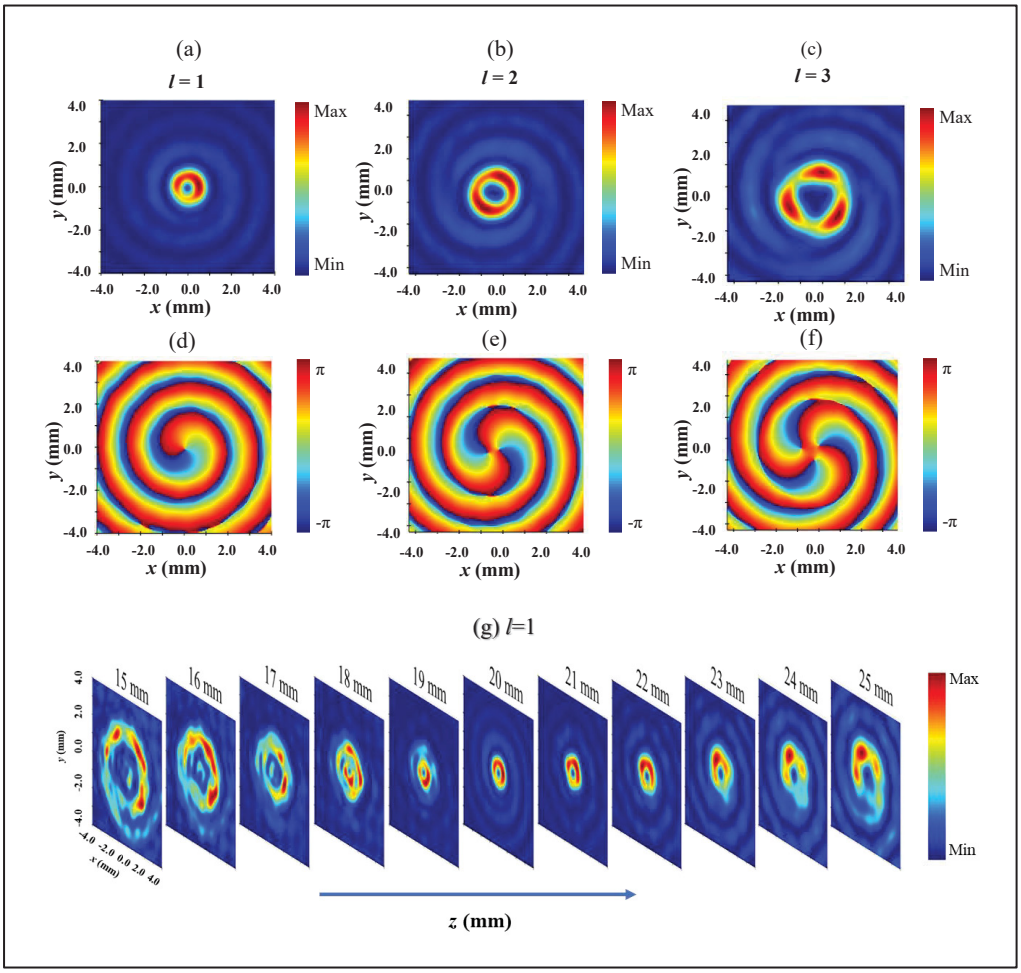

Figure-A I-2 (a–c) Simulated electric-field distributions of the spiral zone plate for topological charges l=1, l=2 and l=3; (d–f) corresponding phase distributions.
(g) Electric-field distribution along the propagation (z) axis from 15 to 25 mm, showing the focused vortex at approximately 20 mm

mm to 25 mm, as presented in Fig. A I-2(g). The results show a clear convergence of the vortex beam, with the strongest field confinement occurring at approximately 20 mm, corresponding to the designed focal length of the SZP. At this position, a well-defined focused vortex with a central intensity null is observed, confirming both the focusing functionality and the preservation of the vortex phase structure upon propagation.

Overall, these FDTD simulation results validate the effectiveness of the printed spiral zone plates in simultaneously achieving phase modulation, vortex beam generation, and focusing in

the THz regime, and provide a solid theoretical foundation for the experimental demonstrations presented in this annex.

I.3 Fabrication and experimental results

The spiral zone plates were fabricated using an industrial roll-to-roll (R2R) continuous press combined with flexographic printing on a flexible substrate, employing a silver (Ag) nanoparticle ink (PFI-600, NovaCentrix, Austin, TX, USA). Following printing, the SZPs were dried using hot-air treatment at temperatures up to 100° C. The resulting printed structures exhibited an electrical conductivity of 4.4×10^6 S/m. The thicknesses of the printed SZP pattern and the PET substrate were 352 nm and 125 µm, respectively. Representative photographs of the fabricated SZPs are presented in Fig. A I-3(i-iii).

To characterize the fabricated spiral zone plates, the THz-SZP was placed in a collimated THz beam with a diameter of approximately 2 inches, and the resulting intensity distributions were measured at the focal plane using a bolometric THz camera (MICROXCAM-384i-THz). The measurements were performed at the focal position f immediately downstream of the THz-SZP. In this experimental setup, intense broadband THz pulses were generated using a lithium niobate ($LiNbO_3$) crystal (Guiramand et al., 2022).
For each SZP sample, the corresponding vortex beam was recorded at its designed focal plane, which depends on the operating frequency of the zone plate. Owing to the broadband nature of

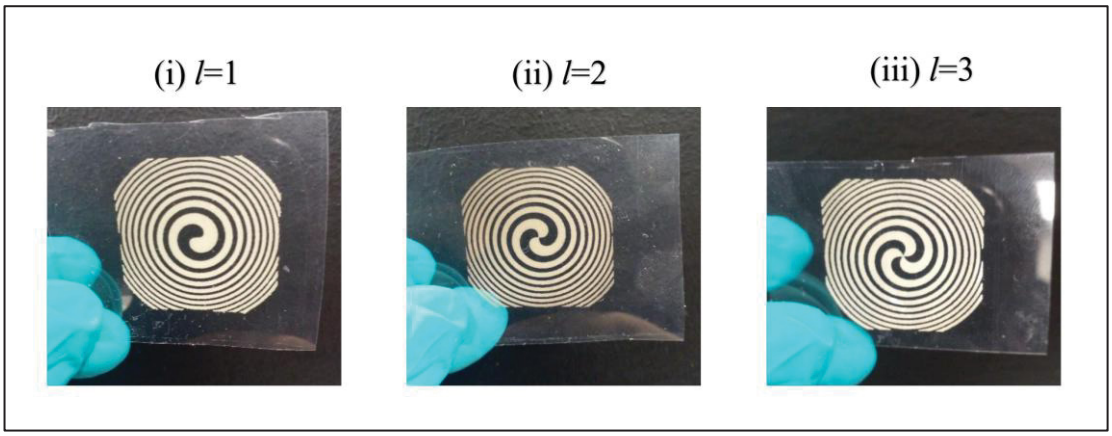

Figure-A I-3 Fabricated spiral zone plate based on flexography for (i) l=1, (ii) l=2 and (iii) l=3

the THz source, a THz bandpass filter (BPF) (Ahmad et al., 2023) was introduced into the beam path immediately after THz generation to spectrally select the desired frequency component. The employed BPF had a center frequency of 0.36 THz with a bandwidth of 180 GHz. A schematic view of the experimental configuration is shown in Fig. A I-4(i). This filtering step ensured that the experimentally observed focal behavior corresponded to the simulated operating conditions.

Figures A I-4(ii–iv) present the experimentally measured field distributions in the *xy* plane at the focal point in transmission mode for topological charges l=1, l=2 and l=3, respectively.

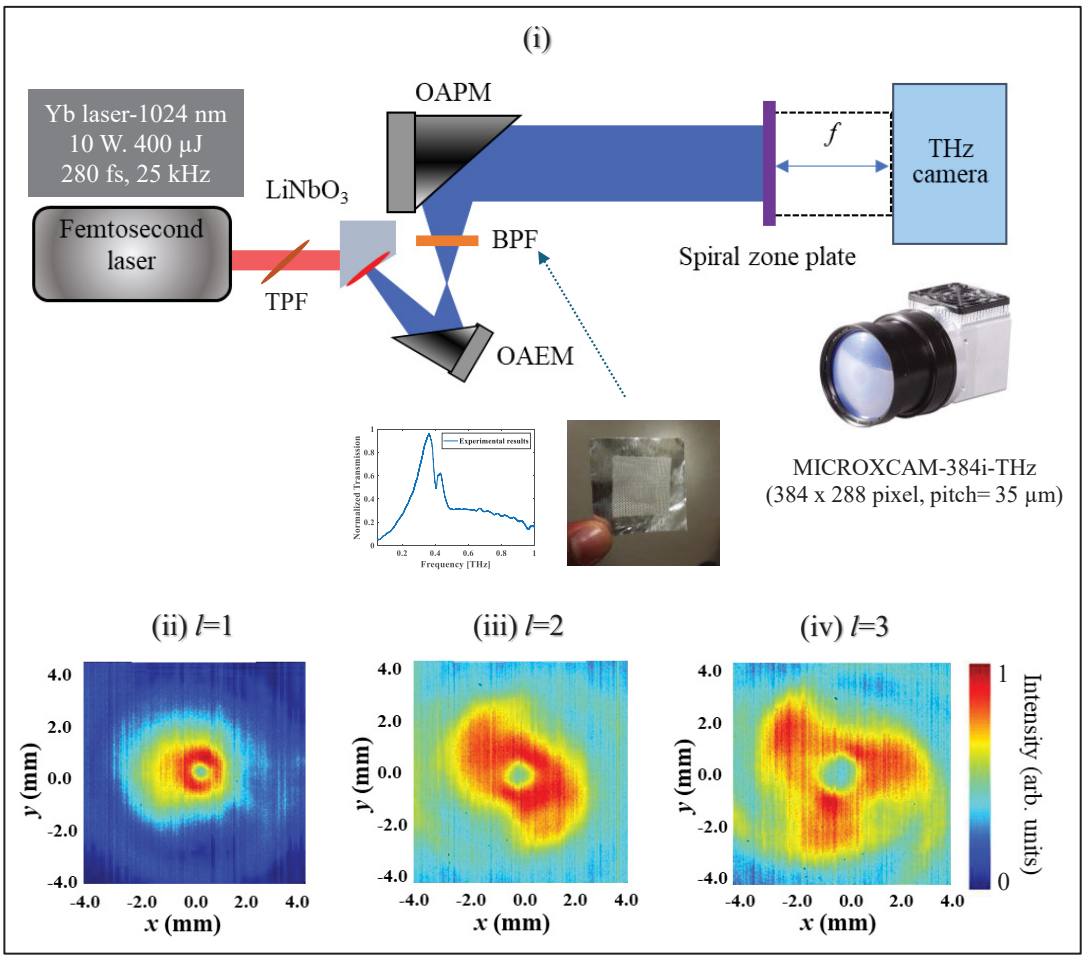

Figure-A I-4 (i) Layout of the experimental setup for transmission-based characterization of the spiral zone plate; (ii–iv) measured field distributions obtained using a THz microbolometric camera for topological charges (ii) l=1, (iii) l=2, and (iv) l=3. TPF stands for tilted pulse front technique

The measured vortex patterns exhibit features consistent with the corresponding simulated results shown in Fig. A I-2, indicating good agreement between experiment and simulation. Minor discrepancies between simulation and experiment can be attributed primarily to the finite bandwidth of the THz source and filter, as well as fabrication tolerances inherent to the printing process.

To further investigate reflection-based vortex beam generation using the spiral zone plate, the experimental configuration was modified accordingly, and the THz microbolometric camera was repositioned to record the reflected field, as illustrated in Fig. A I-5(i). This rearranged setup enables direct observation of the vortex beam formed upon reflection from the SZP, providing an alternative measurement geometry to the transmission-based configuration discussed earlier.

The experimentally obtained amplitude distribution measured with the THz camera in the reflection mode is shown in Fig. A I-5(ii). The recorded field distribution exhibits a clear intensity null at the beam center, which is a defining characteristic of vortex beams. The

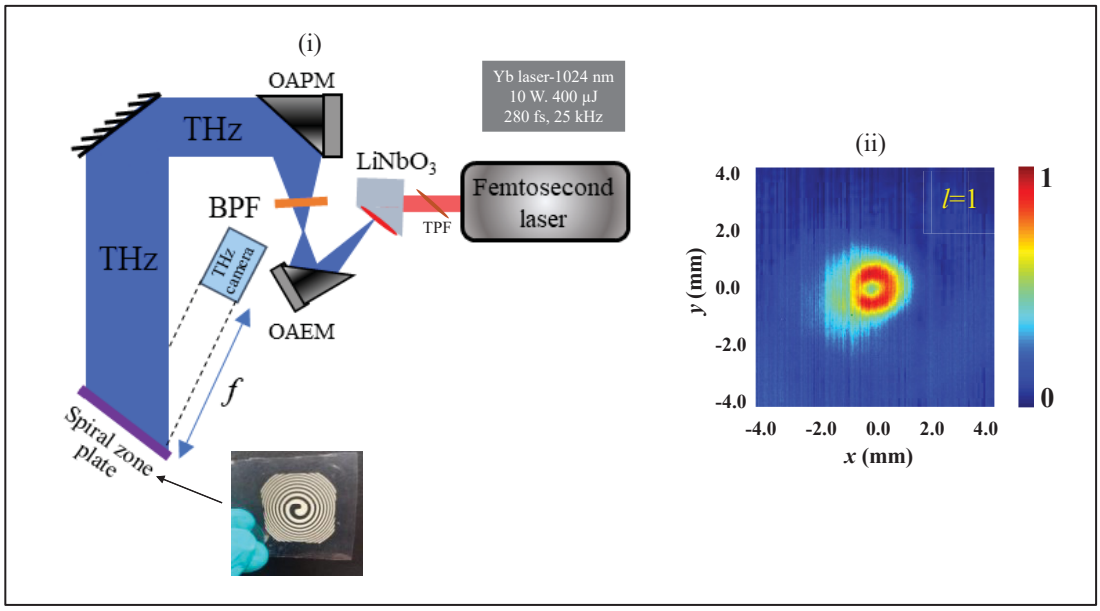

Figure-A I-5 (i) Layout of the experimental setup for reflection-based characterization of the spiral zone plate; (ii) measured field distribution for topological charge l=1 obtained using a THz microbolometric camera

presence of this central null in the reflected configuration confirms that the SZP effectively imparts the desired spiral phase profile under reflection, consistent with the behavior observed in transmission.

These results demonstrate that the printed SZPs support vortex beam generation in both transmission and reflection geometries, thereby extending their functional versatility. The ability to operate in reflection as well as transmission provides a more comprehensive framework for SZP-based THz wavefront engineering and may facilitate integration into compact or folded THz optical systems.

I.4 Summary

This work demonstrates the feasibility of generating THz vortex beams using spiral zone plates fabricated through printable electronics techniques. By combining numerical modeling with experimental characterization using a THz imaging camera, the phase-engineering capability of flexography-printed spiral zone plates is systematically validated. The results highlight printable electronics as a scalable and cost-effective approach for producing large-area THz diffractive optics and suggest potential integration of such phase-manipulating elements into future THz systems for imaging, sensing, and wireless communication applications.

ANNEX II

TERAHERTZ POLARIMETRIC SPECTROMETER USING CMOS DETECTOR

This annex is based on extended versions of the following two conference papers: R. Ahmad, F. Blanchard, and R. Al Hadi, “Characterization and Polarization Sensitivity Analysis of CMOS Terahertz Detector," *Photonics North (PN)*, 2025; and R. Ahmad, X. Ropagnol, R. Al Hadi, and F. Blanchard, “Terahertz Polarimetric Spectrometer Using CMOS Detector,” *International Topical Meeting on Microwave Photonics (MWP)*, 2025.

Overview

This annex presents a compact THz polarimetric spectrometer based on a CMOS detector with a linearly polarized antenna, enabling polarization-sensitive detection. Unlike the Schottky-based polarimetric spectrometer described in the main thesis, where the detector is polarization-insensitive and polarization modulation is achieved using a polarization-sensitive FSS wheel, the CMOS detector employed here provides intrinsic polarization selectivity. The system operates at two discrete frequency bands and measures four linear polarization orientations. Simulation results are first analyzed and subsequently validated using experimental data. The primary objective of this annex is to evaluate the response of distinct PS-FSS analyzer orientations using a polarization-sensitive detector and to examine the resulting polarization behavior, thereby highlighting the differences between polarization-sensitive and polarization-insensitive detection schemes.

II.1 Introduction

Polarization-sensitive THz measurements provide valuable insight into the anisotropic and birefringent properties of materials (Zhou et al., 2012; Castro-Camus et al., 2006). While the main chapters of this thesis focus on a Schottky-diode-based THz polarimetric spectrometer employing polarization-insensitive THz detector, an alternative approach based on polarization-sensitive detection is explored here using a CMOS-based THz detector with a linearly polarized antenna.

As an initial step, the CMOS THz detector is characterized using a frequency-tunable continuous-wave (CW) THz system to evaluate its response as a function of polarization angle. This characterization establishes the intrinsic polarization sensitivity of the detector and provides a foundation for its use in polarization-resolved measurements. Following this analysis, the same CMOS detector is integrated into a compact multispectral THz polarimetric spectrometer by incorporating a frequency-selective polarizer, enabling simultaneous spectral and polarization discrimination within a simplified system architecture.

Unlike polarization-insensitive detectors, where polarization contrast is introduced exclusively through external modulation elements, the CMOS detector employed in this work incorporates a linearly polarized antenna, providing inherent polarization selectivity at the detection stage. However, as in the Schottky-based polarimetric spectrometer, polarization-resolved measurements are realized through the combined use of a PS-FSS wheel, which enables controlled polarization and spectral discrimination. The primary objective of this study is to evaluate the feasibility of extracting polarization-dependent responses, specifically through the analysis of the PS-FSS analyzer orientations, using a polarization-sensitive CMOS detector, and to examine the resulting polarization behavior across two distinct frequency bands. Numerical simulations are first performed to analyze the expected response, followed by experimental measurements that validate the simulated predictions.

The results discussed in this annex highlight the differences between detector-intrinsic and externally modulated polarization sensitivity and demonstrate the potential of CMOS-based THz detectors for compact, scalable, and cost-effective polarimetric spectrometer implementations.

II.2 Characterization of CMOS THz detector

The CMOS THz detector investigated in this study was fabricated using standard silicon technology. The detector architecture consists of differential NMOS detectors coupled to a linearly polarized antenna, which is implemented within the back-end-of-line (BEOL) metal stack. The antenna radiates through the silicon substrate and can be excited in different modes depending on the incident polarization state. To enhance the effective collection efficiency, the

chip was mounted on a silicon lens, thereby increasing the effective collection angle and optical throughput of the detector. In addition, a baseband amplifier was integrated on-chip to amplify the detected signal and facilitate interfacing with the data acquisition system (Hadi et al., 2019).

The layout and image of the experimental setup used for detector characterization is illustrated in Figure-A II-1(a-b). The broadband CW THz response of the CMOS detector was measured using a commercial TOPTICA TeraScan system. A TPX lens placed immediately after the THz emitter was used to collimate the beam and ensure efficient coupling to the silicon lens attached to the CMOS sensor. During the initial measurements, the polarization orientation of the THz emitter was aligned parallel to that of the detector antenna. The corresponding normalized detector responses are shown in Fig. A II-1(c) together with the response of a CW photomixer receiver. As evident from Fig. A II-1(c), the CMOS THz detector exhibits a

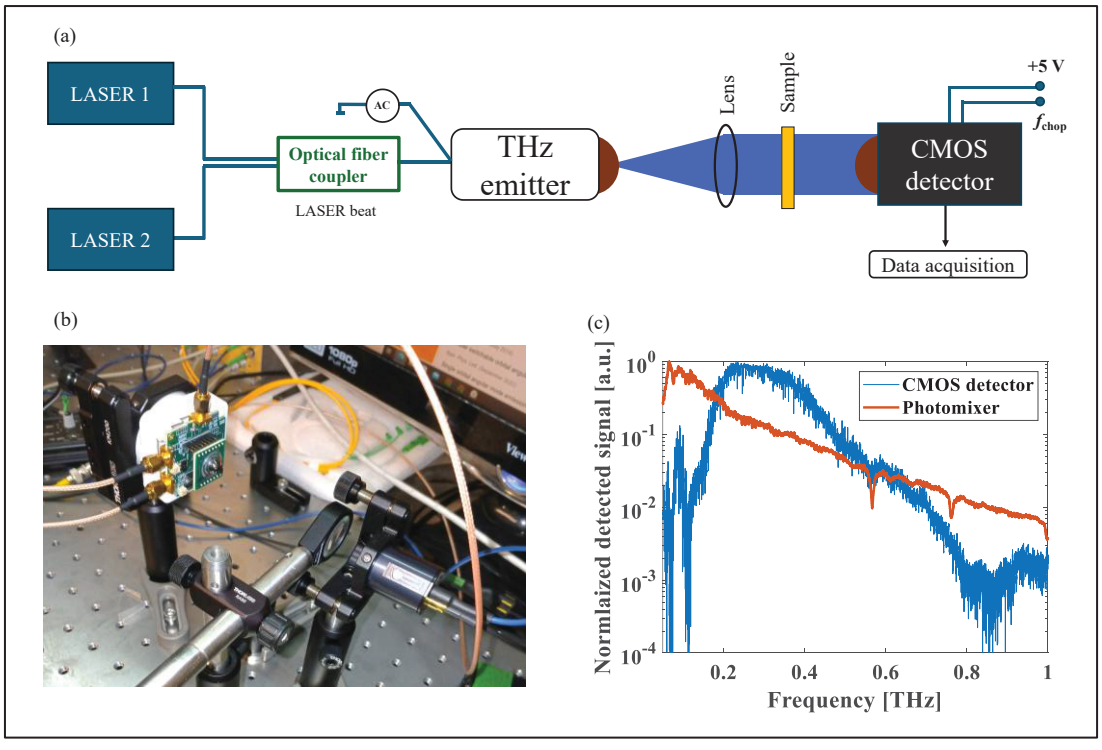

Figure-A II-1 (a) Experimental setup for the characterization of a CMOS detector using a continuous-wave (CW) THz source; (b) photograph of the experimental setup; and (c) comparison of the normalized detected signals of the CMOS detector and a photomixer, highlighting the broadband response

comparable dynamic response over the measured frequency range, indicating its suitability for broadband CW THz detection. These results indicate that the CMOS detector provides sufficient sensitivity and stability for spectroscopic measurements and suggest that it represents a strong candidate in applications similar to those reported in (Sebastian et al., 2026), particularly where compactness, scalability, and system integration are critical.

II.3 Methodology

II.3.1 Polarimetric model and intensity expression

The detected intensity $P_{(\alpha)}$ corresponding to an analyzer orientation α is expressed using the Jones matrix formalism as (Menzel et al., 2015, Neshat & Armitage, 2012):

$$p_{(\alpha)} = \left\| \begin{bmatrix} \cos^2(\alpha) & \cos(\alpha)\sin(\alpha) \\ \cos(\alpha)\sin(\alpha) & \sin^2(\alpha) \end{bmatrix} \cdot \left[J_{rotated} E_{in} \right] \cdot D \right|^2 \qquad \text{(A-II-1)}$$

where E_{in} denotes the incident THz electric-field vector and D represents the effective detection vector of the CMOS THz detector. Both the THz emitter and the CMOS detector employ linearly polarized antennas, ensuring sensitivity to polarization changes induced by the sample. The polarization evolution introduced by a birefringent sample is described by the rotated Jones matrix J_{rotated}, which accounts for the phase retardation between orthogonal axes as a function of the sample rotation angle θ.

II.3.2 Polarimetric response and Stokes parameter extraction

The rotated Jones matrix describing the polarization response of a birefringent sample is given by (Menzel et al., 2015; Neshat & Armitage, 2012):

$$J_{rotated(\theta)} = \begin{bmatrix} \cos\theta & -\sin\theta \\ \sin\theta & \cos\theta \end{bmatrix} \begin{bmatrix} e^{i\frac{\Delta\phi}{2}} & 0 \\ 0 & e^{-i\frac{\Delta\phi}{2}} \end{bmatrix} \begin{bmatrix} \cos\theta & \sin\theta \\ -\sin\theta & \cos\theta \end{bmatrix} \qquad \text{(A-II-2)}$$

where $\Delta\phi$ is the phase retardation introduced by the birefringent material. This phase delay depends on the material birefringence, thickness, and operating frequency.

Normalized intensity responses measured at analyzer orientations of 0°, 45°, 90°, and 135° are used to extract the Stokes parameters. In the simulations, the analysis was performed at two representative frequencies, 0.33 THz and 0.41 THz, corresponding to the operating bands of the system. For each frequency, the sample was rotated from 0° to 180° in 10° increments, and the transmitted signals were recorded for analyzer angles of 0°, 45°, 90°, and 135°. The corresponding simulated intensity responses p_0, p_{45}, p_{90} and p_{135} at 0.33 THz and 0.41 THz are shown in Figs. A II-2(a) and A II-2(b), respectively. These responses illustrate the polarization-dependent transmission behavior of the system as a function of sample rotation angle at the selected frequencies.

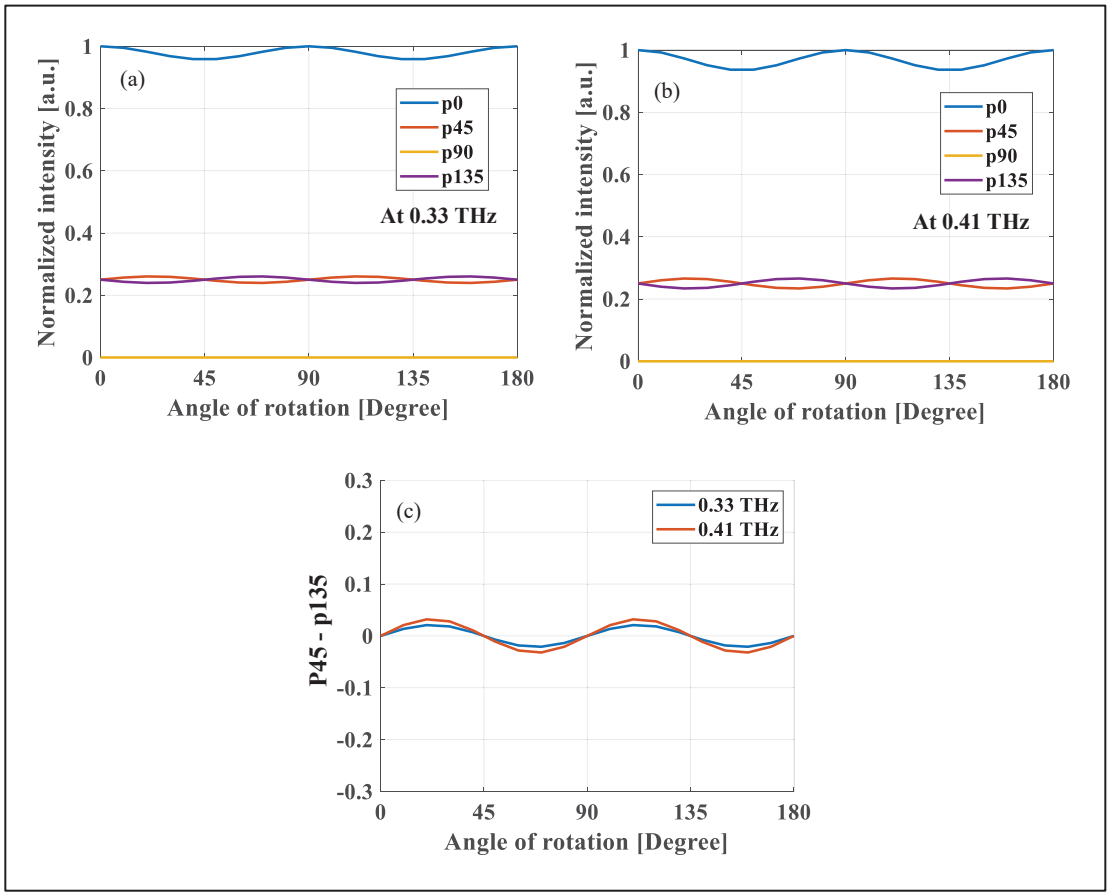

Figure-A II-2 Simulated normalized intensity as a function of the sample rotation angle for analyzer orientations of 0°, 45°, 90°, and 135° at (a) 0.33 THz and (b) 0.41 THz; (c) corresponding Stokes S_2 parameters for the two frequencies as a function of the sample rotation angle

Due to the intrinsically polarization-sensitive nature of the CMOS detector, the detected signal is strongly dependent on the alignment between the incident THz electric field and the detector's integrated antenna polarization axis. As a result, when the analyzer is oriented at 90°, the detected signal remains close to the noise floor and exhibits no observable modulation as the sample is rotated. Consequently, a direct evaluation of the Stokes parameter $S_1=p_0-p_{90}$ is not feasible in this configuration, since the p_{90} component does not reliably capture polarization-dependent variations.

This behavior highlights an important distinction between polarization-insensitive detection schemes and detector architectures with built-in polarization selectivity. While the CMOS detector enables compact and efficient polarization-sensitive measurements, its intrinsic polarization response limits the direct extraction of certain Stokes parameters (S_0, S_1) using conventional analyzer-rotation methods. Therefore, alternative reconstruction approaches based on intensity differences and combinations across multiple polarization states could be employed.

However, the Stokes parameter S_2 can be obtained from the difference between the 45° and 135° intensity components as

$$S_2 = P_{45} - P_{135} \tag{A-II-3}$$

The angular dependence of the Stokes parameter S_2 provides a direct measure of the polarization modulation induced by the birefringent sample and enables the extraction of polarization-dependent material properties. In particular, S_2 is sensitive to the relative phase difference introduced between orthogonal polarization components as the sample is rotated, making it a useful parameter for probing linear birefringence in anisotropic materials. As shown in Fig. A II-2(c), the evolution of S_2 with frequency reveals a systematic increase in modulation amplitude at higher frequencies. This behavior reflects the increasing phase retardation experienced by the THz wave as the optical path difference between the ordinary and extraordinary axes becomes larger with decreasing wavelength. Such a frequency-dependent trend is consistent with the expected response of a linearly birefringent medium, in which the phase retardation scales with both the birefringence and the operating frequency.

II.4 Experimental results

The experimental setup schematic and corresponding photograph are shown in Figure-A II-3(a-b). To ensure a well-defined polarization state, the THz radiation generated by a photoconductive antenna is first passed through a wire-grid polarizer placed before the sample. A rotatable metallic wheel incorporating PS-FSS is positioned between the sample and the linearly polarized CMOS THz detector. The PS-FSS wheel provides two distinct operating frequency bands, each realized at four angular orientations (0°, 45°, 90°, and 135°), enabling frequency- and polarization-resolved intensity measurements, as illustrated in Figure-A II-3(c).

The number of PS-FSS elements integrated on the metallic wheel can be extended to accommodate additional resonant frequencies, allowing polarization analysis over a broader

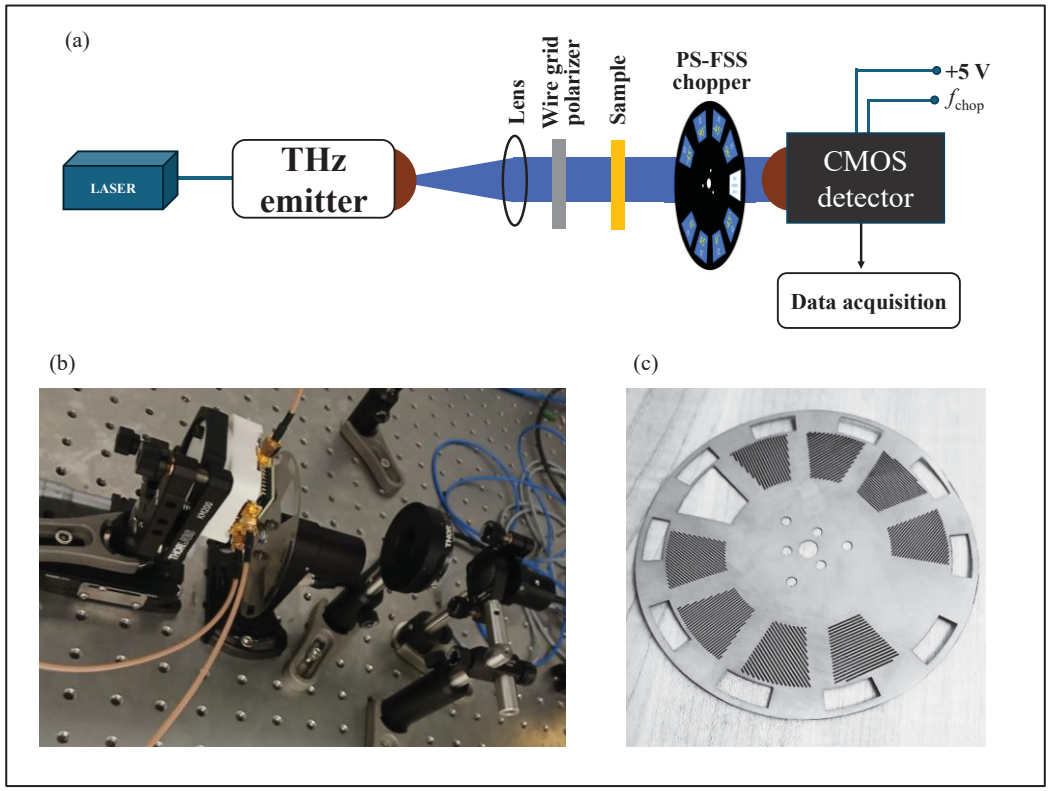

Figure-A II-3 (a) Schematic of the experimental setup; (b) photograph of the experimental setup; and (c) fabricated chopper wheel incorporating frequency-selective polarizers oriented at 0°, 45°, 90°, and 135° for two discrete frequencies of 0.33 THz and 0.41 THz

THz spectral range. The CMOS THz detector is biased at +5 V and operated with a modulation frequency of 10 kHz. An on-chip baseband amplifier enhances the detected signal for efficient interfacing with the data acquisition system. The recorded signals are acquired using an ultrafast data acquisition card and assembled into a ten-element intensity matrix, comprising two values corresponding to the open and blocked reference slots and eight values representing the four polarization orientations at two frequency bands. The complete polarization response matrix is obtained within a few seconds for each sample rotation angle.

To validate the system performance, a stacked 1-mm-thick *x*-cut quartz crystal was characterized as a birefringent sample. The sample was rotated from 0° to 180°, and the corresponding polarization-resolved intensities p_0, p_{45}, p_{90}, and p_{135} at the two operating

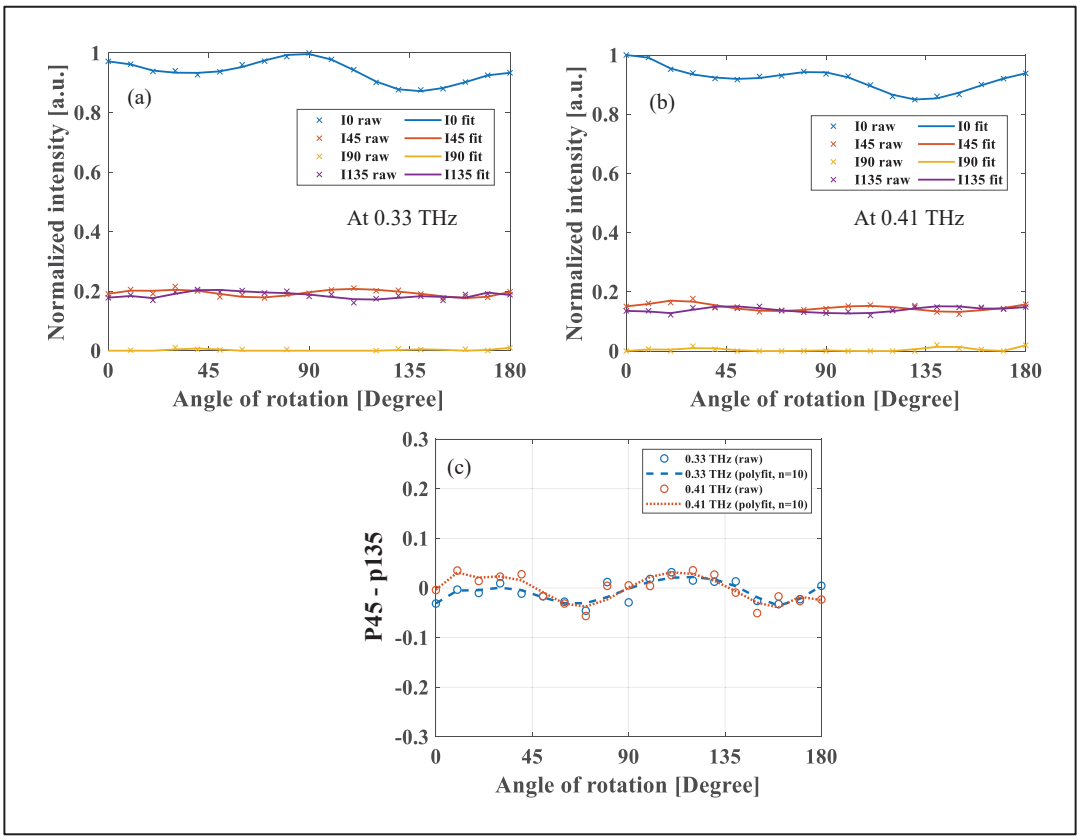

Figure-A II-4 Experimentally obtained normalized intensity as a function of the sample rotation angle for analyzer orientations of 0°, 45°, 90°, and 135° at (a) 0.33 THz and (b) 0.41 THz; (c) corresponding Stokes S_2 parameters for the two frequencies as a function of the sample rotation angle

frequencies are shown in Figure-A II-4(a-b). The experimental measurements exhibit strong agreement with the simulated responses. Using the differential intensities measured at 45° and 135°, the Stokes parameter S_2 was extracted for both frequency bands, as shown in Figure-A II-4(c). Two pronounced peaks are observed near 22.5° and 112.5°, with corresponding minima at 67.5° and 157.5°. The close agreement between experimental and simulated results confirms the accuracy and robustness of the proposed polarimetric spectrometer.

II.5 Conclusion

This annex has demonstrated the feasibility of implementing a compact THz polarimetric measurement approach using a CMOS-based THz detector with a linearly polarized antenna, combined with PS-FSS. Following an initial polarization characterization of the CMOS detector using a CW THz system, the same detector was successfully integrated into a multispectral polarimetric spectrometer operating at discrete frequency bands.

The results confirm that polarization-dependent responses can be reliably extracted using a polarization-sensitive detector, enabling the evaluation of Stokes parameters without relying on polarization-insensitive detection schemes. Although simplified in architecture, the presented approach captures key polarization features of birefringent materials and shows good agreement with simulation results. Overall, this annex supports the broader thesis objective by illustrating an alternative, scalable pathway toward fast, cost-effective, and frequency-selective THz polarimetric systems, with potential relevance for compact polarimetric sensing and imaging applications.

ANNEX III

IDENTIFICATION AND CHARACTERIZATION OF BIREFRINGENT MATERIALS USING TERAHERTZ PYROELECTRIC DETECTOR

Overview

In this annex, a simple THz polarimetric measurement approach using a pyroelectric detector is explored for static characterization of birefringent materials. A broadband photoconductive antenna serves as the THz source, while polarization information is obtained through external modulation combined with frequency-selective polarizers, enabling polarization analysis at selected THz frequency bands. Although the slow temporal response of the pyroelectric detector limits dynamic measurements, this method provides a cost-effective and conceptually simple reference platform, offering an alternative perspective to the faster Schottky- and CMOS-based polarimetric systems discussed in the main body of the thesis and annex respectively.

III.1 Introduction

To investigate anisotropic material properties such as birefringence and dichroism, THz polarimetric systems have been developed to analyze changes in the polarization state of THz radiation after interaction with matter (Kim et al., 2011). Numerous THz polarimetric techniques have been reported, demonstrating high accuracy and sensitivity; however, many rely on complex, bulky, and costly experimental setups, which restrict their practical deployment and broader accessibility (Norris et al., 2019; Zhang, et al., 2009; Morris et al., 2012).

In recent years, efforts have been directed toward simplifying THz polarimetric architectures by employing compact and cost-effective detectors. Among these, pyroelectric THz detectors are attractive due to their broadband response, room-temperature operation, and simple implementation. In this annex, a THz polarimetric measurement system based on a pyroelectric detector is presented as a supplementary and comparative study to the Schottky- and CMOS-based systems discussed in the main body of the thesis and annex respectively. The system

enables polarization-dependent transmission measurements by rotating the sample orientation from 0° to 180°, allowing the extraction of anisotropic material responses using a straightforward, intensity-based approach. Although limited by the inherently slow temporal response of pyroelectric detectors, this configuration provides a simple and cost-effective platform for static THz polarimetric characterization and serves as a useful reference for evaluating detector-dependent trade-offs in THz polarimetric systems.

III.2 Methodology

A standard polarimetric configuration employing two wire-grid polarizers was implemented to determine the polarization state of THz electromagnetic waves. According to Malus's law, the transmitted intensity $I(\theta)$ after the second polarizer depends on the relative orientation of the polarizers and is given by

$$I(\theta) = I_0 \cos^2(\theta_i) \tag{A-III-1}$$

where I_0 is the incident intensity and θ_i denotes the angle between the polarization axis of the incident wave and the transmission axis of the analyzer. After the second wire-grid polarizer, the transmitted THz intensity is therefore governed by the relative angle between the two polarizers as well as the polarization state of the incident wave.

The experimental configuration employing two wire-grid polarizers is illustrated in Fig. A III-1(a). Polarization-dependent measurements were performed under both co-polarized and cross-polarized configurations. The samples under investigation were mounted on a rotation stage and rotated from 0° to 180° in 10° increments to extract polarization-dependent transmission characteristics.

The experimental setup consisted of a laser fiber-coupled broadband THz photoconductive antenna (THz-P-Tx LTP180909, TOPTICA Photonics) serving as the emitter, and a pyroelectric detector as the receiver, as shown in Figure-A III-1(a). The emitted THz radiation was intensity-modulated at a chopping frequency of 25 Hz to enable lock-in-style detection with the pyroelectric detector. Four off-axis parabolic (OAP) mirrors were used to guide and focus the THz beam through the polarization optics and the sample region.

A T-RAD digital radiometer was employed to acquire and record the detected signal as a function of the sample rotation angle. Due to the inherent thermal sensitivity of pyroelectric detectors and their susceptibility to environmental noise, signal averaging was performed to improve measurement stability. For each rotation angle, 1000 data points were recorded and averaged to mitigate thermal fluctuations and enhance the signal-to-noise ratio.

III.3 Results and discussion

The polarization-dependent transmission of a quartz crystal with a thickness of 0.4 mm was investigated to demonstrate the capability of the proposed THz polarimetric system. Figure-A III-1(b-c) shows the measured transmission response under both co-polarized and cross-polarized configurations as the sample was rotated over a full angular range of 0° to 180°. Pronounced periodic maxima and minima are observed in both configurations, indicating clear polarization-dependent modulation induced by the birefringent nature of the quartz crystal.

The magnitude of the modulation between the transmission maxima and minima is directly related to the birefringence of the sample. As expected, the angular positions of the maxima and minima exhibit complementary behavior between the co-polarized and cross-polarized measurements, confirming the anisotropic optical response of the crystal. This opposite trend arises from the phase retardation introduced between the ordinary and extraordinary axes as the sample orientation is varied.

Although the measurements were performed with a rotation step size of 10° to provide detailed angular resolution, coarser angular increments, such as 22.5°, could be sufficient for rapid identification and qualitative characterization of birefringent materials. Moreover, the periodic modulation observed over a full rotation cycle suggests that the proposed scheme may be exploited to extract additional physical parameters of anisotropic materials, including relative birefringence strength and principal optical axis orientation.

To characterize the quartz crystal using frequency-selective polarimetric metrics, a frequency-selective polarizer (FSP) based on a rectangular-slot FSS was employed with peak center frequency = 0.33 THz, as shown in Fig. A III-2(a). The FSP acts as a narrowband polarization

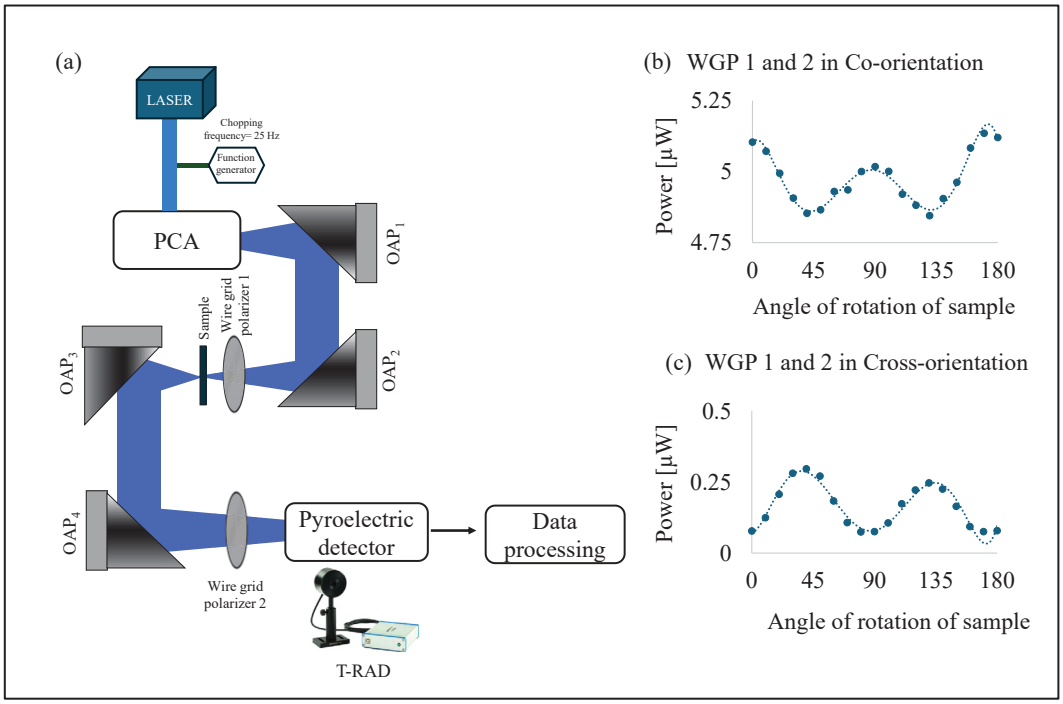

Figure-A III-1 (a) Experimental schematic with a wire-grid polarizer analyzer placed before the T-RAD detector; (b–c) measured power versus sample rotation angle for co- and cross-oriented wire-grid polarizers

analyzer, enabling polarization-resolved measurements at discrete spectral bands determined by the FSS resonance. This approach allows the extraction of polarization information without requiring broadband polarization optics or time-domain scanning.

When the WGP and the FSP were aligned in a co-oriented configuration, a clear periodic modulation was observed in the co-polarized response p_0, as illustrated in Fig. A III-2(b). This modulation arises from the rotation of the birefringent quartz sample, which introduces a frequency-dependent phase retardation between the orthogonal polarization components of the incident THz field. The resulting polarization state evolves with rotation angle, leading to an oscillatory intensity response after projection onto the polarization axis defined by the FSP.

In contrast, when the FSP was rotated by 90° with respect to the WGP, the cross-polarized component p_{90} was measured as shown in Fig. A III-2(c). The reduced modulation observed with the WGP–FSP cross oriented configuration arises from the narrowband, frequency-

selective nature of the FSP, which limits the detected cross-polarized signal compared to the broadband polarization conversion measured using two crossed wire-grid polarizers. This behavior confirms the polarization selectivity of the rectangular-slot FSS and highlights its effectiveness as a frequency-selective polarization analyzer.

Using the measured p_0 and p_{90} responses, the frequency-selective Stokes parameter S_1 can be directly extracted, providing quantitative information on the linear polarization contrast along the principal axes. Although not implemented in the present measurements, rotating the FSP to 45° and 135° would enable the acquisition of the additional polarization components p_{45} and p_{135}, from which the Stokes parameter $S_2=p_{45}-p_{135}$ could be determined. Together, the S_0, S_1 and S_2 parameters allow the calculation of the degree of linear polarization (DoLP) and the angle of linear polarization (AoLP), thereby providing a complete description of the linear polarization

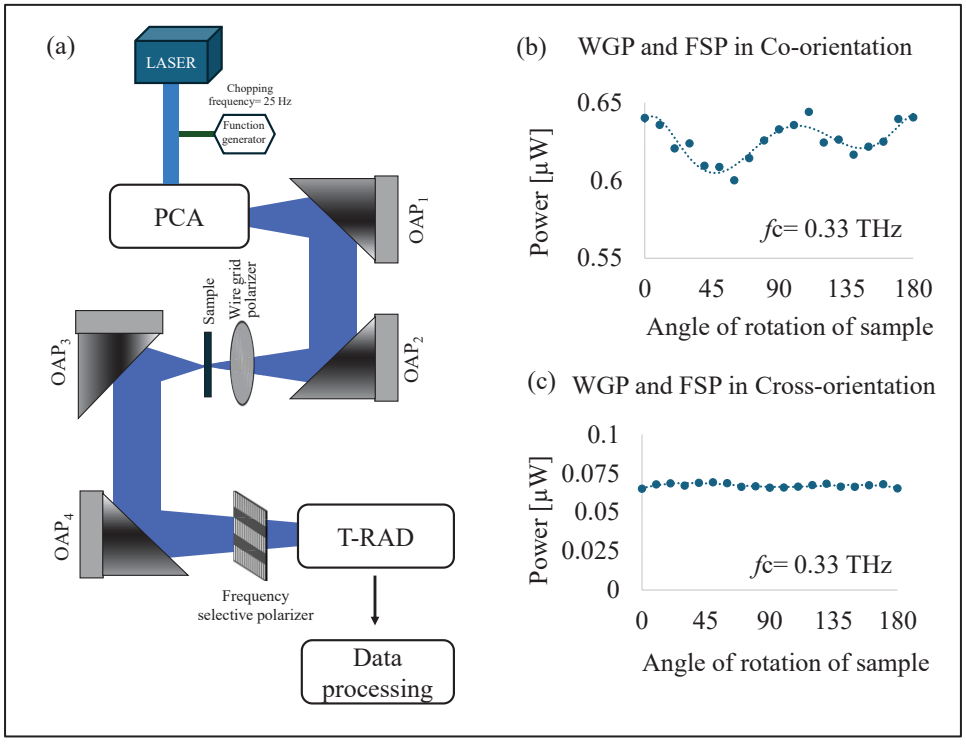

Figure-A III-2 (a) Schematic of the experimental setup incorporating a frequency-selective polarizer positioned in front of the T-RAD detector; (b–c) measured power levels as a function of the rotation angle of the sample while wire-grid polarizer and frequency-selective polarizer for (b) co-oriented and (c) cross-oriented configurations

state at the selected frequency. The detailed formulation and extraction of these parameters are presented in Chapter 5 of this thesis.

Despite the inherently slow response of the pyroelectric detector, the experimental results demonstrate that it provides adequate sensitivity to resolve small polarization-dependent intensity variations arising from anisotropic effects in the THz regime. These findings confirm the suitability of the proposed pyroelectric-based polarimetric approach for static characterization of birefringent materials.

III.4 Conclusion

A compact and straightforward THz polarimetric system has been demonstrated for the characterization of birefringent materials using a minimal number of optical components. The polarization-dependent intensity modulation, manifested through periodic maxima and minima in the measured transmission curves, enables reliable identification and qualitative characterization of birefringent samples. While the system is inherently limited by the thermal sensitivity of the pyroelectric detector, the implementation of improved thermal isolation and environmental shielding could further enhance measurement precision. Owing to its simplicity, low cost, and room-temperature operation, the proposed approach offers a practical and affordable solution for static THz polarimetric measurements, with potential applicability in industrial and laboratory environments.

RESEARCH CONTRIBUTION

Journal articles

[1] **Redwan Ahmad**, Charles Simard, Rejeena R Sebastian, Jonathan Lafreniere-Greig, Xavier Ropagnol, and François Blanchard, “Terahertz multispectral polarimetric imaging based on intensity measurement” *Photonics Research* (2026). available at https://doi.org/10.1364/PRJ.589189

[2] **Redwan Ahmad**, Xavier Ropagnol, and François Blanchard, “Polarization-sensitive terahertz frequency selective surface based on laser cutting technique,” *Journal of the Optical Society of America B*, vol. 43, no. 3, A152-A163, 2026.

[3] Rejeena Sebastian, **Redwan Ahmad**, Jonathan Lafrenière-Greig, Xavier Ropagnol, and François Blanchard, “Real-Time Sample Identification Using a Fast and Simplified AI-Assisted Terahertz Spectrometer” *IEEE Transactions on Terahertz Science and Technology*, vol. 16, no. 2, p.131–140, 2025.

[4] **Redwan Ahmad,** Xavier Ropagnol, Ngoc Trinh, Chloé Bois, and François Blanchard, “Reconfigurable screen-printed terahertz frequency selective surface based on metallic checkerboard pattern” *Flexible and Printed Electronics*, vol.9, no. 2, p.025005, 2024.

[5] **Redwan Ahmad**, Mariia Zhuldybina, Xavier Ropagnol, Ngoc Trinh, Chloé Bois, Juan Schneider, and François Blanchard, “Reconfigurable terahertz Moiré frequency selective surface based on additive manufacturing technology” *Appl. Sci*., vol.13, no. 5, p.3302, 2023.

Conference paper

[1] **Redwan Ahmad**, Xavier Ropagnol and François Blanchard, "Free-Standing Polarization-Sensitive THz FSS: Fabrication and Characterization," International Topical Meeting on Microwave Photonics (MWP 2025), Quebec city, Canada, 2025.

[2] **Redwan Ahmad**, Richard Al Hadi, and François Blanchard, "Characterization of birefringent materials using polarimetric spectrometer based on CMOS THz detector," International Topical Meeting on Microwave Photonics (MWP 2025), Quebec city, Canada, 2025.

[3] **Redwan Ahmad**, J. Lafreniere-Greig, Xavier Ropagnol and François Blanchard, "Terahertz polarimetric system based on polarization sensitive frequency selective surfaces," 27th Photonics North 2025, Ottawa, Canada, 2025.

[4] **Redwan Ahmad**, François Blanchard and Richard Al Hadi, "Characterization and polarization sensitivity analysis of CMOS terahertz detector," 27th Photonics North 2025, Ottawa, Canada, 2025.

[5] J. Lafrenière-Greig, J. E. Nkeck, **Redwan Ahmad**, and F. Blanchard, "Communication protocol using terahertz metasurfaces," 27th Photonics North 2025, Ottawa, Canada, 2025.

[6] Rejeena Sebastian, **Redwan Ahmad**, J. Lafrenière-Greig, X. Ropagnol, and François Blanchard, "Feature-Dependent Accuracy in Classification Models for Ultrafast THz Spectroscopy using Frequency Selective Surfaces", Optica Advanced Photonics Congress 2024, Québec City, Québec, Canada.

[7] Rejeena Sebastian, **Redwan Ahmad**, J. Lafrenière-Greig, X.Ropagnol, and F.Blanchard, " AI-assisted Enhanced Ultrafast Terahertz Spectroscopy using Frequency Selective Surfaces", SPIE conference in Sensors + Imaging 2024, Proc. SPIE 13203, Sensors and Communication Technologies in the 1 GHz to 10 THz Band, 132030A, 2024.

[8] **Redwan Ahmad**, Léo Guiramand, Mariia Zhuldybina, Xavier Ropagnol, Ngoc Duc Trinh, Chloé Bois, and François Blanchard, "Printed Terahertz Spiral Zone Plate for Vortex Beam Generation,", 48th International Conference on Infrared, Millimeter and Terahertz Waves (IRMMW-THz) 2023, Montreal, QC, Canada.

[9] Rejeena Sebastian, **Redwan Ahmad**, X Ropagnol and F Blanchard,"Investigation of Fast Frequency Selective Qualitative Terahertz Spectroscopy", 48th International Conference on Infrared, Millimeter and Terahertz Waves (IRMMW-THz) 2023, Montreal, QC, Canada.

[10] **Redwan Ahmad**, Léo Guiramand, Mariia Zhuldybina, Xavier Ropagnol and François Blanchard, “Fabrication and characterization of terahertz zone plates based on foil stamping technique,” 25th Photonics North 2023, Montreal, QC, Canada, 2023.

[11] **Redwan Ahmad**, Mariia Zhuldybina, Xavier Ropagnol and François Blanchard, “Terahertz metasurface based on additive manufacturing technology,” 24th Photonics North 2022, Niagara Falls, ON, Canada, pp. 1-1, 2022.

[12] **Redwan Ahmad**, Charles Simard, Rejeena R Sebastian, Jonathan Lafreniere-Greig, Xavier Ropagnol, and François Blanchard, "Compact Terahertz Polarization-Resolved Measurements Using Frequency-Selective Intensity Detection," Accepted in 28th Photonics North 2026, Quebec city, QC, Canada, 2026.

[13] Rejeena Sebastian, Charles Simard, **Redwan Ahmad**, Leyla Agosti Cagalli Burri, Christian Tardif and François Blanchard, "AI-Enhanced Terahertz Spectroscopy for Real-Time Classification of Plastics for Recycling and Sorting Applications," Accepted in 28th Photonics North 2026, Quebec city, QC, Canada, 2026.

Scholarship and grants

- PBEEE - Fonds de recherche du Québec – Nature et technologies (FRQNT) [2022-2025]
- CCTT Grant - Fonds de recherche du Québec – Nature et technologies (FRQNT) [May 2022- August 2022]

BIBLIOGRAPHY

ACST GmbH. (n.d.). Quasi-optical detectors. https://acst.de/product-category/quasi-optical-detectors

Ahmad, R., Zhuldybina, M., Ropagnol, X., & Blanchard, F. (2022). Terahertz metasurface based on additive manufacturing technology. 2022 Photonics North (PN), 1. https://doi.org/10.1109/pn56061.2022.9908255

Ahmad, R., Zhuldybina, M., Ropagnol, X., Trinh, N. D., Bois, C., Schneider, J., & Blanchard, F. (2023). Reconfigurable Terahertz Moiré Frequency selective surface based on additive manufacturing technology. Applied Sciences, 13(5), 3302. https://doi.org/10.3390/app13053302

Ahmad, R., Ropagnol, X., Trinh, N. D., Bois, C., & Blanchard, F. (2024). Reconfigurable screen-printed terahertz frequency selective surface based on metallic checkerboard pattern. Flexible and Printed Electronics, 9(2), 025005. https://doi.org/10.1088/2058-8585/ad3bca

Ahmad, R., Lafreniere-Greig, J., Ropagnol, X., & Blanchard, F. (2025). Terahertz Polarimetric System Based on Polarization Sensitive Frequency Selective Surfaces. Photonics North (PN), 1–2. https://doi.org/10.1109/pn66844.2025.11097179

Ahmad, R., Blanchard, F., & Hadi, R. A. (2025b). Characterization and Polarization Sensitivity Analysis of CMOS Terahertz Detector. Photonics North 2025, 1–2. https://doi.org/10.1109/pn66844.2025.11097144

Ahmad, R., Ropagnol, X., & Blanchard, F. (2026). Polarization-sensitive terahertz frequency selective surface based on laser cutting technique. Journal of the Optical Society of America B, 43(3), A152-A163. https://doi.org/10.1364/josab.578338

Akter, N., Karabiyik, M., & Pala, N. (2019). Highly Tunable, Flexible and Stretchable Frequency Selective Surface-Based THz Bandpass Filter. IEEE Photonics Conference (IPC), 1–2. https://doi.org/10.1109/ipcon.2019.8908502

Altmann, K., Reuter, M., Garbat, K., Koch, M., Dabrowski, R., & Dierking, I. (2013). Polymer stabilized liquid crystal phase shifter for terahertz waves. Optics Express, 21(10), 12395. https://doi.org/10.1364/oe.21.012395

Anwar, R., Mao, L., & Ning, H. (2018). Frequency Selective Surfaces: A review. Applied Sciences, 8(9), 1689. https://doi.org/10.3390/app8091689

Applegate, M. B., Istfan, R. E., Spink, S., Tank, A., & Roblyer, D. (2020). Recent advances in high speed diffuse optical imaging in biomedicine. APL Photonics, 5(4). https://doi.org/10.1063/1.5139647

Aqlan, B., Himdi, M., Vettikalladi, H., & Le-Coq, L. (2021a). A 300-GHz low-cost high-gain fully metallic Fabry–Perot cavity antenna for 6G terahertz wireless communications. Scientific Reports, 11, 7703. https://doi.org/10.1038/s41598-021-87076-3

Aqlan, B., Himdi, M., Vettikalladi, H., & Le-Coq, L. (2021b). A circularly polarized Sub-Terahertz antenna with Low-Profile and High-Gain for 6G wireless communication systems. IEEE Access, 9, 122607–122617. https://doi.org/10.1109/access.2021.3109161

Auston, D. H. (1975). Picosecond optoelectronic switching and gating in silicon. Applied Physics Letters, 26(3), 101–103. https://doi.org/10.1063/1.88079

Auston, D. H., & Smith, P. R. (1983). Generation and detection of millimeter waves by picosecond photoconductivity. Applied Physics Letters, 43(7), 631–633. https://doi.org/10.1063/1.94468

Auston, D. H., Cheung, K. P., & Smith, P. R. (1984). Picosecond photoconducting Hertzian dipoles. Applied Physics Letters, 45(3), 284–286. https://doi.org/10.1063/1.95174

Azad, A. K., Kort-Kamp, W. J. M., Sykora, M., Weisse-Bernstein, N. R., Luk, T. S., Taylor, A. J., Dalvit, D. a. R., & Chen, H. (2016). Metasurface Broadband Solar Absorber. Scientific Reports, 6, 20347. https://doi.org/10.1038/srep20347

Azemi, S. N., Ghorbani, K., & Rowe, W. S. T. (2013). A reconfigurable FSS using a spring resonator element. IEEE Antennas and Wireless Propagation Letters, 12, 781–784. https://doi.org/10.1109/lawp.2013.2270950

Aznabet, M., Navarro-Cia, M., Kuznetsov, S. A., Gelfand, A. V., Fedorinina, N. I., Goncharov, Y. G., Beruete, M., Mrabet, O. E., & Sorolla, M. (2008). Polypropylene-substrate-based SRR- and CSRR- metasurfaces for submillimeter waves. Optics Express, 16(22), 18312. https://doi.org/10.1364/oe.16.018312

Badamchi, Z., Trinh, N. D., Bois, C., & Djerafi, T. (2022). Printed fractal folded Coplanar-strips-fed array rectenna for IOE applications. Progress in Electromagnetics Research C, 125, 161–177. https://doi.org/10.2528/pierc22080606

Baek, J., Kim, J., Seol, J. H., & Kim, M. (2024). All-dielectric polarization-sensitive metasurface for terahertz polarimetric imaging. Scientific Reports, 14, 7544. https://doi.org/10.1038/s41598-024-58297-z

Baek, N., Lee, Y., Kim, T., Jung, J., & Lee, S. A. (2022). Lensless polarization camera for single-shot full-Stokes imaging. APL Photonics, 7(11). https://doi.org/10.1063/5.0120465

Balanis, C. A. (2005). Antenna theory: Analysis and design (3rd ed.). Hoboken, NJ: Wiley.

Balos, V., Wolf, M., Kovalev, S., & Sajadi, M. (2023). Optical rectification and electro-optic sampling in quartz. Optics Express, 31(8), 13317. https://doi.org/10.1364/oe.480339

Banerjee, S., Yettapu, G., Sarkar, S., & Mandal, P. (2021). Broadband terahertz spectroscopy. In Progress in optical science and photonics (pp. 117–142). https://doi.org/10.1007/978-981-33-6084-6_5

Barakat, R. (1998). Jones matrix equivalence theorems for polarization theory. European Journal of Physics, 19(3), 209–216. https://doi.org/10.1088/0143-0807/19/3/001

Beckh, C., Sulzer, P., Fritzsche, N., Riek, C., & Leitenstorfer, A. (2021). Analysis of subcycle Electro-Optic sampling without background. Journal of Infrared Millimeter and Terahertz Waves, 42, 701–714. https://doi.org/10.1007/s10762-021-00789-4

Beruete, M., Sorolla, M., Campillo, I., Dolado, J. S., Martín-Moreno, L., Bravo-Abad, J., & García-Vidal, F. J. (2004). Enhanced millimeter-wave transmission through subwavelength hole arrays. Optics Letters, 29(21), 2500. https://doi.org/10.1364/ol.29.002500

Blanchard, F., Razzari, L., Bandulet, H., Sharma, G., Morandotti, R., Kieffer, J. C., Ozaki, T., Reid, M., Tiedje, H. F., Haugen, H. K., & Hegmann, F. A. (2007). Generation of 1.5 μJ single-cycle terahertz pulses by optical rectification from a large aperture ZnTe crystal. Optics Express, 15(20), 13212. https://doi.org/10.1364/oe.15.013212

Blanchard, F., Ooi, K., Tanaka, T., Doi, A., & Tanaka, K. (2012). Terahertz spectroscopy of the reactive and radiative near-field zones of split ring resonator. Optics Express, 20(17), 19395. https://doi.org/10.1364/oe.20.019395

Blanchard, F., Doi, A., Tanaka, T., & Tanaka, K. (2013). Real-Time, Subwavelength Terahertz Imaging. Annual Review of Materials Research, 43, 237–259. https://doi.org/10.1146/annurev-matsci-071312-121656

Blanchard, F., Ropagnol, X., Hafez, H., Razavipour, H., Bolduc, M., Morandotti, R., Ozaki, T., & Cooke, D. G. (2014). Effect of extreme pump pulse reshaping on intense terahertz emission in lithium niobate at multimilliJoule pump energies. Optics Letters, 39(15), 4333. https://doi.org/10.1364/ol.39.004333

Blanchard, F., Sumida, K., Wolpert, C., Tsotsalas, M., Tanaka, T., Doi, A., Kitagawa, S., Cooke, D. G., Furukawa, S., & Tanaka, K. (2014b). Terahertz phase contrast imaging of sorption kinetics in porous coordination polymer nanocrystals using differential optical resonator. Optics Express, 22(9), 11061. https://doi.org/10.1364/oe.22.011061

Bonnassieux, Y., Brabec, C. J., Cao, Y., Carmichael, T. B., Chabinyc, M. L., Cheng, K., Cho, G., Chung, A., Cobb, C. L., Distler, A., Egelhaaf, H., Grau, G., Guo, X., Haghiashtiani, G., Huang, T., Hussain, M. M., Iniguez, B., Lee, T., Li, L., . . . Wu, Y. (2021). The

2021 flexible and printed electronics roadmap. Flexible and Printed Electronics, 6(2), 023001. https://doi.org/10.1088/2058-8585/abf986

Born, N., Reuter, M., Koch, M., & Scheller, M. (2013). High-Q terahertz bandpass filters based on coherently interfering metasurface reflections. Optics Letters, 38(6), 908. https://doi.org/10.1364/ol.38.000908

Born, N., Gente, R., Al-Naib, I., & Koch, M. (2015). Laser beam machined free-standing terahertz metamaterials. Electronics Letters, 51(13), 1012–1014. https://doi.org/10.1049/el.2015.0655

Boyd, R. W. (2008). Nonlinear optics (3rd ed.). Academic Press.

Brinkmann, S., Vieweg, N., Gärtner, G., Plew, P., & Deninger, A. (2016). Towards quality control in pharmaceutical packaging: screening folded boxes for package inserts. Journal of Infrared Millimeter and Terahertz Waves, 38, 339–346. https://doi.org/10.1007/s10762-016-0345-y

Burford, N. M., & El-Shenawee, M. O. (2017). Review of terahertz photoconductive antenna technology. Optical Engineering, 56(1), 010901. https://doi.org/10.1117/1.oe.56.1.010901

Camacho, M., Nekovic, A., Freer, S., Penchev, P., Boix, R. R., Dimov, S., & Navarro-Cia, M. (2020). Symmetry and Finite-Size effects in Quasi-Optical extraordinarily THZ transmitting arrays of tilted slots. IEEE Transactions on Antennas and Propagation, 68(8), 6109–6117. https://doi.org/10.1109/tap.2020.2985770

Cao, H., & Nahata, A. (2004). Resonantly enhanced transmission of terahertz radiation through a periodic array of subwavelength apertures. Optics Express, 12(6), 1004. https://doi.org/10.1364/opex.12.001004

Carelli, P., Chiarello, F., Cibella, S., Di Gaspare, A., Leoni, R., Ortolani, M., & Torrioli, G. (2012). A fast terahertz spectrometer based on frequency selective surface filters. Journal of Infrared Millimeter and Terahertz Waves, 33, 505–512. https://doi.org/10.1007/s10762-012-9884-z

Carletti, L., McDonnell, C., Leon, U. A., Rocco, D., Finazzi, M., Toma, A., Ellenbogen, T., Della Valle, G., Celebrano, M., & De Angelis, C. (2023). Nonlinear THz Generation through Optical Rectification Enhanced by Phonon–Polaritons in Lithium Niobate Thin Films. ACS Photonics, 10(9), 3419–3425. https://doi.org/10.1021/acsphotonics.3c00924

Castro-Camus, E., Lloyd-Hughes, J., Fraser, M. D., Tan, H. H., Jagadish, C., & Johnston, M. B. (2006). Detecting the full polarization state of terahertz transients. Proceedings of SPIE, the International Society for Optical Engineering/Proceedings of SPIE, 6120, 61200Q. https://doi.org/10.1117/12.660717

Castro-Camus, E., Koch, M., & Hernandez-Serrano, A. I. (2020). Additive manufacture of photonic components for the terahertz band. Journal of Applied Physics, 127(21). https://doi.org/10.1063/1.5140270

Chai, X., Ropagnol, X., Mora, L. S., Raeiszadeh, S. M., Safavi-Naeini, S., Blanchard, F., & Ozaki, T. (2020). Stokes–Mueller method for comprehensive characterization of coherent terahertz waves. Scientific Reports, 10, 15426. https://doi.org/10.1038/s41598-020-72049-9

Chen, C. (1973). Transmission of microwave through perforated flat plates of finite thickness. IEEE Transactions on Microwave Theory and Techniques, 21(1), 1–6. https://doi.org/10.1109/tmtt.1973.1127906

Chen, H., Padilla, W. J., Zide, J. M. O., Gossard, A. C., Taylor, A. J., & Averitt, R. D. (2006). Active terahertz metamaterial devices. Nature, 444, 597–600. https://doi.org/10.1038/nature05343

Chen, K., Li, Z., Liu, J., Duan, R., Wang, Y., Zhang, W., Cai, B., Chen, L., & Zhu, Y. (2013). A study of FSS in Terahertz Range for Polarization Modulation Purpose. IEEE Photonics Technology Letters, 25(16), 1613–1615. https://doi.org/10.1109/lpt.2013.2271584

Chen, K., Wang, Y., Liu, J., Bai, Y., Bu, T., Cai, B., Zhu, Y., & Zhuang, S. (2015). Polarization dependent dual-band EIT-like effect and its application in THz range. Optics Communications, 363, 69–73. https://doi.org/10.1016/j.optcom.2015.11.002

Chen, X., & Pickwell-MacPherson, E. (2022). An introduction to terahertz time-domain spectroscopic ellipsometry. APL Photonics, 7(7). https://doi.org/10.1063/5.0094056

Chen, Y., Wang, J., Hu, Z., Gao, T., Zhu, W., & Wang, X. (2020). Fabrication of large-scale freestanding THz wire grid polarizers by femtosecond laser micromachining. Optik, 212, 164655. https://doi.org/10.1016/j.ijleo.2020.164655

Cheng, Y. Z., Withayachumnankul, W., Upadhyay, A., Headland, D., Nie, Y., Gong, R. Z., Bhaskaran, M., Sriram, S., & Abbott, D. (2014). Ultrabroadband plasmonic absorber for Terahertz waves. Advanced Optical Materials, 3(3), 376–380. https://doi.org/10.1002/adom.201400368

Cherniak, V., Kubiczek, T., Kolpatzeck, K., & Balzer, J. C. (2023). Laser diode based THz-TDS system with 133 dB peak signal-to-noise ratio at 100 GHz. Scientific Reports, 13, 13476. https://doi.org/10.1038/s41598-023-40634-3

Chernyadiev, A. V., But, D. B., Ivonyak, Y., Ikamas, K., & Lisauskas, A. (2024). A CMOS-integrated terahertz near-field sensor based on an ultra-strongly coupled meta-atom. Scientific Reports, 14, 11483. https://doi.org/10.1038/s41598-024-61971-x

Chimot, N., Mangeney, J., Joulaud, L., Crozat, P., Bernas, H., Blary, K., & Lampin, J. F. (2005). Terahertz radiation from heavy-ion-irradiated In0.53Ga0.47As photoconductive antenna excited at 1.55μm. Applied Physics Letters, 87(19). https://doi.org/10.1063/1.2126110

Compton, R. C., Macfarlane, J. C., Whitbourn, L. B., Blanco, M. M., & McPhedran, R. C. (1984). Babinet's principle applied to ideal beam-splitters for submillimetre waves. Optica Acta: International Journal of Optics, 31(5), 515–524. https://doi.org/10.1080/713821538

Cui, E., Wan, Z., Ke, C., Wu, C., Wang, D., & Lei, C. (2022). Flexible and efficient fabrication of a terahertz absorber by single-step laser direct writing. Optics Express, 30(24), 42944. https://doi.org/10.1364/oe.468753

Dawes, D. H., McPhedran, R. C., & Whitbourn, L. B. (1989). Thin capacitive meshes on a dielectric boundary: theory and experiment. Applied Optics, 28(16), 3498. https://doi.org/10.1364/ao.28.003498

Debus, C., & Bolivar, P. H. (2007). Frequency selective surfaces for high sensitivity terahertz sensing. Applied Physics Letters, 91(18). https://doi.org/10.1063/1.2805016

Dhillon, S. S., Vitiello, M. S., Linfield, E. H., Davies, A. G., Hoffmann, M. C., Booske, J., Paoloni, C., Gensch, M., Weightman, P., Williams, G. P., Castro-Camus, E., Cumming, D. R. S., Simoens, F., Escorcia-Carranza, I., Grant, J., Lucyszyn, S., Kuwata-Gonokami, M., Konishi, K., Koch, M., . . . Johnston, M. B. (2017). The 2017 terahertz science and technology roadmap. Journal of Physics D Applied Physics, 50(4), 043001. https://doi.org/10.1088/1361-6463/50/4/043001

Dong, B., Ma, H., Wang, J., Shi, P., Li, J., Zhu, L., Lou, J., Feng, M., & Qu, S. (2019). A thermally tunable THz metamaterial frequency-selective surface based on barium strontium titanate thin film. Journal of Physics D Applied Physics, 52(4), 045301. https://doi.org/10.1088/1361-6463/aaebef

Ebrahimi, A., Nirantar, S., Withayachumnankul, W., Bhaskaran, M., Sriram, S., Al-Sarawi, S. F., & Abbott, D. (2015). Second-Order Terahertz Bandpass frequency selective surface with miniaturized elements. IEEE Transactions on Terahertz Science and Technology, 5(5), 761–769. https://doi.org/10.1109/tthz.2015.2452813

Erhard, M., Fickler, R., Krenn, M., & Zeilinger, A. (2017). Twisted photons: new quantum perspectives in high dimensions. Light Science & Applications, 7, 17146. https://doi.org/10.1038/lsa.2017.146

Esakkimuthu, M., Suseela, S. B., Sankarrajan, R., Gupta, A., & Prabhu, S. (2019). Microfabrication of low cost frequency selective surface for terahertz wave by laser ablation. Journal of Electronic Materials, 48, 2423–2429. https://doi.org/10.1007/s11664-019-07008-w

Euler, M., Fusco, V., Cahill, R., & Dickie, R. (2010). 325 GHz single layer Sub-Millimeter Wave FSS based split slot ring linear to circular polarization convertor. IEEE Transactions on Antennas and Propagation, 58(7), 2457–2459. https://doi.org/10.1109/tap.2010.2048874

Falade, O. P., Jilani, S. F., Ahmed, A. Y., Wildsmith, T., Reip, P., Rajab, K. Z., & Alomainy, A. (2018). Design and characterisation of a screen-printed millimetre-wave flexible metasurface using copper ink for communication applications. Flexible and Printed Electronics, 3(4), 045005. https://doi.org/10.1088/2058-8585/aaf0eb

Farid, A., Laurita, N. J., Tehrani, B., Hester, J. G., Tentzeris, M. M., Armitage, N. P., Farid, A., Laurita, N. J., Tehrani, B., Hester, J. G., Tentzeris, M. M., & Armitage, N. P. (2016). Inkjet printed Wire-Grid polarizers for the THZ frequency range. Journal of Infrared Millimeter and Terahertz Waves, 38, 276–282. https://doi.org/10.1007/s10762-016-0330-5

Fast, D. B., Gerke, T. D., Goncharov, Y., Lebedev, S. P., Komandin, G., & Kozlov, V. G. (2011). Wire-grid THz polarizers manufactured by laser micromachining of metal films on a polymer membrane. International Conference on Infrared, Millimeter, and Terahertz Waves, 1–2. https://doi.org/10.1109/irmmw-thz.2011.6104851

Fattinger, C., & Grischkowsky, D. (1989). Terahertz beams. Applied Physics Letters, 54(6), 490–492. https://doi.org/10.1063/1.100958

Ferguson, B., & Zhang, X. (2002). Materials for terahertz science and technology. Nature Materials, 1, 26–33. https://doi.org/10.1038/nmat708

Ferraro, A., Zografopoulos, D. C., Missori, M., Peccianti, M., Caputo, R., & Beccherelli, R. (2016). Flexible terahertz wire grid polarizer with high extinction ratio and low loss. Optics Letters, 41(9), 2009. https://doi.org/10.1364/ol.41.002009

Ferraro, A., Zografopoulos, D. C., Caputo, R., & Beccherelli, R. (2017). Broad- and Narrow-Line Terahertz filtering in Frequency-Selective surfaces patterned on thin Low-Loss polymer substrates. IEEE Journal of Selected Topics in Quantum Electronics, 23(4), 1–8. https://doi.org/10.1109/jstqe.2017.2665641

Ferraro, A., Zografopoulos, D. C., Caputo, R., & Beccherelli, R. (2017b). Angle-resolved and polarization-dependent investigation of cross-shaped frequency-selective surface terahertz filters. Applied Physics Letters, 110(14), 141107. https://doi.org/10.1063/1.4979804

Formanek, F., Brun, M., Umetsu, T., Omori, S., & Yasuda, A. (2009). Aspheric silicon lenses for terahertz photoconductive antennas. Applied Physics Letters, 94(2), 021113. https://doi.org/10.1063/1.3072357

Furlan, W. D., Ferrando, V., Monsoriu, J. A., Zagrajek, P., Czerwińska, E., & Szustakowski, M. (2016). 3D printed diffractive terahertz lenses. Optics Letters, 41(8), 1748. https://doi.org/10.1364/ol.41.001748

Gao, N., Xie, C., Li, C., Jin, C., & Liu, M. (2011). Square optical vortices generated by binary spiral zone plates. Applied Physics Letters, 98(15), 151106. https://doi.org/10.1063/1.3581044

García-Vidal, F. J., Moreno, E., Porto, J. A., & Martín-Moreno, L. (2005). Transmission of Light through a Single Rectangular Hole. Physical Review Letters, 95, 103901. https://doi.org/10.1103/physrevlett.95.103901

Ge, S., Chen, P., Shen, Z., Sun, W., Wang, X., Hu, W., Zhang, Y., & Lu, Y. (2017). Terahertz vortex beam generator based on a photopatterned large birefringence liquid crystal. Optics Express, 25(11), 12349. https://doi.org/10.1364/oe.25.012349

Gentec-EO. (n.d.). T-RAD terahertz power meter. https://www.gentec-eo.com/products/t-rad

George, D. K., Stier, A. V., Ellis, C. T., McCombe, B. D., Černe, J., & Markelz, A. G. (2012). Terahertz magneto-optical polarization modulation spectroscopy. Journal of the Optical Society of America B, 29(6), 1406. https://doi.org/10.1364/josab.29.001406

Ghann, W., & Uddin, J. (2017). Terahertz (THz) spectroscopy: a Cutting-Edge technology. In InTech eBooks. https://doi.org/10.5772/67031

Ghavidel, A., Kokkonen, M., & Myllymäki, S. (2021). A double layer FSS filter for sub-THz applications. Scientific Reports, 11, 19773. https://doi.org/10.1038/s41598-021-99256-2

Ghosh, G. (1999). Dispersion-equation coefficients for the refractive index and birefringence of calcite and quartz crystals. Optics Communications, 163(1–3), 95–102. https://doi.org/10.1016/s0030-4018(99)00091-7

Grischkowsky, D., Keiding, S., Van Exter, M., & Fattinger, C. (1990). Far-infrared time-domain spectroscopy with terahertz beams of dielectrics and semiconductors. Journal of the Optical Society of America B, 7(10), 2006. https://doi.org/10.1364/josab.7.002006

Grossman, E. N., Dietlein, C. R., & Luukanen, A. (2006). Terahertz circular variable filters. Proceedings of the ESA Workshop on Millimetre-Wave Technology and Applications, 258, 353–358. https://www.nist.gov/publications/terahertz-circular-variable-filters

Gu, P. G. P., Chang, F. C. F., Tani, M. T. M., Sakai, K. S. K., & Pan, C. P. C. (1999). Generation of coherent CW-Terahertz radiation using a tunable Dual-Wavelength external cavity laser diode. Japanese Journal of Applied Physics, 38(11A), L1246. https://doi.org/10.1143/jjap.38.l1246

Guerboukha, H., Nallappan, K., Cao, Y., Seghilani, M., Azaña, J., & Skorobogatiy, M. (2019). Planar Porous components for Low-Loss Terahertz Optics. Advanced Optical Materials, 7(15). https://doi.org/10.1002/adom.201900236

Guerboukha, H., Amarasinghe, Y., Shrestha, R., Pizzuto, A., & Mittleman, D. M. (2021). High-volume rapid prototyping technique for terahertz metallic metasurfaces. Optics Express, 29(9), 13806. https://doi.org/10.1364/oe.422991

Guiramand, L., Nkeck, J. E., Ropagnol, X., Ozaki, T., & Blanchard, F. (2022). Near-optimal intense and powerful terahertz source by optical rectification in lithium niobate crystal. Photonics Research, 10(2), 340. https://doi.org/10.1364/prj.428418

Guiramand, L., Lafrenière-Greig, J., Ropagnol, X., & Blanchard, F. (2024). Near-field terahertz electro-optical imaging based on a polarization image sensor. New Journal of Physics, 26, 103007. https://doi.org/10.1088/1367-2630/ad817e

Gurjar, N., Bailey, K., & El-Shenawee, M. (2024). Polarimetry terahertz imaging of human breast cancer surgical specimens. Journal of Medical Imaging, 11(06), 065503. https://doi.org/10.1117/1.jmi.11.6.065503

Gurjar, N., Ware, M. E., & El-Shenawee, M. (2024b). Experimental characterization of a fully polarimetric pulsed terahertz spectroscopy system. Frontiers in Physics, 12. https://doi.org/10.3389/fphy.2024.1317576

Hadi, R. A., Sherry, H., Grzyb, J., Zhao, Y., Forster, W., Keller, H. M., Cathelin, A., Kaiser, A., & Pfeiffer, U. R. (2012). A 1 K-Pixel video camera for 0.7–1.1 Terahertz imaging applications in 65-Nm CMOS. IEEE Journal of Solid-State Circuits, 47(12), 2999–3012. https://doi.org/10.1109/jssc.2012.2217851

Hadi, R. A., Lo, M. K., & Zhao, Y. (2019). Quasi-optical high-frequency sensing techniques in silicon technologies (Conference Presentation). Terahertz, RF, Millimeter, and Submillimeter-Wave Technology and Applications XII; 109171F. https://doi.org/10.1117/12.2516127

Hakamada, Y., Matoba, M., Sakurai, H., & Konishi, K. (2024). Fabrication of THz metalens by ultraviolet femtosecond laser ablation. Terahertz, RF, Millimeter, and Submillimeter-Wave Technology and Applications XVII; 128850R. https://doi.org/10.1117/12.3002130

Han, J., Kim, I., Ryu, J., Kim, J., Cho, J., Yim, G., Park, H., Min, B., & Choi, M. (2015). Rotationally reconfigurable metamaterials based on moiré phenomenon. Optics Express, 23(13), 17443. https://doi.org/10.1364/oe.23.017443

Han, M., Smith, D., Ng, S., Vilagosh, Z., Anand, V., Katkus, T., Reklaitis, I., Mu, H., Ryu, M., Morikawa, J., Vongsvivut, J., Appadoo, D., & Juodkazis, S. (2022). THZ filters made

by laser ablation of stainless steel and kapton film. Micromachines, 13(8), 1170. https://doi.org/10.3390/mi13081170

Han, R., Zhang, Y., Kim, Y., Kim, D. Y., Shichijo, H., Afshari, E., & O, K. K. (2013). Active terahertz imaging using Schottky diodes in CMOS: array and 860-GHz pixel. IEEE Journal of Solid-State Circuits, 48(10), 2296–2308. https://doi.org/10.1109/jssc.2013.2269856

Han, S., Ko, H., Park, J., Kim, N., Yoon, Y., Shin, J., Kim, D. Y., Lee, D. H., & Park, K. H. (2013b). InGaAs Schottky barrier diode array detector for a real-time compact terahertz line scanner. Optics Express, 21(22), 25874. https://doi.org/10.1364/oe.21.025874

Han, S., Ko, H., Kim, N., Lee, W., Moon, K., Lee, I., Lee, E. S., Lee, D. H., Lee, W., Han, S., Choi, S., & Park, K. H. (2014). Real-time continuous-wave terahertz line scanner based on a compact 1 × 240 InGaAs Schottky barrier diode array detector. Optics Express, 22(23), 28977. https://doi.org/10.1364/oe.22.028977

Hao, X., Chen, Y., Liu, M., Min, X., Cheng, X., Wang, Q., Xu, Q., Zhang, X., & Han, J. (2024). Recent advances in terahertz manipulations using C-Shape-Split-Ring-Resonator metasurfaces (Review). Advanced Optical Materials, 12(15). https://doi.org/10.1002/adom.202302975

Harrington, R. F. (2001). Time-harmonic electromagnetic fields. Wiley-Interscience.

Harris, Z. B., Xu, K., & Arbab, M. H. (2024). A handheld polarimetric imaging device and calibration technique for accurate mapping of terahertz Stokes vectors. Scientific Reports, 14, 17714. https://doi.org/10.1038/s41598-024-68530-4

He, C., He, H., Chang, J., Chen, B., Ma, H., & Booth, M. J. (2021c). Polarisation optics for biomedical and clinical applications: a review. Light Science & Applications, 10, 194. https://doi.org/10.1038/s41377-021-00639-x

He, F., Zhou, Y., Ye, Z., Cho, S.-H., Jeong, J., Meng, X., & Wang, Y. (2021b). Moiré patterns in 2D materials: A review. ACS Nano, 15(4), 5944–5958. https://doi.org/10.1021/acsnano.0c10435

He, J., Wang, X., Hu, D., Ye, J., Feng, S., Kan, Q., & Zhang, Y. (2013). Generation and evolution of the terahertz vortex beam. Optics Express, 21(17), 20230. https://doi.org/10.1364/oe.21.020230

He, J. W., Dong, T., Xu, Z. L., Chi, B. H., Xu, Y., Zhao, Y. H., Tian, X. J., & Zhang, Y. (2021). Flexible terahertz metasurface lens fabricated by ink-jet printing. 46th International Conference on Infrared, Millimeter and Terahertz Waves (IRMMW-THz), 1–2. https://doi.org/10.1109/irmmw-thz50926.2021.9567385

Headland, D., Withayachumnankul, W., Webb, M., Ebendorff-Heidepriem, H., Luiten, A., & Abbott, D. (2016). Analysis of 3D-printed metal for rapid-prototyped reflective terahertz optics. Optics Express, 24(15), 17384. https://doi.org/10.1364/oe.24.017384

Hebling, J., Almasi, G., Kozma, I., & Kuhl, J. (2002). Velocity matching by pulse front tilting for large area THz-pulse generation. Optics Express, 10(21), 1161. https://doi.org/10.1364/oe.10.001161

Heidari, A. (2015). Terahertz Technology in the future of health and medical applications. In Springer series in bio-/neuroinformatics (pp. 663–670). https://doi.org/10.1007/978-3-319-12817-7_28

Heller, E., Xu, K., Harris, Z. B., & Arbab, M. H. (2025). Terahertz Mie scattering in tissue: diffuse polarimetric imaging and Monte Carlo validation in highly attenuating media models. Journal of Biomedical Optics, 30(06), 066001. https://doi.org/10.1117/1.jbo.30.6.066001

Hernandez-Serrano, A. I., Weidenbach, M., Busch, S. F., Koch, M., & Castro-Camus, E. (2016). Fabrication of gradient-refractive-index lenses for terahertz applications by three-dimensional printing. Journal of the Optical Society of America B, 33(5), 928. https://doi.org/10.1364/josab.33.000928

Higashira, T., Kageyama, T., Kashiwagi, K., Miyashita, H., Takano, K., Nakajima, M., & Lee, S. (2017). Influence of distance between metal squares in checkerboard patterns on transmittance characteristics in the infrared region. Journal of Infrared Millimeter and Terahertz Waves, 38, 1098–1106. https://doi.org/10.1007/s10762-017-0403-0

Hirori, H., Doi, A., Blanchard, F., & Tanaka, K. (2011). Single-cycle terahertz pulses with amplitudes exceeding 1 MV/cm generated by optical rectification in LiNbO3. Applied Physics Letters, 98(9). https://doi.org/10.1063/1.3560062

Hoffmann, M. C., Yeh, K., Hebling, J., & Nelson, K. A. (2007). Efficient terahertz generation by optical rectification at 1035 nm. Optics Express, 15(18), 11706. https://doi.org/10.1364/oe.15.011706

Hong, J. T., Park, D. J., Yim, J. H., Park, J. K., Park, J., Lee, S., & Ahn, Y. H. (2013). Dielectric constant engineering of Single-Walled carbon nanotube films for metamaterials and plasmonic devices. The Journal of Physical Chemistry Letters, 4(22), 3950–3957. https://doi.org/10.1021/jz4020053

Hong, J. T., Park, S. J., Park, J.-Y., Lee, S., & Ahn, Y. H. (2017). Terahertz slot antenna devices fabricated on Silver Nanowire Network Films. Optical Materials Express 7(5), 1679-1685. https://doi.org/10.1364/OME.7.001679

Huang, J., Hu, B., Wang, G., Wang, Z., Li, J., Liu, J., & Zhang, Y. (2023). BICs-enhanced active terahertz wavefront modulator enabled by laser-cut graphene ribbons. Photonics Research, 11(7), 1185. https://doi.org/10.1364/prj.491562

Huang, S., Wu, G., Chen, B., Chan, K., Xia, M., Fromenteze, T., Decroze, C., & Chan, C. H. (2021). Terahertz Multi-Spectral Mueller Matrix polarimetry on leaf using only Orthogonal-Polarization measurements. IEEE Transactions on Terahertz Science and Technology, 11(6), 609–619. https://doi.org/10.1109/tthz.2021.3090111

Huang, S., Wu, G., Chan, K., Chen, B., Xia, M., Fromenteze, T., Decroze, C., & Chan, C. H. (2021b). Demonstration of a terahertz multi-spectral 3×3 Mueller matrix polarimetry system for 2D and 3D imaging. Optics Express, 29(10), 14853. https://doi.org/10.1364/oe.417448

Hyun, W. J., Lim, S., Ahn, B. Y., Lewis, J. A., Frisbie, C. D., & Francis, L. F. (2015). Screen printing of highly loaded silver inks on plastic substrates using silicon stencils. ACS Applied Materials & Interfaces, 7(23), 12619–12624. https://doi.org/10.1021/acsami.5b02487

Imai, R., Kanda, N., Higuchi, T., Konishi, K., & Kuwata-Gonokami, M. (2014). Generation of broadband terahertz vortex beams. Optics Letters, 39(13), 3714. https://doi.org/10.1364/ol.39.003714

Institut National d'Optique [INO] (n.d.). MICROXCAM-384i-THz terahertz camera. https://www.ino.ca/en/solutions/thz/microxcam-384i-thz/

Irimia-Vladu, M., Glowacki, E. D., Sariciftci, N. S., & Bauer, S. (2017). Green materials for electronics. https://doi.org/10.1002/9783527692958

Ishak, N. S., Zainal, N., Seman, F. C., & Shah, S. M. (2022). Fabrication and characterisation of Frequency Selective Surface (FSS) for Terahertz Sensing Application. Journal of Physics Conference Series, 2250, 012010. https://doi.org/10.1088/1742-6596/2250/1/012010

Isić, G., Vasić, B., Zografopoulos, D. C., Beccherelli, R., & Gajić, R. (2015). Electrically tunable critically coupled terahertz metamaterial absorber based on nematic liquid crystals. Physical Review Applied, 3(6). https://doi.org/10.1103/physrevapplied.3.064007

Isic, G., Sinatkas, G., Zografopoulos, D. C., Vasic, B., Ferraro, A., Beccherelli, R., Kriezis, E. E., & Belic, M. (2019). Electrically tunable Metal–Semiconductor–Metal terahertz metasurface modulators. IEEE Journal of Selected Topics in Quantum Electronics, 25(3), 1–8. https://doi.org/10.1109/jstqe.2019.2893762

Iwami, K., Ogawa, C., Nagase, T., & Ikezawa, S. (2020). Demonstration of focal length tuning by rotational varifocal moiré metalens in an ir-A wavelength. Optics Express, 28(24), 35602. https://doi.org/10.1364/oe.411054

Jackson, J. D. (1999). Classical electrodynamics (3rd ed.). John Wiley & Sons.

Jang, D., Sung, J. H., Lee, S. K., Kang, C., & Kim, K. (2020). Generation of 0.7 mJ multicycle 15 THz radiation by phase-matched optical rectification in lithium niobate. Optics Letters, 45(13), 3617. https://doi.org/10.1364/ol.393913

Jang, D., Ryu, H., Maeng, I., Lee, S., Seo, M., Oh, S. J., & Lee, S. (2023). All-dielectric terahertz metalens using 3D-printing. Optics and Lasers in Engineering, 171, 107834. https://doi.org/10.1016/j.optlaseng.2023.107834

Jepsen, P. U., Jacobsen, R. H., & Keiding, S. R. (1996). Generation and detection of terahertz pulses from biased semiconductor antennas. Journal of the Optical Society of America B, 13(11), 2424. https://doi.org/10.1364/josab.13.002424

Jepsen, P., Cooke, D., & Koch, M. (2010). Terahertz spectroscopy and imaging – Modern techniques and applications. Laser & Photonics Review, 5(1), 124–166. https://doi.org/10.1002/lpor.201000011

Jepsen, P. U. (2019). Phase Retrieval in Terahertz Time-Domain Measurements: a "how to" Tutorial. Journal of Infrared Millimeter and Terahertz Waves, 40, 395–411. https://doi.org/10.1007/s10762-019-00578-0

Jia, W., & Sensale-Rodriguez, B. (2022). Terahertz metamaterial modulators based on wide-bandgap semiconductor lateral Schottky diodes. Optical Materials Express, 12(3), 940. https://doi.org/10.1364/ome.451027

Jilani, S. F., Falade, O. P., Wildsmith, T., Reip, P., & Alomainy, A. (2019). A 60-GHz Ultra-Thin and flexible metasurface for Frequency-Selective wireless applications. Applied Sciences, 9(5), 945. https://doi.org/10.3390/app9050945

Jin, Y., Kim, G., & Jeon, S. (2006). Terahertz dielectric properties of polymers. Journal of the Korean Physical Society, 49(2), 513–517. http://www.jkps.or.kr/journal/download_pdf.php?spage=513&volume=49&number=2

Kashiwagi, K., Xie, L., Li, X., Kageyama, T., Miura, M., Miyashita, H., Kono, J., & Lee, S. (2016). Inkjet-printed silver-nanoparticle THz metamaterial. 41st International Conference on Infrared, Millimeter, and Terahertz Waves (IRMMW-THz), 1–2. https://doi.org/10.1109/irmmw-thz.2016.7758981

Kashiwagi, K., Xie, L., Li, X., Kageyama, T., Miura, M., Miyashita, H., Kono, J., & Lee, S. (2018). Flexible and stackable terahertz metamaterials via silver-nanoparticle inkjet printing. AIP Advances, 8(4), 045104. https://doi.org/10.1063/1.5006867

Katzenellenbogen, N., & Grischkowsky, D. (1991). Efficient generation of 380 fs pulses of THz radiation by ultrafast laser pulse excitation of a biased metal-semiconductor interface. Applied Physics Letters, 58(3), 222–224. https://doi.org/10.1063/1.104695

Kim, D. H., Mohyuddin, W., Woo, D. S., Choi, H. C., & Kim, K. W. (2017). Design of a 75–140 GHz high-pass printed circuit board dichroic filter. Review of Scientific Instruments, 88(3), 034704. https://doi.org/10.1063/1.4977935

Kim, N., Shin, J., Sim, E., Lee, C. W., Yee, D., Jeon, M. Y., Jang, Y., & Park, K. H. (2009). Monolithic dual-mode distributed feedback semiconductor laser for tunable continuous-wave terahertz generation. Optics Express, 17(16), 13851. https://doi.org/10.1364/oe.17.013851

Kim, Y., Yi, M., Kim, B. G., & Ahn, J. (2011). Investigation of THz birefringence measurement and calculation in Al_2O_3 and $LiNbO_3$. Applied Optics, 50(18), 2906. https://doi.org/10.1364/ao.50.002906

Kohlhaas, R. B., Breuer, S., Nellen, S., Liebermeister, L., Schell, M., Semtsiv, M. P., Masselink, W. T., & Globisch, B. (2019). Photoconductive terahertz detectors with 105 dB peak dynamic range made of rhodium doped InGaAs. Applied Physics Letters, 114(22), 221103. https://doi.org/10.1063/1.5095714

Komlenok, M. S., Volodkin, B. O., Knyazev, B. A., Kononenko, T. V., Kononenko, V. V., Konov, V. I., Soifer, V. A., Pavel'ev, V. S., Tukmakov, K. N., & Choporova, Y. Y. (2015). Fabrication of a multilevel THz Fresnel lens by femtosecond laser ablation. Quantum Electronics, 45(10), 933–936. https://doi.org/10.1070/qe2015v045n10abeh015890

Kondo, S., Suzuki, K., Saito, T., & Asada, H. (2003). Intense photoluminescence and strong stimulated emission in microcrystalline CSPBCL3Films. Japanese Journal of Applied Physics, 42, No. 9R, 5660–5664. https://doi.org/10.1143/jjap.42.5660

Kong, D., Wu, X., Wang, B., Gao, Y., Dai, J., Wang, L., Ruan, C., & Miao, J. (2018). High resolution continuous wave terahertz spectroscopy on solid-state samples with coherent detection. Optics Express, 26(14), 17964. https://doi.org/10.1364/oe.26.017964

Kubiczek, T., Kolpatzeck, K., Schultze, T., & Balzer, J. C. (2022). 3D printed Terahertz filter as a broadband frequency reference. 2022 47th International Conference on Infrared, Millimeter and Terahertz Waves (IRMMW-THz), 1–2. https://doi.org/10.1109/irmmw-thz50927.2022.9895494

Kubiczek, T., Kolpatzeck, K., Schultze, T., & Balzer, J. C. (2024). A highly Frequency-Selective 3D-Printed dielectric structure for the terahertz range. Journal of Infrared Millimeter and Terahertz Waves, 45, 322–336. https://doi.org/10.1007/s10762-024-00973-2

Landy, N. I., Sajuyigbe, S., Mock, J. J., Smith, D. R., & Padilla, W. J. (2008). Perfect metamaterial absorber. Physical Review Letters, 100, 207402. https://doi.org/10.1103/physrevlett.100.207402

Lapray, P., Gendre, L., Foulonneau, A., & Bigué, L. (2018). An FPGA-based pipeline for micropolarizer array imaging. International Journal of Circuit Theory and Applications, 46(9), 1675–1689. https://doi.org/10.1002/cta.2477

Laperashvili, T., Kvitsiani, O., Imerlishvili, I., & Laperashvili, D. (2010). Terahertz pulse detection by the GaAs Schottky diodes. Proceedings Volume 7728, Nonlinear Optics and Applications IV; 77281K. https://doi.org/10.1117/12.854048

Le, H., Pradhani, C., Penchev, P., Nasrollahi, V., Karkantonis, T., Wang, Y., Dimov, S., & Ramos-De-Campos, J. A. (2021). Laser precession machining of cross-shaped terahertz bandpass filters. Optics and Lasers in Engineering, 149, 106790. https://doi.org/10.1016/j.optlaseng.2021.106790

Lee, J., Seo, M., Park, D., Kim, D., Jeoung, S., Lienau, C., Park, Q., & Planken, P. (2006). Shape resonance omni-directional terahertz filters with near-unity transmittance. Optics Express, 14(3), 1253. https://doi.org/10.1364/oe.14.001253

Lee, S., Gee, S., Kang, C., & Kee, C. (2010). Terahertz wave transmission properties of metallic periodic structures printed on a photo-paper. Journal of the Optical Society of Korea, 14(3), 282–285. https://doi.org/10.3807/josk.2010.14.3.282

Lee, S., Lee, D., Kim, C., Jhon, Y. M., Son, J., & Seo, M. (2017). Terahertz transmission control using polarization-independent metamaterials. Optics Express, 25(10), 11436. https://doi.org/10.1364/oe.25.011436

Lepeshov, S., Gorodetsky, A., Krasnok, A., Rafailov, E., Belov, P. (2017). Enhancement of terahertz photoconductive antenna operation by optical nanoantennas. Laser & Photonics Review, 11(1). https://doi.org/10.1002/lpor.201600199

Li, B., Zeng, Y., Chen, B., & Chan, C. H. (2019). Terahertz Frequency-Selective Surface with polarization selection and conversion characteristics. IEEE Transactions on Terahertz Science and Technology, 9(5), 510–519. https://doi.org/10.1109/tthz.2019.2928171

Li, H., Cao, Q., Liu, L., & Wang, Y. (2018). An improved multifunctional active frequency selective surface. IEEE Transactions on Antennas and Propagation, 66(4), 1854–1862. https://doi.org/10.1109/tap.2018.2800727

Li, J., Shah, C. M., Withayachumnankul, W., Ung, B. S., Mitchell, A., Sriram, S., Bhaskaran, M., Chang, S., & Abbott, D. (2013). Mechanically tunable terahertz metamaterials. Applied Physics Letters, 102(12). https://doi.org/10.1063/1.4773238

Li, L. W., Oh, J., Miller, H., Capasso, F., & Rubin, N. A. (2025). Flat, wide field-of-view imaging polarimeter. Optica, 12(6), 799. https://doi.org/10.1364/optica.546883

Li, Q., Ding, S., Yao, R., & Wang, Q. (2010). Real-time terahertz scanning imaging by use of a pyroelectric array camera and image denoising. Journal of the Optical Society of America A, 27(11), 2381. https://doi.org/10.1364/josaa.27.002381

Li, S., Shen, Z., Yin, W., Zhang, L., & Chen, X. (2021). 3D printed cross-shaped terahertz metamaterials with single-band, multi-band and broadband absorption. Optical Materials, 122, 111739. https://doi.org/10.1016/j.optmat.2021.111739

Li, S., Zhang, L., & Chen, X. (2021b). 3D-printed terahertz metamaterial absorber based on vertical split-ring resonator. Journal of Applied Physics, 130(3). https://doi.org/10.1063/5.0056276

Li, S., Shen, Z., Yin, W., Zhang, L., & Chen, X. (2022). 3D-printed terahertz metamaterial for electromagnetically induced reflection analogue. Journal of Physics D Applied Physics, 55(32), 325003. https://doi.org/10.1088/1361-6463/ac708c

Li, X., Lin, L., Wu, L., Yin, W., & Mao, J. (2017). A bandpass graphene frequency selective surface with tunable polarization rotation for THZ applications. IEEE Transactions on Antennas and Propagation, 65(2), 662–672. https://doi.org/10.1109/tap.2016.2633163

Li, X., Li, J., Li, Y., Ozcan, A., & Jarrahi, M. (2023). High-throughput terahertz imaging: progress and challenges. Light Science & Applications, 12, 233. https://doi.org/10.1038/s41377-023-01278-0

Lin, Y., Yao, H., Ju, X., Chen, Y., Zhong, S., & Wang, X. (2017). Free-standing double-layer terahertz band-pass filters fabricated by femtosecond laser micro-machining. Optics Express, 25(21), 25125. https://doi.org/10.1364/oe.25.025125

Lin, Z., Xu, Z., Liu, P., Liang, Z., & Lin, Y. (2019). Polarization-sensitive terahertz resonator using asymmetrical F-shaped metamaterial. Optics & Laser Technology, 121, 105826. https://doi.org/10.1016/j.optlastec.2019.105826

Liu, J., Zhu, Z., Li, W., Lu, W., & Xu, Z. (2025b). Polarized image fusion strategy based on multi-scale feature fusion. Optics Express, 33(13), 27294. https://doi.org/10.1364/oe.567677

Liu, S., Xu, F., Zhan, J., Qiang, J., Xie, Q., Yang, L., Deng, S., & Zhang, Y. (2022). Terahertz liquid crystal programmable metasurface based on resonance switching. Optics Letters, 47(7), 1891. https://doi.org/10.1364/ol.452347

Liu, T., Tani, M., & Pan, C. (2003). THz radiation emission properties of multienergy arsenic-ion-implanted GaAs and semi-insulating GaAs based photoconductive antennas. Journal of Applied Physics, 93(5), 2996–3001. https://doi.org/10.1063/1.1541105

Liu, Y., Ouyang, C., Xu, Q., Su, X., Yang, Q., Ma, J., Li, Y., Tian, Z., Gu, J., Liu, L., Han, J., Shi, Y., & Zhang, W. (2022). Moiré-driven electromagnetic responses and magic

angles in a sandwiched hyperbolic metasurface. Photonics Research, 10(9), 2056. https://doi.org/10.1364/prj.462119

Liu, Y., & Pasiskevicius, V. (2025). Generation of THz vector and scalar vortex beams by optical rectification along threefold symmetry axis in zinc blende crystals. APL Photonics, 10(4), 046101. https://doi.org/10.1063/5.0254769

Louisos, D., McLamb, M., Boreman, G. D., Zhang, J., Willis, A., Hofmann, T., & Touma, J. E. (2024). THz-Frequency Free-Standing Bi-Layer wire grid Polarizers Fabricated by Stereolithography. IEEE Research and Applications of Photonics in Defense Conference (RAPID), 01–02. https://doi.org/10.1109/rapid60772.2024.10647039

Lowry, S. N., Bergen, L. E., Herbert, M. J., Hartley, I. D., Reid, M. E., & Collier, C. M. (2025). Polarization-resolved terahertz time-domain imaging enabled by single pixel imaging. APL Photonics, 10(7), 076120. https://doi.org/10.1063/5.0275429

Luo, L., Chatzakis, I., Wang, J., Niesler, F. B. P., Wegener, M., Koschny, T., & Soukoulis, C. M. (2014). Broadband terahertz generation from metamaterials. Nature Communications, 5, 3055. https://doi.org/10.1038/ncomms4055

Lv, X., Ako, R. T., Bhaskaran, M., Sriram, S., Fumeaux, C., & Withayachumnankul, W. (2022). Frequency-Selective-Surface-Based mechanically reconfigurable terahertz Bandpass filter. IEEE Transactions on Terahertz Science and Technology, 12(3), 257–266. https://doi.org/10.1109/tthz.2022.3148816

Ma, C., Xiao, B., Zhou, D., & Xiao, L. (2021). A novel tunable terahertz wave modulator based on graphene and frequency selective surface (FSS). Optics Communications, 478, 126375. https://doi.org/10.1016/j.optcom.2020.126375

Ma, Z., Li, P., Chen, S., & Wu, X. (2022). Optical generation of strong-field terahertz radiation and its application in nonlinear terahertz metasurfaces. Nanophotonics, 11(9), 1847–1862. https://doi.org/10.1515/nanoph-2021-0714

Maeng, I., Kim, J., & Choi, H. (2012). Ultrabroadband Terahertz Spectroscopy. In Convergence of Terahertz Sciences in Biomedical Systems (pp. 219–229). https://doi.org/10.1007/978-94-007-3965-9_12

Manikandan, E., Sreeja, B., Radha, S., & Bathe, R. N. (2018a). Direct laser fabrication of five-band symmetric terahertz metamaterial with Fano resonance. Materials Letters, 229, 320–323. https://doi.org/10.1016/j.matlet.2018.07.044

Manikandan, E., Sreeja, B. S., Radha, S., Bathe, R. N., Jain, R., & Prabhu, S. (2018b). A rapid fabrication of novel dual band terahertz metamaterial by femtosecond laser ablation. Journal of Infrared Millimeter and Terahertz Waves, 40, 38–47. https://doi.org/10.1007/s10762-018-0543-x

Mansourian, M., Zhuldybina, M., Ropagnol, X., Trinh, N. D., Bois, C., & Blanchard, F. (2021). Fabrication and charactrization of a terahertz polarizer from a roll-to-roll printer. 2021 Photonics North (PN), 1. https://doi.org/10.1109/pn52152.2021.9597903

Martens, S., Gompf, B., & Dressel, M. (2009). Characterization of continuous-wave terahertz sources: laser mixing versus backward-wave oscillators. Applied Optics, 48(29), 5490. https://doi.org/10.1364/ao.48.005490

Masson, J., & Gallot, G. (2006). Terahertz achromatic quarter-wave plate. Optics Letters, 31(2), 265. https://doi.org/10.1364/ol.31.000265

Mehdi, I., Schlecht, E., Chattopadhyay, G., & Siegel, P. H. (2003). Terahertz local oscillator sources: performance and capabilities. Proceedings Volume 4855, Millimeter and Submillimeter Detectors for Astronomy. https://doi.org/10.1117/12.459185

Menzel, M., Michielsen, K., De Raedt, H., Reckfort, J., Amunts, K., & Axer, M. (2015). A Jones matrix formalism for simulating three-dimensional polarized light imaging of brain tissue. Journal of the Royal Society Interface, 12(111), 20150734. https://doi.org/10.1098/rsif.2015.0734

Minkevičius, L., Voisiat, B., Mekys, A., Venckevičius, R., Kašalynas, I., Seliuta, D., Valušis, G., Račiukaitis, G., & Tamošiu¯Nas, V. (2013). Terahertz zone plates with integrated laser-ablated bandpass filters. Electronics Letters, 49(1), 49–50. https://doi.org/10.1049/el.2012.3509

Minkevičius, L., Indrišiūnas, S., Šniaukas, R., Voisiat, B., Janonis, V., Tamošiūnas, V., Kašalynas, I., Račiukaitis, G., & Valušis, G. (2017). Terahertz multilevel phase Fresnel lenses fabricated by laser patterning of silicon. Optics Letters, 42(10), 1875. https://doi.org/10.1364/ol.42.001875

Missori, M., Pilozzi, L., & Conti, C. (2022). Terahertz waves dynamic diffusion in 3D printed structures. Scientific Reports, 12, 8613. https://doi.org/10.1038/s41598-022-12617-3

Miyamoto, K., Kang, B. J., Kim, W. T., Sasaki, Y., Niinomi, H., Suizu, K., Rotermund, F., & Omatsu, T. (2016). Highly intense monocycle terahertz vortex generation by utilizing a Tsurupica spiral phase plate. Scientific Reports, 6, 38880. https://doi.org/10.1038/srep38880

Miyamoto, K., Sano, K., Miyakawa, T., Niinomi, H., Toyoda, K., Vallés, A., & Omatsu, T. (2019). Generation of high-quality terahertz OAM mode based on soft-aperture difference frequency generation. Optics Express, 27(22), 31840. https://doi.org/10.1364/oe.27.031840

Molteni, L. M., Manzolli, J., Pirzio, F., Agnesi, A., Piccinno, G., Laporta, P., & Galzerano, G. (2023). Versatile OSCAT time-domain THz spectrometer. Optics Express, 31(8), 12289. https://doi.org/10.1364/oe.482396

Moon, K., Choi, J., Shin, J., Han, S., Ko, H., Kim, N., Park, J., Yoon, Y., Kang, K., Ryu, H., & Park, K. H. (2014). Generation and Detection of Terahertz Waves Using Low-Temperature-Grown GaAs with an Annealing Process. ETRI Journal, 36(1), 159–162. https://doi.org/10.4218/etrij.14.0213.0319

Morris, C. M., Aguilar, R. V., Stier, A. V., & Armitage, N. P. (2012). Polarization modulation time-domain terahertz polarimetry. Optics Express, 20(11), 12303. https://doi.org/10.1364/oe.20.012303

Müller, R., Gutschwager, B., Hollandt, J., Kehrt, M., Monte, C., Müller, R., & Steiger, A. (2015). Characterization of a Large-Area Pyroelectric Detector from 300 GHz to 30 THz. Journal of Infrared Millimeter and Terahertz Waves, 36, 654–661. https://doi.org/10.1007/s10762-015-0163-7

Multi-Plastics. (n.d.). LCF® 4000 clear polyester. Retrieved February 25, 2024, from https://multi-plastics.com/products/lcf-4000-clear-polyester/

Nakagawa, M., Okano, M., & Watanabe, S. (2022). Polarization-sensitive terahertz time-domain spectroscopy system without mechanical moving parts. Optics Express, 30(16), 29421. https://doi.org/10.1364/oe.460259

Nakanishi, A., & Satozono, H. (2020). Terahertz optical properties of wood–plastic composites. Applied Optics, 59(4), 904. https://doi.org/10.1364/ao.379758

Nakano, K., Suzuki, M., Abe, T., Mori, T., Takahashi, H., Irie, M., & Takinami, K. (2024). Optically Transparent Dual-Polarized Metasurface at 150 GHz Using Laser Cutting Technology. IEEE International Symposium on Antennas and Propagation and INC/USNC-URSI Radio Science Meeting, 1369–1370. https://doi.org/10.1109/ap-s/inc-usnc-ursi52054.2024.10687106

Nakata, Y., Urade, Y., Nakanishi, T., & Kitano, M. (2013). Plane-wave scattering by self-complementary metasurfaces in terms of electromagnetic duality and Babinet's principle. Physical Review B, 88(20). https://doi.org/10.1103/physrevb.88.205138

Nakata, Y., Fukawa, K., Nakanishi, T., Urade, Y., Okimura, K., & Miyamaru, F. (2019). Reconfigurable terahertz Quarter-Wave plate for helicity switching based on Babinet inversion of an anisotropic checkerboard metasurface. Physical Review Applied, 11(4). https://doi.org/10.1103/physrevapplied.11.044008

Nauroze, S. A., & Tentzeris, M. M. (2019). A thermally actuated fully Inkjet-Printed Origami-Inspired multilayer frequency selective surface with Continuous-Range tunability using Polyester-Based substrates. IEEE Transactions on Microwave Theory and Techniques, 67(12), 4944–4954. https://doi.org/10.1109/tmtt.2019.2946074

Neshat, M., & Armitage, N. P. (2012). Improved measurement of polarization state in terahertz polarization spectroscopy. Optics Letters, 37(11), 1811. https://doi.org/10.1364/ol.37.001811

Neshat, M., & Armitage, N. P. (2012b). Terahertz time-domain spectroscopic ellipsometry: instrumentation and calibration. Optics Express, 20(27), 29063. https://doi.org/10.1364/oe.20.029063

Neu, J., & Schmuttenmaer, C. A. (2018). Tutorial: An introduction to terahertz time domain spectroscopy (THz-TDS). Journal of Applied Physics, 124(23). https://doi.org/10.1063/1.5047659

Nivas, J. J., Papari, G. P., Hu, M., Purushothaman, A., Mazaheri, Z., Amoruso, S., & Andreone, A. (2025). Femtosecond laser direct writing of complementary THz metasurfaces using a structured vortex beam. Optics & Laser Technology, 181, 111831. https://doi.org/10.1016/j.optlastec.2024.111831

Norris, T., Cheng, G., Choi, W. J., Jang, H., & Kotov, N. A. (2019). Terahertz time-domain polarimetry for generalized anistropic and chiral materials," Proceedings Volume 10917, Terahertz, RF, Millimeter, and Submillimeter-Wave Technology and Applications XII; 1091704. https://doi.org/10.1117/12.2516383

Nouman, M. T., Hwang, J. H., & Jang, J. (2016). Ultrathin Terahertz Quarter-wave plate based on Split Ring Resonator and Wire Grating hybrid Metasurface. Scientific Reports, 6, 39062. https://doi.org/10.1038/srep39062

Ornik, J., Zhang, Y., Schneider, M., Taherkhani, M., Alaboz, H., & Koch, M. (2019). THz gratings produced by laser cutting. 44th International Conference on Infrared, Millimeter, and Terahertz Waves (IRMMW-THz), 1–2. https://doi.org/10.1109/irmmw-thz.2019.8873930

Ortiz-Martinez, M., Castro-Camus, E., & Hernandez-Serrano, A. I. (2019). Guided-Mode filters for terahertz frequencies fabricated by 3D printing. Journal of Infrared Millimeter and Terahertz Waves, 40, 731–737. https://doi.org/10.1007/s10762-019-00602-3

Pan, W., Huang, C., Chen, P., Pu, M., Ma, X., & Luo, X. (2013). A beam steering horn antenna using active frequency selective surface. IEEE Transactions on Antennas and Propagation, 61(12), 6218–6223. https://doi.org/10.1109/tap.2013.2280592

Papari, G. P., Nivas, J. J., Hu, M., Amoruso, S., & Andreone, A. (2023). Lumped-element models of THz metasurfaces based on split-ring resonators and their complementary form. Optics Continuum, 2(4), 801. https://doi.org/10.1364/optcon.480940

Paraipan, A. A., Gonzalez-Hernandez, D., Reddy, I. V. a. K., Balistreri, G., Zanotto, L., Shalaby, M., Morandotti, R., Liberale, C., & Razzari, L. (2024). Scanless spectral

imaging of terahertz vortex beams generated by High-Resolution 3D-Printed spiral phase plates. Small Science, 4(12), 2400352. https://doi.org/10.1002/smsc.202400352

Park, J. W., Kang, B. H., & Kim, H. J. (2019). A review of low-temperature solution-processed metal oxide thin-film transistors for flexible electronics. Advanced Functional Materials, 30(20), 1904632. https://doi.org/10.1002/adfm.201904632

Penchev, P., Shang, X., Dimov, S., & Lancaster, M. (2016). Novel manufacturing route for scale up production of Terahertz Technology devices. Journal of Micro and Nano-Manufacturing, 4(2), 021002. https://doi.org/10.1115/1.4032688

Pinnock, S. W., Roh, S., Biesner, T., Pronin, A. V., & Dressel, M. (2023). Generation of THZ vortex beams and interferometric determination of their topological charge. IEEE Transactions on Terahertz Science and Technology, 13(1), 44–49. https://doi.org/10.1109/tthz.2022.3221369

Poojali, J., Ray, S., Pesala, B., Chittit, K., & Arunachalam, K. (2017). Quad band Polarization Insensitive Millimeter Wave Frequency Selective Surface for Remote Sensing. IEEE Antennas and Wireless Propagation Letters, 16, 1796-1799. https://doi.org/10.1109/lawp.2017.2679204

Pryce, I. M., Aydin, K., Kelaita, Y. A., Briggs, R. M., & Atwater, H. A. (2011). Characterization of the tunable response of highly strained compliant optical metamaterials. Philosophical Transactions of the Royal Society a Mathematical Physical and Engineering Sciences, 369(1950), 3447–3455. https://doi.org/10.1098/rsta.2011.0122

Radivon, A. V., Katyba, G. M., Raginov, N. I., Chernykh, A. V., Ezerskii, A. S., Tsiplakova, E. G., Rakov, I. I., Paukov, M. I., Starchenko, V. V., Arsenin, A. V., Spector, I. E., Zaytsev, K. I., Krasnikov, D. V., Petrov, N. V., Nasibulin, A. G., Volkov, V., & Burdanova, M. G. (2024). Expanding THz Vortex Generation Functionality with Advanced Spiral Zone Plates Based on Single-Walled Carbon Nanotube Films. Advanced Optical Materials, 12(17), 2303282. https://doi.org/10.1002/adom.202303282

Raffoul, J., LeMaster, D., & Hirakawa, K. (2022). Framework for improving DoLP and AoLP reconstruction quality in microgrid polarimeters. Optics Express, 30(26), 48004. https://doi.org/10.1364/oe.475379

Rohrbach, D., Kang, B. J., & Feurer, T. (2021). 3D-printed THz wave- and phaseplates. Optics Express, 29(17), 27160. https://doi.org/10.1364/oe.433881

Rouvalis, E., Renaud, C. C., Moodie, D. G., Robertson, M. J., & Seeds, A. J. (2010). Traveling-wave Uni-Traveling Carrier Photodiodes for continuous wave THz generation. Optics Express, 18(11), 11105. https://doi.org/10.1364/oe.18.011105

Sahu, M., & Chaudhuri, P. R. (2024). Frequency selective surface for third harmonic generation using complementary split ring resonator at THz frequencies. Journal of Modern Optics, 71(7–8), 255–265. https://doi.org/10.1080/09500340.2024.2407072

Salem, B., Morris, D., Aimez, V., Beerens, J., Beauvais, J., & Houde, D. (2005). Pulsed photoconductive antenna terahertz sources made on ion-implanted GaAs substrates. Journal of Physics Condensed Matter, 17(46), 7327. https://doi.org/10.1088/0953-8984/17/46/016

Schneider, A., Neis, M., Stillhart, M., Ruiz, B., Khan, R. U. A., & Günter, P. (2006). Generation of terahertz pulses through optical rectification in organic DAST crystals: theory and experiment. Journal of the Optical Society of America B, 23(9), 1822. https://doi.org/10.1364/josab.23.001822

Schlecht, M. T., Preu, S., Malzer, S., & Weber, H. B. (2019). An efficient Terahertz rectifier on the graphene/SiC materials platform. Scientific Reports, 9, 11205. https://doi.org/10.1038/s41598-019-47606-6

Schuster, F., Coquillat, D., Videlier, H., Sakowicz, M., Teppe, F., Dussopt, L., Giffard, B., Skotnicki, T., & Knap, W. (2011). Broadband terahertz imaging with highly sensitive silicon CMOS detectors. Optics Express, 19(8), 7827. https://doi.org/10.1364/oe.19.007827

Sebastian, R. R., Ahmad, R., Lafrenière-Greig, J., Ropagnol, X., & Blanchard, F. (2024). AI-assisted ultrafast and efficient terahertz spectrometer using frequency selective surfaces. Proceedings Volume 13203, Sensors and Communication Technologies in the 1 GHz to 10 THz Band; 132030A. https://doi.org/10.1117/12.3030981

Sebastian, R., Ahmad, R., Lafrenière-Greig, J., Ropagnol, X., & Blanchard, F. (2026). Real-Time material identification using a fast and simplified AI-Assisted terahertz spectrometer. IEEE Transactions on Terahertz Science and Technology, 16(2), 131–140. https://doi.org/10.1109/tthz.2025.3603959

Selvanayagam, M., & Eleftheriades, G. V. (2013). Discontinuous electromagnetic fields using orthogonal electric and magnetic currents for wavefront manipulation. Optics Express, 21(12), 14409. https://doi.org/10.1364/OE.21.014409

Semenov, A., Cojocari, O., Hübers, H., Song, F., Klushin, A., & Müller, A. (2010). Application of Zero-Bias Quasi-Optical Schottky-Diode detectors for monitoring Short-Pulse and weak terahertz radiation. IEEE Electron Device Letters, 31(7), 674–676. https://doi.org/10.1109/led.2010.2048192

Shiri, Y., Guerboukha, H., & Mittleman, D. M. (2023). Terahertz Beam Steering with Curved Metasurfaces. Journal of Infrared Millimeter and Terahertz Waves, 44, 397–406. https://doi.org/10.1007/s10762-023-00918-1

Siday, T., Vabishchevich, P. P., Hale, L., Harris, C. T., Luk, T. S., Reno, J. L., Brener, I., & Mitrofanov, O. (2019). Terahertz Detection with Perfectly-Absorbing Photoconductive Metasurface. Nano Letters, 19(5), 2888–2896. https://doi.org/10.1021/acs.nanolett.8b05118

Silalahi, H. M., Chen, Y., Shih, Y., Chen, Y., Lin, X., Liu, J., & Huang, C. (2021). Floating terahertz metamaterials with extremely large refractive index sensitivities. Photonics Research, 9(10), 1970. https://doi.org/10.1364/prj.433335

Singh, S., Eisenmann, M., Aso, Y., & Somiya, K. (2025). Complete birefringence and Jones matrix characterization using arbitrary polarization. Optics Express, 33(8), 17462. https://doi.org/10.1364/oe.558774

Sizov, F., & Rogalski, A. (2010). THz detectors. Progress in Quantum Electronics, 34(5), 278–347. https://doi.org/10.1016/j.pquantelec.2010.06.002

Sobornytskyy, N., Lisauskas, A., Weickhmann, C., Jakobi, R., Semenov, A., Hubers, H., Muller, R., Hoehl, A., & Cojocari, O. (2013). Quasi optical Schottky diode detectors for fast ultra-wideband detection. 38th International Conference on Infrared, Millimeter, and TerahertzWaves (IRMMW-THz), 1–2. https://doi.org/10.1109/irmmw-thz.2013.6665618

Srinivasan, N., Caglayan, C., Nahar, N., & Sertel, K. (2017). High-resolution polarimetric THz imaging for biomedical applications. 2017 IEEE International Symposium on Antennas and Propagation & USNC/URSI National Radio Science Meeting, 793–794. https://doi.org/10.1109/apusncursinrsm.2017.8072439

Su, W., Guo, W., Wang, Z., Chen, P., Gong, C., Lin, L., & Liu, W. (2019). Printing flexible terahertz metasurface of optical transparency. Journal of Physics D: Applied Physics, 52(9), 095107. https://doi.org/10.1088/1361-6463/aaf84c

Sun, D., Qi, L., & Liu, Z. (2020). Terahertz broadband filter and electromagnetically induced transparency structure with complementary metasurface. Results in Physics, 16, 102887. https://doi.org/10.1016/j.rinp.2019.102887

Sushko, O., Pigeon, M., Donnan, R. S., Kreouzis, T., Parini, C. G., & Dubrovka, R. (2017). Comparative study of Sub-THZ FSS filters fabricated by inkjet printing, microprecision material printing, and Photolithography. IEEE Transactions on Terahertz Science and Technology, 7(2), 184–190. https://doi.org/10.1109/tthz.2017.2662582

Suzuki, M., & Tonouchi, M. (2005). Fe-implanted InGaAs photoconductive terahertz detectors triggered by 1.56μm femtosecond optical pulses. Applied Physics Letters, 86(16), 163504. https://doi.org/10.1063/1.1901817

Takano, K., Yokoyama, H., Ichii, A., Morimoto, I., & Hangyo, M. (2011). Wire-grid polarizer sheet in the terahertz region fabricated by nanoimprint technology. Optics Letters, 36(14), 2665. https://doi.org/10.1364/ol.36.002665

Takano, K., Miyamaru, F., Akiyama, K., Miyazaki, H., Takeda, M. W., Abe, Y., Tokuda, Y., Ito, H., & Hangyo, M. (2014). Crossover from capacitive to inductive electromagnetic responses in near self-complementary metallic checkerboard patterns. Optics Express, 22(20), 24787. https://doi.org/10.1364/oe.22.024787

Takazato, A., Kamakura, M., Matsui, T., Kitagawa, J., & Kadoya, Y. (2007). Terahertz wave emission and detection using photoconductive antennas made on low-temperature-grown InGaAs with 1.56μm pulse excitation. Applied Physics Letters, 91(1), 011102. https://doi.org/10.1063/1.2754370

Takazato, A., Kamakura, M., Matsui, T., Kitagawa, J., & Kadoya, Y. (2007b). Detection of terahertz waves using low-temperature-grown InGaAs with 1.56μm pulse excitation. Applied Physics Letters, 90(10), 101119. https://doi.org/10.1063/1.2712503

Taleb, F., Al-Naib, I., & Koch, M. (2020). Free-Standing complementary asymmetric metasurface for terahertz sensing applications. Sensors, 20(8), 2265. https://doi.org/10.3390/s20082265

Tan, H., Meng, J., & Crozier, K. B. (2024). Multianalyte Detection with Metasurface-Based Midinfrared Microspectrometer. ACS Sensors, 9(11), 5839–5847. https://doi.org/10.1021/acssensors.4c01220

Tani, M., Matsuura, S., Sakai, K., & Nakashima, S. (1997). Emission characteristics of photoconductive antennas based on low-temperature-grown GaAs and semi-insulating GaAs. Applied Optics, 36(30), 7853. https://doi.org/10.1364/ao.36.007853

Tani, M., Herrmann, M., & Sakai, K. (2002). Generation and detection of terahertz pulsed radiation with photoconductive antennas and its application to imaging. Measurement Science and Technology, 13(11), 1739. https://doi.org/10.1088/0957-0233/13/11/310

Tao, H., Landy, N. I., Bingham, C. M., Zhang, X., Averitt, R. D., & Padilla, W. J. (2008). A metamaterial absorber for the terahertz regime: design, fabrication and characterization. Optics Express, 16(10), 7181. https://doi.org/10.1364/oe.16.007181

TeraSense. (2018, April 11). *Imaging of beams from TDS and FDS spectroscopy systems*. https://terasense.com/applications/tds-fds-systems/

TeraSense. (n.d.). Terahertz imaging cameras. TeraSense Inc. https://terasense.com/products/sub-thz-imaging-cameras/

Thavamani, D., Sivasamy, R., Nair, P., Sahoo, A., & Krishnan, S. (2024). Design and fabrication of sub-terahertz filter using maskless femto second laser micromachining

process. Optics Communications, 554, 130163. https://doi.org/10.1016/j.optcom.2023.130163

Tian, Q., Xu, H., Wang, Y., Liang, Y., Tan, Y., Ning, X., Yan, L., Du, Y., Li, R., Hua, J., Huang, W., & Tang, C. (2021). Efficient generation of a high-field terahertz pulse train in bulk lithium niobate crystals by optical rectification. Optics Express, 29(6), 9624. https://doi.org/10.1364/oe.419709

Tokizane, Y., Kristensen, M. H., Ohno, S., Degert, J., Freysz, E., Brasselet, E., Yasui, T., & Abraham, E. (2025). Frequency-multiplexed terahertz multiple vortex beam generation. Applied Physics Letters, 126(19), 191106. https://doi.org/10.1063/5.0261433

Tonouchi, M. (2007). Cutting-edge terahertz technology. Nature Photonics, 1, 97–105. https://doi.org/10.1038/nphoton.2007.3

Tóth, G., Polónyi, G., & Hebling, J. (2023). Tilted pulse front pumping techniques for efficient terahertz pulse generation. Light Science & Applications, 12, 256. https://doi.org/10.1038/s41377-023-01293-1

Van Der Valk, N. C. J., Van Der Marel, W. a. M., & Planken, P. C. M. (2005). Terahertz polarization imaging. Optics Letters, 30(20), 2802. https://doi.org/10.1364/ol.30.002802

Van Exter, M., Fattinger, C., & Grischkowsky, D. (1989). Terahertz time-domain spectroscopy of water vapor. Optics Letters, 14(20), 1128. https://doi.org/10.1364/ol.14.001128

Vegesna, S., Zhu, Y., Zhao, Y., Fan, Z., Bernussi, A., & Saed, M. (2014). Terahertz frequency selective surface with reconfigurable polarization characteristics using vanadium dioxide. Journal of Electromagnetic Waves and Applications, 28(1), 83–90. https://doi.org/10.1080/09205071.2013.857278

Voisiat, B., Bičiūnas, A., Kašalynas, I., & Račiukaitis, G. (2011). Band-pass filters for THz spectral range fabricated by laser ablation. Applied Physics A, 104, 953–958. https://doi.org/10.1007/s00339-011-6456-3

Voisiat, B., Indrišiūnas, S., Šniaukas, R., Minkevičius, L., Kašalynas, I., & Račiukaitis, G. (2017). Laser processing for precise fabrication of the THz optics. Proceedings Volume 10091, Laser Applications in Microelectronic and Optoelectronic Manufacturing (LAMOM) XXII; 100910F. https://doi.org/10.1117/12.2253634

Vugmeyster, I. D., Whitaker, J. F., & Merlin, R. (2012). GaP based terahertz time-domain spectrometer optimized for the 5-8 THz range. Applied Physics Letters, 101(18). https://doi.org/10.1063/1.4764545

Walther, M., Ortner, A., Meier, H., Löffelmann, U., Smith, P. J., & Korvink, J. G. (2009). Terahertz metamaterials fabricated by inkjet printing. Applied Physics Letters, 95(25), 251107. https://doi.org/10.1063/1.3276544

Wang, G., Tian, H., Wang, J., Li, S., Guo, W., & Zhou, Z. (2022). Electronically controlled flexible terahertz metasurface based on the loss modulation of strontium titanate. Optics Letters, 47(1), 94. https://doi.org/10.1364/ol.446069

Wang, X., Cui, Y., Sun, W., Ye, J., & Zhang, Y. (2010). Terahertz polarization real-time imaging based on balanced electro-optic detection. Journal of the Optical Society of America A, 27(11), 2387. https://doi.org/10.1364/josaa.27.002387

Wang, Z., Wang, G., Hu, B., Liu, W., Huang, J., Xiong, C., Zhang, Y., Liu, J., & Wang, Y. (2022). Fast-printed, large-area and low-cost terahertz metasurface using laser-induced graphene. Carbon, 187, 256–265. https://doi.org/10.1016/j.carbon.2021.11.010

Wang, Z., Yue, S., Hou, Y., Wang, R., Zhang, S., Fu, Y., Li, M., Xue, M., Zhang, K., & Zhang, Z. (2025). Full-Stokes polarimetric detection infrared metalens with reduced coma under a large angle of incidence based on the quadratic phase. Optical Materials Express, 15(10), 2362. https://doi.org/10.1364/ome.574709

Ward, D. W., Beers, J. D., Feurer, T., Statz, E. R., Stoyanov, N. S., & Nelson, K. A. (2004). Coherent control of phonon-polaritons in a terahertz resonator fabricated with femtosecond laser machining. Optics Letters, 29(22), 2671. https://doi.org/10.1364/ol.29.002671

Ward, D., Statz, E., & Nelson, K. (2006). Fabrication of polaritonic structures in $LiNbO_3$ and LiTaO3 using femtosecond laser machining. Applied Physics A, 86, 49–54. https://doi.org/10.1007/s00339-006-3721-y

Ward, J., Schlecht, E., Chattopadhyay, G., Maestrini, A., Gill, J., Maiwald, F., Javadi, H., & Mehdi, I. (2004). Capability of THz sources based on Schottky diode frequency multiplier chains. 2004 IEEE MTT-S International Microwave Symposium Digest (IEEE Cat. No.04CH37535), 1587–1590. https://doi.org/10.1109/mwsym.2004.1338884

Warren, A. C., Katzenellenbogen, N., Grischkowsky, D., Woodall, J. M., Melloch, M. R., & Otsuka, N. (1991). Subpicosecond, freely propagating electromagnetic pulse generation and detection using GaAs:As epilayers. Applied Physics Letters, 58(14), 1512–1514. https://doi.org/10.1063/1.105162

Watanabe, S. (2018). Terahertz Polarization Imaging and its applications. Photonics, 5(4), 58. https://doi.org/10.3390/photonics5040058

Wen, J., Zhao, Q., Peng, R., Yao, H., Qing, Y., Yin, J., & Ren, Q. (2022). Progress in water-based metamaterial absorbers: a review. Optical Materials Express, 12(4), 1461. https://doi.org/10.1364/ome.455723

Wietzke, S., Jansen, C., Jung, T., Reuter, M., Baudrit, B., Bastian, M., Chatterjee, S., & Koch, M. (2009). Terahertz time-domain spectroscopy as a tool to monitor the glass transition in polymers. Optics Express, 17(21), 19006. https://doi.org/10.1364/oe.17.019006

Winnerl, S., Peter, F., Nitsche, S., Dreyhaupt, A., Zimmermann, B., Wagner, M., Schneider, H., Helm, M., & Kohler, K. (2008). Generation and detection of THZ radiation with scalable antennas based on GAAS substrates with different carrier lifetimes. IEEE Journal of Selected Topics in Quantum Electronics, 14(2), 449–457. https://doi.org/10.1109/jstqe.2007.910104

Withayachumnankul, W., Fischer, B. M., & Abbott, D. (2008). Numerical removal of water vapour effects from terahertz time-domain spectroscopy measurements. Proc. A 1 September, 464(2097), 2435–2456. https://doi.org/10.1098/rspa.2007.0294

Withayachumnankul, W., Fischer, B. M., Lin, H., & Abbott, D. (2008b). Uncertainty in terahertz time-domain spectroscopy measurement. Journal of the Optical Society of America B, 25(6), 1059. https://doi.org/10.1364/josab.25.001059

Wolff, L. B., & Andreou, A. G. (1995). Polarization camera sensors. Image and Vision Computing, 13(6), 497–510. https://doi.org/10.1016/0262-8856(95)94383-b

Wood, C. D., Hatem, O., Cunningham, J. E., Linfield, E. H., Davies, A. G., Cannard, P. J., Robertson, M. J., & Moodie, D. G. (2010). Terahertz emission from metal-organic chemical vapor deposition grown Fe:InGaAs using 830 nm to 1.55 μm excitation. Applied Physics Letters, 96(19), 194104. https://doi.org/10.1063/1.3427191

Wu, J., Xu, X., & Wei, L. (2020). Active metasurfaces for manipulatable terahertz technology*. Chinese Physics B, 29(9), 094202. https://doi.org/10.1088/1674-1056/aba613

Wu, L., Zhong, S., Huang, J., & Liu, T. (2019). Broadband Frequency-Selective rasorber with Varactor-Tunable interabsorption band transmission window. IEEE Transactions on Antennas and Propagation, 67(9), 6039–6050. https://doi.org/10.1109/tap.2019.2916739

Wu, Q., & Zhang, X. (1996). Design and characterization of traveling-wave electrooptic terahertz sensors. IEEE Journal of Selected Topics in Quantum Electronics, 2(3), 693–700. https://doi.org/10.1109/2944.571769

Wu, X., Ma, J., Zhang, B., Chai, S., Fang, Z., Xia, C., Kong, D., Wang, J., Liu, H., Zhu, C., Wang, X., Ruan, C., & Li, Y. (2018). Highly efficient generation of 02 mJ terahertz

pulses in lithium niobate at room temperature with sub-50 fs chirped Ti:sapphire laser pulses. Optics Express, 26(6), 7107. https://doi.org/10.1364/oe.26.007107

Wu, Z., Chen, X., Zhang, Z., Heng, L., Wang, S., & Zou, Y. (2019b). Design and optimization of a flexible water-based microwave absorbing metamaterial. Applied Physics Express, 12(5), 057003. https://doi.org/10.7567/1882-0786/ab0f66

Xia, B. G., Zhang, D. H., Meng, J., Huang, J., Yao, C. F., & Zhang, J. S. (2013). Terahertz FSS for space borne passive remote sensing application. Electronics Letters, 49(22), 1398–1399. https://doi.org/10.1049/el.2013.2407

Xiao, H., Shi, M., & Chen, J. (2019). Electromagnetic function textiles. In IntechOpen eBooks. https://doi.org/10.5772/intechopen.85586

Xu, K., Bayati, E., Oguchi, K., Watanabe, S., Winebrenner, D. P., & Arbab, M. H. (2020). Terahertz time-domain polarimetry (THz-TDP) based on the spinning E-O sampling technique: determination of precision and calibration. Optics Express, 28(9), 13482. https://doi.org/10.1364/oe.389651

Xu, K., Harris, Z. B., & Arbab, M. H. (2023). Polarimetric imaging of back-scattered terahertz speckle fields using a portable scanner. Optics Express, 31(7), 11308. https://doi.org/10.1364/oe.482733

Xu, K., & Arbab, M. H. (2024a). Terahertz polarimetric imaging of biological tissue: Monte Carlo modeling of signal contrast mechanisms due to Mie scattering. Biomedical Optics Express, 15(4), 2328. https://doi.org/10.1364/boe.515623

Xu, K., Harris, Z. B., Vahey, P., & Arbab, M. H. (2024b). THz polarimetric imaging of carbon Fiber-Reinforced composites using the portable handled Spectral Reflection (PHASR) scanner. Sensors, 24(23), 7467. https://doi.org/10.3390/s24237467

Xu, X., Xu, R., & Lin, Y. (2021). Tunable terahertz double split-ring metamaterial with polarization-sensitive characteristic. Optics & Laser Technology, 141, 107103. https://doi.org/10.1016/j.optlastec.2021.107103

Yadav, R., Ludwig, F., Faridi, F. R., Klopf, J. M., Roskos, H. G., Preu, S., & Penirschke, A. (2023). State-of-the-Art room temperature operable Zero-Bias Schottky Diode-Based Terahertz Detector up to 5.56 THz. Sensors, 23(7), 3469. https://doi.org/10.3390/s23073469

Yan, R., Arezoomandan, S., Sensale-Rodriguez, B., & Xing, H. G. (2016). Exceptional terahertz wave modulation in graphene enhanced by frequency selective surfaces. ACS Photonics, 3(3), 315–323. https://doi.org/10.1021/acsphotonics.5b00639

Yang, F., Tan, T. C., Prakash, S., Kumar, A., Ariando, A., Singh, R., Wang, N., & Pitchappa, P. (2024). Reconfigurable Wide-Angle Beam-Steering terahertz metasurfaces based on

vanadium dioxide. Advanced Optical Materials, 12(9), 2302047. https://doi.org/10.1002/adom.202302047

Yang, R., Lou, J., Zhang, F., Zhu, W., Xu, J., Cai, T., Fu, Q., Li, H., & Fan, Y. (2021). Active Control of Terahertz Toroidal Excitations in a Hybrid Metasurface with an Electrically Biased Silicon Layer. Advanced Photonics Research, 2(12), 2100103. https://doi.org/10.1002/adpr.202100103

Yang, X., Zeng, Y., Liu, X., Zhou, J., Gan, L., Chen, H., & Yu, J. (2020). Low-loss frequency selective surface for multi-band THz transmission measurement. Microwave and Optical Technology Letters, 62(5), 1860–1865. https://doi.org/10.1002/mop.32246

Yatooshi, T., Ishikawa, A., & Tsuruta, K. (2015). Terahertz wavefront control by tunable metasurface made of graphene ribbons. Applied Physics Letters, 107(5), 053105. https://doi.org/10.1063/1.4927824

Yeh, K., Hoffmann, M. C., Hebling, J., & Nelson, K. A. (2007). Generation of 10μJ ultrashort terahertz pulses by optical rectification. Applied Physics Letters, 90(17), 171121. https://doi.org/10.1063/1.2734374

Youn, Y., Omar, A. A., Kim, D., Chang, S., & Hong, W. (2023). Low-Profile wideband D-Band absorber utilizing resistive Thin-Film Screen-Printing. IEEE Transactions on Components Packaging and Manufacturing Technology, 13(4), 580–582. https://doi.org/10.1109/tcpmt.2023.3271962

Yudistira, H. T., Tenggara, A. P., Nguyen, V. D., Kim, T. T., Prasetyo, F. D., Choi, C., Choi, M., & Byun, D. (2013). Fabrication of terahertz metamaterial with high refractive index using high-resolution electrohydrodynamic jet printing. Applied Physics Letters, 103(21), 211106. https://doi.org/10.1063/1.4832197

Yurduseven, O., Ye, S., Fromenteze, T., Wiley, B. J., & Smith, D. R. (2019). 3D conductive polymer printed metasurface antenna for Fresnel focusing. Designs, 3(3), 46. https://doi.org/10.3390/designs3030046

Zhai, D., Yang, Y., Geng, Z., Cui, B., & Zhao, R. (2018). A High-Selectivity THZ filter based on a flexible polyimide film. IEEE Transactions on Terahertz Science and Technology, 8(6), 719–724. https://doi.org/10.1109/tthz.2018.2872414

Zhai, D., Hérault, E., Garet, F., & Coutaz, J. (2021). Terahertz generation from ZnTe optically pumped above and below the bandgap. Optics Express, 29(11), 17491. https://doi.org/10.1364/oe.421282

Zhan, Y., & Fan, C. (2023). Investigation on the tunable and polarization sensitive three-band terahertz graphene metamaterial absorber. Materials Research Express, 10(5), 055802. https://doi.org/10.1088/2053-1591/acd61d

Zhang, C., Hu, J., Dong, Y., Zeng, A., Huang, H., & Wang, C. (2021). High efficiency all-dielectric pixelated metasurface for near-infrared full-Stokes polarization detection. Photonics Research, 9(4), 583. https://doi.org/10.1364/prj.415342

Zhang, D., Matloubian, M., Kim, T., Fetterman, H., Chou, K., Praskash, S., Deshpandey, C., Bunshah, R., & Daly, K. (1991). Quasi-optical millimeter-wave band-pass filters using high-T/sub c/ superconductors. IEEE Transactions on Microwave Theory and Techniques, 39(9), 1493–1497. https://doi.org/10.1109/22.83823

Zhang, L., Zhong, H., Deng, C., Zhang, C., & Zhao, Y. (2009). Polarization sensitive terahertz time-domain spectroscopy for birefringent materials. Applied Physics Letters, 94(21), 211106. https://doi.org/10.1063/1.3143613

Zhang, L., Zhong, H., Deng, C., Zhang, C., & Zhao, Y. (2010). Characterization of birefringent material using polarization-controlled terahertz spectroscopy. Optics Express, 18(19), 20491. https://doi.org/10.1364/oe.18.020491

Zhang, L., Zhou, C., Liu, B., Ding, Y., Ahn, H., Chang, S., Duan, Y., Rahman, M. T., Xia, T., Chen, X., Liu, Z., & Ni, X. (2024). Real-time machine learning–enhanced hyperspectro-polarimetric imaging via an encoding metasurface. Science Advances, 10(36). https://doi.org/10.1126/sciadv.adp5192

Zhang, R., Cui, Y., Sun, W., & Zhang, Y. (2008). Polarization information for terahertz imaging. Applied Optics, 47(34), 6422. https://doi.org/10.1364/ao.47.006422

Zhang, S., Li, C., Ke, L., Fang, B., Lu, J., Ma, X., & Jing, X. (2023). All-dielectric terahertz wave metagrating lens based on 3D printing low refractive index material. Infrared Physics & Technology, 133, 104775. https://doi.org/10.1016/j.infrared.2023.104775

Zhang, X., Tian, Z., Yue, W., Gu, J., Zhang, S., Han, J., & Zhang, W. (2013). Broadband Terahertz Wave Deflection Based on C-shape Complex Metamaterials with Phase Discontinuities. Advanced Materials, 25(33), 4567–4572. https://doi.org/10.1002/adma.201204850

Zhang, Y., Qiao, S., Sun, L., Shi, Q. W., Huang, W., Li, L., & Yang, Z. (2014). Photoinduced active terahertz metamaterials with nanostructured vanadium dioxide film deposited by sol-gel method. Optics Express, 22(9), 11070. https://doi.org/10.1364/oe.22.011070

Zhang, Y., Qiao, S., Liang, S., Wu, Z., Yang, Z., Feng, Z., Sun, H., Zhou, Y., Sun, L., Chen, Z., Zou, X., Zhang, B., Hu, J., Li, S., Chen, Q., Li, L., Xu, G., Zhao, Y., & Liu, S. (2015). Gbps Terahertz External Modulator Based on a Composite Metamaterial with a Double-Channel Heterostructure. Nano Letters, 15(5), 3501–3506. https://doi.org/10.1021/acs.nanolett.5b00869

Zhang, Z., Dai, Z., Wang, Y., Chu, C., Su, Q., Kosareva, O., Zhang, N., Lin, L., & Liu, W. (2020). Fabricating THz spiral zone plate by high throughput femtosecond laser air

filament direct writing. Scientific Reports, 10, 13965. https://doi.org/10.1038/s41598-020-70997-w

Zhao, F., Li, Z., Li, S., Dai, X., Zhou, Y., Liao, X., Cao, J. C., Liang, G., Shang, Z., Zhang, Z., Wen, Z., Li, H., & Chen, G. (2022). Terahertz metalens of hyper-dispersion. Photonics Research, 10(4), 886. https://doi.org/10.1364/prj.439481

Zhao, H., Wang, X., He, J., Guo, J., Ye, J., Kan, Q., & Zhang, Y. (2017). High-efficiency terahertz devices based on cross-polarization converter. Scientific Reports, 7, 17882. https://doi.org/10.1038/s41598-017-18013-6

Zhao, H., Li, Y., Jia, G., Li, N., Ji, Z., & Gu, J. (2018). Comparing analysis of multispectral and polarimetric imaging for mid-infrared detection blindness condition. Applied Optics, 57(24), 6840. https://doi.org/10.1364/ao.57.006840

Zhao, Y., Ye, Y., Zhang, R., Ren, Y., & Ren, X. (2022b). Fabrication of frequency-selective surface by picosecond laser direct writing. Journal of Laser Applications, 34(3), 032013. https://doi.org/10.2351/7.0000641

Zhou, J., Chowdhury, D. R., Zhao, R., Azad, A. K., Chen, H., Soukoulis, C. M., Taylor, A. J., & O'Hara, J. F. (2012). Terahertz chiral metamaterials with giant and dynamically tunable optical activity. Physical Review B, 86(3), 035448. https://doi.org/10.1103/physrevb.86.035448

Zhou, X., Lu, Y., Liu, H., Wu, Q., Xu, X., Chen, L., Li, Z., Wang, R., Guo, J., & Xu, J. (2023). One-step precise machining of terahertz microstructures on chip-scale lithium niobate via laser dispersion engineering. Materials Today Physics, 35, 101102. https://doi.org/10.1016/j.mtphys.2023.101102

Zhu, X., Wu, L., Guo, Y., & Wu, W. (2014). Tunable graphene FSS for terahertz applications. IEEE Antennas and Propagation Society International Symposium (APSURSI), 2104–2105. https://doi.org/10.1109/aps.2014.6905379

Zhuldybina, M., Ropagnol, X., Trudeau, C., Bolduc, M., Zednik, R. J., & Blanchard, F. (2019). Contactless In Situ Electrical Characterization Method of Printed Electronic Devices with Terahertz Spectroscopy. Sensors, 19(3), 444. https://doi.org/10.3390/s19030444

Zhuldybina, M., Ropagnol, X., Bois, C., Zednik, R. J., & Blanchard, F. (2020). Printing accuracy tracking with 2D optical microscopy and super-resolution metamaterial-assisted 1D terahertz spectroscopy. npj Flexible Electronics, 4, 21. https://doi.org/10.1038/s41528-020-00083-8

Zhuldybina, M., Beliveau, L., Mansourian, M., Ropagnol, X., Trinh, N. D., Bois, C., & Blanchard, F. (2021). Mass-production of terahertz devices. 46th International Conference on Infrared, Millimeter and Terahertz Waves (IRMMW-THz), 1–2. https://doi.org/10.1109/irmmw-thz50926.2021.9566995

Zhuldybina, M., Ropagnol, X., & Blanchard, F. (2021b). Towards in-situ quality control of conductive printable electronics: a review of possible pathways. Flexible and Printed Electronics, 6(4), 043007. https://doi.org/10.1088/2058-8585/ac442d

Zuo, J., Bai, J., Choi, S., Basiri, A., Chen, X., Wang, C., & Yao, Y. (2023). Chip-integrated metasurface full-Stokes polarimetric imaging sensor. Light Science & Applications, 12, 218. https://doi.org/10.1038/s41377-023-01260-w